THE JOURNAL OF

PHYSICAL

CHEMISTRY

THE JOURNAL OF
PHYSICAL CHEMISTRY

Editorial Information

Instructions for authors are printed in the first issue of each volume. Please conform to these instructions when submitting manuscripts.

Manuscripts for publication should be submitted to *The Journal of Physical Chemistry,* Department of Chemistry, University of Minnesota, Minneapolis, Minn. 55455. Correspondence regarding **accepted papers and proofs** should be directed to the Editorial Department at the address below.

Page charges of $60.00 per page may be paid for papers published in this journal. Payment does not affect acceptance or scheduling of papers.

Bulk reprints or photocopies of individual articles are available. For information write to Business Operations, Books and Journals Division at the ACS Washington address.

Requests for **permission to reprint** should be directed to Permissions, Books and Journals Division at the ACS Washington address. The American Chemical Society and its Editors assume no responsibility for the statements and opinions advanced by contributors.

Subscription and Business Information

1977 Subscription rates—including surface postage

	U.S.	PUAS	Canada, Foreign
Member	$24.00	$33.00	$34.00
Nonmember	96.00	105.00	106.00
Supplementary material	15.00	19.00	20.00

Air mail and air freight rates are available from Membership & Subscription Services, at the address below.

New and renewal subscriptions should be sent with payment to the Office of the Controller at the ACS Washington address. **Changes of address** must include both old and new addresses with ZIP code and a recent mailing label. Send all address changes to Membership & Subscription Services. Please allow six weeks for change to become effective. **Claims for missing numbers** will not be allowed if loss was due to failure of notice of change of address to be received in the time specified: if claim is dated (a) North America—more than 90 days beyond issue date, (b) all other foreign—more than 1 year beyond issue date; or if the reason given is "missing from files". Hard copy claims are handled by Membership & Subscription Services.

Microfiche subscriptions are available at the same rates but are mailed first class to U.S. subscribers, air mail to the rest of the world. Direct all inquiries to Special Issues Sales, at the ACS Washington address or call (202) 872-4554. **Single issues** in hard copy and/or microfiche are available from Special Issues Sales at the ACS Washington address. Current year $4.75. Back issue rates available from Special Issues Sales. **Back volumes** are available in hard copy and/or microform. Write to Special Issues Sales at the ACS Washington address for further information. **Microfilm** editions of ACS periodical publications are available from volume 1 to the present. For further information, contact Special Issues Sales at the ACS Washington address. **Supplementary material** mentioned in the journal appears in the microfilm edition. Single copies may be ordered directly from Business Operations, Books and Journals Division, at the ACS Washington address.

	U.S.	PUAS, Canada	Other Foreign
Microfiche	$2.50	$3.00	$3.50
Photocopy			
1–7 pages	4.00	5.50	7.00
8–20 pages	5.00	6.50	8.00

Orders over 20 pages are available only on microfiche, 4 × 6 in., 24X, negative, silver halide. Orders must state photocopy or microfiche if both are available. Full bibliographic citation including names of all authors and prepayment are required. Prices are subject to change.

Notice to Authors last printed in the issue of January 13, 1977

THE JOURNAL OF

PHYSICAL CHEMISTRY

■ Supplementary and/or miniprint material for this paper is available separately (consult the masthead page
for ordering information); it will also appear following the paper in the microfilm edition of this journal.

* In papers with more than one author, the asterisk indicates the name of the author to whom inquiries about
the paper should be addressed.

AUTHOR INDEX

A Study of Chemi-ionization in the Reaction of Oxygen Atoms with Acetylene

C. Vinckier,[†] Michael P. Gardner,[‡] and Kyle D. Bayes*

Department of Chemistry, University of California, Los Angeles, California 90024 (Received May 27, 1977)

Publication costs assisted by the National Science Foundation

The saturation current method has been used to measure the rate of chemi-ion formation during the reaction of oxygen atoms with acetylene in a low pressure flow system. For comparison, the vacuum ultraviolet chemiluminescence was also monitored. Both the rate of chemi-ionization and the chemiluminescence intensity were proportional to the square of the oxygen atom concentration times the first power of the acetylene concentration. The number of chemi-ions formed per acetylene molecule reacted can be expressed as, $\Phi_i = \{(2.3 \pm 0.9) \times 10^{-19} \text{ cm}^3 \text{ molecules}^{-1}\}[O]$. The quenching of chemi-ion formation by molecular oxygen followed a Stern–Volmer law with a half-quenching concentration of O_2 of 1.8×10^{14} molecules cm^{-3}. While the rate of chemi-ion formation was independent of total pressure (3–7 Torr of He), substituting a few percent of Ar, N_2, CO, CO_2, or CF_4 for He resulted in significant increases in ion formation. Similar effects were observed on the chemiluminescence. A general mechanism of chemi-ionization is discussed. At least two intermediates, probably electronically excited, appear to be necessary to explain the above observations. The mechanisms of chemi-ionization and vacuum ultraviolet chemiluminescence appear to be very similar.

Introduction

The ion concentration in many hydrocarbon flames is much larger than expected for thermodynamic equilibrium at the flame temperature.[1-3] This has been attributed to chemi-ionization, which is a chemical reaction between neutral species that is sufficiently energetic to result in ionic products.

Chemi-ionization has also been observed in the reaction of oxygen atoms with hydrocarbons, especially acetylene.[4-7] Since in these systems the gas is essentially at room temperature, all spontaneous ionization must be the result of nonequilibrium processes. An understanding of the acetylene system is important because many hydrocarbons give acetylene as an intermediate when they burn and because the ion yield per carbon atom is larger for acetylene than for other fuels.

Previous studies have not established the overall rate law for chemi-ionization. However, there is good evidence

that HCO^+ is the primary chemi-ion in the acetylene–oxygen atom system[7] and that reaction 1 is the major

$$O + CH \rightarrow HCO^+ + e^- \tag{1}$$

chemi-ionization reaction.[8]

The overall kinetics of the acetylene–oxygen atom reaction have been studied and several intermediates, such as CH_2, HC_2O, and C_3H_3, have been detected.[9-19] Also CH, in both its ground and excited states, can be detected,[20] but the mechanism of CH formation is not understood.

The present study uses the saturation current technique[21] to measure the rate of chemi-ionization. This involves applying sufficient electric field to the reacting gases to collect all of the ions being formed, while avoiding high fields which can cause secondary ionization. For comparison, the vacuum ultraviolet chemiluminescence has also been monitored. This emission occurs from several electronically excited states of CO, thought to be formed in reaction 2.[22-25] Both chemi-ionization and chemilu-

$$O + CCO \rightarrow CO^* + CO \tag{2}$$

minescence in the vacuum ultraviolet represent very energetic reaction paths (6–8 eV) and it has been noted

† Present address: Katholieke Universiteit Leuven, Departement Scheikunde, Celestijnenlaan 200F, 3030 Heverlee, Belgium.
‡ Present address: TRW Systems, One Space Park, Redondo Beach, Calif. 90278.
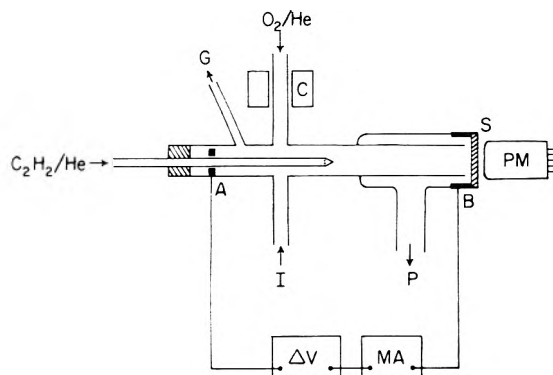
Figure 1. Schematic diagram of the apparatus. The O_2/He mixture flowed through a discharge in a microwave cavity, C, past the sapphire window, S, and out to a rotary pump, P (2.3 L s^{-1}). Other connections were for adding other gases, I, and for the pressure gages, G. The microammeter, MA, measured the saturation current and the photomultiplier, PM, measured the chemiluminescent intensity.

that there is probably a connection between the two.[26]

Apparatus

A schematic diagram of the apparatus is given in Figure 1. The cylindrical Pyrex reactor had an inner diameter of 17 mm and a reaction zone of approximately 70 mm length. Two electrodes, A and B, were mounted well outside the reaction zone in order to avoid loss of oxygen atoms or other reactive species on the metal surfaces. Electrode A was a copper ring, while electrode B was the metal tube of a metal-to-sapphire window seal. An electrical voltage difference, ΔV, was applied between the two electrodes, and the resulting current was measured (Keithly, Model 153 microammeter). For small ΔV, the current increased with applied voltage. At larger ΔV, the current became independent of ΔV; this constant current is called the saturation current, i_s. It is interpreted as the region where all ions formed in the reaction zone are being collected at the electrodes.[21] At still higher fields, the current began to increase again due to secondary ionization; this region was avoided. As the experimental conditions were varied, ΔV was always varied to make sure that current measurements were being made within the plateau region, typically about 50 V wide. Varying the electrode spacing from 12 to 25 cm did not change the value of i_s. Saturation currents were achieved for reduced fields of about 12 townsend (1 td = 10^{-17} V cm^{-1} (molecules cm^{-3})$^{-1}$).

A sapphire window was mounted at the downstream end of the reaction zone and the chemiluminescence detected by a photomultiplier (EMI 6255 CD) having a cadmium photocathode. Air was excluded from the region between the window and the photomultiplier by a gentle flow of nitrogen at atmospheric pressure. The photomultiplier was sensitive only to the region 165–210 nm; spectroscopic studies have shown that for the acetylene–oxygen atom system, the emission in this spectral region is dominated by the fourth positive system of CO.[24]

The acetylene, as a 1% mixture in He, was introduced through the central Pyrex tube (5 mm o.d.) which had five radially directed pinholes at its tip. Oxygen atoms were generated by flowing a 0.5% O_2 in He mixture through a microwave discharge (2450 MHz, 50 W), and their concentration was determined by titration with a NO_2–O_2 mixture using the visual endpoint.[27] The linear flow velocity was about 10 m s^{-1} giving a residence time of 7 ms within the reaction zone. Using the known rate constant for the overall reaction and a stoichiometry of two oxygen atoms per acetylene molecule,[11,28] it can be calculated that
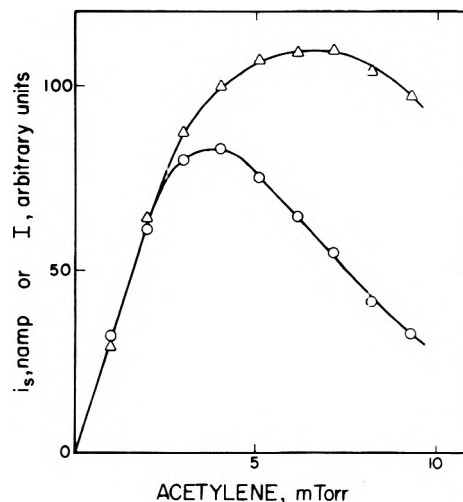
Figure 2. The saturation current i_s ($\triangle$) and the vacuum-ultraviolet chemiluminescence intensity I (O) as a function of acetylene pressure. The total pressure was 5 Torr, $[O]_0$ was 4.2 mTorr, and reaction time was 7 ms.

the total consumption of acetylene within 7 ms was 3.6% per mTorr of oxygen atoms present, while the oxygen atom consumption was 7.3% per mTorr of acetylene present. The average concentrations present during the reaction, $[O]$ and $[C_2H_2]$, were calculated from the initial concentrations, $[O]_0$ and $[C_2H_2]_0$, using one-half of the above consumption figures.

Total pressures were measured with a calibrated diaphragm gauge (Wallace and Tiernan). The addition of components was made by successive small decreases in the He flow followed by a small increase in the component mixture, so that the total pressure returned to its original value; these pressure increments, accurate to ±0.02 Torr, were followed with a quartz spiral manometer (Texas Instruments). All measurements were made at 23 ± 3 °C.

The slopes of straight lines were determined by the method of least squares and 90% confidence limits were calculated by the Student's t method.

Experimental Results

Both the saturation current, i_s, and the vacuum-ultraviolet chemiluminescence were linearly dependent on the initial acetylene concentration, up to approximately 3 mTorr (Figure 2). At higher acetylene concentrations, both quantities reached a maximum and then decreased, due probably to the increasing depletion of oxygen atoms during the 7-ms contact time. Subsequent measurements were made with 3 mTorr or less of acetylene.

Variation of the oxygen atom concentration showed an approximate quadratic dependence of both i_s and the vacuum-ultraviolet chemiluminescence on $[O]$. The log–log plot in Figure 3 gives measurements at 3, 5, and 7 Torr total pressure; no pressure dependence is evident for either phenomenon. Least-square lines have slopes of 1.76 ± 0.15 for i_s and 1.83 ± 0.20 for the vacuum-ultraviolet emission.

This approximate second-order dependence on oxygen atoms is complicated by the molecular oxygen that is also present. Since it was observed that the chemi-ionization was inhibited by additional amounts of O_2, quantitative measurements on this effect were made. Simple Stern–Volmer plots, as shown in Figure 4, were linear when plotted against the total molecular oxygen, both that added as O_2 and the undissociated oxygen that had been through the discharge. The intercepts of these plots then should give the reciprocal of the ionization current in the absence of O_2, $(i_s)_0$.
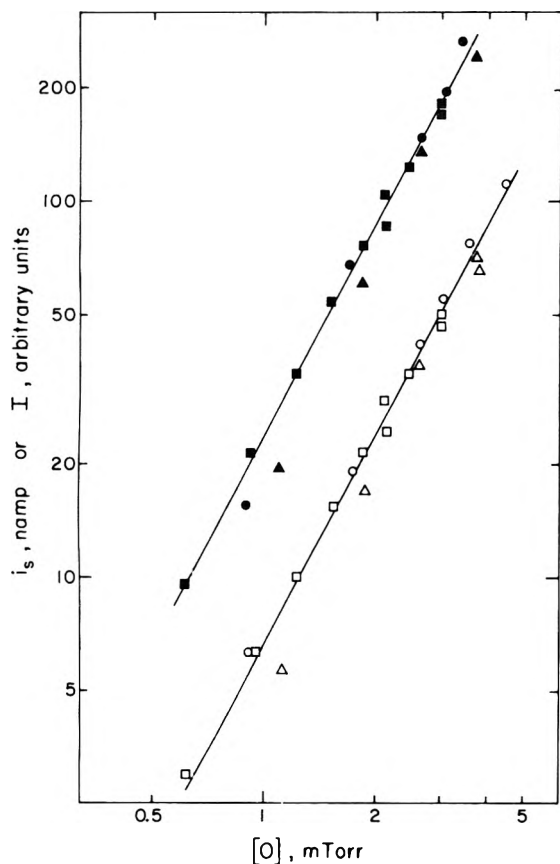
Figure 3. A log–log plot of the saturation current i_s (open symbols) and the vacuum–ultraviolet chemiluminescence intensity (filled symbols) as a function of the initial oxygen atom concentration for three different total pressures: 3 Torr ($\square$, $\blacksquare$); 5 Torr ($\triangle$, $\blacktriangle$); 7 Torr (O, ●). The reaction time was 7 ms and $[C_2H_2]_0$ was 3 mTorr.
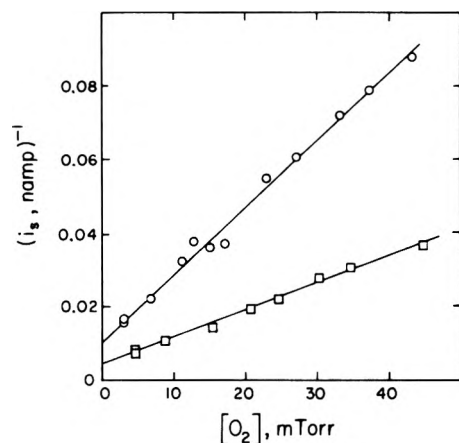
Figure 4. Stern–Volmer plots of the quenching of the saturation current by molecular oxygen. The total pressure was 5 Torr, the reaction time was 7 ms, the $[C_2H_2]_0$ was 3 mTorr, and $[O]_0$ was 5.7 mTorr ($\square$) or 3.8 mTorr (O).

When the values of $(i_s)_0$ (see Table I) are compared with the oxygen atom concentrations, the quadratic dependence suggested by Figure 3 is preserved. This is shown in Figure 5, where the quantity $(i_s)_0[O]^{-1}[C_2H_2]^{-1}$ is plotted against [O]. The linear dependence in Figure 5 combined with the initial linear portion of Figure 2 suggests that the rate law for chemi-ionization is

$$(i_s)_0 = k_i[C_2H_2][O]^2 Ve \tag{I}$$

$$k_i = (3.6 \pm 0.8) \times 10^{-32} \text{ cm}^6 \text{ molecules}^{-2} \text{ s}^{-1} \tag{II}$$

where V is the reaction volume for which i_s is measured, and e the electronic charge. This relationship can also be

TABLE I: Conditions Used to Determine Inhibition of Chemi-ionization by Molecular Oxygen

Run	Total pressure, Torr	$[O]_0$, mTorr	$[C_2H_2]_0$, mTorr	$(i_s)_0$, nA	$(i_s)_0[O]^{-1}[C_2H_2]^{-1}$, nA mTorr^{-2}
1	5	1.7	3	16.7	3.79
2	5	3.8	3	100	10.6
3	5	5.7	3	235	17.2
4	5	3.8	1.5	45	8.97
5	5	2.2	3	32	5.67
6	5	4.2	3	118	11.4
7	3	3.1	3	63	8.06
8	7	3.8	3	111	11.75
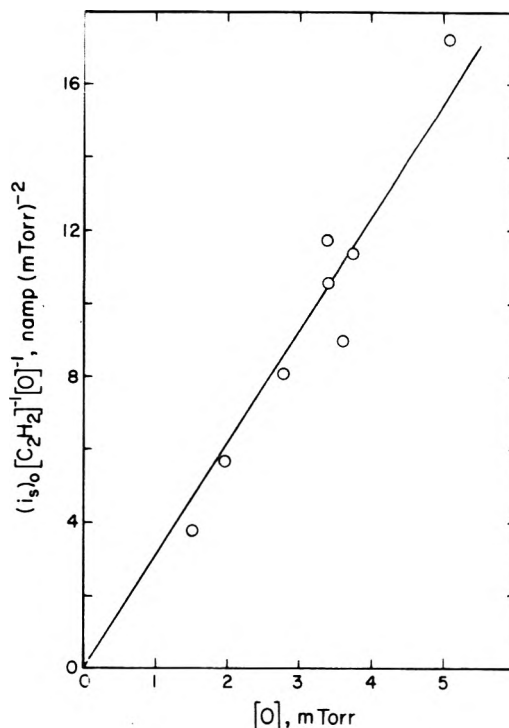
Figure 5. The extrapolated saturation current, $(i_s)_0$, divided by the product $[O][C_2H_2]$ as a function of the oxygen atom concentration. The reaction conditions are given in Table I. Both [O] and $[C_2H_2]$ are average values, corrected for partial consumption.

expressed as an ion yield, Φ_i, defined as the number of chemi-ions formed per acetylene molecule reacted:

$$\Phi_i = (i_s)_0/k_1[C_2H_2][O]Ve = \alpha[O] \tag{III}$$

$$\alpha = k_i/k_1 = (2.3 \pm 0.9) \times 10^{-19} \text{ cm}^3 \text{ molecule}^{-1} \tag{IV}$$

The constants k_i and α have been evaluated from the slope of the line in Figure 5. The uncertainties in the concentrations, k and k_1 all contribute to the large uncertainty in α.

By using expression I for the uninhibited ion current, it was possible to fit all of the molecular oxygen quenching data into a single Stern–Volmer plot, Figure 6. The fact that quenching data for a variety of different conditions fit reasonably well to a single straight line implies that to a good approximation

$$i_s = \frac{k_i[C_2H_2][O]^2 Ve}{1 + k_c[O_2]} \tag{V}$$

Note that the molecular oxygen quenching is a function of the absolute $[O_2]$, and not of the ratio $[O_2]/[O]$. When all of the data in Figure 6 are fitted to a line that is forced to go through unity, a value for k_q of $(5.7 \pm 0.3) \times 10^{-15}$ cm^3 molecule^{-1} results.
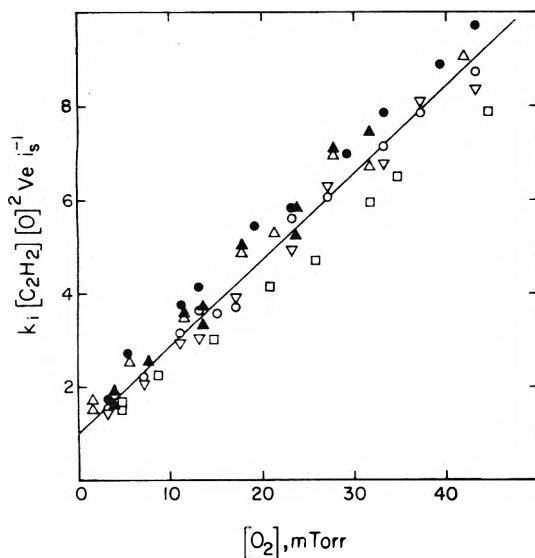
Figure 6. A test of eq V. The reaction conditions are given in Table I: run 1 (△); run 2 (○); run 3 (□); run 4 (●); run 7 (▲); run 8 (▽).
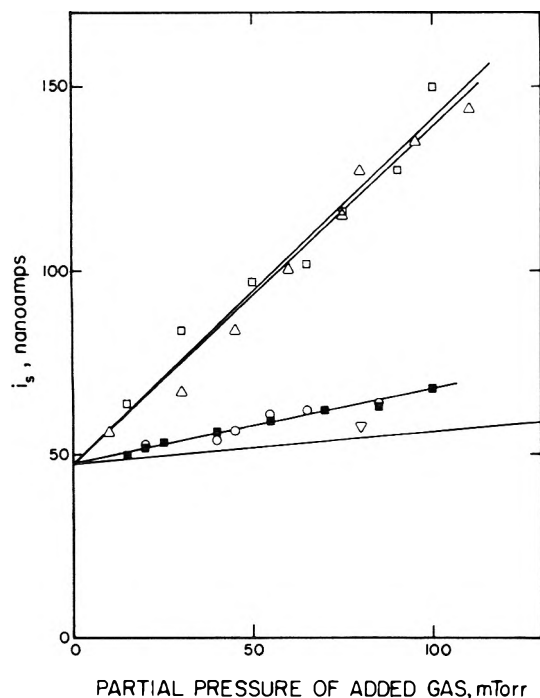
Figure 7. The saturation current as a function of the partial pressure of helium replaced with another gas: Ar (▽); N_2 (□); CO (○); CF_4 (△); CO_2 (□). The total pressure was 3 Torr, the reaction time 7 ms, and the initial concentrations $[O]_0 = 3.1$ mTorr and $[C_2H_2]_0 = 3$ mTorr.

Molecular oxygen also strongly quenched the vacuum-ultraviolet emission. Partial pressures of O_2 in the range of 5–10 mTorr reduced the vacuum-ultraviolet signal by 50%. However, unlike the results with the saturation current, the relative quenching did not follow a simple Stern–Volmer plot and it depended on both $[O_2]$ and $[O]$. The effects of O_2 on the chemiluminescence were not studied extensively.

The addition of other gases affected both i_s (Figure 7) and the vacuum-ultraviolet emission (Figure 8). For both of these figures, the total pressure was held constant, so that when 100 mTorr of CO_2 was added, for example, the He pressure was decreased by the same amount. For the pressure range studied, the added gases increased the saturation current in a linear manner. The data have been fitted to the equation

$$i_s = (i_s)_0 \{1 + k_M [M]\} \tag{VI}$$
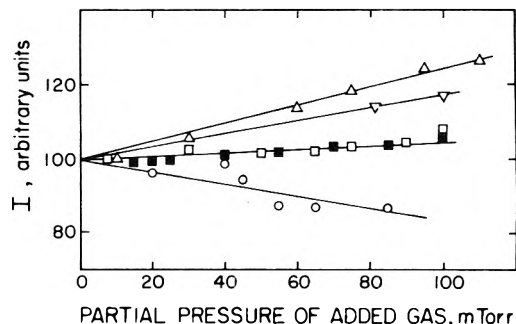
Figure 8. The vacuum-ultraviolet chemiluminescence intensity as a function of the partial pressure of helium replaced with another gas. The conditions and symbols are the same as in Figure 7.

TABLE II: Results of Fitting Eq VI to Figures 7 and 8

	k_M, Torr^{-1}	
Added gas	Saturation current	Chemiluminescence
Ar	1.9	1.7
N_2	4.3	0.45
CO	4.4	-1.6
CF_4	19	2.4
CO_2	20	0.56
H_2	-10	-10

with the resulting constants given in Table II. The effects of added gases on the vacuum-ultraviolet emission are similar and so the data of Figure 8 have been fitted to an equation analogous to (VI). It was established by direct titration that these gas substitutions did not alter the oxygen atom concentration significantly.

The increase in i_s as CO_2 is added (Figure 7) is not the result of a new chemi-ion being formed; by sampling and mass analyzing the ions using the apparatus described previously,[7] it was shown that HCO^+ is the primary chemi-ion both with and without 200 mTorr of added CO_2.

Discussion

Summary and Comparison with Previous Results. The three major results of this study are as follows: (a) that the total chemi-ionization is proportional to the first power of the acetylene concentration and the square of the oxygen atom concentration (eq I); (b) that the inhibition of chemi-ionization by molecular oxygen follows a simple Stern–Volmer law (eq V); and (c) that the substitution of one inert gas for another can have a significant effect on the chemi-ion yield (Figure 7). The first power dependence on acetylene is in accord with previous results[6] and with the large linear range of the flame ionization detector.[29] The second-power dependence on oxygen atoms has not been reported previously for chemi-ionization, but it has for the vacuum-ultraviolet chemiluminescence.[30,31] The significance of these results for the mechanism of chemi-ionization will be discussed later.

The observed ion yields (ions formed per acetylene molecule reacted) are within a factor of 10 of those reported previously. For the extrapolated conditions shown in Figure 5, the ion yields are (9 to 40) × 10^{-6}. Hand and Kistiakowsky[23] estimated a yield of 1 × 10^{-6} from shock tube experiments, while for the typical flame ionization detector used with gas chromatographs, a yield of about 6 × 10^{-6} ions per acetylene molecule may be calculated.[29] It should be emphasized that the present results are derived from very dilute systems at room temperature and so comparison of numerical values and even rate laws to those obtained at the higher temperatures of most com-

bustion systems is of questionable validity.

Higher ion yields have been reported by Arrington et al.[6] for experiments similar to those reported here, but with higher oxygen atom concentrations; when their ion yields are recalculated using the recommended value[28] for k_1 of 1.58×10^{-13} cm^3 molecule^{-1} s^{-1}, ion yields of 165×10^{-6} for 21 mTorr of $[O]_0$ and 180×10^{-6} for 30 mTorr of $[O]_0$ result. When these ion yields are inserted into eq III, values for the constant α are 2.4×10^{-19} and 1.8×10^{-19} cm^3 molecule^{-1}, in excellent agreement with the value determined above.[32] Yields of vacuum-ultraviolet quanta were not measured during the present study, but previous estimates[22,24] have been in the range of $(1-5) \times 10^{-5}$ quanta per acetylene molecule.

The inhibition of chemi-ionization by molecular oxygen has been known for many years.[4] Equation V now places this effect on a quantitative basis, showing that the inhibition follows a Stern–Volmer type equation. It is noteworthy that the rate of quenching is independent of He pressure and of oxygen atom concentration over the range studied. The effect of O_2 on the chemi-ionization observed in real flames is quite different from that described by eq V, probably due to interconnected effects (temperature, oxygen atom concentration, etc.) in real flames.[33]

When only 3% of the helium carrier gas is replaced with various inert gases, there are strong effects on the chemi-ionization (Figure 7) and smaller but still significant effects on the vacuum-ultraviolet chemiluminescence (Figure 8). However, there is no strong effect upon varying the total helium pressure between 3 and 7 Torr.

Similar effects in the vacuum-ultraviolet emission were discovered by Fontijn and Johnson,[31] where at low pressure the emission intensity was proportional to the pressure of added gas, but at higher pressures (>3 Torr) the pressure dependence was much less. However, even in the higher pressure range, different inert gases gave different plateau values. Quantitative comparison is difficult because the experiments were done differently, but qualitatively, the effects were similar; vacuum-ultraviolet emission was favored in the sequence, Ar > N_2 > He. The only other gas common to both studies, CO_2, appear to give opposite trends. However, in the study of Fontijn and Johnson, the CO_2 inhibited the chemiluminescence when added to 0.8 Torr of Ar (already a good emission stimulant) while in Figure 8, substituting CO_2 for He enhances the emission slightly. Thus, these two observations on the behavior of CO_2 are probably not contradictory.

The effect of substituting one inert gas for another is not compatible with a change in the rate of diffusion of intermediates to the walls. The substitution of only 0.05 Torr of CO_2 for He (less than 2%) doubles the ion current; the average diffusion coefficient for some intermediate should change only slightly for this substitution, not by a factor of 2. Comparison of the values of k_M for saturation current (Table I) suggests a vibrational relaxation or energy transfer process; the diatomic molecules are better than Ar or He, while the polyatomic CO_2 and CF_4 are much more effective. Molecular hydrogen appears to be a special case for both chemi-ionization and chemiluminescence, perhaps interferring chemically with some step in the process. Carbon monoxide is clearly a special case for the chemiluminescence because some of the fourth positive emission will experience radiation trapping when large amounts of CO are added.

Mechanism of Chemi-ionization and Chemiluminescence. The above observations lead to some specific requirements for proposed mechanisms. The overall rate of

consumption of acetylene in this system should be proportional to $[O][C_2H_2]$ since the overall reaction is first order[9] both in [O] and $[C_2H_2]$. The observed dependance on the product $[O]^2[C_2H_2]$ indicates that the efficiency of producing chemi-ions or chemiluminescence is proportional to [O]; a second step involving the reaction of some intermediate with another oxygen atom is required to give the overall $[O]^2$ dependance.

Since the proposed reactions that are responsible for chemi-ionization and CO chemiluminescence both involve an oxygen atom, namely, reactions 1 and 2, it would be

$$O + CH \rightarrow HCO^+ + e^-$$

$$O + C_2O \rightarrow CO^* + CO$$
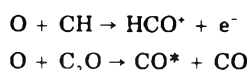
natural to associate the second power of [O] to these steps. However, the oxygen atom concentration will not appear in the kinetic rate law unless there is an alternate reaction pathway for the intermediates; if CH always reacts with oxygen atoms, increasing the [O] will not affect the yield of chemi-ions.

Are there alternate destruction paths for CH and C_2O? Other chemical reactions seem unlikely for the present experimental conditions. Since the chemi-ionization yield is still increasing for oxygen atom concentrations of 5 mTorr, the alternate destruction path of CH would have to be even faster than the reaction O + CH. The reaction CH + C_2H_2 cannot be the dominant alternate path, since that would change the overall rate expression. No other molecule has a high enough concentration to compete with oxygen atoms unless the overall reaction between CH and O is very slow, which seems unlikely.[34] Similar arguments apply to C_2O.

Diffusion to the walls might be an alternate loss process for CH and C_2O. This possibility would require that capture of the intermediates by oxygen atoms be more efficient at higher total pressures, whereas Figure 2 shows that both ion production and chemiluminescence are the same at 3 and 7 Torr.

Consideration of all of the above leads to a generalized mechanism for the chemi-ionization that involves at least two intermediates, A* and B*:

$$O + C_2H_2 \rightarrow (C_2H_2O)^* \tag{a}$$

$$(C_2H_2O)^* \rightarrow \text{other products } (CH_2, CO, HC_2O, \text{ etc.}) \tag{b}$$

$$(C_2H_2O)^* + M \rightarrow A^* \tag{c}$$

$$A^* + M \rightarrow \text{other products} \tag{d}$$

$$A^* \rightarrow B^* \tag{e}$$

$$B^* + O \rightarrow HCO^+ \tag{f}$$

$$B^* \rightarrow \text{other products} \tag{g}$$

$$B^* + O_2 \rightarrow \text{other products} \tag{h}$$
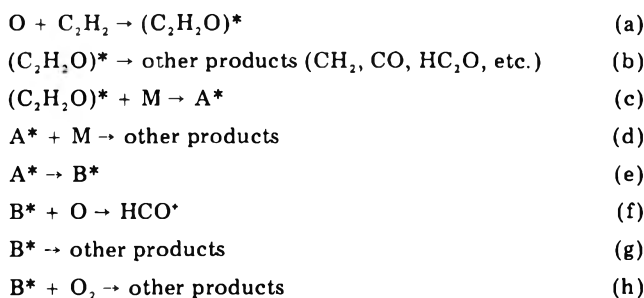
The initial step is formation of the collision complex $(C_2H_2O)^*$ which rapidly decomposes to a variety of fragments, $CH_2 + CO$, $HC_2O + H$, and $C_2O + H_2$.[28] If, however, the energy-rich complex makes a stabilizing collision with an unreactive molecule M before it decomposes, then it will form an intermediate A* as shown in reaction c. This intermediate A* can then either be quenched by further collisions with M, reaction d, or undergo a spontaneous conversion to intermediate B*, reaction e. Three alternatives are given for B*: reaction with an oxygen atom to eventually form HCO$^+$, reaction f (this need not be a single elementary reaction but could, for example, involve formation of CH, which then always reacts with another oxygen atom); the spontaneous conversion of B* into other products, reaction g; or reaction of B* with molecular oxygen, reaction h. A similar

mechanism also involving two intermediates, but not necessarily the same two intermediates, could be written for the vacuum-ultraviolet chemiluminescence.

Use of the steady state approximation for $(C_2H_2O)^*$, A^*, and B^* results in the following expression for the rate of chemi-ionization:

$$\frac{d(HCO^+)}{dt} =$$

$$\frac{k_a k_e k_f [O]^2 [C_2H_2]}{\{k_b + k_c[M]\}\{k_f[O] + k_g + k_h[O]_2\}} \times$$

$$\frac{k_c[M]}{k_d[M] + k_e} \qquad (VII)$$

If k_b is much larger than $k_c[M]$, if $k_d[M]$ is much larger than k_e, and if $k_f[O]$ is much smaller than either k_g or $k_h[O_2]$, then this expression reduces to

$$\frac{d(HCO^+)}{dt} = \frac{k_a k_c k_e k_f [O]^2 [C_2H_2]}{k_b k_d k_g \{1 + k_h[O_2]k_g^{-1}\}} \qquad (VIII)$$

which has the same kinetic form as the empirical eq V. The first two approximations say that the production of A^* from $(C_2H_2O)^*$, and of HCO^+ from B^*, are inefficient processes. This is compatible with the observation that the overall chemi-ion yield is small, $\sim 10^{-5}$.

The approximation, $k_d[M] \gg k_e$, results in a pressure independent chemi-ionization rate, because M is participating in both the formation and destruction of A^*. However, the rate of ion formation will depend on the nature of M, since the rate constants k_c and k_d remain in eq VIII and they will be different for different collision partners (cf. the Lewis–Rayleigh nitrogen afterglow, where the emission intensity depends on the nature of inert gas but is independent of the pressure of the inert gas[34]). If this interpretation is correct, the chemi-ion yield should eventually decrease with decreasing pressure, and finally be proportional to pressure. While this experiment has not yet been tried, just such an effect is observed in the CO chemiluminescence (see Figure 6 of ref 31). Thus it appears that a mechanism in which inert gas forms an intermediate and also destroys the same or another intermediate, can explain both the inert gas effects shown in Figures 7 and 8 and the overall pressure effects observed for the vacuum-ultraviolet chemiluminescence. A similar mechanism involving the triplet states of CO was proposed by Fontijn and Johnson[31] for the vacuum-ultraviolet emission.

The above mechanism is not being proposed as a unique explanation of all experiments. However it does incorporate several aspects which appear necessary to explain the experimental observations, namely: a nonreactive molecule forming an intermediate in one step and destroying an intermediate in another; separation of the M-quenching step from the O_2-quenching step; and a second oxygen atom reaction that is kinetically visible.

A specific selection of the important intermediates for chemi-ionization and CO chemiluminescence is not possible at the present time. It is probable that either A^* or B^*, or both, are electronically excited molecules. The electronic excitation would make it easier for the intermediates to react to give high energy products and the excitation could be degraded, either by collisions, by radiation, or by internal conversion.

Several of the molecules and free radicals in these systems have excited states that could be involved. Both calculations and experiments[35,36] indicate that ketene has

two triplet electronic states that would be accessible in reaction c. The CH molecule has a metastable quartet state only 0.74 eV above its doublet ground state,[37] and, similarly, C_2O should have two metastable singlet states less than 1 eV above the triplet ground state.[38] Carbon monoxide has several metastable states, both singlet and triplet,[25] that can be formed in reaction 2. Although little is known about the electronic states of HC_2O, simple molecular orbital arguments suggest that there should be at least one low lying electronically excited state.

References and Notes

(1) W. J. Miller, *Oxid. Combust. Rev.*, **3**, 97 (1968).
(2) A. Fontijn, *Prog. React. Kinet.*, **6**, 75 (1971).
(3) W. J. Miller, *Symp. (Int.) Combust.* [*Proc.*], *14th*, 307 (1973).
(4) A. Fontijn and G. L. Baughman, *J. Chem. Phys.*, **38**, 1784 (1963).
(5) W. J. Miller, A. Fontijn, and J. M. Hogan, *Symp. (Int.) Combust.* [*Proc.*], *10th*, 545 (1965).
(6) C. A. Arrington, W. Brennen, G. P. Glass, J. V. Michael, and H. Niki, *J. Chem. Phys.*, **43**, 1489 (1965).
(7) M. P. Garner, C. Vinckier, and K. D. Bayes. *Chem. Phys. Lett.*, **31**, 318 (1975).
(8) J. Peeters and C. Vinckier, *Symp. (Int.) Combust.* [*Proc.*], *15th*, 969 (1975).
(9) C. A. Arrington, W. Brennen, G. P. Glass, J. V. Michael, and H. Niki, *J. Chem. Phys.*, **43**, 525 (1965).
(10) J. O. Sullivan and P. Warneck, *J. Phys. Chem.*, **69**, 1749 (1965).
(11) J. M. Brown and B. A. Thrush, *Trans. Faraday Soc.*, **63**, 630 (1967).
(12) G. S. James and G. P. Glass, *J. Chem. Phys.*, **50**, 2268 (1969).
(13) J. N. Bradley and R. S. Tse, *Trans. Faraday Soc.*, **65**, 2685 (1969).
(14) A. A. Westenberg and N. deHaas, *J. Phys. Chem.*, **73**, 1181 (1969).
(15) K. Hoyermann, H. Gg. Wagner, and J. Wolfrum, *Z. Phys. Chem. (Frankfurt am Main)* 63, 193 (1969).
(16) D. G. Williamson and K. D. Bayes, *J. Phys. Chem.*, **73**, 1232 (1969).
(17) D. G. Williamson, *J. Phys. Chem.*, **75**, 4053 (1971).
(18) I. T. N. Jones and K. D. Bayes, *Symp. (Int.) Combust.* [*Proc.*], *14th*, 277 (1973).
(19) I. T. N. Jones and K. D. Bayes, *Proc. R. Soc. London, Ser. A*, **335**, 547 (1973).
(20) R. Bleekrode and W. C. Nieuwpoort, *J. Chem. Phys.*, **43**, 3680 (1965).
(21) J. Lawton and F. J. Weinberg, *Proc. R. Soc. London, Ser. A*, **227**, 468 (1964).
(22) G. B. Kistiakowsky and L. W. Richards, *J. Chem. Phys.*, **36**, 1707 (1962).
(23) C. W. Hand and G. B. Kistiakowsky, *J. Chem. Phys.*, **37**, 1239 (1962).
(24) K. H. Becker and K. D. Bayes, *J. Chem. Phys.*, **48**, 653 (1968).
(25) K. D. Bayes, *J. Chem. Phys.*, **52**, 1093 (1970).
(26) A. G. Gaydon and H. G. Wolfhard, "Flames. Their Structure, Radiation and Temperature", 2nd ed., Chapman and Hall, London, 1960, p 323.
(27) F. Kaufman, *J. Chem. Phys.*, **28**, 352 (1958); I. R. Slagle, J. A. Samlaska, F. J. Pruss, Jr., and D. Gutman, *J. Phys. Chem.*, **78**, 208 (1974).
(28) J. T. Herron and R. E. Huie, *J. Phys. Chem. Ref. Data*, **2**, 467 (1973).
(29) J. C. Sternberg, W. S. Galloway, and D. T. L. Jones, "The Mechanism of Flame Ionization Detectors" in Gas Chromatography, N. Brenner, J. E. Cullen, and M. D. Weiss, Ed., Academic Press, New York, N.Y., 1962, pp 231-267.
(30) F. F. Marmo, J. P. Padur, and P. Warneck, *J. Chem. Phys.*, **47**, 1438 (1967).
(31) A. Fontijn and S. E. Johnson, *J. Chem. Phys.*, **59**, 6193 (1973).
(32) It should be noted, however, that these authors also find that the chemi-ion yield is proportional to the first power of the oxygen atom concentration (see Figure 4b of ref 6), rather than the square dependence observed above. The reason for this decrepancy is not clear, but it may be related to the high acetylene concentration (2.16 × 10^{15} molecules cm^{-3}) they used to determine the oxygen atom dependence; this would have caused severe depletion of oxygen atoms before or within the ion collection region (the actual contact time for Figure 4b is not given; it was probably several milliseconds). Their ion yields, as calculated above, should avoid this complication since the acetylene concentrations for those measurements were a factor of 10 lower. A square dependence on atomic oxygen would explain

another observation that perplexed the authors of ref 6; in their flow experiments the rate of chemi-ion formation decayed faster than the decay of oxygen atoms.

(33) E. M. Bulewicz and P. J. Padley, *Symp. (Int.) Combust. [Proc.]*, *9th*, 638 (1963).

(34) B. A. Thrush and M. F. Golde, *Rep. Prog. Phys.*, **36**, 1285 (1973).

(35) J. E. Del Bene, *J. Am. Chem. Soc.*, **94**, 3713 (1972).

(36) J. Vogt, M. Jungen, and J. L. Beauchamp, *Chem. Phys. Lett.*, **40**, 500 (1976).

(37) A. Kasdan, E. Herbst, and W. C. Lineberger, *Chem. Phys. Lett.*, **31**, 78 (1975).

(38) K. D. Bayes, *J. Am. Chem. Soc.*, **85**, 1730 (1963).

The Cleavage of C₅H₅HgBr by Aqueous Solutions Containing H⁺ and Br⁻ [1]

Sherif E. Ibrahim and Maurice M. Kreevoy*

Chemical Dynamics Laboratory, Department of Chemistry, University of Minnesota, Minneapolis, Minnesota 55455 (Received February 2, 1977)

Cyclopentadienylmercuric bromide forms a series of complexes with bromide ion up to and including $C_5H_5HgBr_4^{3-}$, in which mercury is pentacoordinated. The lower complexes are stable enough to be observed spectroscopically. The pentacoordinated complex is required by acidolysis kinetics. These complexes are cleaved by Brønsted acids to give cyclopentadiene and mercuric bromide or its bromide complexes. All the cleavage steps show general acid catalysis by carboxylic acids and substantial primary hydrogen isotope effects. In all cases the product of isotopic fractionation factors for the untransferred protons of the transition state is greater than unity, and that for the transferred proton is less than unity, as required by theory. Except for the cleavage of $C_5H_5HgBr_4^{3-}$, the results are consistent with a simple acidolysis as the rate-determining step. In the latter case the product of fractionation factors for untransferred protons is 3.8, which is larger than the upper value, 2.1, thought to be allowed for direct proton transfer from H_3O^-. This may be due to an accumulation of errors, but, if it is real, it suggests that the rate- and product-determining steps may not be the same.

This paper extends earlier studies on the acidolysis of allylic mercuric halides[2-5] to the cleavage of cyclopentadienylmercuric bromide by acid in the presence of bromide ion (eq 1) in aqueous solution. New features

$$C_5H_5HgBr + Br^- + HA \rightarrow C_5H_6 + HgBr_2 + A^- \qquad (1)$$
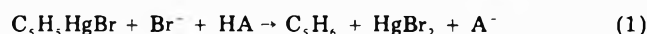
which appear in this case include the following: (a) Cyclopentadienylmercuric bromide, unique among alkylmercuric halides in which the alkyl groups contain no highly electronegative atoms, complexes strongly with bromide ion in dilute solutions. The equilibrium constant for the reaction shown in eq 2, K_2, is larger than the

$$C_5H_5HgBr + Br^- \overset{K_2}{\rightleftharpoons} C_5H_5HgBr_2^- \qquad (2)$$
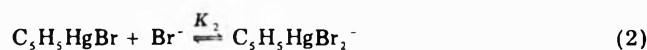
analogous constant for $HgBr_2$.[6] (b) At (Br⁻) > 10^{-2} M the cleavage reaction is dominated by paths involving an apparently pentacoordinate mercury, in the reactive intermediate, $C_5H_5HgBr_4^{3-}$. Related observations have been made for the acidolysis of 4-pyridiomethylmercuric chloride,[7] but were interpreted differently. There is no obvious alternative to a pentacoordinate mercury in rationalizing the present observations.

Acidolysis of $C_5H_5HgBr_3^{2-}$, $C_5H_5HgBr_2^-$, and C_5H_5HgBr has also been demonstrated. All of these pathways have been shown to be subject to general acid catalysis by carboxylic acids, with a Brønsted coefficient of about 0.5. All have kinetic solvent isotope effects well above unity. Each has a fractionation factor for its transferring proton between 0.10 and 0.25.[8] These observations are best accommodated by a mechanism involving fast, reversible, complexing of Br⁻ to the mercury atom, followed by rate-determining acidolysis of the carbon–mercury bond.

Results

Activity Coefficients. In the work that follows, ions are involved. Since the ionic strength was low in most ex-

periments (usually below 0.02 M, always below 0.2 M) and the solvent was 4% methanol–96% water in almost all our experiments, we chose an ideal solution in such a solvent as our reference state. Formally neutral substances were assigned activity coefficients of unity, throughout. By analogy with the isopropenylmercuric bromide cleavage[9] eq 3 was assumed for γ', the activity coefficient of the

$$-\log \gamma' = \frac{0.5\mu^{1/2}}{1 + \mu^{1/2}} - 0.4\mu \qquad (3)$$

transition state for cleavage of cyclopentadienylmercuric bromide by H⁺. The activity coefficients of other singly charged ions were assumed to be equal, designated γ, and approximated by means of eq 4; for doubly charged ions equ 5 used, and for triply charged ions, equ 6. In eq 3-6

$$-\log \gamma = \frac{0.5\mu^{1/2}}{1 + \mu^{1/2}} - 0.1\mu \qquad (4)$$

$$-\log \gamma_2 = \frac{2\mu^{1/2}}{1 + \mu^{1/2}} - 0.4\mu \qquad (5a)$$

$$\gamma_2 = \gamma^4 \qquad (5b)$$

$$-\log \gamma_3 = \frac{4.5\mu^{1/2}}{1 + \mu^{1/2}} - 0.9\mu \qquad (6a)$$

$$\gamma_3 = \gamma^9 \qquad (6b)$$

the coefficients of $\mu^{1/2}$ are based on theory.[10] The coefficients of μ are of reasonable general magnitude and that in eq 4 has many analogies,[10] but those in eq 5 and 6 were chosen for convenience and cannot be strongly defended. In addition, eq 3-6 have, in many cases, been used at concentrations beyond their normal range of reliability. To give them more credibility they have been tested by measuring rates at constant (H⁺) and (Br⁻), with varying $NaClO_4$ concentrations, and generally found to adequately
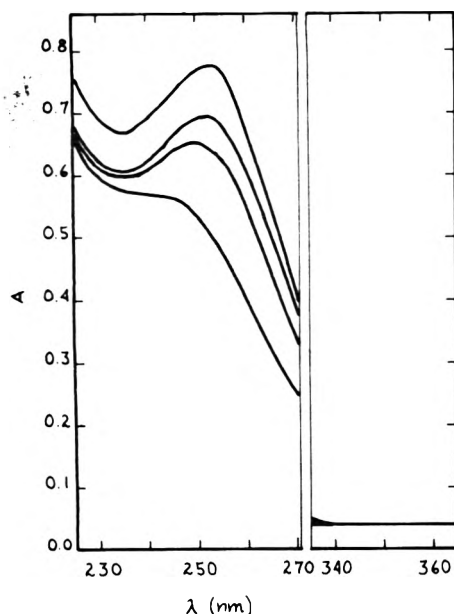
Figure 1. UV spectra of C_5H_5HgBr, 7×10^{-5} M, in aqueous solution containing 3% methanol and varying (Br^-). In order of increasing intensity, the (Br^-) was zero, 1.3×10^{-3}, 5.2×10^{-3}, and 9.7×10^{-3}. Reference solutions were identical except for the absence of C_5H_5HgBr. The spectra are interrupted between 270 and 335 nm to show that they reach a common base line outside of the region of absorption.

describe the effect of this electrolyte on the observed rate constant.

Complexing of Cyclopentadienyl Bromide with Bromide Ion. When C_5H_5HgBr is dissolved in water (containing 4% methanol by volume) its UV spectrum shows a shoulder around 240 nm but no maximum above 225 nm. If 10^{-3} M NaBr is added to such solutions, a distinct peak appears at 250 nm. As more Br^- is added, this peak gradually increases in intensity and changes somewhat in shape. A series of spectra are shown in Figure 1. These changes are consistent with the formation of bromide complexes, $C_5H_5HgBr_2^-$ and $C_5H_5HgBr_3^{2-}$.

Because the absorption, A, builds up sharply at low (Br^-) and comes to a nearly constant value, K_2 and the extinction coefficients, ϵ_2, for $C_5H_5HgBr_2^-$ are fairly well defined. The best values are 7.5×10^2 for K_2 and 1.0×10^4 for ϵ_2^{260}.

The equilibrium constant for the formation of $C_5H_5HgBr_3^{2-}$ from $C_5H_5HgBr_2^-$, K_3, is less than 100, but is otherwise not well defined. At (Br^-) above 5×10^{-3} M, A increases gradually as a function of (Br^-) and does not reach a constant value at any accessible value of (Br^-). Measurements become increasingly unreliable at (Br^-) > 10^{-2}, as the higher bromide complexes of C_5H_5HgBr enter into irreversible side reactions. In consequence, values of K_3, 4.0, and ϵ_3^{260}, 2×10^4, which fit the results that have been chosen without any contention that they are unique. These parameters were used to fit the experimental A values according to eq 7 and 8. $(C_5H_5HgBr)_0$ is the total

$$\frac{A}{(C_5H_5HgBr)_0} =$$

$$\left(\frac{\epsilon_1 + \epsilon_2 K_2(Br^-) + \epsilon_3 K_2 K_3(Br^-)^2/\gamma^2}{a} \right) \quad (7)$$

$$a = 1 + K_2(Br^-) + K_2K_3(Br^-)^2/\gamma^2 \quad (8)$$

concentration of cyclopentadienylmercury compounds, without regard for their state of complexation. Values of K_2 between about 500 and 1000 can be accomodated by making corresponding changes in ϵ_2, but outside of these limits systematic descrepancies between calculated and
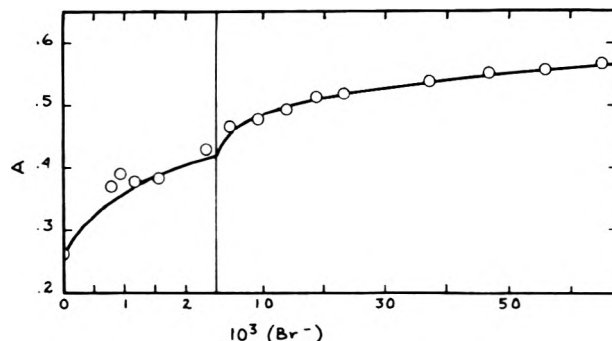
Figure 2. Absorbance at 260 nm of solutions containing 5×10^{-5} M C_5H_5HgBr as a function of added NaBr concentration. Reference solutions were identical except for the absence of C_5H_5HgBr. The solid line represents eq 7 with the indicated parameters. Note the change of scale in the abscissa.

observed A values are clearly evident. Therefore the values of K_2 and ϵ_2^{260} are uncertain by about 25%. The fit of eq 7 to the A values at 260 nm with these parameters is shown in Figure 2. Comparable fits can be obtained at 250 and 280 nm.

Kinetics. Rates were measured by observing the change in A at 250 nm, at 25.0 ± 0.1 °C, in aqueous solutions containing 4% methanol. (Methanol, between 2 and 10% of the solvent by volume, was shown to cause changes of no more than a few percent in the observed rate constants. A small amount of methanol was essential in making up the reaction mixtures.) The initial concentrations of C_5H_5HgBr were between 10^{-4} and 10^{-5} M. At (Br^-) below about 10^{-2} M the molar absorbance of C_5H_5HgBr and its bromide complexes is greater than that of $HgBr_2$, and the absorbance of the reacting solutions decreased with time. Above 10^{-2} M Br^-, absorbance increased with time. In either case, pseudo-first-order rate constants, k_1, were evaluated using eq 9.[11]

$$k_1 = \frac{2.303}{t - t_0} \log \frac{A_0 - A_\infty}{A_t - A_\infty} \quad (9)$$

When the (Br^-) was below ~0.02 M, plots of log $(A_t - A_\infty)$ against t were linear, as required by eq 9. At higher (Br^-) such plots were initially curved, approaching linearity only at high fractional conversions. Such behavior has been previously observed for the cleavage of allylmercuric iodide by acid and I^-.[4] It has been attributed to cleavage via disproportionation.[4] This mechanism requires that the curvature be eliminated by addition of small amounts of mercuric halide, and it was, as illustrated in Figure 3. In general the initial $HgBr_2$ concentration in such experiments was made about equal to the initial C_5H_5HgBr (between 10^{-4} and 10^{-5} M). This behavior, incidentally, strengthens our contention that the spectroscopic changes shown in Figures 1 and 2 are due to complexing by the C_5H_5HgBr, as it shows that little or no $HgBr_2$ could have been present as a contaminant in our C_5H_5HgBr preparations.

Rate constants were evaluated by subjectively fitting the best possible straight line to the plots of log $(A_t - A_\infty)$ against t.

Products. The mercurial product was identified by means of its UV spectrum. Under all conditions reported in this paper, product spectra were identical with those obtained from $HgBr_2$ in the presence of the appropriate (Br^-).

The only organic product was identified as cyclopentadiene by GLPC. It was also isolated as its Diels–Alder adduct with tetracyanoethylene at several (Br^-) spanning the range of the kinetic studies. To mimic the conditions of the rate measurements, these product iso-
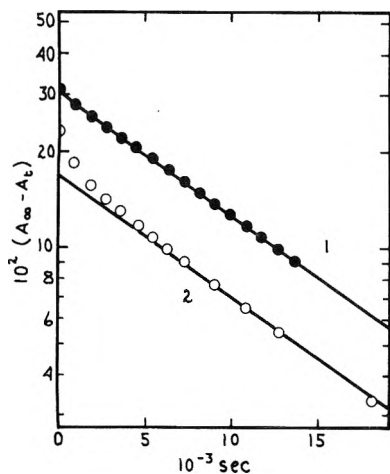
Figure 3. Applicability of eq 9 with and without initially added $HgBr_2$. Curve 1 (closed circles) was generated by a solution that initially contained 3×10^{-5} M HgBr; curve 2 (open circles) by a solution that initially contained none. Both initially contained 3×10^{-5} M C_5H_5HgBr, 3.3×10^{-2} M sodium acetate, and 3.3×10^{-2} M acetic acid. The slopes of the two straight lines are equal and give a value of 8.95×10^{-5} s^{-1} for k_1. The circles are not error circles; they merely identify the points. The expected experimental error in A is quite small.

lations were carried out with solutions initially $\sim 10^{-4}$ M in substrate, so that the theoretical yield of adduct was about 8 mg. The actual yields were about 40% of theoretical. This quite plausibly reflects the manipulative losses in handling such small quantities of material in large volumes of solvent, and does not suggest the formation of another, unobserved, product.

Rate as a Function of (H^+), (Br^-), and μ. At each of four (Br^-), ranging from 9×10^{-3} to 2×10^{-1} M, k_1 was found to be a linear function of (H^+) (provided by $HClO_4$) with nonzero intercept. These nonzero intercepts were confirmed by results obtained with buffer solutions, described below.

At fixed (H^+), k_1 increases continuously as a function of (Br^-), but no functional form could be found for this dependence without taking account of the buildup of the Br^- complexes of the substrate. If the substrate itself, and each of its Br^- complexes, $C_5H_5HgBr_{(n+1)}{}^{n-}$, undergoes uncatalyzed (or water-catalyzed) cleavage and an H^+-catalyzed cleavage we are led to eq 10. Each k_{Br_n} and k_{HBr_n}

$$ak_1 = \Sigma \Gamma_n k_{Br_n}(Br^-)^n + (H^+)\Sigma \Gamma_n{}'k_{HBr_n}(Br^-)^n \quad (10)$$

in eq 10 is a product of an infinite dilution rate constant and the equilibrium constant for the formation of the relevant Br^- complex. Each Γ_n and $\Gamma_n{}'$ is a ratio of activity coefficients which can be evaluated using eq 3–6. Equation 8 defines a. Equation 10 rationalizes the dependence of k_1 on (H^+) at constant (Br^-), and can give a satisfactory account of the dependence of ak_1 on (Br^-), *but only if the summations are taken up to n equal to 3.*

The (H^+)-independent term in eq 10 is usually no more than a few percent of ak_1. In the solutions containing the highest (Br^-) and the lowest (H^+) it rose only to 40% of ak_1. The k_{Br_n} were, therefore, evaluated separately, with the help of results obtained in buffer solutions. Extrapolation of measured k_1 values in buffer solutions to infinitely dilute buffers gave the k_1 values appropriate to solutions with low known (H^+), at the same four (Br^-) referred to above. These results were combined with the strong acid k_1 values. The linear plot obtained at each (Br^-) was extrapolated to zero (H^+). A typical example of such a plot is shown in Figure 4. These four intercepts, $k_1{}^0$, were fitted to eq 11. Significant, nonzero values were

$$ak_1{}^0 = \Sigma \Gamma_n k_{Br_n}(Br^-)^n \quad (11)$$
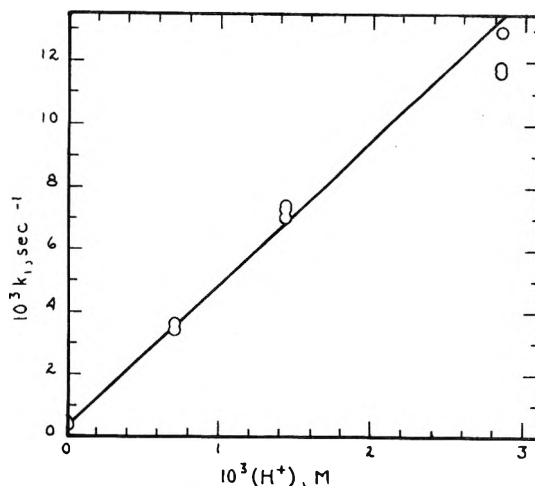
Figure 4. Rate as a function of (H^+) at constant (Br^-), 0.070 M. Two points (at (H^+) of 8×10^{-6} and 1.8×10^{-5}, k_1 of 4.5×10^{-4} and 3.3×10^{-4}) were derived from measurements in buffer solutions. The rest were derived from measurements in $HClO_4$ solutions. The intercept is 3.25×10^{-4} s^{-1}.

TABLE I: Parameters of Eq 10

n	Γ_n	$\Gamma_n{}'$	$k_{Br_n}{}^a$	$k_{HBr_n}{}^b$
0	1	γ/γ'	c	$2.5 \pm 0.3 \times 10^{-2}$
1	1	γ^2	c	31 ± 6
2	γ^{-2}	γ^2	0.7	$1.56 \pm 0.11 \times 10^4$
3	γ^{-6}	1	12	$4.06 \pm 0.14 \times 10^5$

^{a} Data with which to make a statistical estimate of uncertainty for these parameters are lacking. ^{b} The uncertainties are probable errors. ^{c} The data did not require a nonzero value for these parameters.

found for k_{Br_2} and k_{Br_3}. The are 0.7 and 12, and are shown in Table I. With these values eq 11 reproduces the four $k_1{}^0$ values with an average discrepancy of 6% and a maximum discrepancy of 12%. It is not meant to imply that k_{Br_0} and k_{Br_1} are identically zero, but nonzero values were not required to fit the limited range of $k_1{}^0$ values available. No positive values of k_{Br_0} and k_{Br_1} would allow the results to be fitted without a substantial value for k_{Br_3}. The results do not permit a meaningful statistical estimate of the uncertainty of k_{Br_2} and k_{Br_3}, but errors of 50% would not be surprising, with compensating errors in other k_{Br_n}, a, or in the Γ_n. The only thing that can be reliably claimed is that this set of parameters permits eq 11 to represent satisfactorily the small H^+-independent term in eq 10.

With this approximation of the (H^+)-independent term in eq 10 in hand, we have used 83 values of k_1 to evaluate the k_{HBr_n} in eq 10 by the method of least squares. The quantity k_2 is defined by eq 12. It should be equal to

$$k_2 = a(k_1 - k_1{}^0)/(H^+) \quad (12)$$

$\Sigma \Gamma_n{}'k_{HBr_n}(Br^-)^n$. The sums of the squares of the fractional residuals, Δ, defined in eq 13, were minimized, using a CDC

$$\Delta = \frac{k_2 - \Sigma \Gamma_n{}'k_{HBr_n}(Br^-)^n}{k_2} \quad (13)$$

6600 digital computer.[12] The resulting best values of k_{HBr_0} through k_{HBr_3} are given in Table I. With these values eq 12 reproduces the k_2's with an average $|\Delta|$ of 0.1, and without systematic trends. Table II gives averages of experimental k_1 values at five (Br^-) and, for comparison, those given by eq 10. The discrepancies are typical. Considering that error in $k_1{}^0$, $\Gamma_n{}'$, and a, as well as experimental errors in k_1, all accumulate in Δ, the discre-

TABLE II: Representative Experimental and
Calculated Values of k_1

(H$^+$), M	(Br$^-$), M	$10^3 k_1$,[a] s^{-1}	$10^3 k_1$,[b] s^{-1}
1.08×10^{-1}	9.32×10^{-4}	3.07	2.72
3.56×10^{-2}	2.32×10^{-3}	1.74	1.73
1.42×10^{-2}	1.86×10^{-2}	5.62	6.32
3.42×10^{-3}	8.96×10^{-2}	13.6	15.2
1.42×10^{-3}	2.14×10^{-1}	24.6	25.8

[a] Mean experimental values; the means of one to four
determinations. The typical uncertainty of the measure-
ment is about ±5%. [b] Calculated from eq 10, using a
values given by eq 8 and other parameters as indicated in
Table I.
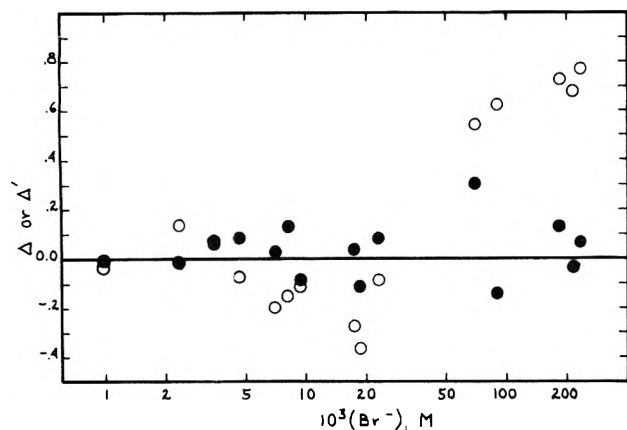
Figure 5. Fractional residuals, Δ, as a function of (Br$^-$). Open circles
are Δ' values, corresponding to $\Sigma \Gamma_n' k_{HBr_n}$(Br$^-$)^n terminated at an n of
2. Closed circles are Δ values; the summation was taken up to an
n of 3.

pancies are entirely acceptable. No reasonable adjustment
of the other parameters would permit eq 12 to reproduce
the k_2 values satisfactorily without a nonzero value for
k_{HBr_3}, and the fit was not significantly improved if a
nonzero value of k_{HBr_4} was included.

If $\Sigma \Gamma_n' k_{HBr_n}$(Br$^-$)^n was arbitrarily terminated at an n of
2, the average $|\Delta|$ rose to 0.4, and Δ shows distinct trends
when plotted as a function of (Br$^-$), as shown in Figure 5.
Further, the "best" value of k_{HBr} has a physically unac-
ceptable, negative value.

Our formulation of electrolyte effects was tested by
measuring k_1 at each of three fixed (Br$^-$), ranging from 10^{-1}
to 10^{-3} M, with NaClO$_4$ added, so as to produce ionic
strengths up to 0.5. The results are compared with the
predicted functions in Figure 6. The agreement is rea-
sonable. The trends seem to be reasonably well repre-
sented even when the absolute values are less so. It is
notable that the overall electrolyte effects, both calculated
and observed, are in no case very large.

General Acid Catalysis. Values of k_1 were measured in
equimolar carboxylic acid-carboxylate buffers at each of
a number of (Br$^-$), ranging from just below 10^{-2} to just
above 10^{-1} M. The carboxylic acids used were pivalic,
acetic, chloroacetic, and cyanoacetic. For acetic acid, at
each (Br$^-$), these values were found to be correlated by eq
14, as shown in Figure 7. The results for pivalic acid were

$$ak_1 = I_{HA} + (HA)S_{HA} \qquad (14)$$

similar. The slopes, S_{HA}, are functions of the nature of HA
and the (Br$^-$). The I_{HA} should be the ak_1 appropriate for
low, calculable (H$^+$) and known (Br$^-$). The (Br$^-$) do not,
however, correspond to those used in evaluating the k_{Br_n}
(eq 11). To get such values, the I_{HA} for each acid were
plotted as a function of (Br$^-$) and connected by smooth
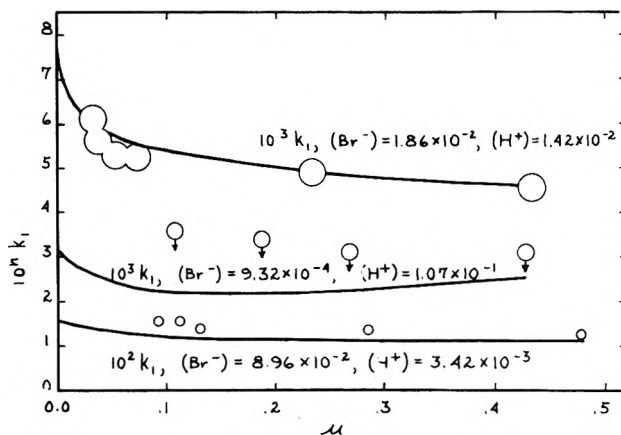
Figure 6. The effect of added electrolyte (NaClO$_4$) on k_1, calculated
(solid lines) and observed (open circles). Rate constants have, in each
case, been multiplied by an appropriate power of ten, as indicated, to
get them onto a common scale.
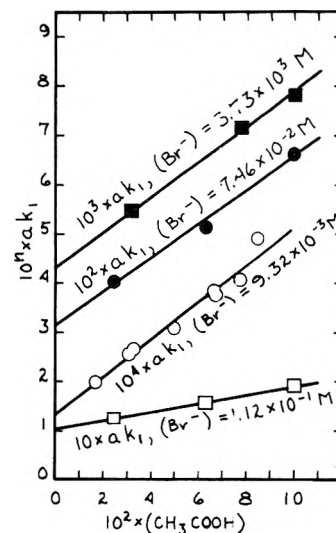
Figure 7. Variation of k_1 with (Br$^-$) and (CH$_3$COOH). In all of these
experiments the (CH$_3$COO$^-$) equaled the (CH$_3$COOH).

curves. From these curves the needed ak_1 values were
taken. Equation 10 correlated such values along with those
obtained in HClO$_4$ solutions without visible discontinuities.

For chloroacetic and cyanoacetic acids, even at constant
buffer ratio, the (H$^+$) is expected to vary significantly with
buffer concentration. In these cases I_{HA} was evaluated
separately, using eq 10, for each set of conditions. S_{HA} was
then obtained by plotting $ak_1 - I_{HA}$ as a function of (Br$^-$).
These plots were also linear within the uncertainty of the
points, and resembled, in their scatter, those shown in
Figure 7.

By analogy with the strong acid case (eq 10) S_{HA} should
be given by eq 15. As Γ_2'' is γ^{-2} and Γ_3'' is γ^{-6}, plots such

$$S_{HA} = \Sigma \Gamma_n'' k_{HABr_n}(Br^-)^n \qquad (15)$$

as those in Figure 7 need not be linear even at constant
(Br$^-$). The limited data, and the fact that substantial
concentrations of ionic NaBr are present, apparently
obscure the curvature. The data are insufficient to reliably
evaluate the individual k_{HABr_n}. However, the pivalic acid
results provide further support for the inclusion of cubic
terms in such equations, because its S_{HA} clearly rises as
(Br$^-$)^3 for the higher (Br$^-$).

Kinetic Isotope Effects. Sixty-one measurements of k_1^D
were made in D$_2$O, with various (D$^+$) and (Br$^-$). (A su-
perscript D is used to distinguish rate constants for re-
actions in D$_2$O. Otherwise the notation is the same as for

TABLE III: Rate Constants and Isotopes Effects in D_2O

n	$k_{DBr_n}^{D\ a}$	$k_{HBr_n}/k_{DBr_n}^{D\ a}$
0	$6.8 \pm 0.5 \times 10^{-3}$	3.8 ± 0.8
1	20.0 ± 1.4	1.6 ± 0.6
2	$2.6 \pm 0.4 \times 10^3$	5.8 ± 1.3
3	$2.51 \pm 0.06 \times 10^5$	1.6 ± 0.1

^{a} The uncertainties listed are probable errors.

TABLE IV: Competitive Isotope Effects

$10^3(Br^-)$, M	$\phi_t^{\ a}$	F^b			
		0	1	2	3
1.21	0.18	0.5	0.3	0.2	
2.43	0.18	0.1	0.4	0.4	0.1
4.85	0.18	0.1	0.2	0.6	0.1
97.1	0.12	0.8	0.2		

^{a} Each of these values is the average of three to four determinations. The typical spread of the values was ± 0.01. ^{b} The fractional contribution of $k_{HBr_n}(H^+)(Br^-)$ to ak_1, at each (Br^-).

H_2O.) As in H_2O, plots of k_1^D as a function of (D^+) at constant (Br^-) were linear, but in D_2O the intercepts were not distinguishable from zero. Consequently, k_1^D values were correlated by means of eq 16. The resulting rate

$$ak_1^D/(D^+) = \Sigma \Gamma_n' k_{DBr_n}(Br^-)^n \qquad (16)$$

constants and isotope effects are reported in Table III.

The fractional discrepancies between observed and calculated values of k_1^D, Δ^D, are only about half as large as the Δ values, averaging about 0.05. There are no apparent systematic trends. As a further check on the reproducibility of k_1 values over a period of time, eight *additional* measurements in H_2O were interspersed among the measurements in D_2O, spread out over the whole range of (Br^-). These k_1 values were not used in establishing the parameters of eq 10. The average Δ for these k_1 values was 0.04. In spite of the excellent correlation of data obtained with eq 10 and 16, the isotope effects on three of the four k_{HBr_n} cannot be very accurately determined. Possible "trade-offs" between rate constants are responsible for this. The most accurately determined isotope effect is that on k_{HBr_3}.

Fractionation Factor of the Transferred Proton. Under conditions closely resembling those in which kinetic measurements were made, cyclopentadiene was isolated (in approximately 40% yield) as its tetracyanoethylene adduct. These experiments were carried out in H_2O–D_2O mixtures, and the isotopic content of the product was determined mass spectroscopically. (The Diels–Alder adduct cracks back to its precursors in the mass spectrometer, facilitating this determination.) Only C_5H_6 and C_5H_5D were found. The transition state fractionation factor for the transferred proton, ϕ_t, is given by eq 17.[8]

$$\phi_t = (C_5H_5D/C_5H_6)(H/D)_{solv} \qquad (17)$$

The ratio of hydroxylic deuterium to hydroxylic hydrogen in the solvent was determined by near-infrared spectroscopy.[13] Thirteen such experiments were carried out at four (Br^-) ranging from 10^{-3} to 10^{-1} M. The results are given in Table IV. Also given is F, the fractional contribution to k_1 of each of the $k_{HBr_n}(H^+)(Br^-)$ at the given (Br^-). In all of these experiments the acid concentration was high enough that the contributions of the $k_{Br}(Br^-)$ terms were insignificant. ϕ_t is 0.18 for $0 < n < 2$, but 0.11 when n is 3.

Discussion

These results are consistent with a mechanism in which a series of complexes are reversibly formed by the substrate with Br^-, and each of them can be cleaved by an irreversible, rate-determining reaction with an acid. The complex-forming tendency of C_5H_5HgBr appears to be greater than that of any other hydrocarbon-substituted Hg(II) halide; k_2 is about three powers of ten larger than the I^- complexing constant of CH_3HgI,[14] and somewhat larger than the Br^- complexing constant of $HgBr_2$.[6] The relatively large value of K_2 is not entirely surprising, since the anionic character of the cyclopentadienyl group is well known,[15] and the magnitude of Br^- complexing constants of Hg(II) compounds increases with the positive character of the Hg.[6] Fluorocarbon–mercuric halides also complex strongly with halide ions.[16]

More surprising is the conclusion that $C_5H_5HgBr_4^{3-}$ forms at higher (Br^-), albeit at very low concentration. Mercury is usually thought to have a maximum covalence of four.[17] However, there have been scattered reports of higher valent Hg(II) species.[18-21] An expansion of the valence shell of Hg is not implausible since an atom of such a high atomic number has a number of empty orbitals whose energy is probably not far above the energy of the normal valence orbitals. Coad and Johnson[7] have previously observed a term of the third order in Cl^- in the acid cleavage of 4-pyridiomethylmercuric chloride. To avoid postulating an expansion of the valence shell of Hg, these authors suggested a rate-determining attack by chloride on an already protonated substrate. In the present case the observation of general acid catalysis of the cubic term in (Br^-) and its large competitive isotope effect preclude a similar explanation. The only other alternative would be a rapid, *reversible*, formation of a nonbonded but solvent-caged species, $C_5H_5^-\cdot HgBr_4^{2-}$, followed by a rate-determining attack of a proton on carbon, as shown in eq 18–20. While the displacement of $C_5H_5^-$ from Hg

$$C_5H_5HgBr_3^{2-} + Br^- \xrightleftharpoons{fast} C_5H_5^-\cdot HgBr_4^{2-} \qquad (18)$$

$$C_5H_5^-\cdot HgBr_4^{2-} + H^+ \xrightarrow{RD} C_5H_6\cdot HgBr_4^{2-} \qquad (19)$$

$$C_5H_6\cdot HgBr_4^{2-} \xrightarrow{fast} C_5H_6 + HgBr_4^{2-} \qquad (20)$$
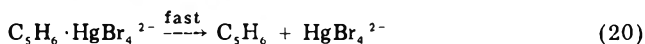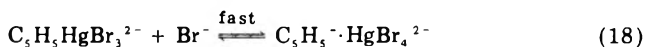
by Br^- is plausible, proton donation by the solvent, water, to $C_5H_5^-$ is spontaneous,[15] as is separation of the two anions without reaction, so it does not seem likely that the solvent-caged species would have a bimolecular attack by H^+ as its major mode of decomposition. The only apparent alternative is the one postulated. In view of this conclusion it now seems possible that the Coad and Johnson observations were also due to the intervention of an intermediate with a pentavalent Hg.

The values of k_{HBr_n}/k_{DBr_n} and ϕ_t are consistent with this mechanism for $n \leq 2$. The apparently discrepant values of k_{HBr_n}/k_{DBr_n} have large uncertainties, and may well all have values around 3. For $n \leq 2$, ϕ_t is 0.18. From this and the k_{HBr_n}/k_{DBr_n} a value of 1.4 is obtained for $\phi_{t,II}$, the transition state fractionation factor for the untransferred protons. All of this is within normal ranges.[8] However, k_{HBr_3}/k_{DBr_3} is only 1.6, and appears quite reliable, while ϕ_t for $n = 3$ appears to be 0.11. These values cannot be reconciled with theory for a simple proton transfer reaction. The derived $\phi_{t,II}$ is 2.0, while the largest value compatible with the previously successful theory is about 1.5.[8] Furthermore, a value close to unity might actually be expected for the secondary solvent isotope effect because the rate-determining protolysis of $C_5H_5HgBr_4^{3-}$ should be very fast and spontaneous.[8] The problem can

be avoided if the rate, in this case, is assumed to be determined by the diffusion-controlled rate of formation of the aquated ion pair, $H^+ \cdot C_6H_5HgBr_4^{3-}$. k_{HBr_3}/k_{DBr_3} is about right for such a process.[21-24] The absolute values of k_{HBr_3} cannot be used to test such a hypothesis because it is the product of an unknown equilibrium constant and a rate constant. ϕ_t would, then, be determined in a separate step and be unrelated to the solvent isotope effect. Unfortunately, it is also possible that k_{HBr_3} and k_{DBr_3}, which are obtained at the end of a long chain of calculations, contain systematic errors which vitiate the solvent isotope effect. It is also possible that transfer isotope effects,[8b] which are neglected in developing the simple theory, become important for the polyvalent anions we are considering here. Neither of these possibilities would jeopardize the other mechanistic conclusions reached above.

Experimental Section

Materials and Solutions. Cyclopentadienylmercuric bromide was prepared from freshly sublimed cyclopentadienylthallium and mercuric bromide by the method of Nesmyanov and Dovoryantseva.[25] It decomposed at 96–97 °C. It was stored in foil-wrapped, brown bottles at 0 °C, and, as judged by its color and UV spectrum, did not show appreciable decomposition for at least a month.

Standard acids and bases were made up in the usual way.[26] Perchloric acid in D_2O was prepared by diluting concentrated perchloric acid with 99.7% D_2O (Aldrich Chemical Co.) to give acid of usable concentration with a deuterium content of at least 98 atom %. All the carboxylic acids, except acetic, were obtained from Aldrich Chemical Co. and were distilled before use. Acetic acid (Reagent grade) was from Baker Chemical Co., and was used without further purification. Buffer solutions were prepared by half-neutralization of the acids with NaOH solutions. Sodium bromide solutions were made up from weighed samples of the solid (G. F. Smith Co., Reagent grade).

Products. The organic reaction product, cyclopentadiene, was isolated by carrying out the reaction on a 200-mL scale, in a 250-mL three-necked flask, using C_5H_5HgBr concentrations and methanol concentrations 2.5 times those used in the kinetic experiments, but otherwise identical conditions. The reaction flask also contained 3 mL of pentane, in which C_5H_5HgBr is not very soluble. When the reaction was complete, N_2 was passed through the stirred product mixture at the rate of about seven bubbles per minute. The gas was passed through a drierite tube and then collected in a 5-mL two-necked flask fitted with a dry ice–acetone condenser and protected from the atmosphere by a drierite tube. After about 2 h the transfer of the pentane and its dissolved product appeared to be complete, but the gas transfer was continued for an additional 4 h to ensure its completion. The product solution was then mixed with 3 mL of tetrahydrofuran containing 5 mg (0.039 mmol) of tetracyanoethylene. The solution was allowed to stand for 24 h at room temperature. Then the solvents were allowed to evaporate, leaving a greyish residue. On recrystallization from a mixture of tetrahydrofuran and pentane, about 3 mg of colorless prisms were obtained, mp 220 °C. The melting point of the tetracyanoethylene adduct of cyclopentadiene is 223 °C.[27] The yield of recrystallized product was about 40%, the rest presumably being lost in the manipulation of such small quantities of material.

Isotopic Composition of the Product. Product derivatives were collected and purified as just described. The tetracyanoethylene adduct was then introduced as a solid into an AEI MS-30 mass spectrometer.[28] In the high

vacuum of the inlet chamber the adduct released, by cracking, quantities of cyclopentadiene sufficient for measurement of mass ratios, even at room temperature. The mass spectra were obtained at 10 eV. The relative abundances of C_5H_6 and C_5H_5D were obtained from eq 21–23. M_m is the relative intensity at the peak for mass,

$$M_{66} = (1 - C^*)RH \tag{21}$$

$$M_{67} = C^*RH + (1 - C^*)RD \tag{22}$$

$$M_{68} = C^*RD \tag{23}$$

m. RH and RD are the relative abundances of C_5H_6 and C_5H_5D, respectively, and C^* is the relative abundance of cyclopentadiene molecules containing ^{13}C. Since the natural abundance of ^{13}C is 1.1%,[29] C^* should have been 0.055. However, experiments with undeuterated cyclopentadiene gave a value of 0.08 ± 0.01, and this was used in subsequent experiments. Equations 21–23 overdetermine the two unknowns, RH and RD, but satisfactory agreement with measured intensities was quite generally obtained. Each spectrum was scanned 4–5 times, giving values of RH/RD which usually spanned no more than 10%. The average values had probable errors of 1–2%.

Kinetic Experiments. Rates were measured in a Beckman DU spectrophotometer or a Cary 15 spectrophotometer, both with conventionally temperature-controlled cell compartments. Reaction mixtures were made up as required and brought to 25.0 °C in a water thermostat. Reaction was initiated by adding the substrate as a solution in methanol. The temperature of reaction mixtures in the spectrophotometer cell compartment was occasionally measured and never differed from 25 °C by more than 0.1 °C.

References and Notes

(1) Supported, in large part, by the National Science Foundation through Grant GP-31360X, to the University of Minnesota.
(2) F. R. Jensen and B. Rickborn, "Electrophilic Substitution of Organomercurials", McGraw-Hill, New York, N.Y., 1968.
(3) M. M. Kreevoy, P. J. Steinwand, and W. V. Kayser, J. Am. Chem. Soc., 88, 124 (1966).
(4) M. M. Kreevoy, D. J. W. Goon, and R. A. Kayser, J. Am. Chem. Soc., 88, 5529 (1966).
(5) M. M. Kreevoy, T. S. Straub, W. V. Kayser, and J. L. Melquist, J. Am. Chem. Soc., 89, 1201 (1967).
(6) D. B. Scaife and H. J. V. Tyrrell, J. Chem. Soc., 392 (1958).
(7) J. R. Coad and M. D. Johnson, J. Chem. Soc. B, 633 (1967).
(8) (a) J. M. Williams and M. M. Kreevoy, Adv. Phys. Org. Chem., 6, 63 (1968); (b) M. M. Kreevoy, "Isotopes in Organic Chemistry", Vol. 2, E. Buncel and C. C. Lee, Ed., Elsevier Scientific Publishing Co., New York, N.Y., 1976, pp 4–13.
(9) M. M. Kreevoy and R. A. Landholm, Int. J. Chem. Kinet., 1, 157 (1969); when combined with the designated activity coefficients of the substrate and H+, eq 3 correctly gives the electrolyte dependence of the acid cleavage of isopropenylmercuric bromide.
(10) G. N. Lewis and M. Randall, "Thermodynamics", McGraw-Hill, New York, N.Y., 1961, Chapter 23.
(11) A. A. Frost and R. G. Pearson, "Kinetics and Mechanism", 2nd ed, Wiley, New York, N.Y., 1961, p 29.
(12) The program was written by Mr. John Sneed of the University of Minnesota Computation Center and is given in full in the Ph.D. Thesis of S. E. Ibrahim, University of Minnesota, 1974, Appendix.
(13) M. M. Kreevoy and T. S. Straub, Anal. Chem., 41, 214 (1969).
(14) R. Barbieri and J. Bjerrum, Acta Chem. Scand., 19, 469 (1965).
(15) A. Streitwieser, Jr., and L. L. Nebenzahl, J. Am. Chem. Soc., 98, 2188 (1976).
(16) H. J. Emelius, and J. J. Lagowski, J. Chem. Soc., 1497 (1959).
(17) A. F. Wells, "Structural Inorganic Chemistry", 4th ed, Oxford University Press, Oxford, 1975, p 918.
(18) R. L. Carlin, J. Raitman, M. Dankleff, and J. O. Edwards, Inorg. Chem., 1, 182 (1962).
(19) R. S. Drago and D. W. Meek, J. Phys. Chem., 65, 1446 (1961).
(20) J. R. S. Sorof, R. C. Aggarwal, and J. Prasad, J. Inorg. Nucl. Chem., 31, 3839 (1969).
(21) K. G. Ashurst, N. P. Finkelstein, and L. A. Goold, J. Chem. Soc. A, 1899 (1971).
(22) F. Hibbert and F. A. Long, J. Am. Chem. Soc., 93, 2836 (1971).
(23) F. Hibbert, J. Chem. Soc., Perkin Trans. 2, 1289 (1973).
(24) J. Albery in "Proton-Transfer Reactions", E. F. Caldin and V. Gold, Ed., Chapman and Hall, London, 1975, pp 294–298.

(25) A. N. Nesmyanov and G. G. Dovoryantseva, *Dokl. Adad. Nauk. SSSR*, **159**, 847 (1964).

(26) I. M. Kolthoff and E. B. Sandell, "Textbook of Quantitative Inorganic Analysis", Macmillan, New York, N.Y., 1943.

(27) W. J. Middleton, R. E. Heckert, E. L. Little, and C. G. Krespan, *J. Am. Chem. Soc.*, **80**, 2783 (1958).

(28) The mass spectrometer was obtained through the National Science Foundation Instrument Grant GP-32797 to the University of Minnesota. We are grateful to Dr. Roger Upham for his very resourceful operation of the instrument.

(29) A. J. Gordon and R. A. Ford, "The Chemist's Companion", Wiley, New York, N.Y., 1972, p 88.

Matrix Isolation Studies of Alkyl Radicals. The Characteristic Infrared Spectra of Primary Alkyl Radicals

J. Pacansky,* D. E. Horne, G. P. Gardini,[†] and J. Bargon

IBM Research Laboratory, San Jose, California 95193 (Received July 25, 1977)

Publication costs assisted by IBM Research Laboratory

Matrix isolation studies are presented which demonstrate that high quality infrared spectra of alkyl radicals may be obtained by photochemical decomposition of diacyl peroxides. The infrared spectrum of the n-propyl radical is shown and data are presented for the n-butyl radical. These result are discussed along with those previously presented for the ethyl radical in order to establish characteristic features for the infrared spectra of alkyl radicals.

Introduction

The infrared spectra of organic radicals larger than methyl are practically nonexistent. In contrast to this undesirable situation are the number of ESR studies that exist by the legions. Of the many reasons why so few vibrational spectra exist the formost is that relatively high radical concentrations are required for detection in the infrared. A conservative estimate is that one needs $\sim 10^6$ more radicals to detect with infrared spectroscopic techniques than for ESR measurements. Here a method is described by which very large concentrations of radicals may be produced for infrared detection. The method is structured after the pioneering work of Lebedev[1] on radical pairs, and, also, the elegant ESR studies of Box[2] and McBride.[3]

The low temperature matrix isolation technique utilizing rare gas matrices has been invaluable in the study of reactive species generated photochemically.[4] In Figure 1 an attempt is made to represent a species R–R in a cavity isolated in solid argon. Upon absorption of ultraviolet light the bond ruptures to produce radicals R· + R·. However, since the activation energy required for recombination is typically zero the original species R–R is re-formed. A solution for the problem of radical recombination is shown in Figure 2. A suitable photochemical precursor R–M–R is synthesized which extrudes an obstruction M upon irradiation. This obstruction prevents radical recombination and, in doing so, allows formation of large concentrations of radicals. The obstruction in the case of an argon matrix may be removed by warming to higher temperatures thus allowing the radicals to recombine and, depending on the particular species involved, disproportionate. This is very important because the radicals serve as their own trapping reagents and in doing so give conclusive chemical evidence for their existence.

[†] Current Address: Istituto Policattedra di Chimica Organica, University of Parma, 43100 Parma, Italy

As an initial system diacyl peroxides were chosen because they decompose to carbon dioxide and radicals upon exposure to heat and ultraviolet light.[1-3,5] The events thus occurring for such a system are summarized in Figure 3.

In a preliminary publication[6] acetyl benzoyl peroxide (I) was chosen to demonstrate the feasibility of this approach because the methyl radical would be produced upon photolysis. Since the infrared spectrum of the methyl radical[7,8] for the most part was known then it served as a useful base upon which other radical spectra could be obtained. Thus, I was isolated in an argon matrix and when subsequently irradiated with light $\lambda > 3000$ Å produced the methyl radical which was easily identified by its infrared spectrum. The infrared spectrum of the methyl radical is characterized by an intense feature at 612 cm^{-1} (the out-of-plane bending mode). Another species was formed upon irradiation that upon warm up to 30 K synchronously disappeared with the methyl radical to form toluene. On this basis the species was identified as the phenyl radical. These results are summarized as follows:

$$PhCO_2O_2CCH_3 \xrightarrow[\text{argon}]{h\nu} \begin{array}{c} \nearrow PhCO_2CH_3 + CO_2 \\ \searrow Ph\cdot + 2CO_2 + \cdot CH_3 \xrightarrow[\text{30 K}]{\Delta} PhCH_3 \end{array}$$
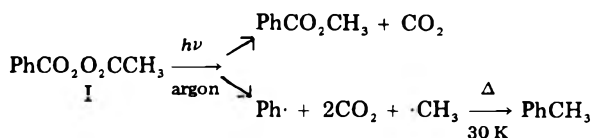
The studies thus far have facilitated the observation of a number of primary and secondary alkyl free radicals. These systems exhibit infrared spectra characteristic of the particular radical center. Since characteristic infrared spectra[9] are of considerable analytical importance they are described at length in this report.

Experimental Section

An infrared spectrometer was constructed that is capable of obtaining spectra in a reflection and total internal reflection mode. With this spectrometer the problems associated with transmission type matrix isolation experiments where a matrix is deposited on a salt substrate
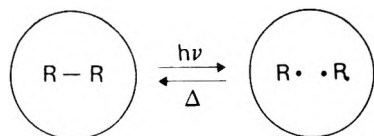
Figure 1. An illustration for the photolysis of a system R–R isolated in a rare gas solid. In this case the radicals R· are inefficiently produced.
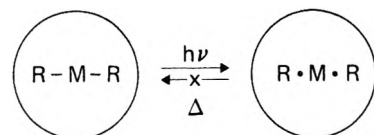
Figure 2. An illustration of a photochemical process that produces large concentrations of radicals. The radical precursor R–M–R isolated in a rare gas solid extrudes an obstruction M upon exposure to ultraviolet light which retards the radical recombination process.
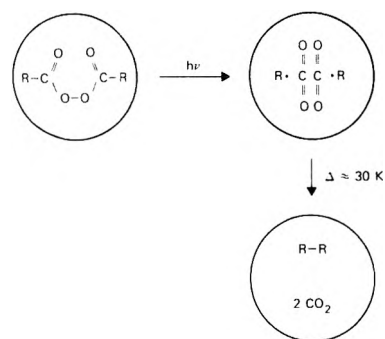
Figure 3. An illustration of the photodecomposition of diacyl peroxides isolated in a rare gas solid. The CO_2 molecules obstruct the radical recombination process. This obstruction may be removed thermally and thus provides direct information for the presence of a particular radical species.

(e.g., thermal contact and thermal conductivity) are overcome by specular reflection off a gold-plated copper block. Spectra are thus obtained by passing the infrared radiation through a matrix which is then reflected off the gold mirror and repassed through the matrix.

Infrared spectra of matrix isolated systems may also be obtained in a total internal reflectance[10] mode using this spectrometer. These results will be published at a future time.

The design of the system for low temperature TIR studies is divided into two parts. In the first part, the infrared spectrometer is subdivided into three sections: the monochromator, double beam goniometer, and detection system. The second part consists of the low temperature, sample handling, and vacuum system.

Infrared Spectrometer. Monochromator. A Spex Industries Incorporated Model 1701 monochromator was chosen for our system. The grating mechanism is of the Czerny–Turner type of the leadscrew cut to a cosecant function. The mirrors have a focal length of 750 mm with an aperature of $f/7$ in the ultraviolet. Five Bosch and Lomb gratings blazed at 8000, 5000, 2500, 625, and 333 cm^{-1} are used to cover the region from 10000 to 250 cm^{-1}. The monochromator is equipped with straight exit and entrance slits adjustable from 0 to 5 mm. Long wavelength pass filters are used to eliminate the second and higher orders of diffracted light.

Double Beam Goniometer. The double beam goniometer was designed by and obtained from Harrick Scientific.[11] Since it is the heart of the spectrometer we give a brief discussion of its operation. A diagram of the goniometer is presented in Figure 4. Three arms are mounted on the goniometer. The first, the refocusing arm, is stationary and is attached to the monochromator.
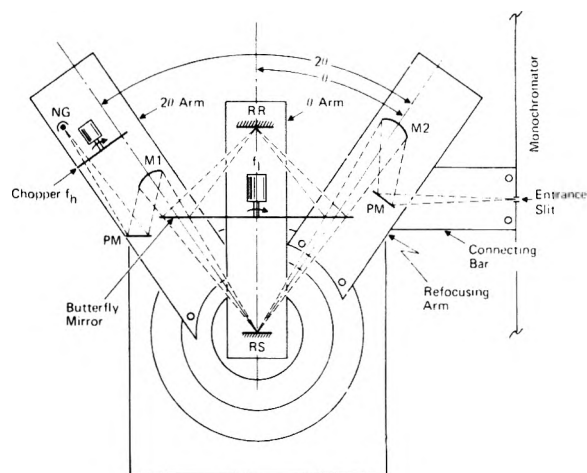
Figure 4. Top view of the double beam goniometer: Nernst glower = NG; M1 and M2 are focusing mirrors; PM = plane mirrors; RR = reflectance reference; RS = reflectance sample; f_h = high-frequency chopper, 73 Hz; f_l = low-frequency chopper, 17 Hz; θ = angle of incidence on the reflectance sample.

The second, the θ arm, is rotated at an angle θ from the refocusing arm while the third arm, the 2θ arm, is rotated at an angle 2θ from the refocusing arm. Consequently, the angle of incidence, i.e., the angle between the infrared radiation incident on the reflectance sample RS and the normal to RS, may be varied θ degrees by movement of the θ and 2θ arms while maintaining optical alignment and focusing of the infrared source on the entrance slits of the monochromator.

The infrared source is mounted on the 2θ arm along with the high-frequency chopper f_h and the focusing mirror M1. The θ arm houses the reflectance sample and reference, RS and RR, and the butterfly mirror which is silvered on one side to reflect the infrared light to RR. The butterfly mirror rotates to alternatively direct the infrared radiation to the sample or reference and also functions as the low frequency chopper f_l.

The Detection System. The principles of the optical detection system are described by Munroe.[12] A diagram of the system is shown in Figure 5. The mirrors, shown as the reflectance sample and reflectance reference in Figure 2, and the low frequency chopper, f_l, are located on the θ arm of the optical goniometer. The infrared source and the high frequency chopper, f_h, are located on the 2θ arm of the optical goniometer. As shown, the system may function in a transmission or reflection mode depending on the location of the sample.

The infrared source is a 1.5 × 14 mm or 4 × 14 mm Nernst glower operated at 2000 K. The radiation is modulated by choppers f_h and f_l at rates of 73 and 17 Hz. The chopper f_l is the butterfly mirror which splits the IR radiation into I, the intensity of the sample beam, and I_0, the intensity of the reference beam. Alternatively, I or I_0 passes through the monochromator and is focused on the detector by an off axis ellipsoidal mirror with a 6 to 1 reduction of the exit split image. The detector is an evacuated thermocouple with a rectangular area of 1 × 3 mm and a CsI window ground into a plano-convex lens. Nominally, the sensitivity of the detector is 2 $\mu V/\mu W$ at 17 Hz.

The voltage output of the detector ranges from several hundred microvolts at 5000 cm^{-1} to several tenths of a microvolt at 300 cm^{-1}. The high impedance, low noise Princeton Applied Research transformer combined with the preamp provides a 10000-fold amplification of this signal, thus the Ithaco 391A lock-in amplifier displays a potential into the millivolt range. The lock-in amplifier
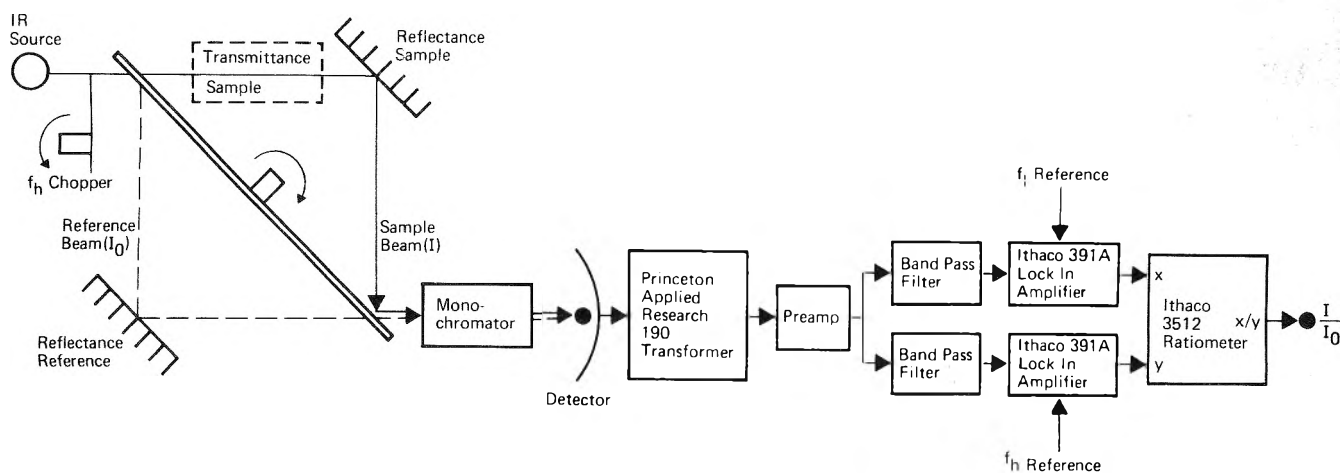
Figure 5. The detection system used for double beam reflectance or transmittance studies.
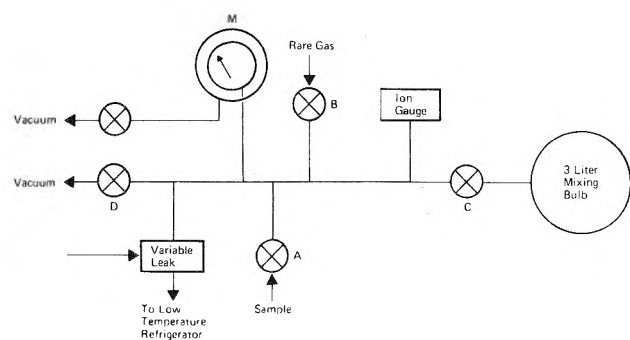
Figure 6. Sample handling system: A = sample inlet valve; B = matrix gas inlet valve; C = mixing bulb valve; D = evacuation valve; M = Wallace and Tiernan differential pressure manometer.

tuned to f_l feeds a signal proportional to $I - I_0$ to the Ithaco 3512 ratiometer while the lock-in tuned to f_h delivers a signal proportional to $I + I_0$. By attenuation of either channel, $I + I_0$ or $I - I_0$ in the ratiometer, I/I_0 is formed and displayed on a strip-chart recorder.

The Low Temperature, Vacuum, and Sample Handling Systems. The heart of the low temperature system is a Displex closed cycle refrigeration system produced by Air Products and Chemicals Inc. The system is capable of operating below 10 K with a 2-W capacity. The temperature is controlled and displayed by an Air Products Model APD-IC-1 indicating temperature controller.

The vacuum system consists of an air-cooled 150 L/s oil diffusion pump equipped with a liquid nitrogen cold trap and mechanical fore pump. The system routinely pumps down to 10^{-7} mmHg.

The sample handling system for samples with at least 0.1 mm vapor pressure is shown in Figure 6. The system is constructed of glass except for the Wallace and Tiernan differential pressure manometer and the Granville-Phillips variable leak whose surfaces exposed to vacuum are stainless steel.

Sufficient sample vapor is introduced into the system by valve A to raise the pressure to 1 mm. Rare gas is introduced into the system by value B to bring the total pressure in the range of 500–700 mm. Valve C is closed and the gas in the 3-L bulb mixed with a magnetic stirrer. The system to the left of valve C is evacuated. With valve D closed the gaseous sample is allowed to fill the entire system. The sample is then introduced into the low temperature refrigerator via the variable leak and the amount deposited recorded by the differential pressure manometer.

The dibutyryl peroxide and dipentyryl peroxide were prepared according to the method outlined by Sheldon and

Kochi.[5] The gaseous mixture of respective peroxide and argon for matrix isolation was prepared by taking the vapor pressure of the peroxide ($\approx$1 mm) and mixing it with 500 mL of argon in the gas handling systems as outlined above. Nominally about 100 mm of this mixture was deposited at a rate of 0.5 mm/min.

Results and Discussion

Molecular systems often contain functional groups which display characteristic infrared spectra.[9] For example carbonyl absorptions have been used not only to identify the presence of a carbonyl bond but in many cases also to determine the particular structure to which the group is attached. In this report it is demonstrated that primary alkyl radicals have characteristic infrared absorptions associated with the radical center and that these absorptions may be used to detect the presence of this particular radical center. This is amply shown by discussing the infrared spectrum of the ethyl radical, and by presenting results on the n-propyl and n-butyl radical.

Ethyl Radical. In a preliminary communication[13] the infrared spectrum of the ethyl radical was presented. Dipropionyl peroxide (II) was isolated in an argon matrix and subsequently irradiated with ultraviolet light with wavelength λ >3000 Å. The results thus obtained are summarized as follows:

$$CH_3CH_2C \overset{\overset{\displaystyle O}{\|}}{\underset{\underset{\displaystyle O}{|}}{\diagdown}} \overset{\overset{\displaystyle O}{\|}}{\underset{\underset{\displaystyle O}{|}}{\diagup}} CCH_2CH_3$$

II

argon 8 K
$h\nu, \lambda$ >3000 Å

$$CH_3CH_2\cdot + 2CO_2 + CH_2CH_2\cdot$$

30 K

$$CH_3CH_2CH_2CH_3 + CH_2CH_2 + CH_3CH_3$$
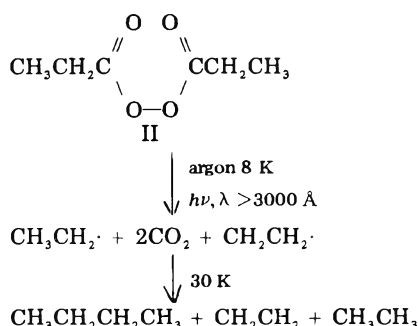
The infrared spectrum and evidence for the presence of the ethyl radical was based upon the synchronous disappearance of the radical spectrum with the appearance of the ethyl radical combination product (n-butane) and disproportionation products (ethane and ethylene).

The n-Propyl Radical. Dibutyryl peroxide (III) was isolated in an argon matrix (1/500). The infrared spectrum recorded with the sample at 8 K is shown in Figure 7. Photolysis with ultraviolet light λ >3000 Å produced carbon dioxide and another new species (Figure 8). This new species is assigned to the n-propyl radical because upon warming to 30 K the infrared spectrum of the new
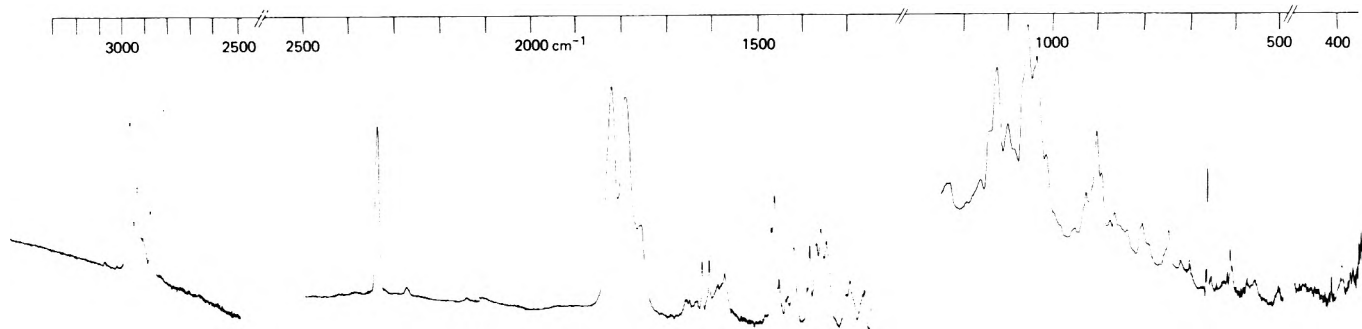
Figure 7. The infrared spectrum of dibutyryl peroxide isolated in an argon matrix (concentration: 1/500).
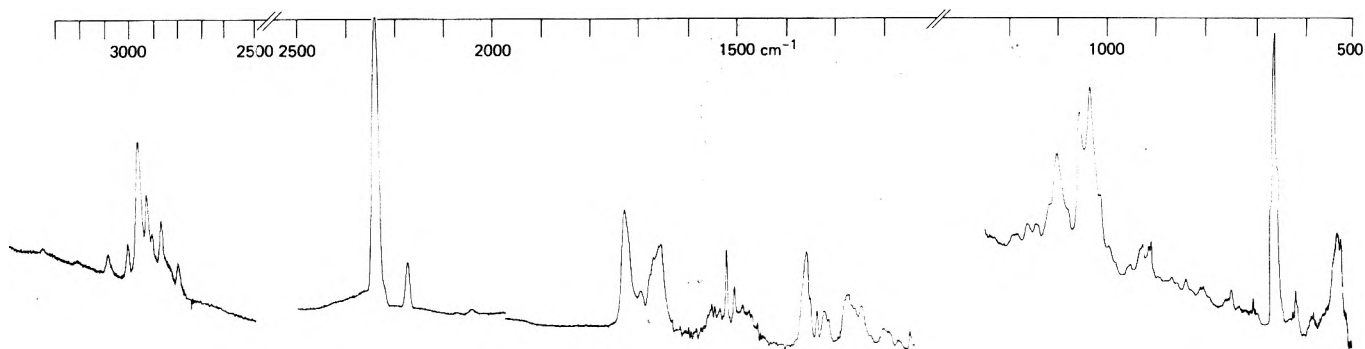
Figure 8. The infrared spectrum of butyryl peroxide in an argon matrix after irradiation with light λ >3000 Å for t = 1950 min. The bands at 2340 cm^{-1} are due to CO_2. Those at $\sim$1800 cm^{-1} are due to residual peroxide carbonyl absorption.

species (Figure 9) disappeared in concert with the appearance of the n-propyl combination product (n-hexane) and disproportionation products (n-propane and propene). These results are summarized as follows:

$$CH_3CH_2CH_2C \overset{\displaystyle O}{\overset{\displaystyle \parallel}{\underset{\displaystyle O-O}{\diagdown}}} \underset{\displaystyle /}{\overset{\displaystyle O}{\overset{\displaystyle \parallel}{}}} CCH_2CH_2CH_3$$

III

$$\downarrow \begin{array}{l} h\nu, \lambda > 3000 \text{ Å} \\ \text{argon, 8 K} \end{array}$$

$$CH_3CH_2CH_2\cdot + 2CO_2 + \cdot CH_2CH_2CH_3$$

$$\downarrow 30 \text{ K}$$

$$CH_3(CH_2)_4CH_3 + CH_2CH_2CH_3 + CH_2{=}CH_2CH_3$$
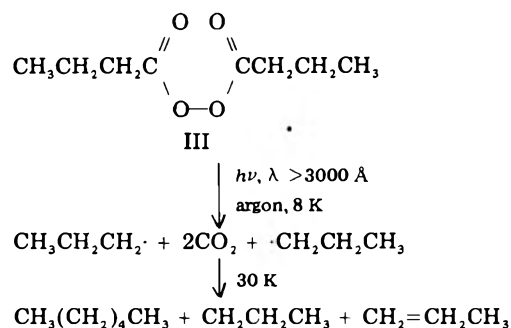
The n-Butyl Radical. Dipentyryl Peroxide (IV) was isolated in an argon matrix (1/500) and irradiated with ultraviolet light. The evidence for the presence of the n-butyl radical is based on the n-butyl radical combination and disproportionation products. These results are summarized as follows:

$$CH_3(CH_2)_3C \overset{\displaystyle O}{\overset{\displaystyle \parallel}{\underset{\displaystyle O-O}{\diagdown}}} \underset{\displaystyle /}{\overset{\displaystyle O}{\overset{\displaystyle \parallel}{}}} C(CH_2)_3CH_3$$

IV

$$\downarrow \begin{array}{l} h\nu, \lambda > 3000 \text{ Å} \\ \text{argon 8 K} \end{array}$$

$$CH_3CH_2CH_2CH_2\cdot + 2CO_2 + \cdot CH_2CH_2CH_2CH_3$$

$$\downarrow 30 \text{ K}$$

$$CH_3(CH_2)_6CH_3 + CH_3CH_2CH_2CH_3 + CH_2{=}CH_2CH_2CH_3$$
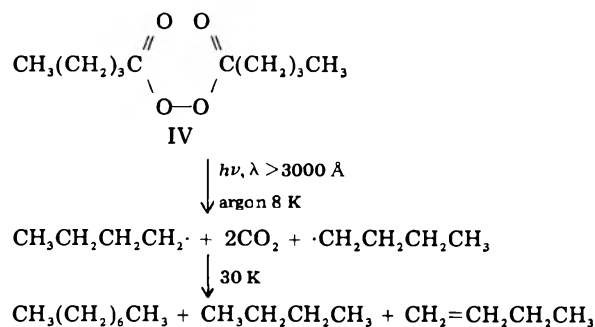
Table I summarizes the vibrational modes observed in the infrared spectra of primary alkyl radicals which are characteristic for this particular class of alkyl radicals and may be used to distinguish primary from secondary and tertiary alkyl radicals, alkanes, and alkenes. Three major

TABLE I: Infrared Active Vibrational Modes Characteristic of Primary Alkyl Radicals

	$CH_3CH_2\cdot$	$CH_3CH_2\cdot$ $CH_2\cdot$	$CH_3(CH_2)_2\cdot$ $CH_2\cdot$
CH stretching vibrations associated with the radical CH_2 group	3112.5 cm^{-1} 3032.5 cm^{-1}	3100 cm^{-1} 3017.5 cm^{-1}	3105 cm^{-1} 3017.5 cm^{-1}
Out-of-plane deformation of the radical center	541 cm^{-1}	530 cm^{-1}	526.5 cm^{-1}
Anomalous band observed in the CH stretching region	2840.0 cm^{-1}	2812.5 cm^{-1}	2800 cm^{-1}

regions exist; each will now be discussed in turn.

The CH Stretching Vibrations Associated with the Radical CH_2 Group. Primary alkyl radicals have two bands above 3000 cm^{-1}. These are assigned to the stretching of the CH bonds on the radical center on the following basis: Photolysis of the deuterated dipropionyl peroxide $CH_3CD_2CO_2O_2CCD_2CH_3$ produces the CH_3CD_2 radical. The infrared spectrum of this species contains no bands above 3000 cm^{-1}. Photolysis of the deuterated peroxide $CD_3CH_2CO_2O_2CCH_2CD_3$ produces the CD_3CH_2 radical. The infrared spectrum of this radical contains the two bands above 3000 cm^{-1} as in CH_3CH_2 but absorptions between 2800 and 3000 cm^{-1} charactertistic of CH stretching frequencies in methyl groups are shifted to lower frequencies. Thus the isotopic studies briefly outlined above clearly show that two absorptions above 3000 cm^{-1} are associated with the stretching of the CH bonds on the radical center. Although detailed isotopic studies have not been performed for the n-propyl and n-butyl radicals this situation is not expected to change. A qualitative description of the bonding about the radical center may be obtained by comparing the absorptions in the CH stretching of the radical center with those for $CH{=}CD_2$.[14] The vibrational CH stretching frequencies for $CH_2{=}CD_2$ are 3095 and 3016 cm^{-1}. These in comparison to those
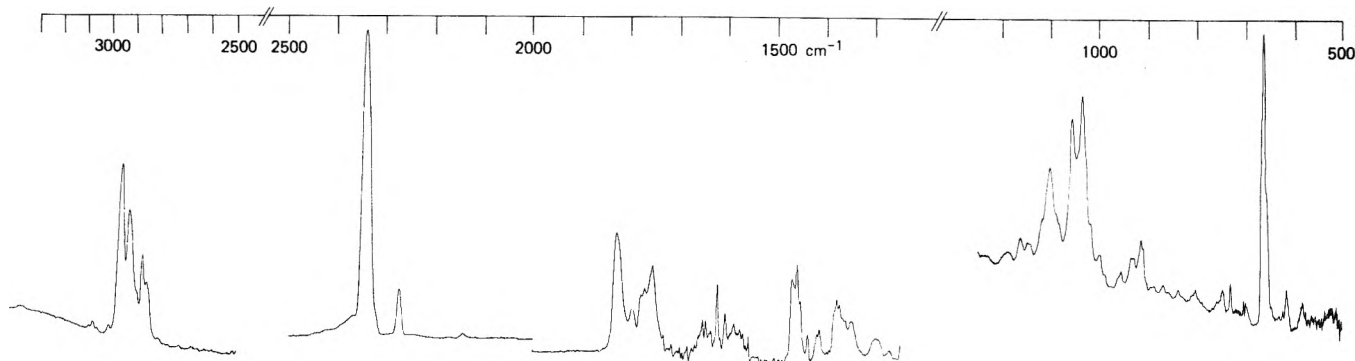
Figure 9. The infrared spectrum of irradiated butyryl peroxide after warm up to 30 K. The spectrum is a composite of propane, propene, and hexane, the disproportionation and combination products of the n-propyl radical.

listed in Table I for the primary alkyl radicals leads us to conclude that the electronic structure of the CH_2 group in each of the radicals probably exists in an sp^2 configuration and hence is planar or nearly planar.

The Out-of-Plane Deformation of the Radical Center. The most intense feature in the infrared spectrum of the methyl radical is the out-of-plane bending mode at 612 cm^{-1}. It is reasonable to expect that for the ethyl radical the out-of-plane deformation should also be an intense feature in the infrared spectrum but shifted to lower frequency due to the additional mass of the methyl group over hydrogen. In addition, as also exhibited by the CH stretching modes on the radical center, progressing from ethyl to n-butyl the frequency of the out-of-plane deformation should converge. In the infrared spectrum of each of the radicals discussed the most intense feature is 541 cm^{-1} (ethyl), 530 cm^{-1} (n-propyl), and 526.5 cm^{-1} (n-butyl). Evidence that these bands are due to the out-of-plane bending mode for each radical is supported by the deuterium isotope experiments discussed above for the ethyl radical. The intense 541-cm^{-1} band in the $CH_3CH_2\cdot$ spectrum shifted with deuterium substitution along with the modes assigned to the CH stetches of the radical center and, thus, is associated with the radical center and is assigned to the out-of-plane deformation mode of the radical center. Similarly, the 530-cm^{-1} band in the n-propyl radical spectrum and the 526.5-cm^{-1} absorption for the n-butyl radical are assigned to the out-of-plane bending modes of the radical centers.

The frequency of the out-of-plane bending modes is rather insensitive to chain length. The greatest changes are seen from ethyl to n-propyl with very little differences between n-propyl and n-butyl. The rather low frequency of this vibration in comparison to the similar mode[14] in $CH_2=CD_2$ (943 cm^{-1}) is a direct reflection of the ease with which the radical center may distort.

Anomalous Band Observed in the CH Stretching Region. The infrared spectrum of each of the radicals observed thus far contains a band in the CH stretching region at an anomalously low frequency. This band is not observed in alkanes and is believed to be a direct manifestation of the radical center. For the ethyl radical this band occurs at 2840 cm^{-1} and is associated with the methyl groups because it is also observed in the isotopic species CH_3CD_2. The n-propyl radical (2812 cm^{-1}) and n-butyl radical (2800 cm^{-1}) each display a band at a slightly lower frequency which is assigned to the methylene group adjacent to the radical center.

The exact nature of the mechanism responsible for this anomalous band is of considerable interest because it may provide a valuable group frequency for the identification of a number of different alkyl radical groups. For example, the 2840-cm^{-1} band indicates a methyl group is adjacent

to a radical center. Preliminary studies on the infrared spectrum of the isopropyl radical which contains a band at 2834-cm^{-1} substantiates this claim.[15] When a methylene group is adjacent to a radical center a band appears at 2800 cm^{-1} as shown by the n-propyl and n-butyl radical.

The infrared spectra of primary alkyl radicals may clearly be distinguished from those for closed shell hydrocarbons by utilizing the absorptions discussed above. In the following discussion it is shown that the same situation holds for secondary and tertiary radicals and most importantly that primary alkyl radicals may be distinguished from secondary and tertiary radicals. This is achieved by presenting preliminary results on the isopropyl radical and predicting the spectrum of the tert-butyl radical.

The infrared spectrum of the isopropyl radical[15] is set aside from primary radicals by two important features. The first is that there is only one absorption above 3000 cm^{-1}, the CH stretching mode of the CH bond on the radical center at the 3045 cm^{-1}. The second feature is a rather low frequency observed at 375 cm^{-1}, tentatively assigned to the out-of-plane bending mode of the radical center.

Thus far no infrared spectra have been obtained for the tert-butyl radical, however, its spectrum is easily predicted. Based on the present studies this system should have no absorptions above 3000 cm^{-1} but should have a band at 2840 cm^{-1} due to an anomalous CH stretch in the methyl groups. In addition the radical center has been shown to have a very low barrier to inversion and a pyramidal geometry by Wood[16] et al., and Koenig and collaborators.[17] These results predict that the "out-of-plane deformation" of the radical center should appear less than 200 cm^{-1}.

Conclusion

The present studies have demonstrated (1) a class of "suitable precursors" from which infrared spectra of organic radicals may be obtained, and (2) characteristic infrared spectra of primary alkyl radicals.

Matrix isolation studies have shown that a large number of diacyl peroxides may be prepared that yield high quality infrared spectra upon exposure to ultraviolet light.

The infrared spectra of primary alkyl radicals are characterized by two absorptions above 3000 cm^{-1} and another at ~530 cm^{-1}. The former two are assigned to the CH stretching frequencies of the radical center and the latter is due to the out-of-plane deformation of the radical. These features indicate an sp^2 electronic configuration about the radical and that the radical center is easily distorted.

Another feature arises in the infrared spectra of alkyl radicals at ~2840 and ~2800 cm^{-1} which is attributed to the presence of a methyl group and a methylene group in

a position β to the radical center.

Acknowledgment. The technical assistance of Mr. Fred Rodgers is gratefully appreciated.

References and Notes

(1) Y. S. Lebedev, *Dokl. Akad. Nauk. SSSR*, **171**, 378 (1966).
(2) H. C. Box, *J. Phys. Chem.*, **75**, 3426 (1971).
(3) N. J. Karch, E. T. Koh, B. L. Whitsel, and J. M. McBride, *J. Am. Chem. Soc.*, **97**, 6729 (1975).
(4) B. Meyer, "Low Temperature Spectroscopy", Elsevier, New York, N.Y., 1971.
(5) R. A. Sheldon and J. K. Kochi, *J. Am. Chem. Soc.*, **92**, 4395 (1970).
(6) J. Pacansky and J. Bargon, *J. Am. Chem. Soc.*, **97**, 6896 (1975).
(7) A. Snelson, *J. Phys. Chem.*, **74**, 537 (1970).
(8) D. E. Milligan and M. E. Jacox, *J. Chem. Phys.*, **47**, 5146 (1967).
(9) L. J. Bellamy, "The Infrared Spectra of Complex Molecules", Chapman and Hall, London, 1975.
(10) N. J. Harrick, "Internal Reflectance Spectroscopy", Interscience, New York, N.Y., 1967.
(11) Harrick Scientific Corp., Ossiuing, N.Y.
(12) D. C. Munroe, Ithaco Data Sheet, IAN-32.
(13) J. Pacasky, G. P. Gardini, and J. Bargon, *J. Am. Chem. Soc.*, **98**, 2665 (1976).
(14) L. M. Sverdlov, M. A. Kovner, and E. P. Krainov, "Vibrational Spectra of Polyatomic Molecules", Wiley, New York, N.Y., 1974.
(15) J. Pacansky, results to be published.
(16) D. E. Wood, L. F. Williams, R. F. Sprecher, and W. A. Lathan, *J. Am. Chem. Soc.*, **94**, 6241 (1972).
(17) T. Koenig, T. Balle, and W. Snell, *J. Am. Chem. Soc.*, **97**, 662 (1975).

Two Clathrate Hydrates of Dimethyl Ether[1]

S. L. Miller,*

Department of Chemistry, University of California, San Diego, La Jolla, California 92037

S. R. Gough, and D. W. Davidson

Division of Chemistry, National Research Council of Canada. Ottawa, Ontario, Canada K1A OR9 (Received May 25, 1977)

Vapor pressure measurements below 0 °C along three-phase equilibrium lines in the dimethyl ether (DME)–water system show the existence and conditions of stability of two DME hydrates. X-ray and composition studies establish that the hydrate stable between –28.5 and –20.7 °C is a cubic structure II clathrate (h_{II}, DME·~17H_2O) and suggest that the hydrate stable below –34.8 °C is a tetragonal clathrate (h_T, DME·~8.6H_2O) isomorphous with bromine hydrate. Between –34.8 and –28.5 °C the composition of the system determines whether h_{II}, h_T, or both are stable. The pressure along the ice melting point curve passes through a maximum value at –18.2 °C as a result of the opposite signs of the enthalpies of fusion of ice and of solution of DME in water.

Dimethyl ether (DME) is a molecule small enough to form a clathrate hydrate, although its high solubility in water could prevent hydrate formation. The possibility of hydrate formation by DME is of interest in the context of the hydrate theories of general anesthesia.[2] A hydrate of DME was reported by von Stackelberg and Müller,[3] but only the unit cell dimension was determined at –30 °C (17.44 Å cubic *Fd3m*, structure II) from a six line x-ray powder pattern. We have investigated the DME–water system and find that there are two hydrates: a higher temperature structure II hydrate and a low temperature hydrate probably isostructural with the tetragonal bromine hydrate.[4] Although structure II hydrates are known to be formed by some 55 molecular species of great diversity of molecular geometry and chemical type,[5,6] the restrictions on the geometry of molecules capable of forming the tetragonal hydrate are so severe that bromine hydrate is the only previously known example of this structure. In addition to defining the stability conditions of these hydrates, our measurements define a region where the vapor pressure of the dimethyl ether–water system decreases dramatically as the temperature is raised from –18 to 0 °C. Dielectric and NMR properties of the two hydrates are described in the paper which follows.[7]

Experimental Section

The hydrates for vapor pressure measurements were prepared in an all glass system with a low temperature bath as previously described.[8] The pressures along three-phase equilibrium lines were read on a mercury manometer to ±0.1 mm with a cathetometer and corrected to Int. mm. The temperatures were measured with a Hewlett-Packard quartz thermometer and checked with mercury thermometers which can be read to ±0.01 °C. Below –35 °C the quartz thermometer was calibrated with an ammonia vapor pressure thermometer. The ice was prepared by grinding with a mortar and pestle at liquid nitrogen temperatures,[8] and degassed by pumping at –5 °C. The dimethyl ether was Matheson CP grade which was purified further by several distillations at low temperature. Samples of known composition were prepared by weighing the dimethyl ether and water and transferring to liquid nitrogen-cooled sample tubes in a vacuum line and sealing under vacuum. Particular care is needed to exclude air from the samples because air greatly stabilizes the structure II hydrate.

The hydrate dissociation pressures were measured by approaching the equilibrium from both the high and low pressure sides. The dissociation pressures for metastable equilibria were obtained by forming the low temperature hydrate below –40 °C, raising the temperature quickly into the metastable region, and following the rise in pressure to the metastable equilibrium value before the pressure dropped to the structure II value. At several temperatures it was possible to measure the equilibrium from both the high and low pressure sides before the low temperature

hydrate reverted entirely to structure II hydrate. The partial pressures of dimethyl ether were calculated from the total measured pressure by subtracting the vapor pressure of ice.

X-ray powder photographs[9] were taken at $\sim$-150 °C in a 6-cm flatplate camera with Mc Kα radiation and were corrected for film shrinkage. Two samples of stoichiometry DME·9.6H$_2$O and one of DME·19H$_2$O were conditioned for several days at -40 and -25 °C, respectively, ground, and transferred to thin-walled capillary tubes in the dry atmosphere above boiling nitrogen. A photograph was also taken of a sample DME·8.55D$_2$O which had been found to give the relatively broad proton resonance line characteristic of the low-temperature form.[7]

The compositions of the hydrates were determined by measurement of the volume of gas which reacted with a known amount of ice. The measuring system was based on that used by Barrer and Edge[10] to study the formation of hydrates of the rare gases. The reaction chamber, a conical flask containing 50 $^1/_8$-in. diameter Monel balls and about 0.1 g of degassed water, was mounted on a mechanical shaker contained in a variable-temperature cold chamber and connected by flexible metal tubing to the gas-handling system. The latter consisted of a mercury manometer, a gas buret, and a dioctyl phthalate filled U-tube which served as a sensitive indicator of pressure change. One arm of the U-tube led to a ballast vessel initially at the same pressure as the line. Absorption of gas was measured at effectively constant pressure from the change in gas buret volume required to restore the pressure difference across the U-tube to zero, slight pressure changes in the system resulting from changes in room temperature being balanced over relatively long equilibration times by corresponding changes in the pressure of the ballast volume.

To form hydrate, ice was slowly cooled from a temperature just above the hydrate–ice–gas equilibrium line. Initial hydrate formation was detected at a temperature about 3 °C below the equilibrium line, at which point shaking was initiated. Thereafter the gas uptake was monitored for several days, with intermittent shaking followed by adjustment of the volume to constant pressure, until further absorption of gas was no longer detected. The volume of gas released when the hydrate decomposed, at a somewhat higher temperature, agreed with the volume absorbed to better than 0.5%.

Results and Discussion

The Structure II DME Hydrate (h_{II}). Dissociation pressures of the high temperature hydrate were measured at ten temperatures between -33.54 and -20.71 °C and are shown in Figure 1. No metastable points could be obtained for this hydrate. Least-squares fit of the data gives

$$\log P_{mm} = 8.0246 - 1292.36/T \qquad (1)$$

with a standard deviation of $\sigma = 0.2\%$ in P.

The 14-line diffraction pattern of the DME·19H$_2$O sample was readily indexed in terms of the cubic structure II clathrate hydrate lattice[3,9] with $a = 17.27 \pm 0.11$ Å (standard deviation) at -150 °C. This is in agreement with von Stackelberg and Müller's value[3] of 17.44 Å at -30 °C.

The composition of this hydrate measured at -24 °C was DME·(17.41 $\pm$ 0.50)H$_2$O. This is clearly a structure II hydrate in which the 16-hedra are nearly fully occupied.[11]

The Tetragonal DME Hydrate (h_T). Dissociation pressures of the stable low temperature hydrate were measured at eight temperatures between -55.13 and -36.09 °C; an additional five measurements between -35.04 and -30.12 °C were made in the metastable region (Figure 1).

Figure 1. Pressure–temperature phase diagram of DME and water: ($\blacklozenge$) quadrupole points; ($\cdots\cdots$) metastable curve of I + h$_T$ + g; (----) h$_T$ + h$_{II}$ + g. The lines are calculated from the equations in the text.

Least-squares fit of these data including the metastable points gives

$$\log P_{mm} = 9.9923 - 1657.52/T - 1.8273 \times 10^{-3}T \qquad (2)$$

$\sigma = 0.2\%$ in P.

The x-ray powder patterns were not sufficient to identify the structure of this hydrate. The patterns given by the three samples showed lines characteristic of varying amounts of structure II and ice, but not solid DME, as impurities. The remaining lines were not consistent with the common cubic structure I clathrate hydrate.[3,12]

The measured composition of the low-temperature hydrate was DME·(8.78 $\pm$ 0.11)H$_2$O at -39 °C and 338 mmHg. The error limit makes a generous allowance for uncertainties in volume and pressure measurement and for possible loss of ice through vaporization.

This hydrate is shown to be a clathrate hydrate by its NMR and dielectric behavior.[7]

Double refraction was clearly observed under a polarizing microscope at low temperatures. The double refraction disappeared and gas was evolved when the temperature was raised and the crystals transformed to the cubic structure II hydrate.

The tetragonal structure, as found for bromine hydrate,[4] contains 172 water molecules which enclose ten 12-hedra, sixteen 14-hedra, and four 15-hedra. The ideal composition for this hydrate is DME·8.60H$_2$O when the 14-hedra and 15-hedra are 100% occupied. The observed composition is consistent with the tetragonal form for 97.9 $\pm$ 1.3% occupancy of the two larger cages but is not consistent with the hexagonal hydrate structure of ideal composition DME·10H$_2$O which is only known to occur in highly distorted form in trimethylamine hydrate.[13] The tetragonal structure also accounts satisfactorily for the un-

usual anisotropy of the reorientational motion of the encaged DME molecules in the low temperature hydrate which is shown by the NMR and dielectric studies.[7] Although all the evidence thus suggests the tetragonal structure for this hydrate, there may be other hydrates of unknown structure consistent with this evidence.

DME differs from cyclopropane[8] and trimethylene oxide[14] which form hydrates of both structure I and structure II. Bromine and DME are approximately the same size ($\sim$6.2 Å) in longest dimension and considerably larger than cyclopropane and trimethylene oxide (both $\sim$5.5 Å), so that bromine and DME may be too large to fit comfortably into the 14-hedra of the structure I hydrate. However, it is possible that a structure I hydrate of DME is stable at temperatures lower than investigated in this study.

The $h_T + h_{II} + g$ Equilibrium Pressures. Between -35.2 and -28.6 °C and with DME/H$_2$O mole ratios between 1/17 and 1/8.6, the tetragonal and structure II hydrates are in equilibrium with DME(g). These dissociation pressures were measured in a system containing 18 wt % DME. The pressure initially corresponded to I + l$_2$ + g, then dropped almost to the I + h$_T$ + g equilibrium pressure, but after several days the pressure rose to the h$_T$ + h$_{II}$ + g equilibrium value. (I is ice, l$_2$ the DME-rich liquid phase.) Five measurements between -33.02 and -29.19 °C (Figure 1) are fitted by

$$\log P_{mm} = 9.8161 - 1718.38/T \tag{3}$$

$\sigma = 0.1$ in P. Along this equilibrium line the reaction is

$$\frac{17}{17 - 8.6} \text{DME} \cdot 8.6 \text{H}_2\text{O} = \frac{8.6}{17 - 8.6} \text{DME} \cdot 17 \text{H}_2\text{O} + \text{DME(g)}$$
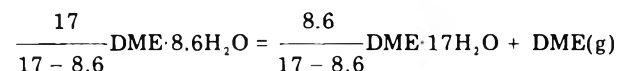
This equilibrium pressure can also be calculated from the I + h + g equilibrium pressures of the two hydrates if ideal stoichiometry is assumed. For the reaction

$$h_{II} = 17 \text{H}_2\text{O(s)} + \text{DME(g)}$$

$$P_{II} a_W{}^{17} = P_{II}{}^0$$

Similarly for h$_T$

$$P_T a_W{}^{8.6} = P_T{}^0$$

$P_{II}{}^0$ and $P_T{}^0$ are the equilibrium pressures for I + h + g, a_w is the activity of water relative to ice, and P_{II} and P_T are the equilibrium pressures at the reduced water activity. In the equilibrium h$_T$ + h$_{II}$ + g, $a_{wII} = a_{wT}$ and $P_{II} = P_T$ give

$$a_W = \left(\frac{P_{II}{}^0}{P_{II}} \right)^{1/17} = \left(\frac{P_T{}^0}{P_T} \right)^{1/8.6}$$

Rearrangement gives

$$\log P_{II} = \log P_T = \frac{17}{17 - 8.6} \log P_T{}^0 - \frac{8.6}{17 - 8.6} \log P_{II}{}^0$$

and from eq 1 and 2

$$\log P_{mm} = 12.0068 - 2031.38/T - 3.6981 \times 10^{-3}T \tag{4}$$

Equation 4 predicts somewhat higher pressures than observed (e.g., 608 mm at -29 °C vs. 600 mm from eq 3). Small changes in the compositions of the hydrates do not change the difference substantially. The origin of the difference lies probably in the errors of the extrapolation

of the h$_T$ dissociation pressures or possibly in the presence of traces of air which alter substantially the stability of these hydrates.

The I + l$_1$ + g Equilibrium. As shown in Figure 1, the pressure in the DME–water system drops as the temperature rises from -18 to 0 °C. The pressures measured at 20 temperatures between -23.00 and -3.42 °C (Figure 1) can be expressed by the equation

$$P_{DME} = -105.90t - 4.290t^2 - 0.05070t^3 \tag{5}$$

$\sigma = 1.2$ mm, where t is the temperature in °C. It is apparent that this univariant system consists of ice, a water-rich DME solution (l$_1$), and DME gas.

The pressure maximum of 812.0 mm at -18.2 °C along the I + l$_1$ + g curve can be understood in terms of the negative enthalpy of solution of gaseous DME and the positive enthalpy of fusion of ice. For 1 mol of DME, the solution reaction is

$$\frac{1 - X}{X} \text{H}_2\text{O(s)} + \text{DME(g)} = \text{DME(aq, } X\text{)} \tag{6}$$

where X is the mole fraction of DME in the solution. Along the three-phase line I + l$_1$ + g

$$\frac{dP}{dT} = \frac{\Delta H}{T \Delta V} = \frac{\Delta H_f (1 - X)/X + \Delta H_s}{T \Delta V} \tag{7}$$

where ΔH_f is the heat of fusion of ice, approximated here as a constant 1436 cal mol^{-1}, and ΔH_s is the heat of solution per mole of DME(g). ΔV is the volume change on solution and is closely approximated by the decrease in the volume of gas ($-RT/P$). Thus

$$\frac{dP}{dT} = -\frac{\Delta H_f (1 - X)/X + \Delta H_s}{RT^2/P} \tag{8}$$

At high mole fractions of DME, only a small amount of ice is melted in dissolving 1 mol of DME, and ΔH_s is the largest term. Since ΔH_s is negative, there is a positive dP/dT. At low mole fractions, much more ice is melted in dissolving 1 mol of DME, and the first term predominates giving a negative dP/dT. At the pressure maximum, we have $dP/dT = 0$, $t = 18.2$ °C, $P = 812.0$ mm, and $X = 0.158$. This gives $\Delta H_s = -7653$ cal, which is in agreement, in view of the approximations made, with $\Delta H_s = -8937$ cal obtained from the temperature dependence of the solubility[15] between -1 and 25 °C and a mole fraction of 0.02.

Equation 8 can be integrated by assuming ΔH_s to be constant, approximating the mole fraction of DME along the line[16] I + l$_1$ + g by $X = 2.371 - 8.68 \times 10^{-3}T$, and using the pressure maximum to evaluate the constant of integration. The result is

$$\log P_{mm} = 14.1786 - 1853.96/T + 1.11566 \log [(1 - 3.661 \times 10^{-3}T)/T] \tag{9}$$

The pressures calculated from this equation are higher by less than 0.5% than the curve given by eq 5 between -22 and -12 °C. This is excellent agreement considering the approximations of constant ΔH_f and ΔH_s and the formula for the freezing point mole fraction.

Other two-component systems in which the pressure decreases as the temperature is raised are known. Aqueous ammonia is analogous to the DME–water system and has a pressure maximum at -17.0 °C and 14.3 mm.[17] Other examples are found in retrograde condensation and some aqueous salt solutions.[18]

The Composition Phase Diagram and the Quadruple Points. The composition phase diagram is shown in Figure
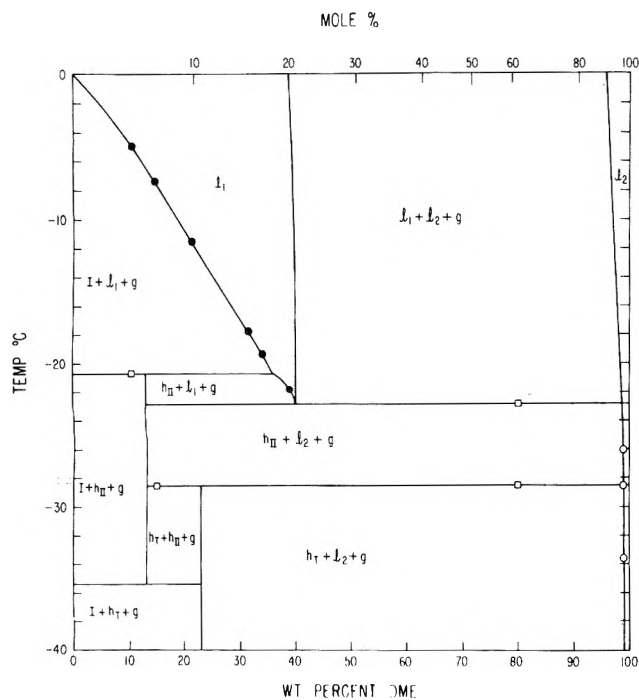
Figure 2. Composition phase diagram of DME and water: measurements of freezing points and compositions of (●) l_1 and (○) l_2; (□) observations of phase changes in sealed tubes.

2. The l_1 line for the $l_1 + l_2 + g$ equilibrium is based on the estimated ratio of l_1 and l_2 in a 41.1 wt % DME sample. This line extends to 35.35 wt % at 24 °C.[19] The l_2 line was estimated from the ratio of the pressure of l_2 in the presence of h_{II} or h_T to that of pure DME(l)[20] at -26.0, -28.5, and -33.5 °C. Assuming Raoult's law, the composition is 97.3 mol % (98.9 wt %) at these three temperatures. This line extends to 93.0 wt % at 25 °C.[19]

Pressures along the h_{II} (or h_T) + l_2 + g curve were measured at seven temperatures between -33.38 and -24.04 °C (Figure 1) and are fitted by

$$\log P_{mm} = 7.4405 - 1136.86/T \qquad (10)$$

$\sigma = 0.2\%$ in P.

$I + h_T + h_{II} + g$. This quadruple point is determined by the intersection of the dissociation pressure curves of $I + h_T + g$ and $I + h_{II} + g$ at -34.82 °C and 400.0 mm. The intersections of $h_T + h_{II} + g$ with $I + h_T + g$ and $I + h_{II} + g$ are at -36.18 and -35.35 °C, respectively. The -34.82 °C value is probably the most accurate, although the error is estimated to be ±0.50 °C because of the acute angle of intersection of the two curves.

$h_T + h_{II} + l_2 + g$. This point is difficult to measure because of the slow rate of interconversion of h_T and h_{II}. For a sample of 80% DME, the reaction $h_T \rightleftarrows h_{II} +$ DME(g) could be observed by appearance and disappearance over several days of the birefringent h_T. This occurred at -28.50 ± 0.50 °C. For 15% DME, the reaction $h_T + h_{II} \rightleftarrows h_{II} + l_2$ could be observed by the appearance and disappearance of l_2. This occurred at -28.63 ± 0.25 °C.

This quadruple point can also be calculated from the intersection of the $h_T + h_{II} + g$ and $h_{II} + l_2 + g$ equilibrium curves. Equations 3 and 10 intersect at -28.36 °C. The

average of these values is -28.50 °C and the dissociation pressure is 621.8 mm.

$h_{II} + l_1 + l_2 + g$. This point was measured by observing the appearance and disappearance of h_{II} in a 80% DME sample ($h_{II} + l_2 \rightleftarrows l_1 + l_2$) at -22.80 ± 0.05 °C. The pressure calculated from eq 10 is 793.3 mm. The directly measured pressure was somewhat lower, 790.8 mm.

$I + h_{II} + l_1 + g$. This point was measured by observing the melting and freezing point of a 10.6% DME solution at -20.71 ± 0.03 °C ($I + h_{II} \rightleftarrows I + l_1$). The pressure measured in a separate experiment was 803.8 mm.

$I + l_1 + l_2 + g$ (Metastable). The intersection of the I $+ l_1 + g$ and $I + l_2 + g$ curves (the latter should be quite close to $h_{II} + l_2 + g$) gives -23.16 °C for the temperature of this quadruple point. The pressure is 781.4 mm. The extension of the $I + l_1 + g$ line meets the $l_1 + l_2 + g$ curve on the composition phase diagram at approximately this temperature.

$I + h_T + l_2 + g$ (Metastable). When h_T is heated over a period of 1 h to -26 °C, it decomposes to ice and l_2. The ice and l_2 eventually form $I + h_{II} + g$ or $h_{II} + l_2 + g$ depending on the composition. The $I + h_T + l_2 + g$ quadruple point is at the intersection of the $I + h_T + g$ and $I + l_2 + g$ curves. This quadruple point is at -25.03 °C and 722.1 mm.

References and Notes

(1) Issued as NRCC No. 16019.
(2) L. Pauling, *Science*, **134**, 15 (1961); S. L. Miller, *Proc. Natl. Acad. Sci. U.S.A.*, **47**, 1515 (1961).
(3) M. von Stackelberg and H. R. Müller, *Z. Elektrochem.*, **58**, 25 (1954).
(4) K. W. Allen and G. A. Jeffrey, *J. Chem. Phys.*, **38**, 2304 (1963).
(5) D. W. Davidson, *Water: Compr. Treat.*, **2**, 115 (1973).
(6) J. A. Ripmeester and D. W. Davidson, *Mol. Cryst. Liq. Cryst.*, in press.
(7) S. R. Gough, S. K. Garg, J. A. Ripmeester, and D. W. Davidson, *J. Phys. Chem.*, following paper in this issue.
(8) D. R. Hafemann and S. L. Miller, *J. Phys. Chem.*, **73**, 1392 (1969).
(9) D. F. Sargent and L. D. Calvert, *J. Phys. Chem.*, **70**, 2689 (1966).
(10) R. M. Barrer and A. V. J. Edge, *Proc. R. Soc. London, Ser. A*, **300**, 1 (1967).
(11) S. R. Gough and D. W. Davidson, *Can. J. Chem.*, **49**, 2691 (1971).
(12) L. Pauling and R. E. Marsh, *Proc. Natl. Acad. Sci. U.S.A.*, **38**, 112 (1952); R. K. McMullan and G. A. Jeffrey, *J. Chem. Phys.*, **42**, 2725 (1965).
(13) D. Pahke, *J. Chem. Phys.*, **48**, 2990 (1968).
(14) R. E. Hawkins and D. W. Davidson, *J. Phys. Chem.*, **70**, 1889 (1966); S. R. Gough, S. K. Garg, and D. W. Davidson, *Chem. Phys.*, **3**, 239 (1974).
(15) The solubility was measured at nine temperatures between -1 and 25 °C. The data are approximated by log (P_{mm}/M) = 14.596 - 2607.6/T - 1.0071 × $10^{-2}T$, σ = 0.3% in P/M, where M is the molar concentration of DME.
(16) The melting points of 10.60, 14.96, 21.50, 31.84, and 34.35 wt % DME solutions were -4.94, -7.40, -11.62, -17.80, and -19.42 °C, respectively.
(17) F. C. Kracek, *J. Phys. Chem.*, **34**, 499 (1930); G. T. Tammann and H. J. Rocha, *Z. Anorg. Chem.*, **209**, 257 (1932).
(18) G. W. Morey and W. T. Chen, *J. Am. Chem. Soc.*, **78**, 4249 (1956); W. W. Ewing, *ibid.*, **59**, 1293 (1937); W. A. West and A. Menzies, *ibid.*, **59**, 1294 (1937).
(19) M. Mannheimer, *Chem. Anal.*, **45**, 8 (1956).
(20) R. M. Kennedy, M. Sagenkahn, and J. G. Aston, *J. Am. Chem. Soc.*, **63**, 2267 (1941).

Dielectric Relaxation and Nuclear Magnetic Resonance Studies of Two Clathrate Hydrates of Dimethyl Ether[1]

S. R. Gough, S. K. Garg, J. A. Ripmeester, and D. W. Davidson*

Division of Chemistry, National Research Council of Canada, Ottawa, Ontario, Canada K1A OR9 (Received May 25, 1977)

Publication costs assisted by the National Research Council of Canada

Continuous-wave NMR and submegahertz dielectric measurements to below 2 K show dimethyl ether molecules encaged in the structure II hydrate to have an exceptional degree of reorientational freedom, the dielectric activation energy being only 0.21 kcal/mol between 5 and 12 K and reorientation becoming almost isotropic at high temperatures. The much more restricted reorientations of ether molecules in the second hydrate are interpreted in terms of a tetragonal hydrate structure which contains 14- and 15-hedral cages. In the preferred orientations the long ether molecular axis lies close to the long axis of the 15-hedral cage and the C–O–C plane close to the equatorial plane of the 14-hedron. With an increase in temperature reorientation of the ether molecules becomes possible, first about the long molecular axis in the 15-hedron and then about the normal to the plane of the molecule in the 14-hedron. In both hydrates rapid rotational tunneling of the methyl groups persists to below 2 K.

A previous report[2] has established the existence of two high hydrates of dimethyl ether (DME), one of which is a cubic clathrate hydrate of von Stackelberg's structure II[3] with ideal composition DME·17H$_2$O. The second hydrate, stable below -35 °C, is a noncubic form inferred[2] to have the tetragonal structure proposed for bromine hydrate[4] with the ideal composition DME·8.6H$_2$O.

We present here the results of dielectric studies of the relaxation of DME and water molecules in the two hydrates and of continuous-wave proton magnetic resonance measurements of the corresponding D$_2$O hydrates.

Dielectric Measurements

Experimental Methods. These were designed for characterization of the relaxation behavior of the water and DME molecules rather than for accurate determination of permittivities. Most measurements were made on hydrate samples prepared in a cell[5] designed for insertion in a liquid helium variable-temperature cryostat. Aqueous solutions saturated under 1 atm of DME vapor at -5 °C were injected into the cell which was then maintained for 2 days in a gas-tight enclosure at either -25 or -40 °C, depending on the hydrate desired, under the vapor pressure of liquid DME at that temperature. Measurements were made[5] at temperatures between 2 and 185 K and at frequencies between 0.1 Hz and 1 MHz. To avoid loss of DME from the sample at high temperatures, a gas-tight cell mounted in a liquid nitrogen cryostat was used for measurements of structure II hydrate at temperatures up to 250 K. Sufficient DME was condensed on ice in this cell, which contained guarded cylindrical electrodes of gold-plated brass, to give DME·~17H$_2$O, the ice was melted, and the sample conditioned for 1 week at -28 °C.

Water Dispersion Regions. Examination of 11 samples at relatively high temperatures showed three regions of dielectric absorption and dispersion which could readily be identified with reorientation of water molecules in the two hydrates and ice. Of these, the frequency of maximum absorption of the low-temperature hydrate was higher by more than one order of magnitude, and that of (impure) ice lower by two orders, than the frequency of maximum absorption by the type II hydrate. The conversion of hydrate II into the second hydrate and ice was observed

to take several days at -40 °C; at much lower temperatures the metastable hydrate II could be preserved indefinitely.

Some experimental complex permittivity plots are shown in Figure 1. The locus illustrated at 160.1 K is for a sample of hydrate II which contained second hydrate, ice, and unreacted DME in quantities too small to be "seen" in the electrical measurements. The loci of this sample have the shapes characteristic of a structure II hydrate.[6]

As expected from the method of preparation, no sample of low-temperature hydrate was free of ice. The absorption of this hydrate is broader than that of structure II and there is clearly a considerably broader distribution of water-molecule reorientation times in the low-temperature structure.

Arrhenius plots of the frequencies of maximum absorption by the water molecules are shown in Figure 2. For the structure II hydrate there is a change in slope formally equivalent to a fall in activation energy of molecular reorientation from 6.8 kcal/mol at temperatures above 185 K to about 5.1 kcal/mol around 125 K. Changes in slope have been invariably found[6] for other structure II hydrates examined over a sufficient range of temperature. The faster relaxation of the low-temperature hydrate, on the other hand, may be described by an activation energy of 5.9 kcal/mol over the full temperature range of measurement.

Temperature Dependence of ϵ_{02}. The permittivity measured on the low-temperature (or high-frequency) side of the water dispersion region (Figure 3) is independent of frequency in our range over a large span of temperature within which it defines the static permittivity ϵ_{02} with respect to reorientation of guest DME molecules, as modified by incomplete filling of the interelectrode region and, for the low-temperature hydrate, by the presence of ice. The broken curve in Figure 3 has been corrected for incomplete filling[7] and is likely to represent the true values of ϵ_{02} of the structure II hydrate to ±0.2. These values are proportional to $1/T$ down to 55 K, i.e., to considerably lower temperatures than for the isostructural hydrates of tetrahydrofuran, trimethylene oxide, acetone, and cyclobutanone which depart appreciably from such proportionality at 100 K or above.[6] Failure of ϵ_{02} to rise as $1/T$ at low temperatures is due to difference in energy
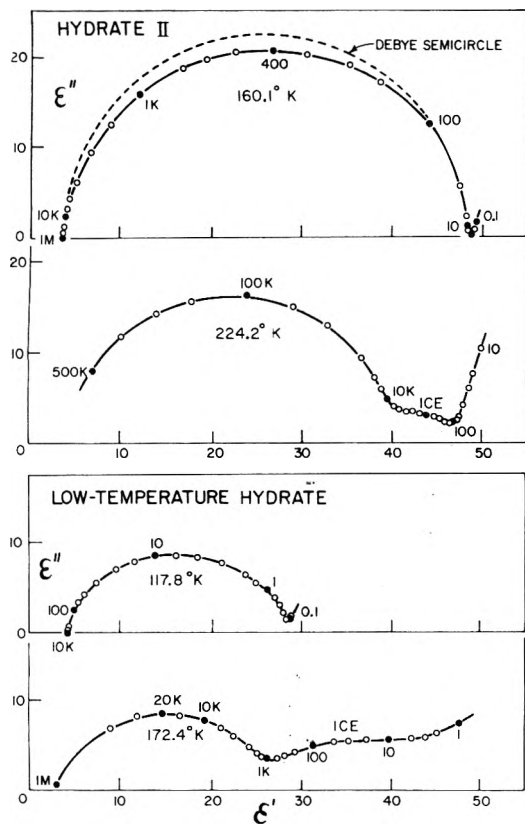
Figure 1. Plots of measured complex permittivity of dimethyl ether hydrates at relatively high temperatures. Frequencies are in Hz.
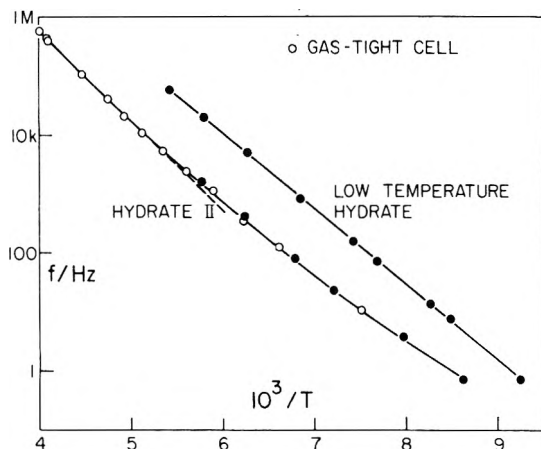
Figure 2. Rate plots of the frequencies of maximum absorption from reorientation of water molecules in dimethyl ether hydrates.

Figure 3. Dependence on temperature of the measured permittivity ϵ_{02} and low-temperature dispersion curves of dimethyl ether hydrates. The broken line is the "corrected" ϵ_{02} curve of hydrate II.
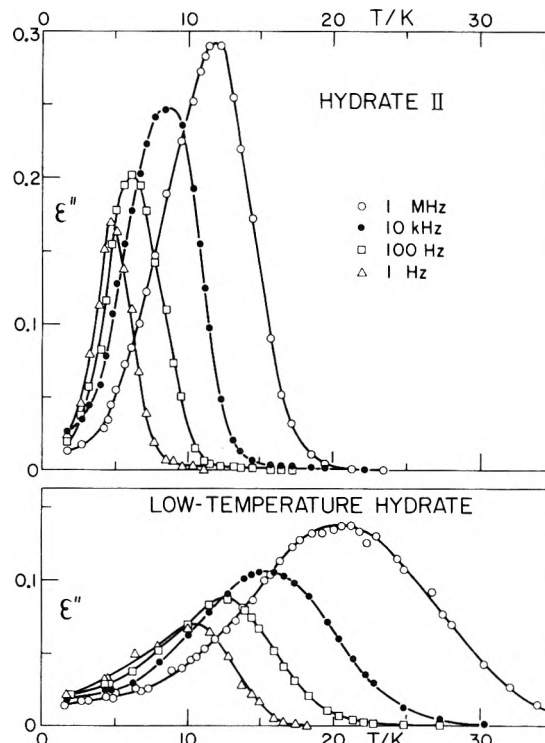
Figure 4. Dielectric absorption curves associated with the reorientation of guest molecules in the hydrates of dimethyl ether.

comparable to kT between preferred orientations of guest molecules. It is inferred that the smaller size of the DME molecule permits it to take up preferred orientations which have more equal energies than is the case of these other guest molecules.

The apparent ϵ_{02} curve of the low temperature hydrate is much flatter (Figure 3). (Small rises in permittivity with increasing temperature near 95 and 130 K probably mark slight melting effects at the ice–solid DME–liquid and hydrate–solid DME–liquid eutectic points, respectively.) No attempt is made to estimate the true ϵ_{02} value of this hydrate, but it is apparent that it must vary relatively little with temperature. This suggests the presence of rather severe geometrical restriction on the orientations available to DME molecules in the cages of this hydrate.

DME Dispersion Regions. A second region of dispersion (Figure 3) and absorption (Figure 4) occurs at submegahertz frequencies and very low temperatures in both

hydrates. The clathrate nature of both hydrates is clearly revealed by the lowness of the temperatures of these absorption regions, which arise from reorientations of DME molecules. At a fixed frequency, the maximum
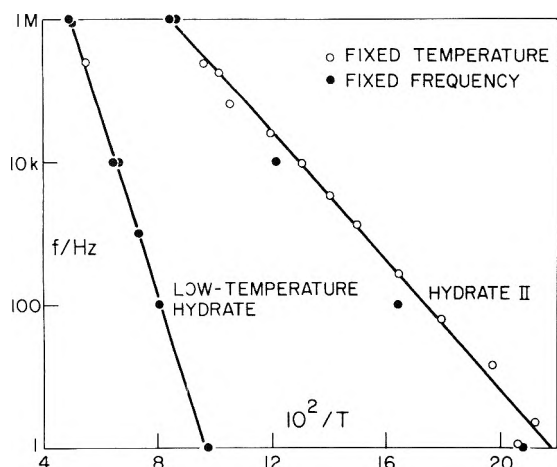
Figure 5. Rate plots of the frequencies of maximum absorption by encaged dimethyl ether molecules.

TABLE I: Dielectric Absorption by Guest Molecules in Clathrate Hydrates

	Temp where max absorption occurs at 10 kHz, K	Activation energy, kcal mol⁻¹	Ref
Structure II			
Dimethyl ether	7.8	0.21	This work
Trimethylene oxide	14.1	0.41	6
1,3-Dioxolane	20.6	0.91	Unpublished
Acetone	21.9	1.02	6
Isoxazole	23.9	1.25	9
Tetrahydrofuran	24.2	0.91	6
Cyclobutanone	35.4	1.44	10
1,4-Dioxane	39.7	1.72	11
1,3-Dioxane	51.4	1.98	Unpublished
Structure I			
Ethylene oxide	30.8	1.41	12
Trimethylene oxide	58.0	2.1	13
Tetragonal Structure			
Dimethyl ether	15.4	0.59	This work

absorption by hydrate II occurs at about half the temperature of maximum absorption by the low-temperature form. In terms of frequency, the dispersion and absorption curves of both hydrates are very broad, a general characteristic of the dielectric relaxation behavior of polar guest molecules in clathrate hydrates.[8] The absorption exhibited by the low-temperature DME hydrate is the broadest yet observed for an enclathrated molecule. There is some indication that the absorption by this hydrate is binodal, that is, that a distinct absorption process at very low temperatures may be superposed on the low-temperature end of the main absorption region.

Frequencies of maximum absorption are plotted in Figure 5. Within uncertainties attributable to the width of the absorption, the rate plots are linear over the range of frequency between 1 Hz and 1 MHz. A systematic difference between the positions of maximum absorption determined for the structure II hydrate from $\epsilon''(f)$ measurements at fixed temperature T and $\epsilon''(T)$ measurements at fixed frequency f appears to be due to the effect on the latter of a pronounced temperature dependence of the amplitude of the absorption. The "activation energies" derived from the plots are 0.21 kcal/mol for structure II and 0.59 kcal/mol for the low-temperature form. Both of these values are low in comparison with values of activation energy previously found for the clathrate hydrates of other ethers and ketones (Table I).
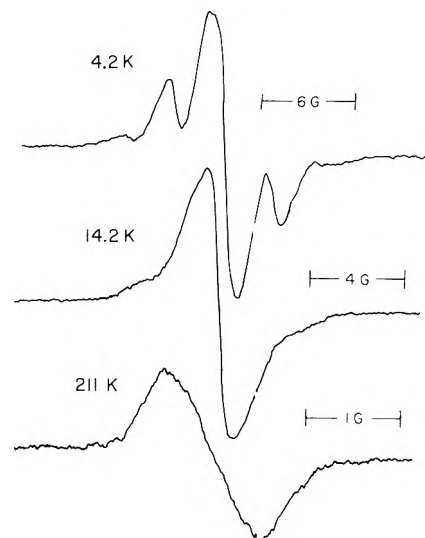
Figure 6. Derivative line shapes of the proton resonance of dimethyl ether in the structure II deuteriohydrate.
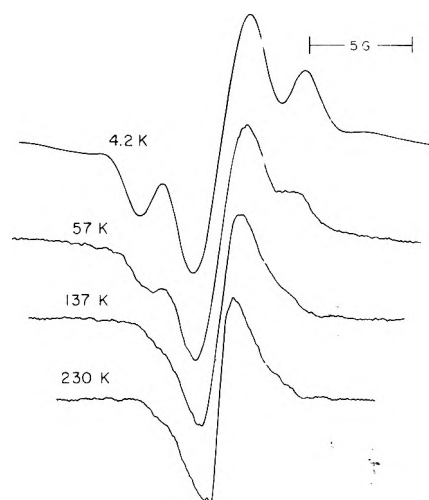
Figure 7. Derivative ¹H NMR line shapes of the low-temperature deuteriohydrate of dimethyl ether.

NMR Measurements

Experimental Methods. Two NMR samples of each deuteriohydrate were prepared in sealed tubes from deaired solutions of compositions about DME·20D₂O and DME·8.8D₂O, excess D₂O (99.7 atom % D) serving to suppress the amount of unreacted ether. These samples were conditioned for about 1 week at -24 and -44 °C, respectively.

Derivatives of the proton absorption were recorded at 14.6 MHz with a marginal-oscillator detector circuit, normally operated at power levels well below saturation. Second moments were corrected for small modulation fields. Temperatures were regulated and measured as before.[12]

Line Shapes. In the region of 4 K the derivative line shapes of the deuteriohydrates of both structures (Figures 6 and 7) clearly show the features characteristic of methyl group rotation in a polycrystalline sample as derived for classical rotation[14] or rather, in view of the low temperatures concerned, for the quantum interchange of protons in the fast tunneling limit.[15] Broadening of this fine structure is mainly determined by the magnetic dipole interactions between rotating methyl groups of the same DME molecule.

For deuteriohydrate II (Figure 6), structure is no longer resolved above 13 K and the shape is almost Gaussian
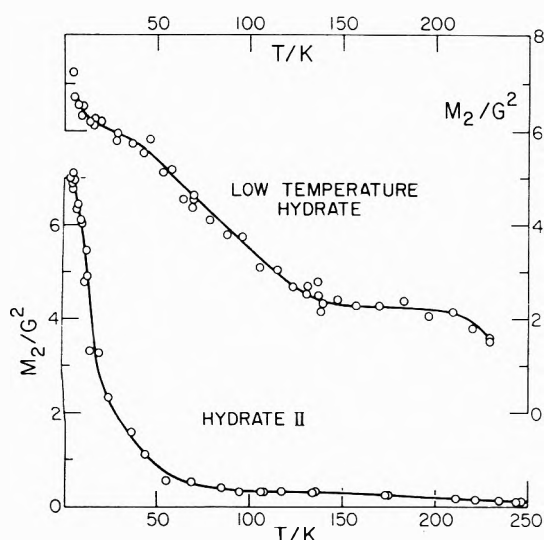
Figure 8. Temperature dependence of the proton second moments of the dimethyl ether deuteriohydrates.

between about 70 and 150 K. At higher temperatures there is less absorption in the tails than given by a Gaussian shape, as is also observed at high temperatures for other clathrate deuteriohydrates.[8]

In the low-temperature form (Figure 7), the triplet structure persists to much higher temperatures and multiple derivative extrema only disappear above about 65 K. Even at the highest temperatures there is much more absorption in the wings than corresponds to Gaussian absorption for the same separation of *extrema*.

Second Moments. Second moments of the proton resonance absorption lines are shown in Figure 8. Near 4 K the second moment of both forms is 7.0 ± 0.2 G^2, a low value which, like the line shape, is only consistent with the persistence of methyl group rotation. Except at the lowest temperatures the second moments of the two forms are quite different.

The greater overall freedom of guest-molecule reorientation in structure II is marked by a fall in second moment to half its low-temperature value at 16 K, followed by an increasingly gradual fall to 0.34 G^2 at 100 K, 0.21 G^2 at 200 K, and 0.07 G^2 at 254 K.

The second moment of the low-temperature form dips sharply to 6.3 G^2 at 12 K, falls more slowly to a value of 5.6 G^2 at 45 K, and thereafter decreases almost linearly with increasing temperature to about 140 K. A well-defined plateau occurs between 150 and 200 K where the second moment remains at 2.2 ± 0.2 G^2. Clearly the reorientation of the DME molecule remains severely restricted in this hydrate at high temperatures, in marked contrast to the usual behavior of molecules enclathrated in hydrates.[8,16]

Interpretation of Second Moments

In this section the experimental second moments are compared with values calculated (Table II) for various models of motion of encaged DME molecules.

To evaluate the intra-DME contribution to the second moment at low temperatures, where the only motion is assumed to be rotation of the methyl groups, we take[17] r_{CO} = 1.410 Å, r_{CH} = 1.095 Å, $\angle COC$ = 111.7°, and all angles at the C atoms to be tetrahedral. For rotation of the methyl groups about the CO bonds, the intra-CH_3 contribution to the second moment is 5.48 G^2. No general analytical expression appears to have been derived for the inter-CH_3 contribution for rotating methyl groups. We estimate this contribution by evaluating the inter-CH_3

TABLE II: Proton Second Moments (G^2) Calculated for Different Modes of Motion of Dimethyl Ether in D_2O Clathrates

	Contribution to second moment[a]			
	Intra-DME	Inter-DME	D_2O[b]	Total
Structure II: DME·17D_2O				
Fixed random orientn of DME	6.83	0.09	0.15	7.07
Isotropic rotn of DME	0	0.063	0.077	0.14
Isotropic rotn of DME and D_2O	0	0.063	0.063	0.13
Isotropic rotn of DME, diffusion of D_2O	0	0.063	0	0.06
Tetragonal Structure: DME·8.6D_2O				
Fixed random orientn of DME	6.83	0.31	0.27	7.41
Fixed orientn of DME in equatorial plane of 14-hedron and along long axis of 15-hedron	6.83	0.18	0.18	7.19
Fixed orientn of DME in equatorial plane of 14-hedron; rotn about long axis of 15-hedron	6.04	0.17	0.17	6.38
Rotn of DME in equatorial plane of 14-hedron and about long axis of 15-hedron	1.94	0.16	0.13	2.23
Isotropic rotn of DME	0	0.18	0.10	0.28
Isotropic rotn of DME, diffusion of D_2O	0	0.18	0	0.18

[a] CH_3 rotation is assumed in all cases. [b] A contribution from 0.3 atom % H in the D_2O supplied is included.

contribution for neither CH_3 group rotating (S_a) and for one CH_3 group rotating (S_b) and by assuming that rotation of the second CH_3 group lowers the second moment by a further factor of S_b/S_a. Averaging of the inverse sixth power of the interproton distance independently over the two circles on which the CH_3 protons lie gives S_a = 1.57 G^2. We find S_b/S_a = 0.928 from the expression of Moskalev,[18] as corrected by Allen et al.,[19] for the second moment contributed by interaction of a rotating CH_3 group and a fixed proton, the position of the latter being averaged over the circle of the second CH_3 group. Thus the estimated inter-CH_3 contribution is $(0.928)^2 \times 1.57$ = 1.35 G^2 for rotating CH_3 groups and the total intra-DME contribution is 6.83 G^2.

Structure II Hydrate. The low-temperature inter-DME and DME–D_2O contributions were obtained[12] for random fixed orientations of the DME molecule in which the center of mass of DME was located at the center of the 16-hedral cage. The protons were taken as randomly distributed over the surface of a sphere of radius 1.54 Å, the distance between the average proton position during methyl-group rotation and the center of mass. The total moment of 7.1 G^2 for structure II (Table II) is in good agreement with the experimental low-temperature value of 7.0 ± 0.2 G^2.

Straightforward calculation of second moments for isotropic reorientation of the guest molecules[12] (Table II) shows that reorientation of DME has become almost isotropic at 200 K and that, at 250 K, interaction between reorienting DME molecules and deuterons has been largely eliminated by translational diffusion of D_2O.

Low-Temperature Hydrate. On the basis of composition, it has already been suggested[2] that the noncubic hydrate stable at low temperatures has probably the same tetragonal $P4_2/mnm$ lattice as has been proposed[4,20] for bromine hydrate. The unit cell of this lattice contains 172 water molecules which form, besides ten pentagonal 12-hedra too small to be occupied by DME or Br_2 molecules, sixteen 14-hedral and four 15-hedral cages. Since the
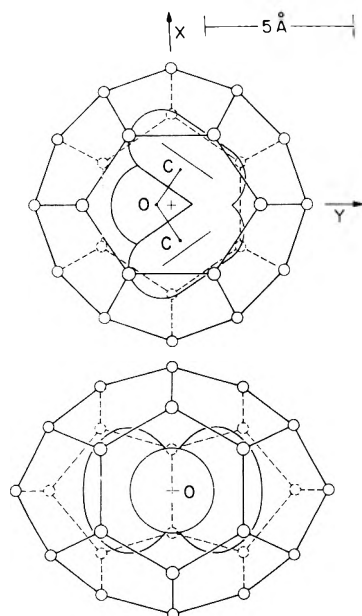
Figure 9. The 14- and 15-hedral cages of the tetragonal hydrate showing the probable preferred orientations of the dimethyl ether molecules.

Figure 10. Second moments above 100 K of DME and some other type II deuteriohydrates.

detailed structure is not known, intermolecular second moments (Table II) have been estimated as follows.

Within the unit cell, the centers of eight 14-hedra occur at positions (j), xxz, the remaining eight 14-hedra at (i), $xy0$, and the four 15-hedra at (g), $x\bar{x}0$.[21] Examination of structural models suggests that for the (j) positions $x \sim 0.181$ and $z \sim 0.250$. Assumption of these values leads to $x = -0.035$, $y = 0.375$ for the (i) sites and $x = 0.106$ for the (g) sites. The cell dimensions ($a = 23.8$, $c = 12.2$ Å) are taken over from bromine hydrate.[4]

It is assumed that the positions of the water molecules which form the 14-hedral cages are the same as for the 14-hedra of structure I. 15-hedra were constructed (cf. Figure 9) with the assumptions that all the O-O bond lengths between water molecules are 2.78 Å and that the hexagonal rings are planar.

To account for the complex temperature dependence of the second moment of this hydrate restrictions on the allowed orientations and on the modes of reorientation of the DME molecules are required. As shown in the Appendix, the dimethyl ether molecule can best be accommodated in the oblate 14-hedron when the COC plane lines in or near to the equatorial plane midway between the opposite hexagonal faces of the cage and in the prolate 15-hedron when the long axis of DME lies along the long cage axis (Figure 9).

Such preferred orientations, since they tend to maximize the distances between CH_3 groups and water molecules, minimize the contribution to the second moment from the D_2O molecules of the lattice. They also reduce the interguest contribution. The low-temperature second moment of 7.4 G^2 calculated for random orientations of DME molecules is thereby reduced to about 7.2 G^2 (Table II), in good agreement with the experimental low temperature value of 7.0 ± 0.2 G^2.

With increase of temperature, reorientation of DME is expected to occur preferentially about an axis parallel to its long axis in the 15-hedron and about an axis perpendicular to the C-O-C plane in the 14-hedron. The former corresponds to rotation about an axis 34.14° removed from the axes of CH_3 rotation and reduces[22] the intra-CH_3 contribution to 1.53 G^2 while leaving the inter-CH_3 contribution unchanged from the value (1.35 G^2) for uncorrelated CH_3 rotation. If the remaining 80% of the DME
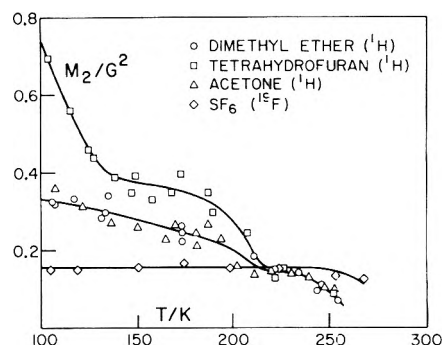
molecules are still confined to fixed equatorial positions in the 14-hedra, the total estimated second moment (Table II) is 6.4 G^2, a value close to the experimental values between 10 and 20 K. If, in addition, the DME molecules in the 14-hedra rotate in the equatorial plane about an axis perpendicular to this plane, the intra-DME contribution of these molecules is reduced by a factor of 4 and the total second moment reduced to 2.2 G^2. This value accounts for the experimental behavior in the plateau region between 150 and 200 K.

Supporting evidence that the low-temperature hydrate is indeed the tetragonal structure is therefore provided by the temperature dependence of the second moment.

Reorientation of Guest Molecules

The present hydrates provide further examples of the broad distributions of guest-molecule reorientation rates very generally shown by dielectric[6,8] and NMR continuous-wave[8,16] and spin-lattice relaxation[11,23] measurements of clathrate hydrates. Thus, the frequencies at which the dielectric absorption of the structure II DME hydrate is half the maximum absorption differ by a factor of 10^6 at 5.5 K. In both hydrates the absorption is markedly asymmetric in $\ln f$ at a fixed temperature (or in $1/T$ at a fixed frequency), being skewed in the direction of increased absorption at frequencies higher (or temperatures lower) than that of maximum absorption. This behavior appears to be a consequence of (a) a distribution of activation energies or barrier heights whose breadth is comparable to the mean (small) activation energy and (b) the tendency for the dielectric relaxation rates to reflect the faster molecular reorientation rates when the molecules have preferred orientations of different energies. (For example, if there are two preferred orientations between which k_1 and k_2 are the jump rates, the dielectric relaxation rate is proportional to $k_1 + k_2$ and for $k_1 \neq k_2$ is determined mainly by the larger.)

From the dielectric absorption still present in the tetragonal hydrate at the lowest temperatures there is reason to suspect (cf. the 1 MHz curve of Figure 4) the presence of a low-temperature absorption process distinct from that responsible for the principal absorption at higher temperatures. In view of the low-temperature behavior of the NMR second moment it is likely that this absorption arises from the reorientation about their long axes of the 20% of the DME molecules present in the 15-hedral cages of the tetragonal hydrate.

Another aspect of the motion is illustrated in Figure 10, in which the second moments of DME·17D_2O and a number of other type II deuteriohydrates are shown for temperatures above 100 K. At these temperatures the dipole reorientation rates of all the encaged molecules are well in excess of 1 GHz. Second moment values appre-

ciably in excess of the intermolecular value of 0.14 G^2 (0.16 G^2 in the case of tetrahydrofuran) for deuteriohydrates of these guest molecules at temperatures to above 200 K (Figure 10) must therefore be attributed to persistence of an appreciable intraguest contribution arising from residual anisotropy in the modes of reorientation of the guest molecules. The value of $(3 \cos^2 \theta - 1)$ remains finite when averaged over all angles θ between the individual interproton vectors and the static magnetic field achieved during many reorientational jumps of the guest molecules. This contribution (0.10 to 0.25 G^2 at 180 K (Figure 10)) to the second moment becomes unobservable only when the reorientation of D_2O molecules becomes appreciably faster than the corresponding frequency half-width (about 2 kHz). Averaging of the motion of the guest molecule then occurs over many cage configurations and the guest molecule effectively "sees" the average cage of tetrahedral symmetry.

As Figure 10 shows, the residual intraguest contribution to the second moment sharply declines and disappears between 180 and 220 K for the type II deuteriohydrates of DME, acetone, and tetrahydrofuran. If the rates of reorientation of D_2O molecules are taken to be $2^{-1/2}$ as great as the frequencies of maximum dielectric absorption by H_2O molecules of the corresponding hydrates, these rates reach 10 kHz at 197, 192, and 202 K, respectively, and the fall in second moment correlates well with D_2O reorientation. At still higher temperatures there is a further drop in second moment associated with diffusion of D_2O molecules.[23]

In contrast, such isotropic averaging of crystal field effects is not necessary for the removal of the intraguest contribution to the second moment for guest molecules which, like SF_6, belong to cubic point groups. This contribution vanishes (below 20 K for SF_6[8,16]) for such molecules in a cage of any symmetry as long as there is sufficiently rapid interchange between the equivalent orientations specified by the symmetry number of the molecule (24 for SF_6).

In the tetragonal hydrate the asymmetry of reorientation of the guest molecules evident from the second moments at all temperatures is due to the low symmetry of the occupied cages. Even when averaged over the disordered orientations of the D_2O molecules, the symmetry[20] of the 14-hedra is no more than m (C_s) and that of the 15-hedra only mm (C_{2v}).

Finally, we note that the persistence of fast methyl group rotation to sub-helium temperatures in both hydrates differs from the more restricted methyl group rotation in solid DME itself for which the second moment[24] approaches 20 G^2 at 77 K. The smaller crystal fields in the hydrates apparently permit a more rapid tunneling than is possible in solid DME.

Appendix

Preferred Orientations of DME Molecules in Cages of the Tetragonal Hydrate. The only orientations of DME in the 15-hedral cage which do not result in serious van der Waals overlap[25] with the water molecules of the cage are those in which the long axis of DME is approximately

parallel to the long axis of the cage. The particular configuration shown in Figure 9 is one of three configurations in which the polar axis of DME points toward the center of a hexagonal ring. In these configurations methyl group rotation may take place without van der Waals overlap as long as the center of mass is displaced by a distance between about 0.05 and 0.50 Å from the center of the cage toward the hexagonal ring. Overall molecular rotation about the long axis may also occur without overlap if accompanied by a small translational "wobble". This observation is consistent with the experimental evidence for the occurrence of this rotation at very low temperatures.

If the 14-hedra of the tetragonal hydrate have the same dimensions as those of structure I, the orientation illustrated in Figure 9 is free of van der Waals overlap as long as the y coordinate of the center of mass lies between about -0.4 and 0.0 Å of the cage center. There are 12 such preferred equatorial orientations (strictly two sets of 4 and 8 orientations for the $\bar{4}2m$ symmetry of the structure I cage) separated by rotations of about 30° around the z axis. Slight van der Waals overlap occurs during such rotation. In symmetry (m vs. $\bar{4}2m$) and probably in dimensions, the 14-hedra of the tetragonal form differ from those of structure I, but it seems likely that reorientations in the equatorial plane remain the most facile ones.

References and Notes

(1) Issued as NRCC No. 16020.
(2) S. L. Miller, S. R. Gough, and D. W. Davidson, *J. Phys. Chem.*, preceding paper in this issue.
(3) M. von Stackelberg and H. R. Müller, *Z. Elektrochem.*, **58**, 25 (1954).
(4) K. W. Allen and G. A. Jeffrey, *J. Chem. Phys.*, **38**, 2304 (1963).
(5) S. R. Gough, *Can. J. Chem.*, **50**, 3046 (1972).
(6) S. R. Gough, R. E. Hawkins, B. Morris, and D. W. Davidson, *J. Phys. Chem.*, **77**, 2969 (1973).
(7) The sample is assumed to be in series with a gap which makes up a fraction δ_s of the interelectrode spacing and in parallel with a void δ_p of the electrode area. Values of $\delta_s = 0.0063$ and $\delta_p = 0.21$ are derived from comparison of "true" values[6] of ϵ_0 (88 at 177 K) and $\epsilon_{\infty2}$ (3.4) with the corresponding experimental values.
(8) D. W. Davidson, *Water: Compr. Treat.*, **2**, 115 (1973).
(9) S. R. Gough, S. K. Garg, J. A. Ripmeester, and D. W. Davidson, *Can. J. Chem.*, **52**, 3193 (1974).
(10) B. Morris and D. W. Davidson, *Can. J. Chem.*, **49**, 1243 (1971).
(11) S. R. Gough, J. A. Ripmeester, and D. W. Davidson, *Can. J. Chem.*, **53**, 2215 (1975).
(12) S. K. Garg, B. Morris, and D. W. Davidson, *J. Chem. Soc., Faraday Trans. 2*, **68**, 481 (1972).
(13) S. R. Gough, S. K. Garg, and D. W. Davidson, *Chem. Phys.*, **3**, 239 (1974).
(14) E. R. Andrew and R. Bersohn, *J. Chem. Phys.*, **18**, 159 (1950).
(15) F. Apayadin and S. Clough, *J. Phys. C*, **1**, 932 (1968).
(16) S. K. Garg and D. W. Davidson in "Physics and Chemistry of Ice", E. Whalley, Ed., Royal Society of Canada, Ottawa, 1973, p 56.
(17) U. Blukis, P. H. Kasai, and R. J. Myers, *J. Chem. Phys.*, **38**, 2753 (1963).
(18) V. V. Moskalev, *Sov. Phys.-Solid State*, **3**, 2218 (1962).
(19) P. S. Allen, A. W. K. Khanzada, and C. A. McDowell, *Mol. Phys.*, **25**, 1273 (1973).
(20) G. A. Jeffrey and R. K. McMullan, *Prog. Inorg. Chem.*, **8**, 43 (1967).
(21) "International Tables for X-ray Crystallography", Vol. 1, The Kynoch Press, Birmingham, 1952.
(22) J. G. Powles and H. S. Gutowsky, *J. Chem. Phys.*, **21**, 1704 (1953).
(23) S. K. Garg, D. W. Davidson, and J. A. Ripmeester, *J. Magn. Reson.*, **15**, 295 (1974).
(24) K. Grude, J. Haupt, and W. Müller-Warmuch, *Z. Naturforsch. A*, **21**, 1231 (1966).
(25) van der Waals radii of 1.4 Å for water and 1.2 and 1.4 Å for H and O atoms of DME are assumed.

Physical Adsorption on Patchwise Heterogeneous Surfaces. 2. Virial Coefficient Theory Analysis of Krypton Adsorption on Graphitized Carbon Black

Frederick A. Putnam[†] and Tomlinson Fort, Jr.*

Department of Chemical Engineering, Carnegie-Mellon University, Pittsburgh, Pennsylvania 15213 (Received February 18, 1977)

Physical adsorption data for krypton adsorbed on graphitized carbon black (gcb) is analyzed by the virial coefficient (VC) theory of adsorption. Both high and low temperature adsorption data are included, and heterogeneity is determined. Strong site heterogeneity of Sterling FT gcb is found to be 0.5 ± 0.1% of the surface, a considerably higher value than previous estimates. Adsorption data taken over a wide temperature range is found to be capable of determining three attributes of the gas–solid potential energy function: capacity, depth, and anharmonicity. The best-fit Lennard-Jones (LJ) Kr-(0001) graphite potential is a 12–3 potential with depth $\epsilon_{gs}/k = 1461 \pm 6$ K and distance parameter $z_0 = 0.23 \pm 0.01$ nm. A LJ 12–6 potential with distance parameter $\sigma_{gg} = 0.36$ nm is used to represent the pair interaction between adsorbed Kr atoms, and the depth of this effective potential is found to be $\epsilon_{gg}/k = 145 \pm 3$ K, in excellent agreement with previous high temperature VC studies. This potential is considerably shallower than the gas phase Kr LJ 12–6 potential, which cannot be reconciled with the present data.

I. Introduction

In a classic series of papers,[1-3] Halsey and co-workers applied the virial coefficient (VC) theory of adsorption to the adsorption of rare gases on a graphitized carbon black (gcb), P33 (2700). The theory was used to analyze "high temperature" (high compared to the two-dimensional Boyle temperature) adsorption data, and an attempt was made to determine the surface area and potential energies of adsorption by fitting the theory to the data. In this paper, the VC theory is applied to "low temperature" adsorption data by including strong site heterogeneity and additional virial coefficients in the model. The results resolve several problems which remained after the study of Halsey et al., as follows:

A. *Heterogeneity*. It has long been known that the surfaces of graphitized carbon blacks are primarily composed of (0001) planes, and a small percentage of "strong sites" which lead to high heats of adsorption.[4,5] Several authors have pointed out that this heterogeneity will have a pronounced effect on the VC results,[5-7] yet heterogeneity was neglected by Sams et al.,[2] and by Ross and Oliver[8] in their analyses of high temperature data. The heterogeneity problem has been discussed in detail by Everett.[6]

The terms "homogeneous", "uniform", and "heterogeneous" are now defined. A "homogeneous" surface has only one type of adsorption site (for example, any low index crystal plane). A "uniform" surface is a homogeneous surface which presents negligibly small barriers to translation across the surface. No real surface is perfectly uniform, though some homogeneous surfaces may be regarded as uniform, especially at high temperatures. "Heterogeneity" denotes the presence of more than one type of adsorption site on a surface.

B. *Surface Area*. A puzzling result of the Halsey study was that the surface area determined by the VC method, $\alpha = 8.38$ m^2/g, using crystallographic radii to determine the gas–solid distance,[2] was considerably smaller than that determined by various methods which used the monolayer capacity to determine the surface area. The BET nitrogen area of the Halsey sample was 12.5 m^2/g,[9] and "step height" and "surface titration" areas determined with Ar, Kr, and Xe were 12.30–12.45 m^2/g.[10] Pierotti and Thomas[7]

showed that treating the gcb surface as heterogeneous with a Gaussian site energy distribution can bring the VC area slightly higher, to 8.73 m^2/g, but this is still significantly lower than 12.5 m^2/g.

C. *Absorbate–Adsorbent (Gas–Solid) Potential Energy*. A number of different Lennard-Jones (LJ) n–m potential energy functions were used by Sams et al., but it was concluded that none of these potentials was to be preferred over the others, as all fit the data about equally well. Ross and co-workers preferred a harmonic form for the adsorbate–adsorbent potential,[8,11,12] which also successfully fit the high temperature data. A more well-defined determination of the adsorbate–adsorbent potential is clearly desirable, especially since some theoretical adsorption studies[13,14] use this potential as a starting point.

D. *Adsorbate–Adsorbate (Gas–Gas) Potential*. The VC results of Sams et al.[3,6,15] indicated that the attractive force between two adsorbed atoms was less than that for two atoms in the gas phase, in agreement with various theoretical predictions. Ross has argued, however, that this conclusion was incorrect, since both heterogeneity[16] and an alternative analysis of Halsey's data including higher virial coefficients[11] can be used to show that the data can be fit with the bulk gas parameters just as well as with "perturbed" parameters. The matter clearly needs to be resolved.

The four problems noted above are actually intimately related. All of the above effects contribute to the measured adsorption data and the effects are by no means independent. In this work strong site heterogeneity is set apart by obtaining the data at low temperatures compared to the difference in adsorption energy between the strong sites and the (0001) surface, and the surface area is taken from an accurate monolayer capacity determination. This procedure effectively separates heterogeneity and surface area from potential energy determination. Finally, a formulation of the VC theory is used which allows both low and high temperature adsorption data to be directly and economically fit to a single equation which yields the potential parameters. This approach enables the four problems stated above to be resolved, as follows: (A) Heterogeneity of a gcb (Sterling FT-M5) is determined by a new nonlinear extrapolation procedure and is found to be considerably greater than previous estimates for similar graphitized carbon blacks. (B) The VC and monolayer capacity surface areas are reconciled when a gas–solid

potential with smaller capacity is used in the VC analysis. (C) A more accurate LJ Kr-(0001) graphite potential is arrived at, and (D) the potential between adsorbed krypton atoms is found to be inconsistent with the bulk gas potential, and in excellent agreement with the results of the studies of Halsey et al.

In this work the surface area of Sterling FT-M5 gcb will be taken to be 11.4 m²/g. This surface area value was determined by identifying the coverages at which the first Kr layer crystallizes in registry with the graphite lattice, and forms a close-packed monolayer. The surface area determination is discussed in detail in the first paper of this series (hereafter referred to as I). The accuracy of this surface area determination was estimated to be ±0.4 m²/g. The effect of this uncertainty on the results will be considered.

The experimental details pertaining to the data used in this study have been presented elsewhere.[2,5,17] The data were collected on high accuracy volumetric adsorption systems, and are available in the supplementary material sections of the original papers.

II. Theory

The virial theory of adsorption isotherm equation in the low-temperature two-dimensional film approximation is[18]

$$\ln\left(\frac{n^\sigma}{pK_H}\right) = 2B_{2d}\left(\frac{n^\sigma}{\alpha}\right) + \frac{3}{2}C_{2d}\left(\frac{n^\sigma}{\alpha}\right)^2 + \ldots \quad (1)$$

where α is the adsorbent surface area, n^σ is the surface excess amount adsorbed per gram of adsorbate, p is the vapor pressure, K_H is the Henry law constant, and B_{2d}, C_{2d}, etc., are two-dimensional virial coefficients. The two-dimensional virial coefficients account for "horizontal" interactions between adsorbate molecules. "Vertical" interactions enter into the Henry law constant, $K_H = K_H^{Cl} + K_H^q$, where

$$K_H^{Cl} = \frac{1}{kT}\int_V \{\exp(-u_s(\mathbf{r})/(kT) - 1\}\,d\mathbf{r} \quad (2)$$

$u_s(\mathbf{r})$ is the potential energy between a single adsorbate molecule and the solid surface. K_H^q is a quantum correction term which is conveniently approximated for a harmonic oscillator potential of frequency ν by the relation[19]

$$K_H = \frac{K_H^{Cl}}{24}\left(\frac{h\nu}{kT}\right)^2 \quad (3)$$

A. *Uniform Surface Approximation.* Gas–solid potentials of varying degrees of sophistication may be fit to adsorption data. In this work the LJ and harmonic potentials have been used, since they are sufficiently flexible to accurately fit the data and yet not so complex that the amount adsorbed is expensive to calculate.

For a uniform or "structureless" surface the potential $u_s(\mathbf{r})$ depends only on z, the vertical distance. The LJ form of this potential

$$u_s(z) = \left(\frac{n}{n-m}\right)\left(\frac{n}{m}\right)^{m/(n-m)} \epsilon_{gs}\left[\left(\frac{z_0}{z}\right)^n - \left(\frac{z_0}{z}\right)^m\right] \quad (4)$$

yields via eq 3[2]

$$K_H^{Cl} = \frac{\alpha z_0}{kT}\sum_{i=0}^{\infty}(ni!)^{-1}\left[\left(\frac{n}{n-m}\right)\left(\frac{n}{m}\right)^{m/(n-m)} \times \left(\frac{\epsilon_{gs}}{kT}\right)\right]^{[2(n-m)+1]/n}\Gamma\left\{\frac{im-1}{n}\right\} \quad (5)$$

TABLE I: Capacity Parameter C_c for Lennard-Jones Potential

Potential exponents		C_c	Potential exponents		C_c
n	m		n	m	
9	3	0.57933	16	3	0.41152
12	3	0.48734	18	3	0.38439
10	4	0.46172	14	4	0.37967
14	3	0.44492	18	4	0.32891

Expanding $u_s(z)$ about its minimum, Hansen[20] obtained the harmonic approximation

$$K_H' = \frac{\alpha z_0 C_c(n,m)}{kT}\left(\frac{kT}{\epsilon_{gs}}\right)^{1/2}\exp\left(\frac{\epsilon_{gs}}{kT}\right) \quad (6)$$

Here α may be regarded as a horizontal capacity parameter and

$$z_0 C_c = \left(\frac{2\pi}{mn}\right)^{1/2}\left(\frac{n}{m}\right)^{1/(n-m)} \quad (7)$$

as a vertical capacity parameter. The frequency of the harmonic oscillator is then

$$\nu = \frac{1}{C_c z_0}\left(\frac{\epsilon_{gs}}{M}\right)^{1/2} \quad (8)$$

where M is the mass of the adsorbate. The parameter C_c is given in Table I for some $n-m$ potentials; note that increasing the exponents of the potential decreases the capacity of the potential.

The expansion of K_H may be carried out to higher terms;[7,20] the next term in the expansion yields a measure of the "anharmonicity" of the potential. At temperatures which are low compared to ϵ_{gs}/k, as in the experiments considered here, a plot of log K_H vs $1/T$ is a very slightly curved line, with slope determined primarily by ϵ_{gs} and intercept determined primarily by $z_0 C_c$. The anharmonicity of the potential changes the curvature of the line, and also alters the slope and intercept to a lesser degree. Figure 1 is a plot of K_H for some of the $n-m$ potentials used in this work. When Henry's law data are fit to the LJ potential, the magnitude of K_H determines the product $z_0 C_c$, the heat of adsorption determines ϵ_{gs}, and the heat capacity of the adsorbate determines the anharmonicity of the potential. There is considerable interaction between these parameters, depending on the temperature range and precision of the experimental data.

The accuracy of the harmonic approximation form K_H' is of interest. Direct numerical comparisons in the low temperature range ($\epsilon_{gs}/kT \approx 15$) show that the value of K_H' is in error by 6% and that $\partial \log K_H/\partial(1/T)$ is in error by 0.5%. The effect of anharmonicity is considerable then, even at low temperatures. Adsorption data may nevertheless successfully be fit to K_H' with excellent agreement; when this is done the fitted frequency and depth of the harmonic potential become "effective" values, which differ from the LJ frequency (as given by eq 8) and depth.

B. *Surface Nonuniformity.* In this section, it is argued that the nonuniformity of the (0001) graphite surface may be neglected for the purposes of the present work.

1. *Vertical Interactions.* The uniform surface approximation is valid for kT large compared to the potential energy variations along the surface. One way to account for nonuniformity is to make α in the preceding equations a "free area". $\alpha = N_s a_f$ rather than the actual area,[21] where N_s is the number of surface unit cells, a_f is the free area of each unit cell

$$a_f = \int_a \exp\{-u_{sm}(\tau)/kT\}\,d\tau \quad (9)$$
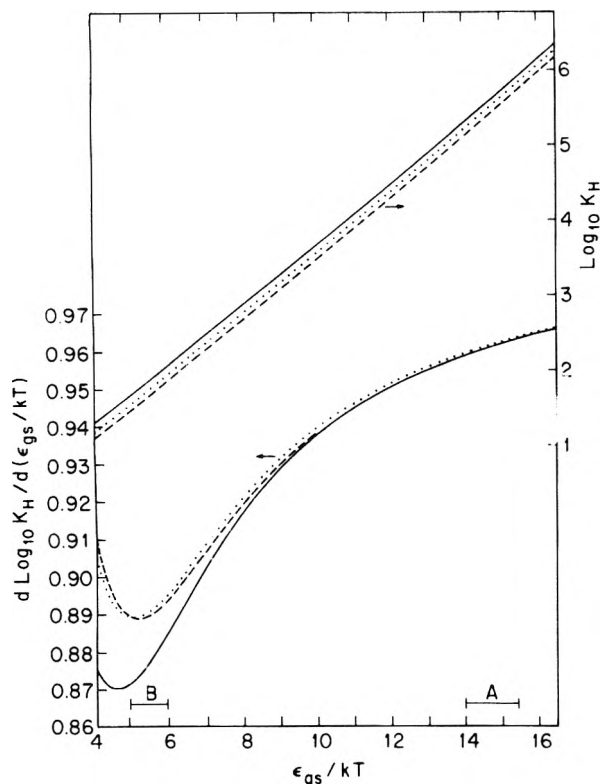
Figure 1. Henry's law constants and their derivatives for some Lennard–Jones $n–m$ potentials: solid lines = 9.3; dotted lines = 10–4; dashed lines = 14–4 potentials. Intervals A and B denote the ranges of the low and high temperature data, respectively.

and $u_{sm}(\tau)$ is the z direction minimum potential over a point τ. Steele has shown that assuming pairwise additivity $u_{sm}(\tau)$ may be very accurately approximated by

$$\mu_{sm} = (2u_0/2)[\cos 2\pi s_1 + \cos 2\pi s_2 + \cos 2\pi(s_1 + s_2)] \qquad (10)$$

where s_1, s_2 span one unit cell and u_0 is the difference in z direction minimized adsorption energy between a preferred adsorption site and a site directly over surface atom. Figure 2 shows the results of an evaluation of the two-dimensional integral. The reduced free area $a^* = a_f/a_f(T \to \infty)$ and the associated configurational energy and heat capacity are shown. The potential u_0 is defined above such that the mean energy is zero. For this choice, a^* is always greater than one. If u_0 is defined such that the zero coincides with the bottom of the potential well, i.e., $u_{sm}' = u_{sm} - 2u_0/3$, then the reduced free area is always less than one. The mean energy zero definition is appropriate to VC theory analyses such as the present one; thus the area found from the analysis will be slightly too large. Consequently the statement of Pierotti and Thomas, that "$N_s a_f$ is always less than the true area; areas determined by fitting K_H data for nonuniform surfaces will in general be too small." [21] does not apply to the present case.

The pairwise additive estimate of u_0/k for the krypton–graphite (0001) system is 41 K.[22] In a recent study, Freeman[23] calculated the krypton–graphite potential using a more rigorous density-functional technique which included nontwo body effects, and obtained $u_0/k \approx 25$ K. Using the value of 41 K as a worst case estimate, we obtain from eq 9, at temperatures near 100 K, $a^* = 1.006$. The 0.6% difference between actual and effective areas is much less than the accuracy to which the surface area is known. Thus the effect of nonuniformity on a^* for the Kr–(0001) graphite system may be neglected.
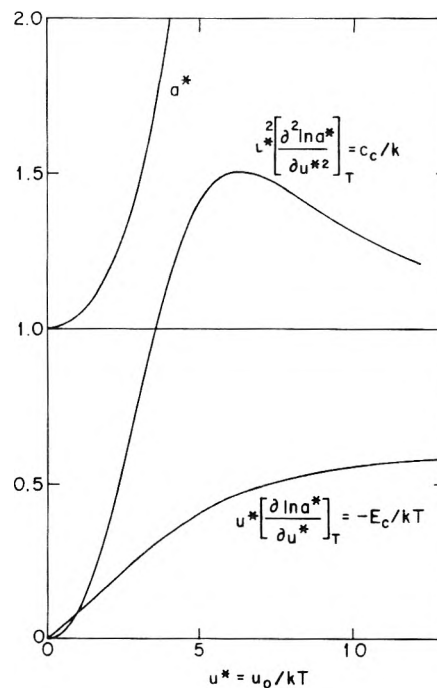
Figure 2. The contribution to the thermodynamic functions of an adsorbed atom due to surface nonuniformity, calculated from eq 9 and 10.
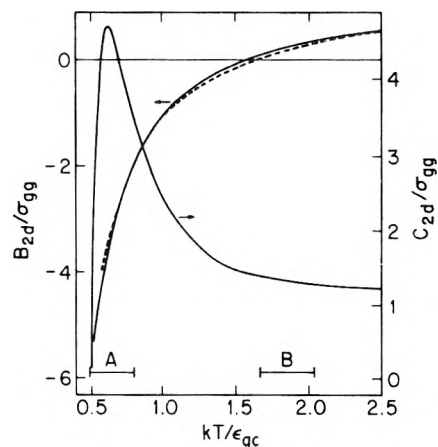
Figure 3. Second and third two-dimensional virial coefficients used in this work. The dashed line shows the second virial coefficient for the nonuniform surface, as calculated by Oh and Kim.[24]

2. *Horizontal Interactions.* The effect of nonuniformity on the second two-dimensional virial coefficient B_{2d} was studied by Oh and Kim[24] and found to be small in the temperature range of the present experiments, $\epsilon_{gg}/kT \approx 0.7$, where ϵ_{gg} is the interaction potential depth for two adsorbed molecules. Figure 3 illustrates the close agreement between the uniform and nonuniform surface second two-dimensional virial coefficients. The influence of nonuniformity on higher virial coefficients has not been studied. In this work uniform surface virial coefficients are employed. The first two of the coefficients are tabulated in the literature as a function of temperature for the LJ 12–6 potential.[11,25] Here, the 12–6 potential must be regarded as an effective pair potential which incorporates the two-body gas phase potential, the r^{-3} long-range repulsion of Pitzer and Sinanoglu[26] or McLachlan,[27] and other nonadditive effects, which are known to be considerable.[28-30] For the fourth through sixth virial coefficients the hard sphere values are employed, with hard sphere diameter equal to the 12–6 potential parameter σ_{gg}.

In the VC study of Sams, Constabaris, and Halsey,[2,3] the gas–solid virial coefficients were first determined from the

TABLE II: Results of Low Temperature Virial Coefficient Theory Fit

n-m	ϵ_{gs}/k, K	z_0, nm	ϵ_{gg}/k, K	σ_{gg}, nm	α, m²/g	n^σ_{ms}, mol/g	Std dev	z_e, nm	$z_0 C_c$, nm	$10^{-12}\nu$, s⁻¹
9–3	1458.7	0.1997	145.2	0.36^a	11.4^a	0.65	8.62	0.240	0.1157	1.31
10–4	1458.5	0.2530	145.2	0.36^a	11.4^a	0.65	8.63	0.295	0.1168	1.30
14–4	1459.0	0.3048	145.2	0.36^a	11.4^a	0.65	8.63	0.340	0.1157	1.31
14–4^b	1461.2	0.2995	145.4	0.36^a	11.4^a	0.66	8.63	0.341	0.1137	1.30
18–4	1458.9	0.3501	145.2	0.36^a	11.4^a	0.65	8.62	0.390	0.1151	1.31
14–4	1457.0	0.3072	143.0	0.373^a	11.4^a	0.67	9.25	0.346	0.1166	1.30
14–4	1432.8	0.3256	171.0^a	0.36^a	11.4^a	1.62	21.3	0.370	0.189	1.22

^{a} Fixed parameter. ^{b} With quantum correction.

data. The intercept of a plot of n^σ/p vs. p yielded K_H, and the intercept of a plot of $(n^\sigma/p - K_H)/p$ vs. p yielded B_{2d}, etc. Once K_H and B_{2d} had been determined for a series of isotherms, the adsorbate–solid and adsorbate–adsorbate potentials were determined. There are several drawbacks to this method. First, it assumes that the isotherm passes through the origin, i.e., that there is no strong-site heterogeneity. This assumption does not hold for the present data. Second, the method depends on the virial series, eq 1, being rapidly convergent, which is much more nearly true for high temperature adsorption than for the present case. Third, it is difficult to relate the precision and interdependence of the potential energy parameters to the original data using this method.

A more preferable approach to determining potential energy functions is to perform a direct multiparameter fit of eq 1 to the data. This method was used by Morrison and Ross[11] and Thomas et al.[31] The multiparameter fit approach overcomes the drawbacks listed above, inverting the experimental data in a single step to obtain the potential parameters and rigorous statistical information about their error and interaction. This approach is used here. Heterogeneity is dealt with by taking the data at very low temperatures compared to the adsorption energy difference between the strong sites and the (0001) plane. If the temperature is low enough, the strong sites become saturated with a monolayer of adsorbed gas at a small pressure, p_{ms}, compared to the pressure range for which the virial equation applies. Since the second layer adsorption energy on the strong sites is much less than the first layer strong site energy, the strong site isotherm above p_{ms} and in the virial region for the (0001) face may be approximated by $n^\sigma = n^\sigma_{ms}$, a constant. This approximation will introduce insignificant error only if the variation in the strong site adsorption is small compared to the amount adsorbed throughout the virial region on the (0001) part of the surface. This condition is satisfied for Sterling FTg-M5, which has less than 1% strong sites.[4,5] At pressures greater than p_{ms} then, the amount adsorbed on the (0001) face, or the weak sites, is given by

$$n^\sigma_{(0001)} = n^\sigma_{ex} - n^\sigma_{ms} \qquad (11)$$

where n^σ_{ex} is the experimental amount adsorbed.

An illustrative calculation, using parameters which apply to the present low temperature VC analysis, will serve to clarify the above point. The BET equation may be written

$$\theta = \frac{n^\sigma}{n^\sigma_m} = \frac{cx}{(1-x)(1-(c-1)x)}$$
$$c = \exp\left[\frac{Q - Q_{sat}}{kT}\right] \qquad (12)$$

where x is the relative pressure p/p_0, Q is the heat of adsorption, and Q_{sat} is the heat of sublimation. For a patchwise heterogeneous surface $\theta(x) = \theta_w(x) + \theta_s(x)$ where θ_s and θ_w are the fractional coverages on the strong and
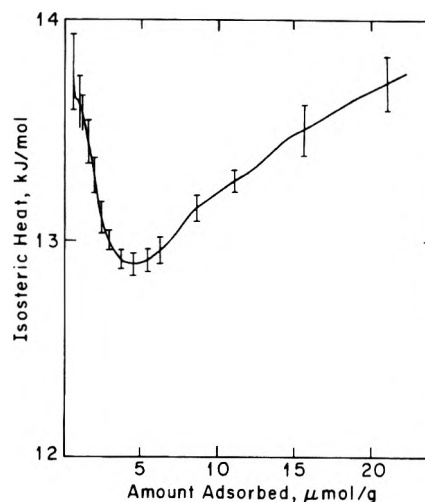
Figure 4. Isosteric heats of adsorption of krypton on Sterling FT graphitized carbon black. The error bars are estimated standard errors obtained from linear regression analysis.

weak sites, respectively. Heat of adsorption values which apply to the Kr–gcb system[5] are $Q_w/k = 1460$ K, $Q_s/k = 2260$ K, and $Q_{sat}/k = 1370$ K. Thus the BET c constants are 7732 and 2.46 for the strong and weak adsorption sites, respectively. Using these values, at $T = 100$ K and $x = 0.014$, $\theta_s = 1.005$ and $\theta_w = 0.034$. At $x = 0.067$, $\theta_s = 1.070$ and $\theta_w = 0.161$. From these data it is readily shown that if the solid surface is composed of 0.5% strong sites, the maximum error in θ_w introduced by assuming θ_s = constant in the region $0.023 \leq \theta \leq 0.160$ is 0.18%. This error is less than the experimental error, so the approximation that the amount adsorbed on the strong sites is constant in the range $0.035 < \theta < 0.16$ is justified.

III. Results

A. *Low Temperature Analysis.* Low temperature adsorption data from I in the range $4.5 < n^\sigma < 21$ μmol/g $(0.035 < \theta < 0.16)$ were fit to the VC theory, eq 1 and 11, by minimizing the weighted sum of squares of differences between predicted and observed pressures. The weights were applied so that the relative rather than absolute pressure errors were minimized. Powell's[32] direct search nonlinear optimization algorithm was used. Computer programs for fitting the theory to the data are available.[33]

The amount adsorbed at which the strong sites become saturated was ascertained from the shape of the isosteric heat curve at low coverage,[45] Figure 4. The high initial q_{st} in Figure 4 is due to adsorption on strong sites. Above $n^\sigma \approx 4.5$ μmol/g, the effect of the strong sites is small, and the isosteric heat rises monotonically due to adsorbate–adsorbate attractive interactions. Thus, in the fit of data to the theory, only data where $n^\sigma > 4.5$ μmol/g were used.

The results of the low temperature fit are presented in Table II. Figure 5 is a plot of the data and the theory. The surface area was fixed at $\alpha = 11.4$ m²/g. For a given

TABLE III: Correlation Matrix and Confidence Levels for Low Temperature Virial Coefficient Theory Fit

	ϵ_{gs}/k	z_0	ϵ_{gg}/k	n^σ_{ms}
ϵ_{gs}/k	1			
z_0	0.998	1		
ϵ_{gg}/k	0.86	0.86	1	
n_{ms}	0.82	0.82	0.45	1
90% confidence levels	± 11 K	± 0.021 nm	± 2.6 K	$\pm 0.10 \ \mu$mol/g

n–m gas–solid potential, there are five possible adjustable parameters, ϵ_{gs}, z_0, σ_{gg}, ϵ_{gg}, and n^σ_{ms}. Due to very strong interaction between ϵ_{gg} and σ_{gg}, the distance σ_{gg} was fixed in most of the fits at its gas phase value, 0.360 nm (see below). Some runs were done with σ_{gg} fixed at 0.373 nm, the value found by Sams.[15] Table III lists the standard deviation of weighted residuals and the frequency of "vertical" vibration in the harmonic approximation of eq 8. An examination of the distribution of weighted residuals shows no systematic deviations.

In a multiparameter fit it is necessary to examine the multicollinearity or degree of interaction[35] of the fitted parameters. In the case of a nonlinear fit confidence contours in the parameter space are defined by surfaces of equal s^2, the sum of squares of weighted residuals. Confidence contours showing the interaction between each pair of parameters were plotted,[33] and the contours showed that the only serious multicollinearity was between ϵ_{gs} and z_0. The interaction among the parameters may be examined in a simpler way by linearizing the model about the minimum in s^2.[36] This approximation allows the correlation matrix for the parameters to be calculated, and also the joint Bonferroni confidence levels for the parameters.[35] The results are given in Table II, which shows a high correlation between ϵ_{gs} and z_0.

B. *Combined High and Low Temperature Analysis.* The low temperature data of I and the high temperature data of Sams et al.[37] were combined together and fit to the same equation as the low temperature data. This procedure involved introducing another adjustable parameter, the ratio of the surface areas of the two different samples of gcb, $\mathcal{Q}_{P33}/\mathcal{Q}_{FT} = \mathcal{Q}(\text{P33}(2700))/\mathcal{Q}(\text{Sterling FTg-M5})$. The high temperature data isotherms of Sams et al. extrapolate at low coverages directly to the origin and it is clear that the effects of heterogeneity are small. It is well known that, as the temperature increases, solid surfaces become more effectively homogeneous. In addition to the effect of high temperature, it may be that the helium calibration technique used in the high temperature experiments effectively prevents strong-site adsorption from being measured.[33] and it may also be that P33(2700) has less heterogeneity than Sterling FTg-M5. In any case, as heterogeneity effects are both small and unknown for P33(2700), n^σ_{ms} was set equal to zero for the fit to eq 1. There were 22 low temperature data points and 17 high temperature points. Each set of data was weighted with a relative error. This relative error was adjusted after a
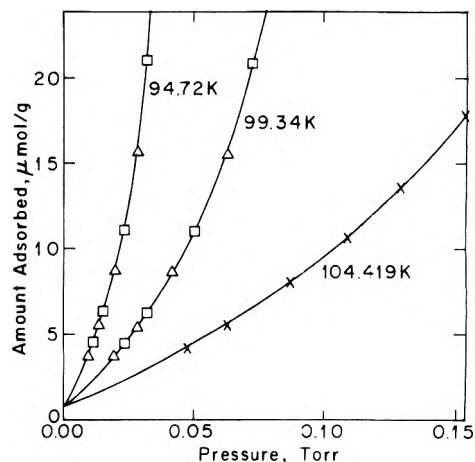
Figure 5. Comparison of data used in the low temperature virial coefficient theory analysis with best-fit theoretical isotherms. The temperatures of the isotherms are 94.72, 99.34, and 104.49 K. The different symbols correspond to different experimental runs.

preliminary fit to make the high and low temperature data equally weighted. The relative weighting of the low temperature to high temperature data points was 1.0:0.43. The high and low temperature ranges are indicated in Figures 1 and 3. The results of the fits are given in Tables III and IV. All errors shown in Tables II and IV are calculated for a joint 90% confidence level.

IV. Discussion

A. *Low Temperature Analysis.* 1. *Adsorbate–Adsorbent Potential.* The ϵ_{gs} values for the four n–m potentials shown in Table II, except for the last entry, are extremely close to each other; they differ by less than 1 K. This marked consistency is in sharp contrast to the results of the high temperature VC analysis of Sams et al., where the ϵ_{gs} values for the 9–3 and 10–4 potentials differ by 26 K. At low temperatures, the fit of theory to data is sensitive to the depth of the gas–solid potential only, not the shape of the potential. Thus, the low temperature data allows the depth ϵ_{gs} to be determined more precisely than previously. In contrast, z_0 increases quite significantly as n and m are increased. This increase is due to the fact that n, m, and z_0 all have an effect on the capacity of the potential. The vertical capacity $z_0 C_c$, however, remains constant for all four of the fits. Thus, the high interaction between ϵ_{gs} and z_0, n, and m prevents accurate values for z_0 from being arrived at.

2. *Adsorbate–Adsorbate Potential.* The correlation coefficients listed in Table II show that the parameter ϵ_{gg} is not strongly coupled to the n–m gas–solid potential parameters. Strong interaction between ϵ_{gg} and σ_{gg} may be seen from a comparison of the two fits which differ only in the fixed value of σ_{gg}. Both fits are accomplished within essentially the same error; the temperature range and coverage of the data are such that only a single parameter of the adsorbate–adsorbate potential can be obtained. This limitation of the data is one reason why a simple 12–6

TABLE IV: Results of Combined Low and High Temperature Virial Coefficient Theory Fit[a]

n–m	ϵ_{gs}/k, K	z_0, nm	ϵ_{gg}/k, K	$\mathcal{Q}_{P33}/\mathcal{Q}_{FTg}$	n^σ_{ms}, μmol/g	Std dev, %
9–3	1458 ± 6	0.20 ± 0.01	145 ± 2	1.04 ± 0.01	0.67 ± 0.09	0.731
12–3	1461 ± 6	0.23 ± 0.01	145 ± 3	1.05 ± 0.04	0.67 ± 0.1	0.720
16–3	1466 ± 6	0.26 ± 0.02	145 ± 3	1.07 ± 0.05	0.66 ± 0.1	0.739
10–4	1441 ± 11	0.30 ± 0.03	146 ± 4	0.98 ± 0.07	0.70 ± 0.15	1.08
14–4	1442 ± 11	0.36 ± 0.04	146 ± 4	0.97 ± 0.07	0.70 ± 0.15	1.13
18–4	1444 ± 11	0.40 ± 0.40	146 ± 4	0.98 ± 0.07	0.70 ± 0.15	1.10

[a] Fixed parameters: $\mathcal{Q}_{FTg} = 11.4$ m^2/g, $\sigma_{gg} = 0.360$ nm.

TABLE V: Correlation Matrix for Combined Low and High Temperature Virial Coefficient Theory Fit

	n^σ_{ms}	ϵ_{gs}	z_0	ϵ_{gg}	α_{FT}/α_{p33}
n^σ_{ms}	1				
ϵ_{gs}	0.79	1			
z_0	0.62	0.91	1		
ϵ_{gg}	0.45	0.84	0.67	1	
α_{FT}/α_{p33}	0.0	0.27	0.65	0.03	1

effective potential for adsorbed Kr is used in this work. More detailed potentials such as the 12-6-3 potential greatly increase the computation time for the theory, yet lead to essentially the same conclusion.[38]

The fit with ϵ_{gg} fixed at 171 K and σ_{gg} fixed at 0.36 nm was a test to learn whether the data could be fitted using the bulk potential parameters for Kr. These potential parameters were obtained from fitting gas phase virial coefficient, B, data at rather higher temperatures than 100 K;[39] ϵ_{gg} values which have been obtained from fitting lower temperature B data are even greater,[40,41] and would even more poorly describe the present data. The attempt showed that the gas phase Kr potential cannot fit the data, for not only was the standard deviation of residuals much higher than that for the rest of the fits, but the deviations of the residuals were highly systematic. These results indicate that this model potential and the data cannot be reconciled. The reason for the deviation of the adsorbate–adsorbate potential from the bulk value has been extensively studied theoretically, and is thought to be due to three-body interactions.[21] As the recent review of Takaishi[42] points out, however, comparisons between theory and experiment are not very meaningful when the relatively crude LJ 12-6 potential is used.

At this point, let us consider why Morrison and Ross[11] found the Ar–gcb data to be consistent with the gas phase potential, while Sams et al., using the same data, found a potential which was significantly shallower than the gas phase potential. (The Ar–gcb data fall in a reduced temperature range kT/ϵ_{gg} which lies between the high and low temperature data for Kr analyzed in this paper.) The important difference between the two analyses is that they used different surface areas for the same sample of P33(2700). Sams et al. used 8.96 m²/g, and Morrison and Ross used 14.3 m²/g, both deriving their surface areas from the VC analysis, but by different methods. There is strong interaction between the surface area and ϵ_{gg}, so that if α is increased ϵ_{gg} will increase to compensate. Clearly an accurate surface area for P33(2700), determined by methods exogenous to the VC analysis, is needed. To check the interaction effect for the low temperature Kr–gcb data, a fit was performed where the potential parameters for Kr were fixed at their gas phase values, and the surface area was treated as an adjustable parameter. A satisfactory fit was only obtained when the surface area had been adjusted upward to 20 m²/g, a value which is far outside the surface area limits known from monolayer capacity, 11.4 ± 4 m²/g.

3. *Heterogeneity.* The parameter n^σ_{ms} is determined by the fit to a lesser precision, 15%, than the other parameters. This is to be expected since it represents the intercept of the virial isotherms on the amount adsorbed axis, and is small compared to the amounts adsorbed which are fitted. The result indicates that the monolayer capacity of the strong sites is 0.5 ± 0.1% of the total monolayer capacity, which is 130 ± 5 μmol/g. This value is considerably higher than the 0.1% for P33(2700) which Graham[4] arrived at by a cruder extrapolation method. As was brought out in I, Graham's method can be expected
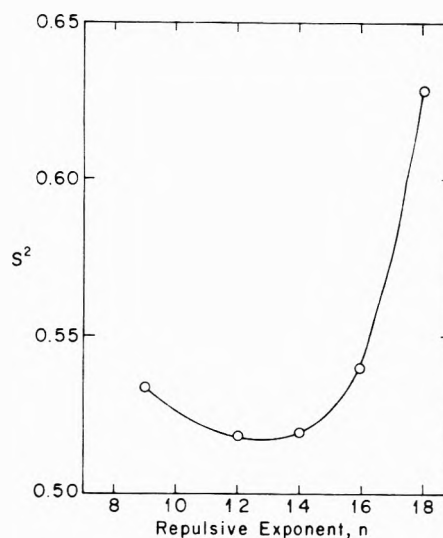
Figure 6. Sum of squares of weighted residuals for n-3 potentials.

to give n^σ_{ms} values which are too small.

B. *Combined High and Low Temperature Analysis.* 1. *Adsorbate–Adsorbent Potential.* The combined analysis was undertaken to more accurately determine the gas–solid potential energy function. A potential is sought which is successful in describing low coverage adsorption data over the entire $0.65 < kT/\epsilon_{gs} < 0.21$ temperature range, which corresponds to a pressure range of about five orders of magnitude. There are three qualities or attributes of potential energy functions which the data contain information about: capacity, depth, and anharmonicity. Capacity is determined by the amount adsorbed in the Henry law regime, independent of temperature. Depth of a potential is determined by the temperature dependence of Henry's law adsorption or, to put it in another way, by the value of the limiting low coverage heat of adsorption q_{st}^0. The anharmonicity of a potential in turn can be determined by temperature dependence of q_{st}^0. Since the energy of the well is considerably larger than kT for both the low and high temperature sets of data, and since both sets of data span a large enough temperature range to accurately determine the isosteric heat of adsorption, both of these sets of data are capable of determining the capacity and depth of a given potential. By combining both sets of data, the anharmonicity can also be found, since the data cover a wide enough temperature range to define the temperature dependence of q_{st}^0. Figure 1 illustrates how q_{st} depends on temperature for various n-m potentials. The n-3 potentials differ from the n-4 potentials in the high temperature regime, but not at low temperatures.

The results of the combined low and high temperature VC analysis, Tables IV and V, indicate that the n-3 potentials are more successful than the n-4 potentials at fitting the data. A like conclusion can also be drawn from an inspection of the results of the separate low and high temperature analyses. These results show that the 9–3 and 12–3 potentials yield essentially the same value for ϵ_{gs} at low and high temperature, but that the 10–4 potential yields widely differing values. If an attractive exponent $m = 3$ is decided upon, the repulsive exponent n may be found by optimizing the fit of theory to data. The sum of squares of weighted residuals, s, for various n-3 potentials is plotted in Figure 6. A minimum is clearly indicated for n values in the 12–14 range. A comparison of the parameters derived from the high and low temperature fit with the parameters derived from the low temperature fit alone indicates that only the 12–3 or 14–3
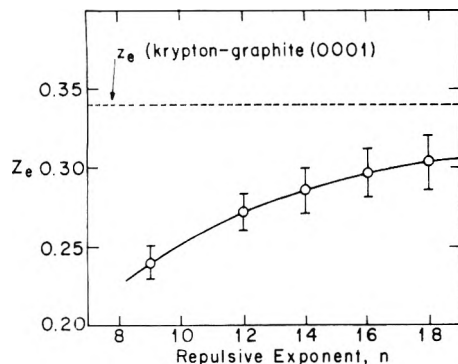
Figure 7. Equilibrium gas–solid distance for n–3 potentials.

potentials yield the same parameters. Thus, these are the only potentials whose fitted parameters do not depend on the temperature range of the fit, or the weighting of the data in a combined fit.

It should be pointed out that the n–3 potentials are only slightly favored over the n–4 potentials on statistical grounds (n–3, $\sigma = 0.73\%$; n–4, $\sigma = 1.1\%$). The fit of Sams et al.'s argon–gcb data, which also covered a wide reduced temperature range, favors the n–3 over the n–4 potentials by about the same amount (n–3, $\sigma = 1.5 \times 10^{-3}$; n–4, $\sigma = 0.72 \times 10^{-3}$).[2,43]

Figure 7 is a plot of z_e, the equilibrium gas–solid distance predicted by the combined fits to various n–3 potentials. As n is increased, z_e increases to keep the capacity of the potential constant. In the absence of interaction between anharmonicity and capacity in the analysis, the bestfit z_e value for various n–m potentials could be predicted from the harmonic approximation, eq 7. In this case, n could be increased until a desired value of z_e was reached. There is considerable interaction between anharmonicity and capacity, however, so that in the combined fits $z_0 C_c$ is not constant for various n–m potentials. The value of z_e can be predicted to be very nearly equal to 0.37 nm on the basis of crystallographic diameters[6] and theoretical calculations.[23] It is apparent from Figures 6 and 7 that a LJ n–3 potential which fits the data and which predicts a gas–solid distance of 0.37 nm cannot be found. This deficiency of the LJ potential could be remedied by shifting the reference plane of the LJ potential outward from the plane passing through the centers of atoms in the outermost plane of the crystal. This kind of a shift in the reference plane of the attractive part of the potential, the z^{-3} part, was predicted recently on theoretical grounds by Zaremba and Kohn.[44]

The value of z_e or z_0 has often been introduced into VC studies as the external parameter necessary to determine the solid surface area by VC analysis with the LJ potential. The results of this study indicate that this procedure is incorrect, since z_e values predicted by LJ potentials which best fit the data are consistently less than z_e values predicted from crystallographic diameters.

The biased z_e values predicted by the best-fit LJ potentials were responsible for the incorrect surface area for gcb determined in previous VC studies.[2,6,7] In these studies a high given z_e (or z_0) value or set of z_e values was imposed from outside the VC analysis. The surface area, an adjustable parameter, then had to be decreased to compensate the overall capacity of the model. Sams et al.[2] used theoretical estimates of the magnitude of the long-range gas–solid interaction as input to the VC theory analysis. This procedure has not been used in the present work, because the adsorption data samples the gas–solid potential very near the surface. Thus, the long-range potential, as expressed by $U(z) = -C_3/z^3$, is not expected to

agree with the attractive term in the LJ potential which fits adsorption data. Bruch and Watanabe[45] recently estimated C_3 to be 2.8×10^{-49} J/m^3. The coefficient of the attractive term in the 12–3 potential with $\epsilon_{gs}/k = 1461$ K and $z_0 = 0.23$ nm is 5.2×10^{-49} J/m^3.

2. *Adsorbate–Adsorbate Potential.* The combined analysis shows that the high temperature data are consistent with essentially the same adsorbate–adsorbate potential as was obtained from the low temperature analysis. This result is expected. The magnitude of the second two-dimensional virial coefficient is considerably greater at low than at high temperature. In addition, the low temperature data extend to higher coverage than the high temperature data. These two factors both contribute to make the adsorbate–adsorbate potential parameter fit be dominated by the low temperature data.

V. Conclusions

It was found that the virial coefficient theory of adsorption could be successfully applied to low temperature, low coverage adsorption on graphitized carbon black (gcb). The virial coefficient theory equation of state was capable of representing the present data to within the accuracy of the data. The low temperature application of the virial coefficient theory showed that only a single parameter of the adsorbate–adsorbate potential energy function could be found. The depth of a Lennard-Jones 12–6 potential with slow collision diameter 0.36 nm was found to be $\epsilon_{gg}/k = 146 \pm 3$ K. The depth of the adsorbate–adsorbate potential energy function could be accurately determined from the low temperature virial coefficient theory analysis. However, the adsorbate–adsorbent potential parameters could be most accurately determined from a combined analysis of low and high temperature adsorption data. The preferred adsorbate–adsorbent potential was a Lennard-Jones 12–3 potential, with depth $\epsilon_{gs}/k = 1461 \pm 6$ K and distance parameter $z_0 = 0.233 \pm 0.01$ nm. The combined analysis allowed a determination of the ratio of the areas of Sterling FT-D5 to P33(2700) graphitized carbon blacks. The ratio was found to be 1.05 ± 0.04.

References and Notes

(1) W. A. Steele and G. D. Halsey, Jr., *J. Chem. Phys.*, **22**, 979 (1954).
(2) J. R. Sams, G. Constabaris, and G. D. Halsey, Jr., *J. Phys. Chem.*, **66**, 2154 (1962).
(3) J. R. Sams, G. Constabaris, and G. D. Halsey, Jr., *J. Chem. Phys.*, **36**, 1334 (1962).
(4) D. Graham, *J. Phys. Chem.*, **61**, 1310 (1957).
(5) F. A. Putnam and T. Fort, Jr., *J. Phys. Chem.*, **79**, 459 (1975).
(6) D. H. Everett, "Surface Area Determination", D. H. Everett and R. H. Ottewill, Ed., Butterworths, London, 1970.
(7) H. E. Thomas and R. A. Pierotti, *Trans. Faraday Soc.*, **7**, 1725 (1973).
(8) S. Ross and J. P. Olivier, "On Physical Adsorption", Interscience, New York, N.Y., 1964.
(9) J. H. Singleton and G. D. Halsey, Jr., *J. Phys. Chem.*, **58**, 1011 (1954).
(10) C. F. Prenzlow, H. R. Beard, and R. S. Brundage, *J. Phys. Chem.*, **73**, 969 (1969).
(11) I. D. Morrison and S. Ross, *Surf. Sci.*, **39**, 21 (1973).
(12) I. D. Morrison, Ph.D. Thesis, Rennsalear Polytechnic Institute, Troy, N.Y., 1975.
(13) L. A. Rowley, D. Nicholson, and N. G. Parsonage, *Mol. Phys.*, **31**, 365 (1976).
(14) E. Giamello, C. Pisani, F. Ricca, and C. Roetti, *Surf. Sci.*, **49**, 401 (1975).
(15) J. R. Sams, *Mol. Phys.*, **9**, 195 (1965).
(16) S. Ross in "Surface Area Determination", D. H. Everett and R. H. Ottewill, Ed., Butterworths, London, 1970.
(17) L. T. Drzal, F. A. Putnam, and T. Fort, Jr., *Rev. Sci. Instrum.*, **45**, 1331 (1974).
(18) W. A. Steele, *Surf. Sci.*, **39**, 149 (1973).
(19) W. A. Steele, "The Solid-Gas Interface", Vol. 1, E. A. Flood, Ed., Marcel Dekker, New York, N.Y., 1964.
(20) R. S. Hansen and J. A. Murphy, *J. Chem. Phys.*, **39**, 1642 (1963).

(21) R. A. Pierotti and H. E. Thomas in "Surface and Colloid Science", Vol. IV, E. Matijevic, Ed., Wiley-Interscience, New York, N.Y., 1971, pp 93–259.
(22) W. A. Steele, Surf. Sci., **36**, 317 (1973).
(23) D. L. Freeman, J. Chem. Phys., **62**, 941 (1975).
(24) B. K. Oh and S. K. Kim, J. Chem. Phys., **61**, 1797 (1974).
(25) B. C. Kriemer, B. K. Oh, and S. K. Kim, Mol. Phys., **26**, 297 (1973).
(26) K. S. Pitzer and O. Sinanoglu, J. Chem. Phys., **32**, 1279 (1960).
(27) A. D. McLashlan, Mol. Phys., **7**, 381 (1964).
(28) A. J. Bennett, Phys. Rev. B. **9**, 741 (1974).
(29) F. Mandel, J. Chem. Phys., **62**, 2261 (1975).
(30) D. L. Freeman, J. Chem. Phys., **62**, 4300 (1975).
(31) H. E. Thomas, R. N. Ramsey, and R. A. Pierotti, J. Chem. Phys., **59**, 6163 (1973).
(32) D. M. Himmelblau, "Applied Nonlinear Programming". McGraw-Hill, New York, N.Y., 1972.
(33) F. A. Putnam, Ph.D. Thesis, Carnegie-Mellon University, Pittsburgh, Pa., 1976.
(34) H. Akima, J. Assoc. Comput. Mach., **17**, 589 (1970).
(35) J. Neter and W. Wasserman, "Applied Linear Statistical Models", Richard D. Irwin, Inc., Homewood, Ill., 1974.

(36) N. R. Draper and H. Smith, "Applied Regression Analysis", Wiley, New York, N.Y., 1966.
(37) G. Constabaris, J. R. Sams, Jr., and G. D. Halsey, Jr., J. Chem. Phys., **36**, 915 (1962).
(38) R. Wolfe and J. R. Sams, Jr., J. Chem. Phys., **44**, 2181 (1966).
(39) J. O. Hirschfelder, C. F. Curtiss, and R. B. Bird, "Molecular Theory of Gases and Liquids", Wiley, New York, N.Y., 1954.
(40) R. Byrne, J. T. Jones, and M. P. Starley, Trans. Faraday Soc., **64**, 1747 (1968).
(41) B. E. F. Fender and G. D. Halsey, Jr., J. Chem. Phys., **36**, 1181 (1962).
(42) T. Takaishi, Prog. Surf. Sci., **6**, 43 (1975).
(43) R. N. Ramsey, H. E. Thomas, and R. A. Pierotti, J. Phys. Chem., **76**, 3171 (1972). This paper contains a correction to the results presented in ref. 2.
(44) E. Zaremba and W. Kohn, Phys. Rev., B, **13**, 2270 (1976).
(45) The isosteric heats were calculated from the five isotherms presented in I. Each isotherm was interpolated at constant amount adsorbed by Akima's method.[34] The isosteric heats were found by linear regression of ln p vs. 1/T. Errors shown in Figure 4 are statistically estimated standard errors from the linear regression.

Physical Adsorption on Patchwise Heterogeneous Surfaces. 3. Continuous Phase Transitions of Krypton Monolayers on (0001) Graphite

Frederick A. Putnam,[†] Tomlinson Fort, Jr.,* and Robert B. Griffiths

Department of Chemical Engineering and Department of Physics, Carnegie-Mellon University, Pittsburgh, Pennsylvania 15213 (Received February 18, 1977)

Experimental vapor pressure data for krypton adsorption on graphitized carbon black are analyzed thermodynamically such that the shapes of the thermodynamic singularities near phase transitions are preserved. The thermodynamic potential and all of its derivatives are calculated in the transition region. The analysis assumes a classical Ehrenfest type second-order transition for the "fluid–solid" monolayer transition. Singularities for this lower-density transition are much more pronounced in the compressibility and heat capacity at constant spreading pressure than in the isosteric heat or heat capacity at constant density. The higher-density phase transition region was investigated by careful differentiation of the experimental isotherms, which revealed a pronounced compressibility minimum at amount adsorbed $n^\sigma = 124 \pm 2$ μmol/g, and compressibility peaks at higher densities. The higher and lower-density peaks appear to all lie on a line of continuous order–disorder transitions, as in helium and nitrogen monolayers on graphite, and certain theoretical models.

I. Introduction

Phase transitions in monolayers of adsorbed gases have been under intensive investigation recently.[1-5] For xenon, krypton, and nitrogen adsorbed on graphite, diffraction experiments have shown that at certain temperatures and pressures, the monolayer can crystallize in registry with the graphite lattice.[1,4,6] While it is now generally accepted that the attainment of registry is associated with phase transitions detectable by thermodynamic measurements, the nature of the phase transitions is not yet fully understood. Krypton vapor pressure isotherms of Thomy and Duval[7,8] showed two "steps" near the monolayer point. The steps were accompanied by isosteric heat peaks.[5,9] These transitions were referred to as a two-dimensional fluid–solid phase change (at lower density), and a rearrangement of the two-dimensional solid (at higher density). In a previous paper[5] (hereafter referred to as I) the present authors argued that the higher and lower density steps both corresponded to in-registry ⇌ out-of-registry transitions. In this paper, the krypton transitions are analyzed

further and compared with similar transitions observed in helium and nitrogen monolayers, and theory.

From the isotherm data presented in I, it is clear that the lower density transitions are more pronounced than the higher density transitions. The lower density transitions appear to be continuous (i.e., of higher order than first). When analyzing the experimental data thermodynamically, conventional techniques of obtaining isosteric quantities break down on the phase transition line, since the derivative of pressure with respect to temperature at constant amount adsorbed cannot be obtained without differentiating across the phase boundary. In I, isosteric quantities were obtained by ignoring this difficulty, which tended to obscure the singularities since the density of the transition is quite temperature dependent. In this work the isosteric and other thermodynamic quantities near the phase transition are obtained by differentiation parallel to the phase boundary, which preserves the singularities.

The higher density transition is not pronounced enough to allow the kind of treatment presented here for the lower density transition. However, the analysis of the lower density transition indicated that the transition is accompanied by a large peak in the compressibility (which can be calculated from the slope of the isotherms). Consequently, the higher density isotherms are analyzed

† Present Address: Department of Chemical Engineering, Massachusetts Institute of Technology, Cambridge, Mass. 02139.
* Address correspondence to this author at the Department of Chemical Engineering.
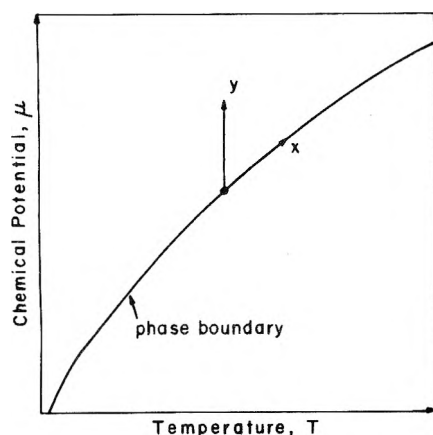
Figure 1. Curvilinear coordinate system for interpolation of experimental data along a line of phase transitions.

by differentiation only. The results yield much more detailed information about the higher density transition than the isosteric heat analysis of I.

II. Thermodynamic Analysis

A. *Lower Density Transition.* It is common in modern thermodynamic treatments of phase transitions to regard the phase boundary as defining a fundamental coordinate system in which to analyze a transition in the space of thermodynamic quantities. In a two-dimensional field space (using the "field", "density", "potential" terminology of Griffiths and Wheeler[10]) a suitable (curvilinear) coordinate system would have one axis x along the phase boundary and the other axis y parallel to a field variable axis, as shown in Figure 1. If the thermodynamic potential is defined in such a coordinate system, it may be differenced or interpolated with respect to x at constant y arbitrarily close to the phase boundary without crossing the phase boundary.

In analyzing the data presented in I, the spreading pressure (a surface excess quantity[11]) was used as the thermodynamic potential, and the fields were chemical potential μ and temperature T. The fundamental thermodynamic equation is

$$d\pi = s^\sigma \, dT + \Gamma^\sigma \, d\mu \tag{1}$$

where the densities s^σ and $\Gamma^\sigma = n^\sigma/\mathcal{Q}$ are the surface excess entropy per unit area and the surface excess amount adsorbed per unit area. The area of the adsorbed layer $\mathcal{Q}$ is the same as the area of the adsorbent and is constant during the experiments. Various thermodynamic quantities of interest may be found by differentiating with respect to T and μ. In terms of the derivatives

$$\left(\frac{\partial\pi}{\partial\mu}\right)_T = \pi_\mu, \quad \left(\frac{\partial\pi}{\partial T}\right)_\mu = \pi_T, \quad \left(\frac{\partial^2\pi}{\partial\mu^2}\right)_T = \pi_{\mu\mu}, \text{ etc.} \tag{2}$$

we have

$$\Gamma^\sigma = \pi_\mu; \quad s^\sigma = \pi_T$$

$$\kappa_T = \pi_{\mu\mu}/\pi_\mu{}^2$$

$$\Delta\bar{H}/T = \pi_{\mu T}/\pi_{\mu\mu} \tag{3}$$

$$c_\mu/T = \pi_{TT}$$

$$c_\pi/T = \pi_{TT} - \pi_T\pi_{\mu T}/\pi_\mu$$

$$c_\rho/T = (\pi_{TT}\pi_{\mu\mu} - \pi_{\mu T}{}^2)/\pi_{\mu\mu}$$

where $\Delta\bar{H}$ is the differential enthalpy, κ_T is the isothermal
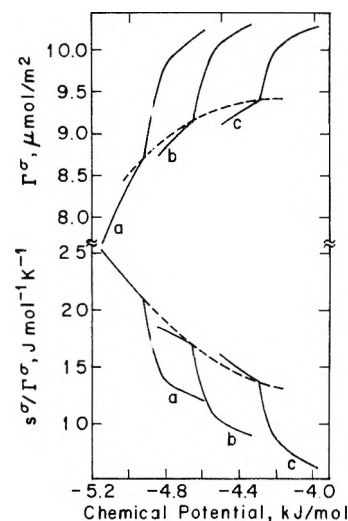
Figure 2. Density and entropy of Kr on gcb near the lower-density phase transition line. Solid lines are lines of constant temperature, as follows: (a) 94.73, (b) 99.34, (c) 104.48 K. The dashed curve indicates the phase transition line.

compressibility, and c_μ, c_τ, and c_ρ are heat capacities at constant chemical potential, spreading pressure, and density. Chemical potential μ is calculated from the vapor pressure, $\mu = RT \ln (p/p_{\text{sat}})$ where p_{sat} defines the standard state. The above quantities then refer to equilibrium between the adsorbed film and the standard state. Thus, $\Delta H = \Delta H_s - q_{\text{st}}$ where ΔH_s is the heat of sublimation of krypton and q_{st} is the isosteric heat of adsorption.

The adsorption isotherms for Kr on gcb in the neighborhood of the transition are plotted in Figure 2. To obtain spreading pressures, the data were interpolated with natural cubic spline curves.[12] For the 94.72 and 99.34 K isotherms, data from only one of the experimental runs, run 24, was used (see supplementary material section in ref 5). There are two reasons for this. First, interpolation of a single run defines a smoother curve than if data from different runs are used, since the adsorption data are obtained by adding measured amounts of krypton to the system between each data point so that the accumulated error in n^σ is much greater than error in n^σ difference between adjacent data points.[13] The relevant errors for each data point are listed along with the data in ref 14. Second, run 24 is preferred over run 25, a replicate experiment, because it contains data points which appear to be located very close to the phase transition (see Figure 1).

Adsorption isotherms for Kr on the (0001) graphite surface were obtained from adsorption isotherms for Kr on gcb by subtracting the adsorption on strong sites, which form a monolayer of capacity 0.67 μmol/g at much lower pressures than the pressure range of monolayer adsorption on the (0001) plane.[15] Multilayer adsorption on the strong sites will have a small but smooth effect on the remainder of the isotherm, as studies on more heterogeneous graphites have shown.[16,17] Cubic splines were used because they define curves which pass exactly through the data points, and do not involve any modelistic asumptions except smoothness. The results of the cubic spline interpolation are a set of coefficients that define the isotherm between adjacent data points i and $i + 1$ by a cubic equation

$$n^\sigma(p) = c_{3i}(p - p_i)^3 + c_{2i}(p - p_i)^2 +$$
$$c_{1i}(p - p_i) + n_i{}^\sigma \tag{4}$$

The spline curves were then integrated from zero pressure
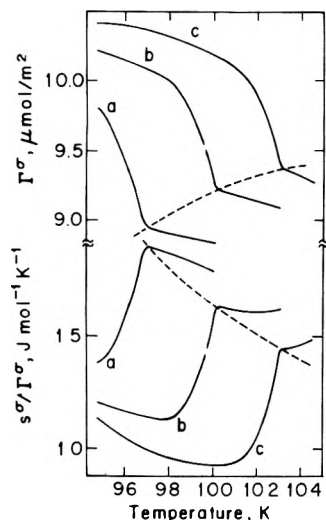
Figure 3. Density and entropy of Kr on gcb near the lower-density phase transition line. Solid lines are lines of constant chemical potential, as follows: (a) 1490, (b) 1016, (c) 566 kJ/mol. The dashed curve indicates the phase transition line.

to obtain the spreading pressure, using the Gibbs adsorption equation

$$\pi(p) = \frac{RT}{\alpha} \int_0^p n^\sigma \, d \ln p \qquad (5)$$

where $\alpha = 11.4 \text{ m}^2/\text{g}^5$. The integration may be performed analytically, so that the $\pi(p)$ isotherm between each pair of data points is defined by π_i, p_i, c_{1i}, c_{2i}, c_{3i}. As pressure increases extremely rapidly at densities just above the transition density, the isotherm data above the transition were interpolated after a log transformation of pressure. The isotherms obtained from the interpolation and their derivatives were examined in detail,[14] and were found to be in good accord with graphical interpolation, and free of spurious oscillations.

The details of the exact shape of the adsorption isotherms very close to the phase transition are unknown except to within the resolution of the data in I. Close examination of the data reveals that it would be consistent with either a classical Ehrenfest type second-order transition (where the slope of the isotherm has a finite discontinuity), or with a λ transition (where the slope of the isotherm becomes logarithmically infinite at the phase transition point).[18] Since the Ehrenfest singularity is the simplest case, and can fit the data precisely, it was assumed. The Ehrenfest singularity assumption is readily implemented by fitting the isotherm on either side of the phase transition point with a separate cubic spline.

The cubic spline procedure outlined above yielded three completely defined isotherms $\pi_j(\mu)$ for the three experimental temperatures, $T_j = 94.72$, 99.34, and 104.49 K. To interpolate the experimental data in the x–y coordinate system described in section II.A, the line of phase transitions was first defined by choosing one data point for each isotherm as the transition point. These points are indicated in Figure 2. Equations for the phase boundary $\mu_b(T)$, $\pi_b(T)$ were then found. Since there are three isotherms, quadratic polynomials were used. Next, the experimental isotherms were transformed into a new coordinate system $\pi_j' = \pi_j - \pi_b(T)$, $\mu_j' = \mu_j - \mu_b(T)$. This transformation maps the line of transitions in the π, μ plane onto the origin in the π', μ' plane. To find the value of π at any point μ_0, T_0 in the μ, T plane, $\mu' = \mu_0 - \mu_p(T_0)$ was found for each isotherm using the cubic splines. The π_j' values were then interpolated on the T axis, again using
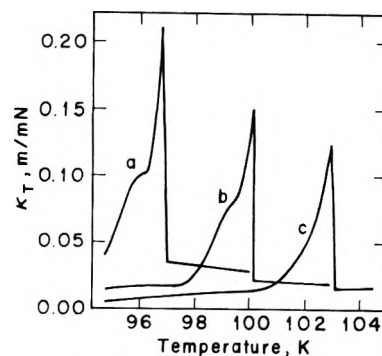
Figure 4. Two-dimensional compressibility of Kr on gcb near the lower-density phase transition. Three lines of constant chemical potential are shown; symbols are as in Figure 3.
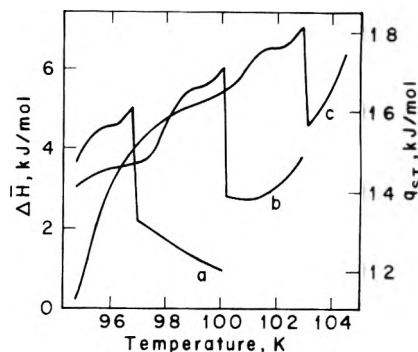
Figure 5. Differential enthalpy and isosteric heat of adsorption of Kr on gcb near the lower-density phase transition. Three lines of constant chemical potential are shown; symbols are as in Figure 3.
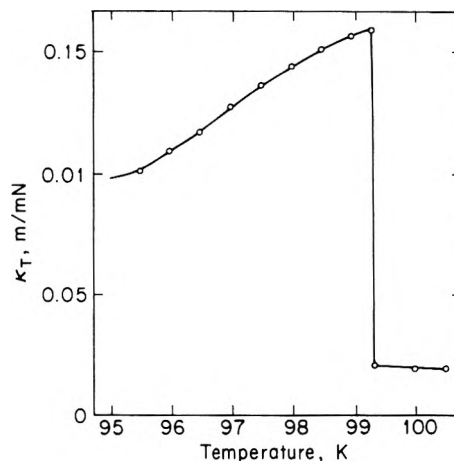
Figure 6. Two-dimensional compressibility of Kr on gcb near the lower-density phase transition of density $\Gamma^\sigma = 9.20 \ \mu\text{mol/m}^2$.

quadratic polynomials since there are three isotherms, to obtain $\pi'(\mu')$ at $T = T_0$. Finally, the spreading pressure was calculated by transforming back to the π, μ coordinate system, $\pi\mu_0$, $T_0 = \pi'(\mu', T_0) + \pi_b(T_0)$.

The calculation of various thermodynamic functions was done by evaluating π on a 3 × 3 grid of size $\mu = 1$ kJ/mol, $T = 0.005$ K, and evaluating the derivatives π_μ, π_T, $\pi_{\mu\mu}$, π_{TT}, and $\pi_{\mu T}$ by well-known finite difference formulas. From the derivatives, various thermodynamic functions were calculated. Differencing across the phase boundary was not allowed. The isotherms and lines of constant μ were easily constructed by simply incrementing one independent variable while holding the other constant. The isosteres or lines of constant amount adsorbed were constructed using a search technique. Computer programs which accomplish the interpolations and calculate various thermodynamic functions along isotherms, lines of con-

TABLE I: Thermodynamic Functions at Phase Transition Points

	Continuous functions					Discontinuous functions		
	T, K	π, mN m⁻¹	μ, J mol⁻¹	π_μ, mmol m⁻²	π_T, mN m⁻¹ K⁻¹	$\pi_{\mu\mu}$, mol² m⁻² J⁻¹	π_{TT}, N m⁻¹ K⁻²	$r_{\mu T}$, mol m⁻² K⁻¹
						3.7×10^{-9}	-2.1×10^{-6}	-7.9×10^{-8}
a[a]	94.730	5.3178	−4917.3	0.00873	0.183			
						1.8×10^{-8}	4.4×10^{-5}	-9.5×10^{-7}
						1.9×10^{-9}	-2.8×10^{-6}	-5.0×10^{-8}
b[a]	99.337	8.4812	−4645.4	0.00915	0.155			
						1.3×10^{-8}	4.3×10^{-5}	-7.8×10^{-7}
						1.3×10^{-9}	1.8×10^{-6}	-7.4×10^{-8}
c[a]	104.48	12.536	−4293.5	0.00940	0.129			
						1.1×10^{-8}	5.8×10^{-5}	-8.2×10^{-7}

[a] Letters refer to isotherms shown in Figure 2.

stant μ, and isosteres are available.[14]

The results of the thermodynamic analysis are shown in Figures 2–6, and in Table I, which lists the locations of the phase transition points and the magnitude of the discontinuities of three points along the phase boundary. Plots of additional thermodynamic variables such as π_{TT}, $\pi_{\mu T}$, $\pi_{\mu\mu}$, c_μ, c_π, and c_ρ are available.[14] The discontinuities in the various second derivatives of the thermodynamic potential must satisfy the Ehrenfest relations, such as

$$\Delta\pi_{\mu T} = \Delta\pi_{TT}\left(\frac{d\mu}{dT}\right)_\lambda = \Delta\pi_{\mu\mu}\left(\frac{dT}{d\mu}\right)_\lambda \qquad (6)$$

$$\Delta c_\rho = (d\Gamma^\sigma/dT)_\lambda \Delta q_{st} \qquad (7)$$

and it is easily verified from Table I that these relations are indeed satisfied.

The accuracy of the various thermodynamic functions which are derived from this analysis depends ultimately on the nature of the original data. No quantitative estimates of the errors in the derivative values are available. The two-dimensional entropy and density are obtained with accuracy comparable to the accuracy of the original data. The compressibility is the most accurate of the second derivatives, since it is essentially the isotherm derivative.[14] The heat capacities are not very accurately obtained, however, since they are second derivatives of the experimental data taken with respect to temperature, and the data are three rather closely spaced isotherms. The nature of the heat capacity singularities is nevertheless consistent with various thermodynamic considerations, as discussed below.

Figures 2 and 3 show first derivatives of the thermodynamic potential plotted vs. field variables with a field held constant. Each of these curves exhibits a discontinuity in slope on the transition line (dotted curve), and as the transition line is crossed by increasing μ at constant T or decreasing T at constant μ, the density increases sharply and the entropy decreases sharply.

It is of interest to compare shapes and the "strengths" of the singularities in various second derivatives of thermodynamic functions in the sense defined by Griffiths and Wheeler (GW).[10] A measure of the magnitude of a singularity is the ratio of the singular part to the non-singular part, or $(a - b)/b$, where a is the value on the ordered side of the transition. The sharp peaks in the second derivatives of π taken with respect to field variables with other field variables held constant, such as $\pi_{\mu\mu}$, π_{TT}, π_μ, c_π, c_μ, and κ_T, Figure 4, are all of similar magnitude and shape, and are suggestive of somewhat unresolved λ peaks. These are all "weak" singularities, in the GW language. The magnitudes of the singularities in second derivatives of π taken with respect to field variables with a density held constant, such as q_{st} and c_ρ, Figure 5, are much
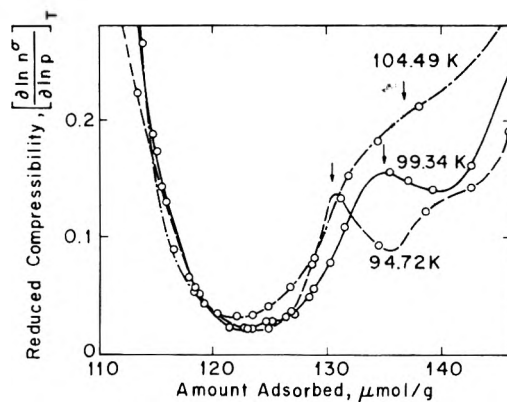
Figure 7. Dimensionless two-dimensional compressibility of Kr on gcb near the higher-density phase transition. Three isotherms are shown, as follows: (a) 94.72, (b) 99.34, (c) 104.49 K.

smaller. These are all "doubly weak" singularities, in line with the GW language, and in the case of true λ transitions would appear as cusps with vertical tangents.

Figures 5 and 6 show that the width of the transition on the temperature axis is much greater for isosteres than for isotherms of lines of constant μ. This is because the phase boundary is more nearly parallel to lines of constant density than to isotherms or lines of constant μ. This suggests that an experiment designed to measure the two-dimensional compressibility for a range of temperatures at constant density might yield very detailed information on the nature of the transition. Such experiments are planned in the near future.

B. *Higher-Density Transition.* The results of section A showed that for this system the thermodynamic variables which exhibit the transitions best are compressibilities and the like. Consequently, the higher density transition was detected by carefully differentiating the adsorption isotherms to obtain the two-dimensional compressibility. Data from all of the runs presented in I were used, because the transition occurs in a region where the isotherm is very nearly horizontal, so that there are fewer data near the transition for each run. A number of differentiation techniques were tried, and all techniques yielded essentially the same features; detailed results appear elsewhere.[14] The best results were obtained with a "cubic spline with smoothing"[19] algorithm, with amount adsorbed as the independent variable, log pressure as the dependent variable, and a pressure error of 1% (standard deviation) allowed for. The results of this differentiation are plotted in Figure 7.

The derivative shown in Figure 7 is a dimensionless compressibility of the two-dimensional film, $(\partial \ln n^\sigma/\partial \ln p)_T$. Each curve has a minimum at $n^\sigma = 124 \pm 2$ μmol/g. The 94.72 and 99.34 K curves also exhibit compressibility peaks, at $n^\sigma = 130$ and 134 μmol/g, respectively. The peak
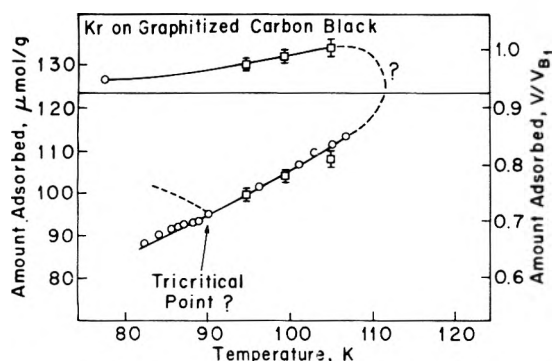
Figure 8. Phase diagram showing line of phase transitions of Kr on graphite. The squares and the left-hand amount adsorbed scale are from this work, for Kr on gcb, and the circles and the right-hand amount adsorbed scale are from Thomy and Duval, ref 7.

is clearly most sharp at the lowest temperature, and becomes broader and moves to higher density as temperature increases. At 104.49 K, only a broad "shoulder" is evident; this is seen as a peak in dn^σ/dp at $n^\sigma = 138$ $\mu mol/g$, however.

III. Discussion

The phase transitions located in this study are plotted and compared with those of Thomy and Duval in Figure 8. In this plot the amount adsorbed scales were adjusted so that the lower-density phase transition points in both studies would fall all along the same line, so that Thomy's $V/V_{B_1} = 1$ corresponds to $n^\sigma = 133.5$ $\mu mol/g$. The upper and lower branches of the line of phase transitions have been joined by a dotted line by analogy with the apparently similar phase transitions for He[20] and N_2[4] monolayers on graphite, where maximum temperatures for the transitions have been found. The maximum temperature is 29.3 K for He,[20] 86 K for N_2,[4] and judging from Figure 8, approximately 112 ± 5 K for Kr. The He transitions were found to be continuous by c_p measurements. For N_2, c_p has recently been measured by Stewart et al.,[3] and the transition also appeared to be of higher order than first. The discontinuity observed by Stewart et al. for the N_2 transition is approximately the same size as the c_p discontinuities given in Table I, $\Delta c_p{}'/k \approx 2$. The isotherm data of Thomy and Duval[7] and Larher[21] seem to indicate that at temperatures less than about 90 K the transition becomes first order, which would imply a tricritical point as was pointed out in I.

Several models have been constructed for the phase transitions discussed in this paper. Stebbins and Halsey[22] and Tsien and Halsey[23] developed a simple model which predicted first-order transitions between mobile and lattice gas monolayer phases. More recently, Price and Venables[24,25] and Bernard et al.[26] have developed similar models, which also predict first-order transitions.

A more sophisticated model of the transitions was developed recently by Campbell and Schick,[27] who applied the Bethe approximation to the triangular lattice gas problem. This approach yielded both continuous and first-order transitions, though for He only first-order transitions were found. The heavier rare gases have not yet been studied with this model.

Although a rigorous solution of the triangular lattice gas has not yet been obtained, the following considerations suggest that it may be consistent with the experimental evidence. In the absence of attractive interactions, and with large nearest-neighbor repulsion (as is the case with Kr, N_2, and Xe), the "hard hexagon" model studied by Gaunt[28] applies. The transition in this model appears to be continuous. In addition, it has been pointed out by

Alexander[29] that the order parameter for the triangular lattice gas has the same symmetry as that of the three-component Potts model. Baxter[30] has shown that the Potts model has a continuous transition in two dimensions, in agreement with the numerical work of Straley and Fisher.[31] This result is a violation of the Landau rule,[32] which forbids a continuous transition in a model of this symmetry, and lends weight to the possibility that the triangular lattice gas can also exhibit a continuous transition, in violation of the same Landau rule.

Mean field solutions for square and cubic antiferromagnets exist.[33] These produce continuous Ehrenfest-like second-order transitions, and the magnetization isotherms and magnetic susceptibilities have essentially the same shapes as the adsorption isotherms and compressibilities of Figures 2 and 12.

The effect of the attractive forces between adsorbate atoms, which increases at lower temperatures, will be to produce a tricritical point by making the transition first order at lower temperatures, as in metamagnets.[34] An example of the nature of the solution expected above the tricritical point is given by Fisher's exact solution[35] of the square lattice gas with nearest neighbor exclusion and weak second neighbor attraction, which predicted a λ transition for the one temperature solved for. The isotherm presented by Fisher has a "step" similar to the steps in the experimental isotherms.

To summarize, the higher and lower density phase transitions near the monolayer point for krypton adsorbed on graphite have been analyzed thermodynamically. Continuous transitions are found, which may be either λ-like or Ehrenfest-like. The krypton transitions appear to be similar to transitions in helium and nitrogen monolayers, which have a maximum temperature. As found in helium, c_p should have a large peak at the maximum temperature for the krypton transition, at about 100 K and $n^\sigma = 124$ $\mu mol/g$. The continuous nature of the transition is in agreement with sufficiently sophisticated theoretical models.

References and Notes

(1) H. M. Kramer and J. Suzanne, *Surf. Sci.*, **54**, 659 (1976).
(2) J. G. Dash, "Films on Solid Surfaces", Academic Press, New York, N.Y., 1975.
(3) D. M. Butler, G. B. Huff, R. W. Toth, and G. A. Stewart, *Phys. Rev. Lett.*, **35**, 1718 (1975).
(4) J. K. Kjems, L. Passell, H. Taub, J. G. Dash, and A. D. Novaco, *Phys. Rev. Lett.*, **32**, 724 (1974).
(5) F. A. Putnam and T. Fort, Jr., *J. Phys. Chem.*, **79**, 459 (1975).
(6) J. J. Lander and J. Morrison, *Surf. Sci.*, **6**, 1 (1967).
(7) A. Thomy and X. Duval, *J. Chim. Phys.*, **67**, 1101 (1967).
(8) A. Thomy, J. Regnier, J. Menaucourt, and X. Duval, *J. Cryst. Growth*, **14**, 159 (1972).
(9) J. Regnier, J. Rouquerol, and A. Thomy, *J. Chim. Phys.*, **72**, 327 (1975).
(10) R. B. Griffiths and J. C. Wheeler, *Phys. Rev. A*, **2**, 1047 (1970).
(11) J. W. Gibbs, "Collected Works", Longmans, Green and Co., New York, N.Y., 1928.
(12) J. G. Herriot and C. H. Reinsch, *Commun. ACM*, **16**, 763 (1973).
(13) L. T. Drzal, F. A. Putnam, and T. Fort, Jr., *Rev. Sci. Instrum.*, **45**, 1331 (1974).
(14) F. A. Putnam, Ph.D. Thesis, Carnegie-Mellon University, Pittsburgh, Pa., 1976.
(15) F. A. Putnam and T. Fort, Jr., *J. Phys. Chem.*, preceding paper in this issue.
(16) A. Thomy, *Carbon*, **9**, 587 (1972).
(17) A. Thomy and X. Duval, *J. Chim. Phys.*, **66**, 1969 (1966).
(18) A. B. Pippard, "Elements of Classical Thermodynamics", Cambridge University Press, Cambridge, 1957, Chapter 9.

(19) C. H. Reinsch, *Numerische Mathematik*, **10**, 177 (1967).
(20) M. Bretz, J. G. Dash, D. C. Hickernell, C. O. McLean, and O. E. Vilches, *Phys. Rev. A*, **8**, 1589 (1973).
(21) Y. Larher, *J. Chem. Soc., Faraday Trans. 1*, **70**, 320 (1974).
(22) J. P. Stebbins and G. D. Halsey, Jr., *J. Phys. Chem.*, **68**, 3863 (1964).
(23) R. Tsien and G. D. Halsey, Jr., *J. Phys. Chem.*, 71, 4012 (1967).
(24) G. L. Price and J. A. Venables, *Phys. Lett.*, **47A**, 19 (1974).
(25) G. L. Price and J. A. Venables, *Surf. Sci.*, **59**, 509 (1976).
(26) C. Bernard, J. Suzanne, M. Bienfait, and P. Hicter, *Surf. Sci.*, **52**, 340 (1975).
(27) C. B. Campbell and M. Schick, *Phys. Rev. A*, **5**, 1919 (1972).
(28) D. S. Gaunt. *J. Chem. Phys.*, **46**, 3237 (1967).

(29) S. Alexander, *Phys. Lett.* **54A**, 353 (1975).
(30) R. J. Baxter, *J. Phys. C.*, **6L**, 445 (1973).
(31) J. P. Straley and M. E. Fisher, *J. Phys. A. Math. Nucl. Gen.*, **6**, 1310 (1973).
(32) L. D. Landau and E. M. Lifshitz, "Statistical Physics", 2nd ed, Pergamon Press, London, 1969, p 442.
(33) V. A. Schmidt and S. A. Friedberg, *J. Appl. Phys.*, **38**, 5319 (1967).
(34) J. A. Griffin and S. E. Schnatterly in "Magnetism and Magnetic Materials-1974," AIP Conference Proceedings No. 24, C. D. Graham, Jr., J. J. Rhyne, and G. H. Lander, Ed., American Institute of Physics, New York, N.Y., 1975, p 195.
(35) M. F. Fisher, *J. Math. Phys.* (N.Y.), **4**, 278 (1963).

Solvent-Dependent Fluorescence of Pyrene-3-carboxaldehyde and Its Applications in the Estimation of Polarity at Micelle–Water Interfaces

K. Kalyanasundaram and J. K. Thomas*

Department of Chemistry and Radiation Laboratory, [1] *University of Notre Dame, Notre Dame, Indiana 46656 (Received November 16, 1976)*

The monomer fluorescence of pyrene-3-carboxaldehyde shows a strong dependence on solvent polarity. The fluorescence in nonpolar solvents such as n-hexane is very weak (quantum yield <0.001), but becomes quite intense in polar solvents (ϕ_F in methanol = 0.15). The fluorescence maximum shows a significant red shift with increased solvent polarity, which is linear with solvent dielectric constant at values greater than ten. This strong dependence of fluorescence on solvent polarity is used to obtain estimates of the polarity at the micelle–water interfaces for various ionic and nonionic detergent micelles. The measured values are in excellent agreement with ζ potential estimates for the micellar Stern layer, derived from double layer theory, and similar estimates using other fluorescence probes. The observed variations in the surface polarity at the micelle–water interfaces in the presence of external additives are also consistent with predictions from other data. The formation of Schiff's base by reaction of pyrenecarboxaldehyde with amines has also been investigated. Data on absorption and emission spectra of Schiff's bases are presented.

Introduction

Micellar aggregates formed by ionic and nonionic detergents are being extensively investigated as model systems. They simulate more complex environmental conditions present in larger bioaggregates such as membranes.[2,3] Fluorescence probe studies[4] with molecules such as pyrene provide detailed information on permeability of micelles with respect to various quencher molecules such as oxygen. These studies may also be used to measure the extent of counterion binding to micellar surfaces. Complementary pulse radiolysis studies[5-9] of reactions of hydrated electrons (e_{aq}^-) with solutes solubilized selectively in the micellar core indicate the marked role played by the surface potential on the kinetics of these reactions. For example, while the rate of reaction of e_{aq}^- with pyrene in anionic sodium lauryl sulfate (NaLS) micelles is decreased 2000 times, compared to homogeneous solution, the rate is enhanced almost 200 times when pyrene is solubilized in cationic cetyltrimethylammonium bromide (CTAB) micelles. Earlier studies interpreted these "unusual" reaction rates of e_{aq}^- with solutes present in the micellar core in terms of double layer potential. At this stage, it is of general interest to directly measure the polarity of micelle–water interfaces, as a prelude to studies at membrane–water interfaces.

This work reports on the strong solvent-polarity dependence of pyrene-3-carboxaldehyde fluorescence which is used to directly measure the polarities of micelle–water interfaces. The present surface polarity measurements are compared with ζ potentials for the micellar Stern layer and data from other measurements.

Experimental Section

Steady-state fluorescence measurements were carried out on an Aminco-Bowman spectrophotofluorimeter. Lifetime studies were carried out utilizing 1.5-ns pulses of Cerenkov light obtained by pulse irradiating a quartz target with a 1.5-ns pulse of 2.3-MeV electrons. The Cerenkov pulses contain mainly UV light and are used to excite the sample. The subsequent luminescence from the irradiated sample was monitored with a rapid (<1-ns risetime) photoelectric monitoring technique.[10]

Pyrene-3-carboxaldehyde (Aldrich) was recrystallized several times from 95% ethanol. All surfactants were from commercial sources, e.g., from Eastman Chemicals, or Matheson Coleman and Bell, and were recrystallized from ethanol–ether mixtures before use. All solvents used were of the highest purity available (spectrograde or AR). Electrolytes NaCl, NaBr, as well as benzyl alcohol were AR grade from Baker Chemicals. The dielectric constant values for various pure solvents and solvent–water mixtures were taken from ref 11-15.

Results and Discussion

1. *Pyrene-3-carboxaldehyde Fluorescence in Homogeneous Solvents.* Excitation of dilute (<10⁻³ M) solutions of pyrene-3-carboxaldehyde, with light of wavelength 360 nm, leads to a blue-violet fluorescence. The fluorescence is due to the monomeric, excited singlet state and displays a strong solvent dependence. The solvent-polarity dependence for the monomer fluorescence is demonstrated in Figures 1 and 2, which show the variations in the fluorescence spectra in methanol–water and dioxane–water
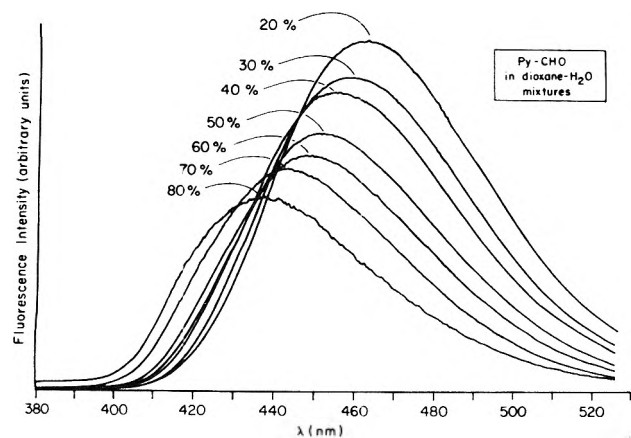
Figure 1. Solvent dependence of pyrene-3-carboxaldehyde in monomer fluorescence in various dioxane–water mixtures [PyCHO] = 10^{-5} M, λ_{exc} 356 nm, % dioxane given.
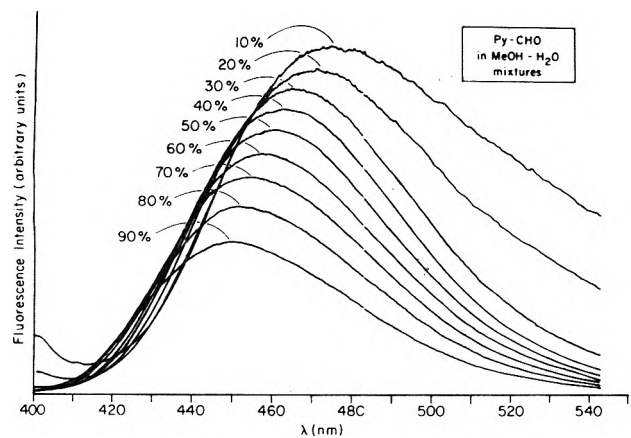
Figure 2. Solvent dependence of pyrene-3-carboxaldehyde monomer fluorescence in various methanol–water mixtures [PyCHO] = 10^{-5} M, λ_{exc} 356 nm, % dioxane given.

Figure 3. Variation of λ_{max}^{fluor} for pyrene-3-carboxaldehyde with solvent dielectric constant ϵ. (O) methanol–water mixtures; (□) ethanol–water mixtures; (∇) dioxane–water mixtures; (ϕ) pure solvents: ϵ (fluorescence maximum): chloroform 4.8 (421); chlorobenzene 5.6 (412); di-chlorobethane 8.9 (416); 1-hexanol 13.5 (440); 2-propanol 18 (438); 1-butanol 17.5 (441); 1-propanol 20.3 (442); ethylene glycol 38 (456); glycerol 43 (456).
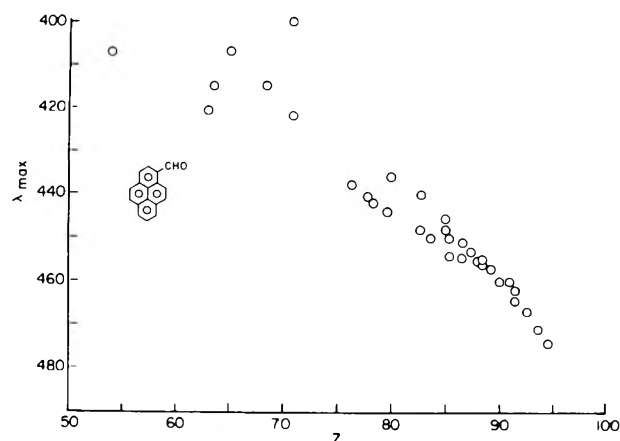
Figure 4. Variation of λ_{max}^{fluor} for pyrene-3-carboxaldehyde with Kosower's Z value for the solvent medium.

TABLE I: Fluorescence Parameters for Pyrene-3-carboxaldehyde

Solvent system	Fluor max, nm	Q yield[a]	τ_f, ns
CH_3OH (100%)	450	0.15	1.95
CH_3OH (80%)	453	0.51	3.20
CH_3OH (50%)	460	0.69	4.00
n-PrOH (100%)	442		1.90
0.02 M CTAC	441		1.80
0.05 M NaLS	455		2.73
Ethylene glycol	454		3.47

[a] Reference 20.

mixtures, respectively. The fluorescence maxima of these curves, along with those in 20 other different pure solvents and in various ethanol–water mixtures, are plotted against the dielectric constant of the solvent medium in Figure 3. It is clearly seen that the fluorescence maxima show a red shift with increased solvent polarity. When the dielectric constant of the solvent medium exceeds ca. 10, the fluorescence maxima shift linearly to longer wavelengths, with increasing dielectric constant ϵ. The fluorescence maxima observed in pure solvents as well as those in different water mixtures of methanol, dioxane, and ethanol all fall on the same line. This indicates that the spectral shifts are due to some bulk properties of the solvent medium and not due to any specific solvent–solute interactions. Representative data on the fluorescence lifetimes for pyrene-3-carboxaldehyde in different solvent media are summarized in Table I. Various solvent polarity scales, such as dielectric constant (ϵ), Grunwald parameter [$(\epsilon - 1)/(2\epsilon + 1)$], Kosower's Z value, and Dimroth's parameter $E_T(30)$ value, have been suggested in the literature to describe solvent polarity on a microscopic scale.[16] Figure 4 presents a correlation of λ_{max}^{fluor} for pyrene-3-carboxaldehyde against the most commonly used polarity scale, viz., Kosower's Z-value. The correlation is as good as that reported for other solvent dependent fluorescence probes such as N-phenylnaphthylamine (NPN)[17] and anilino-naphthalenesulfonates (ANS).[16,18,19]

Almost a decade ago, Brederick et al.[20] reported on the solvent-dependent fluorescence behavior of aromatic aldehydes, including pyrene-3-carboxaldehyde. In nonpolar solvents such as n-heptane, the fluorescence spectrum of pyrene-3-carboxaldehyde is structured with peaks around 400–420 nm, and the quantum yield [$\phi_F < 0.001$] is small. This particular fluorescence is due to an n–π^* transition. However, on increasing the polarity of the solvent media, the π–π^* level which lies close to the n–π^* level is brought below the n–π^* level by solvent relaxation during the lifetime of the excited state. Thus in polar solvents the π–π^* state becomes the fluorescence emitting state. The present study clearly demonstrates a linear variation in the red shift of the λ_{max} for the monomer fluorescence with the solvent dielectric constant ϵ. This occurs as soon as the π–π^* level is brought below the n–π^* state so that the emitting state is of π–π^* character. Presumably a solvent environment with dielectric constant ca. 10 is required to

TABLE II: Estimates on the Polarity at Micelle–Water Interfaces

Micellar system[a]	PyCHO fluor λ_max, nm	PyCHO fluor ε	ζ, mV	Z	PhCOPh abstn[b] $E_T(30)$, kcal/mol	Z	CEPI abstn λ_max, nm	Z	ANS fluor[c] ε	ANS fluor[c] Z
					Anionic					
NaOS (0.3 M)	457	49								
NaLS (0.05 M)	455	45	150	88	58.0	88	350	82	25	82 (TNS)
NaCS (0.02 M)	454	43								
NaL (0.05 M)	452	39								
					Cationic					
DeTAB (0.1 M)	446	28								
DAC (0.1 M)	445	26	125	83						
DTAC (0.1 M)	444	24								
CTAC (0.02 M)	441	18								
CTAB (0.02 M)	440	16	75	80	51.5	79	361	79	36	8515 (1:7 ANS)
									37	85 (DNSA)
CPyC (0.02 M)	444	24	110	82						
					Nonionic					
Triton X-100 (4 mM)	387/412	15		66	42.5	66	366	78	35	85.5 (1:7 ANS)
Igepal CO-630 (4 mM)	389/409	12		66			366	78	35	85.0 (1:8 ANS)
					NaLS + Additives					
NaLS (0.05 M)	455	45	150							
NaLS + 0.2 M NaCl	450	35	120							
NaLS + 4% BzOH	457	49								
NaLS + 6% BzOH	458	51								

[a] NaOS = sodium octyl sulfate; NaLS = sodium lauryl sulfate; NaCS = sodium cetyl sulfate; NaL = sodium laurate; DeTAB = decyltrimethylammonium bromide; DAC = dodecylammonium chloride; CTAB = cetyltrimethylammonium chloride.   [b] Data from PhCOPh taken from Fendler et al.[22]   [c] Data for ANS derivatives taken from Gitler and Cordes,[35] and Shinitzky.[34]

equalize the n–π* and π–π* levels. Bredereck et al., in the reference cited above, present some evidence favoring such a mechanism. In a future report we hope to address ourselves in detail to the exact photophysics involved in this strong solvent dependence. Our goal, as far as this work is concerned, is to demonstrate the usefulness of the linear dependence of pyrene-3-carboxaldehyde fluorescence with solvent polarity as a fluorescence probe in the study of aggregated and other biological macromolecular systems. As pyrene-3-carboxaldehyde is not charged, perturbations of the experimental systems by specific electrostatic charge interactions are expected to be minimal. The next section discusses data on the application of this fluorescence probe in studying micellar assemblies. In passing, we would like to mention that pyrene-3-carboxaldehyde, like pyrene and its other derivatives, also forms excimers at high probe concentrations. While the excimer fluorescence maximum is at 530 nm in nonpolar solvents, it is red shifted to about 560 nm in polar solvents.[21]

2. *Pyrene-3-carboxaldehyde Fluorescence in Micellar Media*. Long chain amphiphilic molecules such as sodium lauryl sulfate (NaLS) and cetyltrimethylammonium bromide (CTAB), in aqueous solutions, above a certain critical concentration, form micellar aggregates. These micelles solubilize a wide variety of hydrophobic and hydrophilic substances.[3] Depending on their molecular structure, the solubilized molecules tend to reside, on an average, either at the micellar interior core or at the micellar surface. For example, NMR and UV spectral studies[3,22-24] have shown that aromatic compounds with hydrophilic groups such as aromatic aldehydes, ketones, and alcohols are solubilized with the their hydrophobic (aromatic) moiety in the micellar core and with the hydrophilic groups protruding into *or* anchored at the micellar surface or double layer. Proton NMR studies similar to those described by Gratzel et al.,[23] and by Erikkson and Gillberg,[24] have confirmed such a mode of solubilization for PyCHO. Monomeric surfactants do not interact with

PyCHO as indicated by the similarity of the fluorescence spectrum of PyCHO in surfactant solutions below the critical micelle concentration cmc to that in pure water.

Table II summarizes representative data for λ_{max}^{fluor} of pyrene-3-carboxaldehyde fluorescence in different cationic, anionic, and nonionic micellar solutions. The dielectric constant estimates for the environment of the probe, from the corresponding fluorescence maxima, read from the plot shown in Figure 3, are also included in this table. For comparison this table also includes similar estimates from the literature for the polarity of micelle–water interfaces: (i) ζ potentials for the Stern layer of the micelle, derived from combined electrophonetic mobility measurements and from solutions of nonlinear Poisson–Boltzmann equation;[5-9,25-33] (ii) Kosower's Z value estimates for the micelle–water interfaces determined with various probes by UV spectral studies.[22,34,35]

The data summarized in Table II provide a direct measure of the polarity of the micelle–water interface region. For a given hydrocarbon chain length, the surface polarity increases on going from anionic to cationic to nonionic micelles. As expected, the polarity is dependent on the nature of the head group. A direct comparison is made with data for three representative micellar systems, NaLS (anionic), CTAB (cationic), and Triton X-100 (nonionic). The data presented in the table show excellent agreement between the pyrene-3-carboxaldehyde estimates with similar data based on benzophenone UV absorption maxima correlations of Fendler et al. (1975) and also with the ζ potential estimates[25-30] for the Stern layer of the micelle. However, the agreement of the pyrene-3-carboxaldehyde values with Z value estimates using *charged* probes such as those based on fluorescence of ANS or UV absorption maxima of 4-carbomethoxypyridinium iodide (CEPI) is poor. It is well known[36] that the charged probes, viz. ANS, interact strongly with monomeric surfactants. Strong Coulombic interactions of these probes with the charged head groups are expected. Hence, surface

polarity estimates based on these charged probes are not expected to be accurate. For the above-mentioned reason, Mast and Haynes[37] recently could not use ANS as a probe to accurately determine critical micelle concentrations (cmc) of charged (cationic and anionic) micelles.

Further evidence to show that the fluorescence maximum of pyrene-3-carboxaldehyde does measure the polarity of the micelle–water interface region may be obtained from studies of the effect of added salts. Addition of 0.2 M NaCl to 0.05 M micellar solutions of NaLS shifts the PyCHO fluorescence maximum from 455 to 450 nm. This indicates a reduction in the surface charges caused by the binding of Na$^+$ ions at the micellar surface. Solutions of nonlinear Poisson–Boltzmann equation also predict a drop in the surface potential at the Stern layer of the micelle by about 30 mV for an increase in the ionic strength of the medium by 0.2. In the presence of electrolytes, the range of the Gouy–Chapman layer drops from about 25 Å in salt-free solution to less than 10 Å at an ionic strength of 0.1 M. Corresponding experiments show that addition of substances such as benzyl alcohol which disrupt the head group structures, thereby reducing the extent of counterions binding, also produce a red shift in the fluorescence maxima of pyrene-3-carboxaldehyde. In the presence of 6% benzyl alcohol, the effective dielectric constant for the micelle–water interface is about 51 as compared to 45 for the benzyl alcohol-free micellar solutions. These studies are being extended to study the nature of the head group structure of phospholipid dispersions and their modulations in the presence of external additives.

The polarity measured by PyCHO agrees well with other measurements for the Stern layer of the micelle. The main effect of solvation of PyCHO will be in the region of the aldehyde group and hence it is reasonable to suggest that the probe samples the environment, i.e., Stern layer, over a span of about 3 Å. The decreased dielectric constant of the micellar surface compared to that of both water is due to the restrictive effect of the micellar surface charge on water molecules in the Stern layer. Addition of sodium chloride introduces more sodium ions into the Stern layer resulting in further construction of water molecules by these ions. A decrease in the microscopic dielectric constant is observed. On the other hand addition of benzyl alcohol causes disruption of the Stern layer, an increase in the mobility of the water molecules, and an increase in the microscopic dielectric constant. The picture drawn is simplified at this stage, and subsequent measurements will try to ascertain any positional changes of PyCHO in the micellar surface on addition of solvents.

3. *Formation of Schiff Bases.* In the presence of primary and secondary amines, pyrene-3-carboxaldehyde forms Schiff's bases, according to the equation:

$$
\underset{H}{\overset{O}{\underset{\backslash}{\overset{\parallel}{PyC}}}} + RNH_2 \rightleftharpoons \underset{H}{\overset{}{PyC=NHR}}
$$
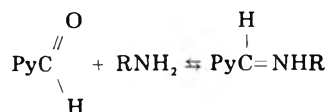
These Schiff's bases have characteristic UV absorption and fluorescence spectra. Figure 5 shows the fluorescence spectrum of pyrene-3-carboxaldehyde when it is solubilized near the surface of the cationic micelle dodecylammonium chloride. The fluorescence spectrum has two maxima, one at λ 445 nm, arising from the normal pyrenecarboxaldehyde fluorescence, and an additional band at λ 498 nm. The additional band is reminescent of the "exciplex" emission from excited complexes of pyrene. However, as will be shown later, the UV absorption spectrum of the system undergoes significant changes suggesting that the
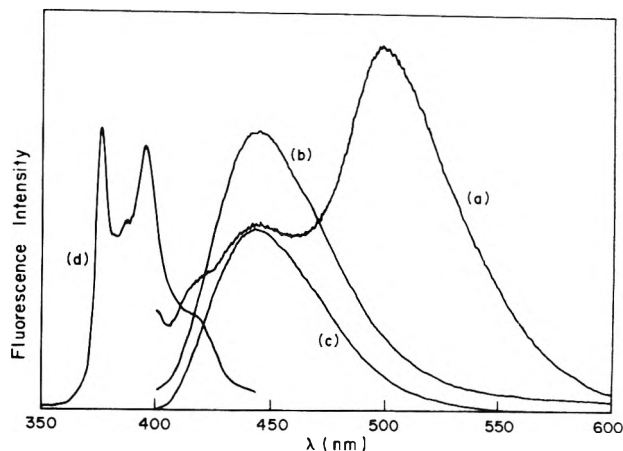
Figure 5. Fluorescence of pyrene-3-carboxaldehyde in (a) 0.1 M dodecylammonium chloride (DAC) in water; (b) 0.1 M DAC with 10^{-3} M HCl added; (c) 0.1 M dodecyltrimethylammonium chloride (DTAC) in water; (d) 0.1 M DAC after reduction with LiAlH$_4$.

emission is from the Schiff's base and not from the amine exciplexes. The high electric charge at the surface of the micelle leads to significant dissociation of the amine hydrochloride and the Schiff's base is formed from the free –NH$_2$ groups of micellar dodecylammonium chloride. Further confirmation of this hypothesis comes from the behavior of the fluorescence when additional acid is added to the system. On addition of 10^{-3} M HCl to the micellar solution, the equilibrium between the amine and the amine salt is moved further toward the amine salt:

$$RNH_2 \cdot HCl \rightleftharpoons R \cdot NH_2 + HCl$$
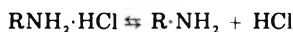
The effect is such that the fluorescence of the Schiff's base disappears completely, leaving the normal fluorescence of pyrene-3-carboxaldehyde, Figure 5b. In micelles formed by dodecyltrimethylammonium chloride (DTAC), the head group –NH$_3$Cl is replaced by N(CH$_3$)$_3$Cl and free amine groups are not present. In these systems only the fluorescence of PyCHO is detected (cf. Figure 5c).

The Schiff's base is efficiently reduced in situ in reducing agents such as LiAlH$_4$ to form the corresponding substituted amines (R'CH$_2$NHR). Figure 5d shows the fluorescence spectrum of the substituted amine formed by LiAlH$_4$ reduction of the Schiff's base. This fluorescence spectrum is characteristic of a pyrene chromophore in monosubstituted pyrenes such as methylpyrene. The assignment of the fluorescence with maximum at 498 nm to Schiff's base has also been confirmed by the observation that a similar fluorescence is exhibited by simple alkyl amines such as dodecylamine on forming a Schiff's base with pyrene-3-carboxaldehyde in methanol.

The UV absorption spectrum of PyCHO is also quite sensitive to the polarity of the solvent medium and to the presence of Schiff's base (Figure 6). In hydrocarbon solvents viz. n-hexane (Figure 6a), the UV absorption spectrum has well-resolved bands with maxima at 391, 372, and 363 nm together with a shoulder around 345 nm. In polar solvents viz. methanol (Figure 6) the spectrum becomes diffused and broad. In the presence of Schiff's bases (Figure 6c) as found in dodecylammonium chloride micelles, the UV absorption undergoes distinctive changes. The most intense peak is now at 363 nm with a significant drop in the UV absorption around 387 nm. The UV absorption in micellar systems is very similar to the Schiff's base absorption formed by simple amines such as dodecylamine and pyrene-3-carboxaldehyde in methanol. The efficient formation of Schiff's bases of pyrene-3-carboxaldehyde is being used to bind the pyrene chromophore
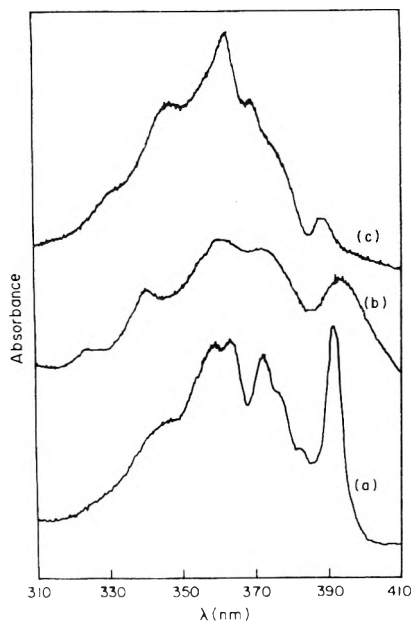
Figure 6. Absorption spectrum of pyrene-3-carboxaldehyde in (a) n-hexane; (b) methanol; (c) in 0.1 M DAC.

to amine groups in bioaggregates such as membranes.

References and Notes

(1) The Radiation Laboratory of the University of Notre Dame is operated under contract with the U.S. Energy Research and Development Administration. This is Document No. NDRL-1710.

(2) C. Tanford, "The Hydrophobic Effect: Formation of Micelles and Biological Membranes", Wiley, New York, N.Y., 1973.

(3) J. H. Fendler and E. J. Fendler, "Catalysis in Micellar and Macromolecular Systems", Academic Press, New York, N.Y., 1975.

(4) M. Gratzel and J. K. Thomas, in "Modern Fluorescence Spectroscopy", Vol. 2, E. L. Wehry, Ed., Plenum Press, New York, N.Y., 1976 p 169.

(5) S. C. Wallace and J. K. Thomas, Radiat. Res., 54, 43 (1973).

(6) M. Gratzel, J. K. Thomas, and L. K. Patterson, Chem. Phys. Lett., 29, 393 (1974).

(7) M. Gratzel, J. J. Kozak, and J. K. Thomas, J. Chem. Phys., 62, 1632 (1975).

(8) M. Gratzel and J. K. Thomas, J. Phys. Chem., 78, 2248 (1974).

(9) L. K. Patterson and M. Gratzel, J. Phys. Chem., 79, 956 (1975).

(10) M. Wong, J. K. Thomas, and M. Gratzel, J. Am. Chem. Soc., 98, 2391 (1976).

(11) R. L. Scheineider, Eastman Org. Chem. Bull., 47, 1 (1973).

(12) R. C. Weast, Ed., "Handbook of Chemistry and Physics", Chemical Rubber Co., Cleveland, Ohio, 1973.

(13) D. C. Turner and L. Brand, Biochemistry, 7, 3381 (1968).

(14) Landolt-Bornstein, Zehlenwerte und funketionen, II Band, 6 Teil, Electrische Eigenschaften I, Springer-Verlag, Berlin, 1959.

(15) C. A. Kerlof and D. A. Short, J. Am. Chem. Soc., 58, 1241 (1936).

(16) E. M. Kosower, "An Introduction to Physical Organic Chemistry", Wiley, New York, N.Y., 1968.

(17) H. Trauble and P. Overath, Biochem. Biophys. Acta, 307, 491 (1973).

(18) C. J. Seliskar and L. Brand, J. Am. Chem. Soc., 93, 5405 (1971).

(19) C. J. Seliskar and L. Brand, J. Am. Chem. Soc., 93, 5414 (1971).

(20) K. Bredereck, Th. Forster, and H. G. Oenstein in "Luminescence of Organic and Inorganic Materials", H. P. Kallman and G. M. Spruch, Ed., Wiley, New York, N.Y., 1960.

(21) P. Kroning, Z. Naturforsch. A, 28, 109 (1973).

(22) J. H. Fendler, E. J. Fendler, G. A. Infante, P. S. Shih, and L. K. Patterson, J. Am. Chem Soc., 97, 89 (1975).

(23) M. Gratzel, K. Kalyanasundaram, and J. K. Thomas, J. Am. Chem. Soc., 96, 7869 (1974).

(24) J. C. Erikkson and G. Gillberg, Acta Chem. Scand., 20, 2019 (1966).

(25) D. Stigter, J. Phys. Chem., 68, 3603 (1964).

(26) D. Stigter, J. Colloid Interface Sci., 23, 379 (1967).

(27) D. Stigter, J. Colloid Interface Sci., 47, 473 (1974).

(28) D. Stigter, J. Phys. Chem., 78, 2480 (1974).

(29) D. Stigter, J. Phys. Chem., 78, 2480 (1974).

(30) D. Stigter, J. Phys. Chem., 79, 1015 (1975).

(31) S. L. Brenner and R. E. Roberts, J. Phys. Chem., 77, 2367 (1973).

(32) A. L. Loeb, J. Th. G. Overbeek, and S. H. Wiersema, "The Electrical Double Layer Around a Colloidal Particle", M.I.T. Press, Cambridge, Mass., 1961.

(33) M. F. Emerson and A. Holtzer, J. Phys. Chem., 71, 1898 (1967).

(34) M. Shinitzky, Isr. J. Chem., 13, 879 (1974).

(35) C. Gitler and E. H. Cordes, Prog. Bioorg. Chem., 2, 1 (1973).

(36) R. R. Hautala, N. E. Schore, and N. J. Turro, J. Am. Chem. Soc., 95, 5508 (1973).

(37) R. C. Mast and L. V. Haynes, J. Colloid Interface Sci., 53, 35 (1975).

Antenna Chlorophyll a and P700. Exciton Transitions in Chlorophyll a Arrays[1]

Lester L. Shipman

Chemistry Division, Argonne National Laboratory, Argonne, Illinois 60439 (Received April 6, 1577)

Exciton calculations have been carried out for 16 distinct cases of randomly generated chlorophyll a arrays to assist in the assessment of various possibilities for the chlorophyll distribution in the thylakoid membrane of green plants. Each of the cases is distinguished by its packing density and by the constraints applied to the orientation of transition dipoles. Each array consists of 40 antenna chlorophyll a molecules with an absorption maximum at 670 nm before transition density coupling and one P700 chromophore with an absorption maximum at 700 nm. Transition density coupling always broadens the absorption bands and sometimes shifts the position of the absorption maxima. Transition density coupling between the P700 chromophore and the antenna chlorophyll molecules shifts the P700 absorption band to lower energies and, for some cases, increases or decreases the dipole strength of the P700 absorption band by as much as 50%. In general, for comparable packing densities, the effects of transition density coupling are more pronounced for two-dimensional arrays than for three-dimensional arrays. The present exciton calculations show that if the various in vivo "forms" of chlorophyll a correspond to exciton transitions in chlorophyll a arrays, then the local chlorophyll concentration in the arrays must be much greater than the average chlorophyll concentration of ~0.1 M in the thylakoid membrane; perhaps the local chlorophyll concentration could be as high as 1 M.

I. Introduction

The primary events of photosynthesis[2-4] in green plants and photosynthetic bacteria are generally considered to take place within photosynthetic units.[5-7] The primary events may be considered to begin with the absorption of

a photon into the antenna pigments and end with a photoinduced electron transfer from a special pair[8,9] of chlorophyll (Chl) molecules to the primary electron acceptor. The vast majority of the Chl molecules in the photosynthetic unit have a light-harvesting function and

are appropriately called antenna Chl. Only a small fraction of the Chl molecules are present in the form of special pairs in the photoreaction centers. The functions of antenna Chl are (a) to present a large cross section for absorption of that portion of the solar emission spectrum that arrives at the locale of the organism, and (b) to transfer the electronic excitation energy to the reaction center at a rate so fast that competing processes such as fluorescence, intersystem crossing, internal conversion, and antenna singlet photochemistry cannot compete favorably. In practice, this means that the rate of electronic excitation energy transfer from antenna to reaction center must be as fast as $\sim 2 \times 10^{10}$ s^{-1} if the antenna is composed of separated Chl molecules and as fast as $\sim 5 \times 10^{11}$ s^{-1} if the antenna is composed of nonfluorescent Chl dimers and oligomers. Thus, the transfer rate requirement for antenna design is more severe for a chlorophyll oligomer, $(Chl)_n$, model for the antenna than for a separated Chl model. In this regard, Duysens[10] has suggested that "binding between the pigments and some cell constituents keeps the pigment molecules separated, in this way preventing the formation of nonfluorescent dimers or polymers".

The detailed nature of the local molecular environment of the Chl molecules in the photosynthetic membrane has long been the subject of speculation and study.[11] The environment has variously been proposed as the polar head region of the lipid bilayer, the nonpolar hydrocarbon region of the lipid bilayer, the interior of membrane–bound globular protein, and the lipid–protein interface. Fenna and Matthews[12-14] have recently determined the positions and orientations of seven bacteriochlorophyll a molecules in a bacteriochlorophyll a–protein subunit. The seven bacteriochlorophyll a molecules are contained within an ellipsoid of dimensions $35 \times 45 \times 15$ Å;[12] thus the area density of the bacteriochlorophyll a molecules in the 35×45 Å ellipse when viewed down the short (15 Å) axis is ~ 177 (Å)^2/molecule. There is convincing evidence that the photoreaction centers are Chl–protein complexes. For example, Reed and Clayton[15] isolated a bacteriochlorophyll a and bacteriopheophytin a containing Chl–protein complex that subsequent characterization studies have shown to have the spectroscopic properties of the in vivo reaction centers in purple photosynthetic bacteria. For green plants, a chlorophyll a (Chl a)–protein complex containing the photoreactive Chl a chromophore (P700) plus ~ 40 antenna Chl a molecules has been isolated.[16]

It is widely believed that the majority of the antenna Chl a (Figure 1) molecules in the photosynthetic membrane are complexed to protein.[17] The strongest evidence that antenna Chl molecules are located in Chl–protein complexes in vivo is that the antenna chlorophylls are obtained in several such complexes after fractionation of detergent-solubilized photosynthetic membranes; furthermore, mutants have been found which lack one or the other of these complexes, and in each case the effects of the mutation correspond to the effects that would be predicted on the basis of the absence of one of the complexes. Antenna Chl is most often studied by its absorption spectrum in the region of the $S_0 \rightarrow S_1$ (Q_y) transition because in this red region of the absorption spectrum of the photosynthetic membranes, only Chl absorbs to any great extent. Various "forms" of antenna Chl have been identified by Gaussian deconvolution of the Q_y band or by examination of the fourth derivative of the Q_y band of in vivo Chl. At room temperature, the major Chl a "forms" have $Q_y(0, 0)$ maxima at ~ 670 and ~ 682 nm.[18-20] At 77 K the major antenna Chl a "forms" have $Q_y(0, 0)$ maxima at ~ 662, ~ 670, ~ 677, and ~ 683 nm.[19,21,22] It has not been
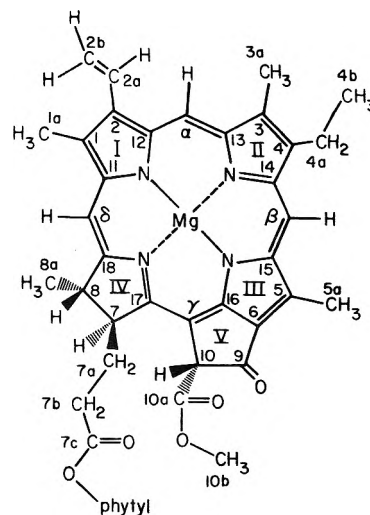
Figure 1. Molecular structure and atomic numbering system for chlorophyll a (Chl a).

conclusively determined if the "forms" of antenna Chl a correspond to (i) monomeric Chl a in distinct molecular environments, (ii) Chl a in differing states of aggregation (oligomers, monolayers, etc.), (iii) exciton transitions due to the interaction of the transition densities on closely spaced Chl a molecules, or (iv) all of the above.

The absorption maximum of the $Q_y(0, 0)$ peak of antenna Chl a in vivo is at ~ 678 nm.[22] One possibility to consider for this red shift relative to monomeric Chl a in vitro (λ_{max} 659–670 nm[20,23,24]) is that the red shift is due to the interaction of Chl a with the amide units of proteins. This possibility is, however, unlikely in view of the in vitro evidence that Chl a in dimethylformamide has a λ_{max} of 664 nm[23] and Chl a·formamide in CCl$_4$ has a λ_{max} of 663 nm.[25]

It is generally believed that the overall Chl concentration in the photosynthetic membrane is in the 0.1–0.2 M range. Because the Chl distribution need not be uniform, it is of interest to consider the possibility that the local Chl concentration may be much higher than 0.1 M. In this regard, the local Bchl a concentration is 0.94 M within the $35 \times 45 \times 15$ Å ellipsoid containing seven Bchl a molecules in the Fenna and Matthews x-ray crystal structure of a Bchl a–protein complex.[12-14] In addition, the ethyl chlorophyllide a concentration in the x-ray crystal structure of ethyl chlorophyllide a·2H$_2$O[26] is 1.9 M and this number serves as an upper bound for the range of concentrations to be considered for in vivo Chl. Similarly, the packing density in the chlorophyllide sheets (ab crystal plane) in the ethyl chlorophyllide a·2H$_2$O[26] crystal is 68.0 Å^2/molecule and this number serves as a lower bound for the area per molecule for two-dimensional packing of in vivo chlorophyll.

In the present study, environmentally nondegenerate exciton theory[27] has been used to calculate the exciton transitions for 16 distinct cases of two- and three-dimensional Chl a arrays. These calculations have provided a basis for consideration of the possibility that the various Chl a "forms" observed in vivo are actually exciton transitions of Chl a arrays. In addition, the effects of the absorption spectrum from transition density coupling between the antenna Chl a molecules and the P700 reaction center chromophore have been computed.

II. Exciton Theory

The exciton formalism used in these calculations was derived especially for Chl aggregates and includes environmental shifts as well as transition density shifts of

TABLE I: Chlorophyll Arrays

Case no.	X_{max}[a]	Y_{max}[a]	Z_{max}[a]	Transition dipole orientation	Figure	μ^2(P700) μ^2(monomer)
1	88.0	88.0	88.0	Spherically random	2A	1.99
2	88.0	88.0	88.0	Circularly random in (x, y) plane	2B	1.98
3	88.0	88.0	88.0	All aligned in x direction	2C	2.00
4	40.8	40.8	40.8	Spherically random	3A	1.92
5	40.8	40.8	40.8	Circularly random in (x, y) plane	3B	1.88
6	40.8	40.8	40.8	All aligned in x direction	3C	1.81
7	229.0	229.0	0	Spherically random	4A	2.00
8	229.0	229.0	0	Circularly random in (x, z) plane	4B	1.97
9	229.0	229.0	0	Circularly random in (x, y) plane	4C	2.05
10	229.0	229.0	0	All aligned in z direction	4D	1.77
11	229.0	229.0	0	All aligned in x direction	4E	2.10
12	72.4	72.4	0	Spherically random	5A	1.97
13	72.4	72.4	0	Circularly random in (x, z) plane	5B	1.85
14	72.4	72.4	0	Circularly random in (x, y) plane	5C	2.37
15	72.4	72.4	0	All aligned in z direction	5D	0.83
16	72.4	72.4	0	All aligned in x direction	5E	2.97

[a] Units are Å.

transition energies. Since this formalism as well as its limitations have been described in detail elsewhere,[27] it will be described only briefly here; the notation of ref 27 will be used. An H'' matrix is constructed whose diagonal elements, H''_{ii}, are the transition energies of the molecules in their molecular environments without transition density coupling of the transitions on different molecules. An off-diagonal element, H''_{ij}, of H'' is the transition density-transition density interaction energy between the transition density on molecule i and the transition density on molecule j. Diagonalization of H'' gives the exciton transition energies (eigenvalues of H'') and the transition moments of the exciton transitions (computed from the eigenvectors of H'' and the transition dipoles on the individual molecules). The transition density-transition density interaction energies have been approximated as the interaction between a point transition dipole on molecule i and a point transition dipole on molecule j. Only the $Q_y(0, 0)$ transition (0-0 vibronic band of the $S_0 \rightarrow S_1$ electronic transition) has been included in the calculations. The exciton calculations have been carried out under the assumption that the individual vibronic bands of the monomers couple independently; this is called weak coupling. The dipole strength of the $Q_y(0, 0)$ band was taken to be 16.8 D^2 [24] for the antenna Chl a molecules and 33.6 D^2 for the P700 chromophore which has been proposed to be a special pair of Chl a molecules with their Q_y transition moments aligned parallel.[9] The diagonal elements, H''_{ii}, were set at 14 925 cm^{-1} (670 nm) for the antenna Chl a molecules and 14 286 cm^{-1} (700 nm) for the P700 chromophore. Photosynthetic membranes are composed primarily of lipid bilayers with embedded intrinsic proteins. Thus, the natural choices for the position of the $Q_y(0, 0)$ absorption maximum of monomeric Chl a in vivo are either 663-664 nm, the position of the absorption maximum in an amide solvent,[23,25] or 670 nm, the position of the absorption maximum in lipid vesicles and multilayers.[28-31] For all of the calculations reported herein, the 670-nm value has been used.

III. Chlorophyll a Arrays

Exciton calculations were carried out for 16 distinct cases of square and cubical Chl a arrays. Each of the arrays consisted of 40 antenna Chl a molecules and one P700 chromophore, which is the composition of the P700 Chl a-protein complex reported by Thornber et al.[16] The six degrees of freedom per molecule were the Cartesian position coordinates of the point transition dipole (X, Y, Z) and the Cartesian components which define the direction and magnitude of the point transition dipole (μ_x, μ_y, μ_z). The 16 cases differ as to the constraints applied to these six degrees of freedom in the generation of arrays. A complete description of the 16 cases is given in Table I. The sizes of the cubic arrays were chosen such that the Chl a concentration was 0.1 M (cases 1-3; 88.0 × 88.0 × 88.0 Å) or 1 M (cases 4-6; 40.8 × 40.8 × 40.8 Å). Similarly, the square arrays were selected such that if the thickness of the layer was 13 Å (the thickness of the layers in the crystal of ethyl chlorophyllide a·2H$_2$O[26]), then the Chl a concentration would be either 0.1 M (cases 7-11; 229.0 × 229.0 × 0.0 Å) or 1 M (cases 12-16; 72.4 × 72.4 × 0.0 Å). In the cubic arrays the transition dipoles were randomly oriented (cases 1 and 4), constrained to lie in the XY plane (cases 2 and 5), or were constrained to lie along the X direction (cases 3 and 6). For the square arrays, the transition dipoles were randomly oriented (cases 7 and 12), constrained to lie in the XZ plane (cases 8 and 13), constrained to lie in the XY plane (cases 9 and 14), constrained to lie along the Z direction (cases 10 and 15), or constrained to lie along the X direction (cases 11 and 16). For those cases where a Cartesian position coordinate $(X, Y, $ or $Z)$ of a point dipole was not constrained to be 0 Å, it was generated by computing a random number between 0 and a maximum value $(X_{max}, Y_{max}, $ or $Z_{max})$ as given in Table I. When a point dipole was randomly generated less than 8.5 Å from a previously generated point dipole, it was rejected and another dipole generated.

IV. Summation of Spectra

For each of the 16 cases described in section III and Table I, 1000 arrays of the 41 point dipoles were generated. For purposes of displaying the average spectra, the dipole strengths of the exciton transitions from all 1000 arrays were summed over 1-nm intervals. For example, the dipole strengths of all exciton transitions that fell between 669.5 and 670.5 nm have been summed and represented by a vertical line at 670 nm whose height is directly proportional to the summed dipole strength. The spectra computed for all 16 cases are displayed in this manner in Figures 2-5. It should be noted that the spectra displayed in Figures 2-5 do not contain contributions from vibrational broadening and therefore the positions of their maxima, but not their shapes, may be compared to experimental spectra.

V. Discussion of Computed Spectra

The transition density coupling among the antenna Chl a states and the transition density coupling between the
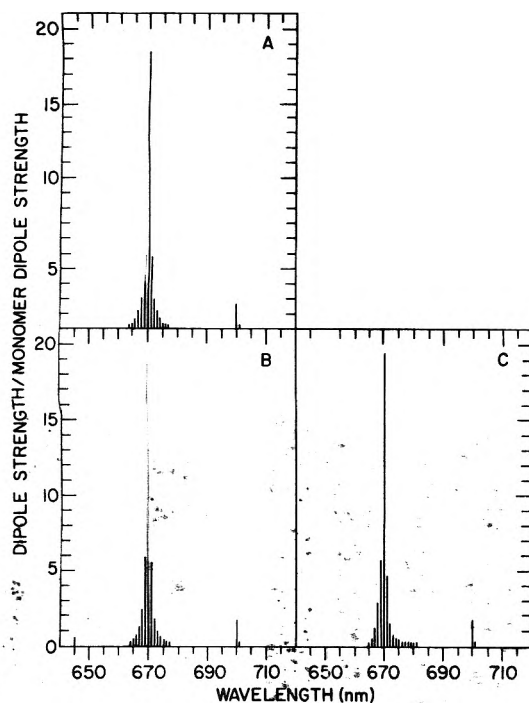
Figure 2. $Q_y(0, 0)$ exciton spectra for 88 × 88 × 88 Å cubic Chl a arrays: (A) case 1, (μ_x, μ_y, μ_z); (B) case 2, $(\mu_x, \mu_y, 0)$; case 3, $(\mu_x, 0, 0)$.

Figure 4. $Q_y(0, 0)$ exciton spectra for 229 × 229 × 0 Å square Chl a arrays: (A) case 7, (μ_x, μ_y, μ_z); (B) case 8, $(\mu_x, 0, \mu_z)$; (C) case 9, $(\mu_x, \mu_y, 0)$; (D) case 10, $(0, 0, \mu_z)$, (E) case 11, $(\mu_x, 0, 0)$.

Figure 3. $Q_y(0, 0)$ exciton spectra for 40.8 × 40.8 × 40.8 Å cubic Chl a arrays: (A) case 4, (μ_x, μ_y, μ_z); (B) case 5, $(\mu_x, \mu_y, 0)$; (C) case 6, $(\mu_x, 0, 0)$.
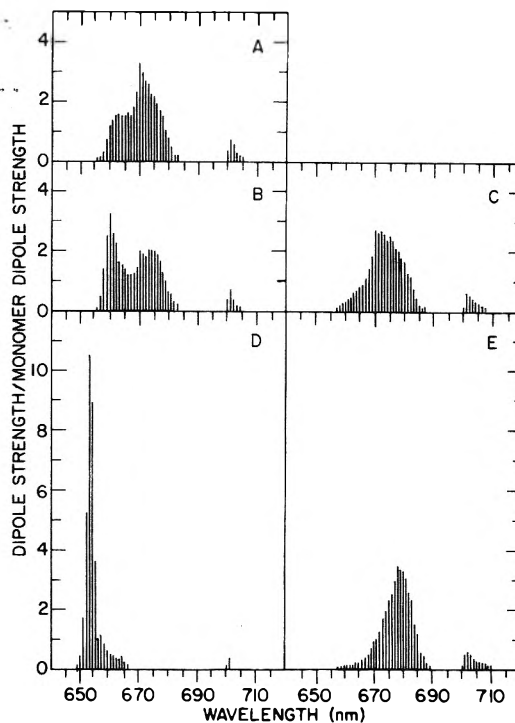
Figure 5. $Q_y(0, 0)$ exciton spectra for 72.4 × 72.4 × 0 Å square Chl a arrays: (A) case 12, (μ_x, μ_y, μ_z); (B) case 13, $(\mu_x, 0, \mu_z)$; (C) case 14, $(\mu_x, \mu_y, 0)$; (D) case 15, $(0, 0, \mu_z)$; (E) case 16, $(\mu_x, 0, 0)$.

antenna Chl a states and the P700 chromophore have significant effects upon the distribution of $Q_y(0, 0)$ exciton transitions. These effects include (a) broadening of the antenna absorption band (all cases), (b) broadening of the P700 band (cases 4–6, 12–16), (c) transfer of dipole strength from the antenna to increase the dipole strength of the P700 band by over 10% (cases 14 and 15), (d) transfer of over 10% of the dipole strength of the P700 band to the antenna band (cases 10 and 15), (e) shift of the P700 band to lower energy (cases 4–6, 12–16), (f) splitting of the

antenna absorption band into two peaks (case 13), and (g) shift of the maximum of the antenna Chl a band from its unperturbed position at 670 to 669 nm (case 10), 600 and 674 nm (case 13), 653 nm (case 15), and 678 nm (case 16).

VI. Conclusions

Among the effects of transition density coupling in Chl a arrays on the absorption spectrum are broadening of absorption bands, exchange of dipole strength between absorption bands, and shifting and sometimes even splitting of bands. The calculations reported herein indicate that, for comparable Chl a packing densities, the effects of transition density coupling are larger for square

arrays than for cubic arrays. At the highest packing density (128 Å²/molecule) studied for square arrays, the effects of transition density coupling are especially noticeable. In particular, spectrum 5C shows that if the transition moments are randomly oriented, but constrained to lie in the plane, $(\mu_x, \mu_y, 0)$, then there is a net red shift of the $Q_y(0, 0)$ band of antenna Chl a. On the other hand, if all the transition moments are pointing perpendicular to the plane, then there is a strong blue shift to 653 nm (spectrum 5D). Finally, if the transition dipoles all point in the same direction in the plane, $(\mu_x, 0, 0)$, then there is a strong red shift to 678 nm (spectrum 5E).

Transition density coupling between the P700 chromophore and the antenna Chl a tends to push the P700 band to the red and to alter the amount of dipole strength in the P700 band. Thus the P700 chromophore, if all the antenna Chl a were removed, would probably have an absorption maximum to the blue of 700 nm. In this regard, it is significant that a recently synthesized Chl a dimer model for P700 has an absorption maximum at 697 nm.[32] This P700 model, when oxidized, displays a Gaussian ESR signal that is essentially identical with the ESR signal (photosignal I) from oxidized P700 in green plants.[32] Also, it is possibly significant that the maximum for P700 bleaching is at 701–704 nm in the intact photosynthetic membrane (antenna Chl a:P700 ratio of several hundred) and at 697 nm in the P700 Chl a–protein complex (antenna Chl a:P700 ratio of approximately 40) studied by Thornber et al.[16]

The present computed spectra, when combined with in vitro visible absorption spectra, may be used to draw several tentative conclusions regarding the nature of the in vivo "forms" of Chl a. First, consider the view that the "forms" correspond to monomeric Chl a in different local environments. With the exception of the absorption spectrum of monomeric Chl a which is coordinated to a metal cation via its ring V keto C=O (676–681-nm absorption maximum),[24] the $Q_y(0, 0)$ absorption maximum for monomeric Chl a falls in the 659–671-nm range.[23,24] Therefore, in vitro visible absorption spectra of monomeric Chl a do not support the view that the solvent medium itself may be responsible for the more red-shifted (λ_{max} >670 nm) "forms". Of particular relevance are the absorption maxima for monomeric Chl a in amide solvents (663–664 nm)[23,25] and the absorption maxima for monomeric Chl a in lipid vesicles and multilayers (670 nm).[28-31] The 662-nm "form" of Chl a could correspond to monomeric Chl a in protein or in the hydrocarbon region of the lipid bilayer. The 670-nm Chl a "form" could correspond to monomeric Chl a in the polar head region of the lipid bilayer. The Chl a "form" near 683 nm could be monomeric Chl a whose ring V keto C=O is coordinated to metal cations (e.g., Mg^{2+}). Now, consider the view that the Chl a "forms" are exciton transitions in arrays of interacting chlorophyll molecules. The present calculations clearly show that this view requires that the local Chl a concentration be of the order of 1 M because, at lower

concentrations, the $Q_y(0, 0)$ transition density interactions are not strong enough to generate the more red-shifted "forms". As the overall Chl a concentration in the membrane is of the order of 0.1 M, this amounts to the assumption that there are local regions of high Chl a concentration. By analogy with the Fenna and Matthews[12-14] x-ray crystal structure of a Bchl a–protein complex (0.94 M local Bchl a concentration), these regions of high Chl a concentration could lie within Chl a–protein complexes.

References and Notes

(1) This work was performed under the auspices of the Division of Physical Research, USERDA.
(2) A. J. Bearden and R. Malkin, *Q. Rev. Biophys.*, **7**, 131 (1975).
(3) W. W. Parson and R. J. Cogdell, *Biochim. Biophys. Acta*, **416**, 105 (1975).
(4) K. Sauer in "Bioenergetics of Photosynthesis", Govindjee, Ed., Academic Press, New York, N.Y., 1975, pp 115–181.
(5) R. Emerson and W. Arnold, *J. Gen. Physiol.*, **15**, 391 (1931–1932).
(6) R. Emerson and W. Arnold, *J. Gen. Physiol.*, **16**, 191 (1932–1933).
(7) R. K. Clayton, *Adv. Chem. Phys.*, **19**, 353 (1971).
(8) J. J. Katz and J. R. Norris, *Curr. Top. Bioenerg.*, **5**, 41–75 (1973).
(9) L. L. Shipman, T. M. Cotton, J. R. Norris, and J. J. Katz, *Proc. Natl. Acad. Sci.*, **73**, 1791 (1976).
(10) L. N. M. Duysens, Doctoral Thesis, Utrecht, 1952, p 78.
(11) J. M. Anderson, *Biochim. Biophys. Acta*, **416**, 191 (1975).
(12) R. E. Fenna and B. W. Matthews, *Nature (London)*, **258**, 573 (1975).
(13) R. E. Fenna and B. W. Matthews in "The Brookhaven Symposium in Biology No. 28", Brookhaven National Laboratory, Upton, N.Y., 1977, pp 170–182.
(14) R. E. Fenna, L. F. Ten Eyck, and B. W. Matthews, *Biochim. Biophys. Res. Commun.*, **75**, 751 (1977).
(15) D. W. Reed and R. K. Clayton, *Biochim. Biophys. Res. Commun.*, **30**, 471 (1973).
(16) J. P. Thornber, R. S. Alberte, F. A. Hunter, J. A. Shiozawa, and K.-S. Kan, in "The Brookhaven Symposium in Biology No. 28", Brookhaven National Laboratory, Upton, N.Y., 1977, pp 132–148.
(17) J. P. Thornber, *Annu. Rev. Plant Physiol.*, **26**, 127 (1975).
(18) C. N. Cederstrand, E. Rabinowitch, and Govindjee, *Biochim. Biophys. Acta*, **126**, 1 (1966).
(19) W. L. Butler and D. W. Hopkins, *Photochim. Photobiol.*, **12**, 439 (1970).
(20) T. M. Cotton, A. D. Trifunac, K. Ballschmiter, and J. J. Katz, *Biochim. Biophys. Acta*, **368**, 181 (1974).
(21) B. A. Gulyaev and F. F. Litvin, *Biofizika*, **12**, 845 (1967).
(22) C. S. French, J. S. Brown, and M. C. Lawrence, *Plant Physiol.*, **49**, 421 (1970).
(23) G. R. Seely and R. G. Jensen, *Spectrochim. Acta.*, **21**, 1835 (1965).
(24) L. L. Shipman, T. M. Cotton, J. R. Norris, and J. J. Katz, *J. Am. Chem. Soc.*, **98**, 8222 (1976).
(25) T. M. Cotton, Ph.D. Dissertation, Northwestern University, 1976.
(26) H.-C. Chow, R. Serlin, and C. E. Strouse, *J. Am. Chem. Soc.*, **97**, 7230 (1975).
(27) L. L. Shipman, J. R. Norris, and J. J. Katz, *J. Phys. Chem.*, **80**, 877 (1976).
(28) A. Steinemann, N. Alamuti, W. Brodmann, O. Marschall, and P. Läuger, *J. Membr. Biol.*, **4**, 284 (1971).
(29) A. J. Hoff, *Photochem. Photobiol.*, **19**, 51 (1974).
(30) D. Walz, *J. Membr. Biol.*, **27**, 55 (1976).
(31) W. Oettmeier, J. R. Norris, and J. J. Katz, *Z. Naturforsch. C*, **31**, 163 (1976).
(32) M. R. Wasielewski, M. H. Studier, and J. J. Katz, *Proc. Natl. Acad. Sci.*, **73**, 4282 (1976).

Experimental Study of a Simple Anomalous Diffusion System by Time-Lag and Transient-State Kinetic Analysis

K. Tsimillis[1] and J. H. Petropoulos*

Physical Chemistry Laboratory, Demokritos Nuclear Research Center, Aghia Paraskevi, Athens, Greece (Received May 18, 1977)

The anomalous diffusion of N_2 and lighter gases in a microporous graphite compact was studied by means of sorption and permeation experiments. The use of refined experimental techniques permitted precise application of the method of time-lag analysis. Confirmatory and supplementary information was obtained by analogous early-time sorption kinetic analysis. Late-time sorption and early-time permeation kinetics have also been considered. It has, thus, proved possible to confirm, refine, and amplify previous results considerably. It is concluded that the method of "multiple compaction" does not necessarily ensure near macrohomogeneity of the resulting compact, and that there are strong reasons for doubting the view that blind pores can be largely responsible for the anomalous diffusion behavior of such compacts. The present results are important from a more general viewpoint, because they confirm the utility and indicate the considerable further potential of the methods of time-lag and transient-state kinetic analysis for the study of anomalous diffusion in general.

Introduction

In anomalous ("non-Fickian") penetrant–membrane systems, different methods of evaluating the diffusion coefficient yield discordant results, or there is deviation from well-known features of normal ("Fickian") kinetics (in which case evaluation of a diffusion coefficient is normally not justified). Deviation from initial proportionality between amount sorbed at time t and $t^{1/2}$ in sorption kinetics is a well-known example; discrepancy between the diffusion coefficients evaluated from the steady-state flux and the time lag in permeation experiments is another. Such deviations or discrepancies may be similar in appearance and yet result from widely different causes. Permanent gases diffusing in microporous plugs or pellets formed by compaction of a powder in a mold offer a good simple physical example of this point. The results of permeation steady-state and time-lag measurements in such systems reveal anomalies, which have been attributed by various authors to either (i) time dependence of the diffusion coefficient D, due to the presence of "blind pores",[1-3] or (ii) variation of D and the solubility coefficient, S, with position in the direction of diffusion, X, due to nonuniform compaction of the pellet,[4] or (iii) a combination of the above causes in certain cases.[2,3]

Thus, in anomalous diffusion systems the task is first to identify unambiguously the cause(s) of the anomaly and secondly to learn as much as possible about its (their) characteristics. This is the aim of the method of time-lag analysis recently developed in our laboratory.[5,6] Application of this method to a simple gas–porous compact system supports (ii) as the actual cause of the observed anomalies.[7] However, the low value of S in such systems in combination with the use of simple equipment necessitated the application of substantial corrections to the data, thus limiting precision and somewhat complicating the method from the practical point of view.[8]

In the present work we demonstrate the application of the aforementioned method in a simpler and more precise way. The need for corrections has been eliminated by increasing the sensitivity of upstream pressure measurement (at the expense of more stringent temperature stability requirements) and by refining the technique of desorption–permeation runs. Because of the novelty of

[1] Present address: Physical Chemistry Laboratory, University of Athens, Athens, Greece.

these experiments, we have sought first of all to confirm and refine our earlier conclusions by studying a N_2–graphite compact system. Secondly, we have extended our study to lighter gases not measurable in the previous apparatus.[7,8] Finally, we have been able to carry analysis of transient-state data further.

Theory

We consider isothermal unidimensional diffusion of a single penetrant in a slab of thickness l in contact with a large reservoir of penetrant on either side (i.e., at $X = 0$ and $X = l$). The diffusion (D) and solubility (S) coefficients are independent of the concentration (C) or activity (a) of the penetrant in the solid, but may depend on X and/or t. (Both C and a refer to unit volume of the medium.) At equilibrium, a equals (by definition[5]) the activity of penetrant in the reservoir (which, for a gas behaving ideally, is given[8] by pT_s/p_sT in cm^3 of gas at NTP/cm^3, where p and T are the actual pressure and temperature, respectively, of the gas in the reservoir, $p_s = 1$ atm and $T_s = 273.2$ K) and $S(X, t \to \infty) = C(X, t \to \infty)/a$. The diffusion process is described by[5,6]

$$\frac{\partial C}{\partial t} = \frac{\partial}{\partial X}\left(P\frac{\partial a}{\partial X}\right) \qquad t > 0, \quad 0 \leqslant X \leqslant l \qquad (1)$$

where $P = DS$ is the permeability coefficient. The quantity of penetrant entering or leaving either reservoir is measured, but the changes in the boundary activities $a(X = 0, t)$, $a(X = l, t)$ [i.e., in the pressures $p(X = 0, t)$, $p(X = l, t)$] are kept negligible, so as to maintain the following boundary conditions (a_0, a_l, a_1 = constants):[5,6,8]

(a) *Permeation Experiments (both Reservoirs in Use)*

$$a(X = 0, t) = a_0$$
$$a(X = l, t) = a_l$$
$$a(X, t = 0) = a_1 \qquad (2)$$

with $a_0 > a_l$ and either $a_1 = a_l$ ("absorption–permeation") or $a_1 = a_0$ ("desorption–permeation"). The permeation curve $Q(X, t)$ ($X = 0$ or l) attains a steady-state asymptote $Q_s(X, t) = Q(X, t \to \infty)$ from which the steady-state flux J_S and the corresponding time lag $L(X)$ are determined. Four time lags can be measured,[5] namely, $L^a(l)$, $L^a(0)$, $L^d(l)$, $L^d(0)$, where the superscripts a and d (also used on Q) refer to absorption and desorption conditions, respectively. Similar experiments can be carried out with the sense of

flow reversed (denoted by asterisks on the relevant L or Q).

(b) *Sorption Experiments (Reservoir at $X = l$ Blocked)*

$$a(X = 0, t) = a_0$$
$$\partial a(X = l, t)/\partial X = 0$$
$$a(X, t = 0) = a_1 \qquad (3)$$

with either $a_0 > a_1$ (absorption) or $a_0 < a_1$ (desorption with simultaneous flow reversal). The sorption curve, denoted by $Q(t)$ to distinguish it from the corresponding (and, at small t, coincident) permeation curve $Q(X = 0, t)$, attains a final equilibrium value $Q_\infty = Q(t \to \infty)$.

For a normal ("Fickian") diffusion system S and D or P (all constant) are obtainable from any suitable combination of the steady-state, equilibrium, or transient-state quantities referred to above.[9]

In our view, the best way to analyze an anomalous (or simply an unknown) diffusion system is to determine (U = cross sectional area of the slab)

$$S_{\mathrm{expt}} = l^{-1} \int_0^l S(X, t \to \infty) \, dX =$$
$$Q_\infty/U l |a_0 - a_1| \qquad (4)$$

$$P_{\mathrm{expt}} = l/\int_0^l dX/P(X, t \to \infty) =$$
$$S_{\mathrm{expt}} D_{\mathrm{expt}} = lJ_S/U(a_0 - a_l) =$$
$$lQ_s(X, t)/U[t - L(X)](a_0 - a_l) \qquad (5)$$

These integral (constant) parameters define a "corresponding Fickian system"[6] with which the actual system may be compared as follows:

(a) *Time-Lag Analysis.* The four time lags measured may be transformed[5] into: $L^a \equiv L^a(l)$, $\Delta L^a = L^a - L^a(0)$, $\delta L = L^a - L^d(l)$, $\delta \Delta L = \Delta L^a - L^d(l) + L^d(0)$. The "corresponding Fickian system", on the other hand, predicts the following values for these quantities[5,8]

$$6L_s{}^a = 2\Delta L_s{}^a = 2\delta L_s = \delta \Delta L_s = l^2/D_{\mathrm{expt}} =$$
$$U l S_{\mathrm{expt}}(a_0 - a_l)/J_S \qquad (6)$$

The discrepancies or increments between corresponding observed and predicted quantities (subscript E) characterize the anomaly of the system; they are made up of separate additive contributions due to the time dependence and X dependence (subscripts T and h, respectively) of S and D. Thus[6]

$$L_E{}^a = L^a - L_s{}^a = L_T{}^a + L_h{}^a$$

and similar expressions hold for the remaining quantities. The general property[6] $\delta \Delta L_E = \delta \Delta L_T = \delta \Delta L_h = 0$ serves to check the consistency of the measurements as shown later. The remaining "non-Fickian time-lag increments" have properties which enable us to identify and characterize time-dependent and X-dependent anomalies independently of each other.[5,6]

(b) *Transient-State Analysis.* If the system conforms to "Fickian" sorption of permeation kinetics sufficiently closely, one may deduce the corresponding value D_n ($n = 1, 2, \ldots$) of the diffusion coefficient in the standard way.[9] From sorption kinetics we obtain at small and large t, respectively

$$Q(t)/Q_\infty = 2(D_1 t/\pi l^2)^{1/2} \qquad (7)$$

$$1 - Q(t)/Q_\infty = (8/\pi^2) \exp(-D_2 \pi^2 t/4l^2) \qquad (8)$$

Plots of Q_t/Q_∞ vs. $t^{1/2}$ and of $\ln[1 - Q(t)/Q_\infty]$ vs. t yield D_1 and D_2, respectively. For the early-time portion of $Q^a(l, t)$ we have

$$dQ^a(l, t)/dt = 2Q_\infty(D_4/\pi t)^{1/2} \exp(-l^2/4D_3 t) \qquad (9)$$
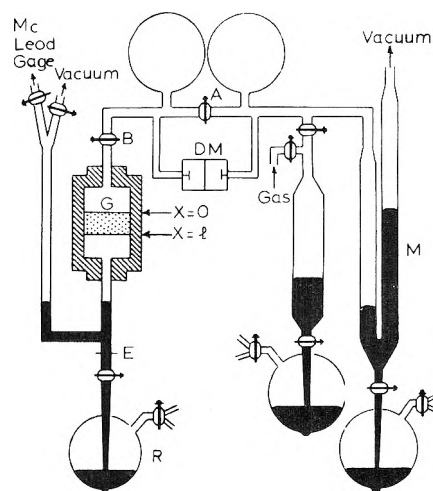
Figure 1. Sorption and permeation apparatus (G = plug, DM = differential pressure gauge).

D_3 and D_4 can be obtained from the (linear) plot of $\ln[t^{1/2} dQ^a(l, t)/dt]$ vs. $1/t$.

Alternatively, especially if there are marked deviations of the above plots from linearity, one may compare the observed curve with the "Fickian" plot obtained by inserting D_{expt} in eq 7–9.

Experimental Section

Materials and Construction of the Compact. The microporous plug used was made by compaction of fine graphite powder (Acheson DAG 620 dispersion of specific surface area 70 m²/g) between two rigid pistons in a cylindrical holder of hardened steel. The powder was added always through the top of the holder in five 0.35-g portions, each addition being followed by compression to ca. 8000 atm for 75 s and gradual decompression over ca. 105 s. Only the upper piston was mobile with respect to the holder during the compression process (cf. Figure 1, ref 7), so that the macroscopic structure of the present plug should approximate to that of plug A in ref 7 and 8. The finished plug had $U = 0.785$ cm²; $l = 1.12_4$ cm; porosity, $\epsilon = 0.12_6$; and specific surface area $A = 140$ m²/cm³ of plug, i.e., hydraulic radius $\epsilon/A = 0.89$ nm (or effective cylindrical pore radius[1] = 1.8 nm).

The gases He, Ne, H₂, and N₂ used were better than 99.95% pure.

Sorption and Permeation Measurements. The plug holder was connected to the sorption and permeation apparatus (Figure 1) via soft metal gaskets and metal flanges followed by metal-to-glass joints, so that the side of the mobile piston during compression was upstream ($X = 0$) initially, i.e., for permeation runs in the "forward sense of flow" (as illustrated in Figure 1 of ref 7).

The upstream reservoir consisted of known volumes V_1 (upper plug surface to tap B, made as small as possible, $\simeq 1.40$ cm³) and V_2 (tap B to tap A = 517.9 cm³). The pressure therein $p(X = 0, t)$ could be monitored against a (constant) reference pressure (p_{ref} read on the mercury manometer M to 0.01 Torr) by means of a Baratron (MKS Instruments) capacitive differential pressure meter DM (all metal sensor, range 0–3 Torr, sensitivity ~ 0.0002 Torr) keeping tap A closed and $p(X = 0, t) > p_{\mathrm{ref}}$ (as recommended by the manufacturer for optimum performance of DM). To minimize the effect of temperature variation on the differential pressure readings: (i) the section of the apparatus from the plug holder to M was enclosed in plastic covers and shielded from radiation, (ii) two equal juxtaposed buffer volumes were placed on either side of

TABLE I: Permeability (in cm²/s × 10⁻⁴) and Time-Lag (in min) Data for N_2

| | Absorption permeation | | | | | Desorption permeation | | | |
| | Downstream | | Upstream | | | Downstream | | Upstream | |
p_0, Torr	Time lag	P_{expt}	Time lag	P_{expt}	p_0, Torr	Time lag	P_{expt}	Time lag	P_{expt}
49.83	92	2.76			49.49	−193	2.76	90	2.80
50.47	92	2.74	−284	2.84	50.05	−197	2.76	92	2.78
73.29	94	2.70	−292	2.74	73.39	−199	2.65	93	2.70
61.63	95	2.63	−302	2.70	62.45	−195	2.67	99	2.65
39.92	96	2.61	−326	2.63	33.02	−194	2.63	92	2.65
94.58	94	2.59	−299	2.67	99.86	−195	2.59	94	2.67
Mean[a]	95	2.61	−309	2.67		−195	2.63	95	2.66
34.23	100	2.55							
65.05	97	2.55	−176	2.65	64.87	−311	2.59	100	2.57
57.26	99	2.57	−184	2.61	64.57	−329	2.55	104	2.59
42.61	103	2.57							
Mean[b]	100	2.56	−180	2.63		−320	2.57	102	2.58

[a] Forward flow (based on last three experimental values; see text). [b] Reverse flow.

tap A; and (iii) the temperature of the room was regulated by circulating the air over a cooler followed by heating coils controlled by means of a proportional temperature controller.

The downstream reservoir contained a McLeod gauge and a mercury reservoir R from which mercury could be raised to block the downstream face of the plug. With the mercury level at mark E, the volume of the reservoir was $V_l = 462.5$ cm³.

The experiments were carried out at 23.35 °C as follows:

(a) Absorption or Absorption Permeation. Initially, the plug, V_1 and V_l are evacuated [$p(X, t = 0) = p_1 = 0$] with the mercury in R up to E (permeation experiment) or raised to the plug surface (absorption experiment) and V_2 is brought to pressure $p_2 > p_{ref}$ with taps A and B closed. Then at $t = 0$, tap B is opened. The initial value $p_0 > p_{ref}$ of the upstream pressure is given by $p(X = 0, t = 0) = p_0 = p_2V_2/(V_1 + V_2) = p_2V_2/V_0$ [$p(X = l, t = 0) = 0$ in the permeation experiment].

(b) Desorption or Desorption Permeation. Initially, V_l is evacuated and the plug with its downstream face blocked is equilibrated with pressure p_1 in the upstream reservoir. Then at $t = 0$: (i) With $p_{ref} \leq p_1$, mercury is withdrawn into R as fast as possible down to level E [desorption–permeation with $p(X = 0, t = 0) = p_1$ and $p(X = l, t = 0) = 0$], or (ii) V_2 is evacuated with tap B closed and, at $t = 0$, with tap A closed and $p_{ref} \simeq 0$, tap B is opened [desorption with $p(X = 0, t = 0) = p_1V_1/(V_1 + V_2)$ and sense of flow reversed].

In all cases, adherence to the prescribed constant boundary conditions (eq 2 and 3) was ensured by maintaining the maximum change of $p(X = 0, t)$, and in the case of permeation of $p(X = l, t)$ also, to within 0.2% of p_0 (absorption) or p_1 (desorption).

Prior to any measurements, the plug was thoroughly outgassed for several days at temperatures up to 225 °C. After completion of the "forward flow" runs, dry N_2 was introduced in the apparatus and the plug holder quickly (to limit contact with the atmosphere) removed and replaced in reversed position (upside down). The plug was then outgassed for several days at temperatures up to 55 °C and the "reverse flow" runs carried out.

Thus, the present apparatus is less flexible than the previous one[8] as far as reversal of the sense of flow is concerned, but has the important advantages that sorption experiments can be carried out with the plug in situ and $Q(l, t)$ in desorption experiments does not require correction.

The dynamic behavior of the upstream compartment of the apparatus was checked in the absence of the plug by replacing the plug holder by a closed cylinder giving approximately the same V_1.

Results and Discussion

Consistency and Reliability of the Measurements. Typical examples of the fluctuation of a static pressure difference, as recorded by the Baratron gauge at $p \simeq 100$ Torr, are shown in Figure 2a, together with the temperature fluctuations recorded near the gauge sensor by a sensitive mercury thermometer. At low p (up to ~0.4 Torr) the Baratron and McLeod gauges usually agreed to within 1%. The pressure change upon gas expansion from V_1 to V_2 with the "closed cylinder" in place was the same within 0.5% for He and Ar, thus indicating absence of significant sorption effects extraneous to the plug in the upstream reservoir.

Figure 2c shows the performance of the Baratron gauge in steady-state permeation measurement to be comparable to that of the McLeod gauge. Even though some fluctuation is evident in the former case (similar to that shown in Figure 2a), there is marked improvement over what could be achieved previously.[8]

Table I lists the detailed steady-state flux and time-lag data obtained with N_2 as a typical example. Table II gives the corresponding mean values for all gases.

The data of Table I are listed in chronological order. Permeability values measured upstream (Baratron gauge) and downstream (McLeod gauge) usually agreed well (~4% maximum discrepancy including all gases). This confirms attainment of the true steady state of permeation and, incidentally, the proper functioning of the apparatus. The former point was further confirmed by prolongation of some experiments (in the case of N_2 to ~16 times L^a as compared with ~6 times L^a normally). Nevertheless a small tendency for P_{expt} to diminish over the considerable period (~2 years) covered by these measurements is evident in Table I. This effect (which incidentally was less noticeable with the lighter gases) can be plausibly attributed to slight gradual changes in the plug (which is left in a state of some strain by the compaction process). For this reason, the earliest runs are not included in the mean values listed for forward flow runs in Table I. However, some small discrepancies between forward and reverse flow runs are not unexpected, because the latter followed on the former, instead of alternating with them as in ref 7 and 8. This is reflected in the somewhat less close concordance between L^a and $L^{a*}(l)$ or $L^d(0)$ and $L^{d*}(0)$ here (Table II) as compared with ref 7. Thus, even though agreement between $\delta\Delta L$ and $\delta\Delta L^*$ was generally close (Table II), it was felt more appropriate to treat time lags for each sense

TABLE II: Experimental Time-Lag Quantities and "Non-Fickian Time-Lag Increments" (in min), Solubility, and Diffusion (in cm²/s) Coefficients

	Forward flow				Reverse flow			
	He	Ne	H₂	N₂	He	Ne	H₂	N₂
$L^a \equiv L^a(l)$	8.2	20.6	9.8	95	9.8	23.5	10.1	100
$L^d(l)$	-22.6	-48.6	-22.7	-195	-33.4	-76.4	-35.0	-320
$L^a(0)$	-33.8	-73.4		-309	-25.1	-48.8		-180
$L^d(0)$	8.4	22.5	11.3	95	10.3	19.0	9.8	102
ΔL^a	41.6	94.9	(45.5)	404	33.5	70.0	(32.6)	277
δL	30.4	70.1	33.2	290	41.8	97.6	44.9	417
$\delta \Delta L$	72.6	165	(78.8)	694	77.2	168	(77.6)	699
L_s^a	12.1	27.5	(13.1)	116	12.9	27.9	(12.9)	116
L_E^a	-4.3	-6.0	(-2.6)	-20.2	-4.4	-6.7	(-3.0)	-19.5
ΔL_E^a	5.3	12.4	(6.1)	57	-5.1	-13.8	(-6.1)	-72
δL_E	-5.9	-12.4	(-6.1)	-57	3.2	13.8	(6.1)	68
L_E^a/L_s^a	-0.35	-0.22	(-0.20)	-0.18	-0.34	-0.24	(-0.23)	-0.17
$\Delta L_E^a/\Delta L_s^a$	0.15	0.15	(0.16)	0.16	-0.13	-0.16	(-0.16)	-0.21

	He	Ne	H₂	N₂
S_{expt}	0.126	0.138	0.211	0.864
$D_{expt} \times 10^4$	2.81	1.27	2.69	0.302

a Quantities in parentheses have been calculated by putting $L^a(0) = L^{d*}(l)$, $L^{a*}(l) = L^d(0)$.
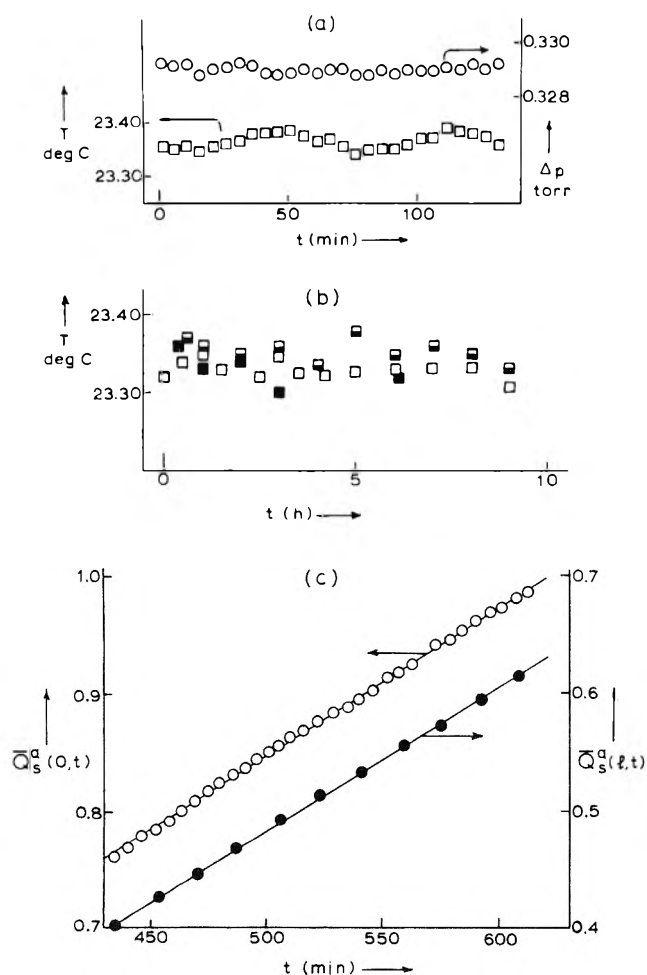
Figure 2. Typical readings of (a) a static pressure differential on the Baratron gauge and corresponding temperature of the surroundings; (b) temperature of the surroundings of the upstream reservoir on three different days; (c) $Q_s^a(l, t)$ (McLeod gauge) and $Q_s^a(0, t)$ (Baratron gauge) in a N₂ experiment [$\bar{Q} = Q/Ula(X = 0, t = 0)$].

of flow separately. Thus L_s^a or ΔL_s^a, δL_s in each case were set equal to $1/6$ or $1/2$, respectively, of the value of $\delta \Delta L$ for the relevant sense of flow (in view of eq 6 and the fact that $\delta \Delta L = \delta \Delta L_s$). The "non-Fickian time lag increments" L_E^a, ΔL_E^a, and δL_E listed in Table II have been evaluated on this basis.
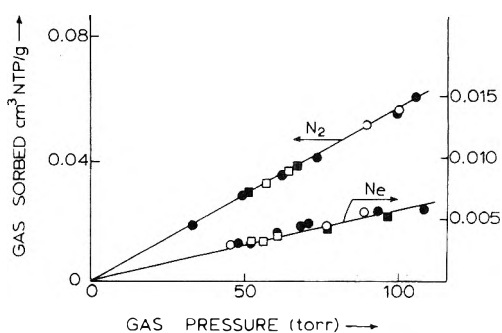
Figure 3. Equilibrium sorption data for N₂ and Ne (lines calculated from $\delta \Delta L$ through eq 6). Equilibrium was attained by: absorption (●, ■), desorption (○, □), forward flow (●, □), or reverse flow (■, ○).

The good agreement shown in Figure 3 between S_{expt} calculated directly by eq 4 (experimental points) and S_{expt} calculated from $\delta \Delta L$ (= $\delta \Delta L_s$) by eq 6 (lines) is a further indication of the consistency of the measurements.

The accuracy of both sets of data depends on the accuracy with which V_1 is known. It was estimated that an error of 0.01 cm³ in V_1 would lead to errors of ~6.5 min and ~9 min in $L^a(0)$, and hence in $\delta \Delta L$, for He and N₂, respectively. The corresponding relative error in S_{expt} would be ~10% (He) and ~1.2% (N₂). V_1 was determined by He expansion assuming negligible adsorption on graphite, in accordance with previous equilibrium sorption measurements with a more sensitive sorption apparatus.[7,8] A useful check on the results obtained is provided by the consistency of the resulting He time-lag data and, in particular, agreement between $L^a(0)$ and $L^{d*}(l)$, the latter being independent of V_1.

Full data were collected for He, Ne, and N₂. In the case of H₂, abnormally high values of $Q^a(0, t)$ or $Q^a(t)$ were obtained by the techniques described above. This anomaly was eliminated when tap A was closed only shortly after opening B, but this precluded direct reliable determination of $Q^a(0, t)$, $Q^a(t)$, and hence of $L^a(0)$, in the case of H₂.

Time-Lag Analysis. In accordance with the above discussion, the N₂ data for a given sense of flow offer the best possibility of precise time-lag analysis on the lines of ref 6. Thus, the most useful tests for pure X dependence of S and D are

$$\delta L_h = -\Delta L_h^a \qquad \delta L_h^* = -\Delta L_h^{a*} \qquad (10)$$

[or the equivalent forms $\delta \Delta L = \Delta L^a + \delta L$ and $\delta \Delta L^* = \Delta L^{a*}$
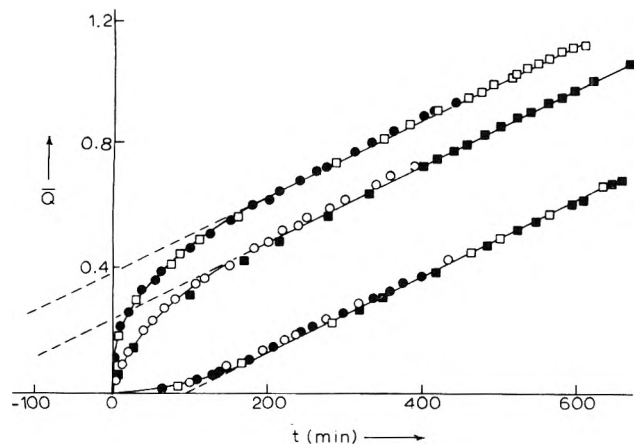
Figure 4. Typical permeation curves for N_2 [$\bar{Q} = Q/Ula(X = 0, t = 0)$]: absorption permeation ($\bullet$, $\blacksquare$); desorption permeation ($\bigcirc$, $\square$); forward flow ($\bullet$, $\bigcirc$); reverse flow ($\blacksquare$, $\square$).

$+ \delta L^*$; or $L^a = L^d(0)$ and $L^{a*} = L^{d*}(0)$].[6,7] Since[5] $\Delta L_T{}^a = 0$, we have $\Delta L_E{}^a = \Delta L_h{}^a$ and

$$\delta L_E = \delta L_h + \delta L_T = -\Delta L_E{}^a + \delta L_T$$

The N_2 data of Table II obey eq 10 (or their equivalent forms) closely. Hence $\delta L_T \cong 0$; the observed time lags can, consequently, be fully explained by X dependence of S and D with greater confidence than before.[7] The reasons for the rather poorer conformity of the said data with the similar relations[6,7] $\delta L_h = -\delta L_h^*$, $\Delta L_h{}^a = -\Delta L_h{}^{a*}$ [or, equivalently, $\Delta L^a = \delta L^*$, $\delta L = \Delta L^{a*}$; or $L^a(0) = L^{d*}(l)$, $L^d(l) = L^{a*}(0)$] are also clear from the above discussion.

The results for the other gases are in keeping with the above conclusion, which confirms the marked nonhomogeneity of a plug made by the method of multiple compaction previously believed to yield macroscopically nearly uniform compacts.[1-3] This belief was apparently the principal reason for attributing the time-lag anomalies observed in such "segmented" compacts to time dependence of D due to the presence of blind pores.[1-3] Among such blind pore theories only those predicting $\delta L_T = 0$ are compatible with the experimental evidence presented here. In view of eq 2 of ref 10, the result $\delta L_T \cong 0$ requires either that (i) the permeability coefficient P is independent of time (in which case $L_T{}^a = 0$ also, as in the model of Goodknight and Fatt[11] in its original or generalized forms[5]), or (ii) that the presumed time dependence of P is exactly the same under absorption and desorption conditions (in which case $L_T{}^a = L_T{}^d(l) \neq 0$).

Transient-State Analysis. Taking again the most reliable data, i.e., those of N_2, we note (Figures 4 and 5) that the following relations (consistent with X dependence of S and D^7) are validated with generally greater precision than previously[7,8]

$$Q^a(l, t) = Q^d(0, t) = Q^{a*}(l, t) = Q^{d*}(0, t)$$

$$Q^a(0, t) = Q^{d*}(l, t) \qquad Q^d(l, t) = Q^{a*}(0, t)$$

$$Q^a(t) = Q^{d*}(t) \qquad Q^d(t) = Q^{a*}(t)$$

Early-time sorption kinetics have received by far the most attention in the literature. Figure 5 shows that there are marked positive or negative deviations from the appropriate "Fickian" line (to the point where no really meaningful D_1 values are deducible by means of eq 7). Curves of similar shapes can arise from time-dependent anomalies, but these would not obey the above relations. Thus, Crank's model of a time-dependent D predicts one shape to be characteristic exclusively of absorption and another of desorption;[9] whereas the same shape is
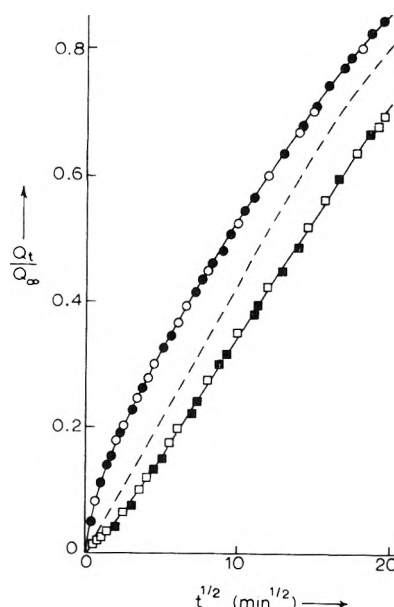
Figure 5. Typical early-time sorption kinetics for N_2: absorption ($\bullet$, $\blacksquare$); desorption ($\bigcirc$, $\square$); forward flow ($\bullet$, $\square$); reverse flow ($\blacksquare$, $\bigcirc$); "Fickian" line corresponding to D_{expt} (- - -).

expected[12] in all cases for a time-dependent S, according to the model of Long and Richman.[13] A similar situation arises in the blind pore model of Fatt et al.[11,14] according to the analysis of ref 5. Here, S is made up of an "open pore component", S_M, plus a "blind pore component", S_B; the latter will be time dependent, if equilibrium between open and blind pores at a given location is not established instantaneously. ($P = D_M S_M$ is independent of time as already noted above.) The variation of S_B with t will be determined by the rate at which a typical blind pore can fill (or empty); this rate will in turn be governed by the appropriate diffusion coefficient D_B and pore length l_B. The present data do not exclude the presence of some additional, but relatively minor, anomaly of this type. However, such an anomaly would be of significant magnitude only if there is (i) an appreciable amount of blind porosity and (ii) an appreciable delay (on the experimental time scale) in establishing equilibrium between open and blind pores at any X. A convenient measure for (ii) is the value of $l_B{}^2 D_M / l_M{}^2 D_B$. Now the length of a typical open pore $l_M \sim l$ is a macroscopic distance, whereas l_B should normally be a microscopic one. Thus, whereas condition (i) may be realized in practice, this is unlikely to be so for (ii); unless it can be claimed that $D_B << D_M$ correspondingly, or that a blind pore can extend over macroscopic distances without branching out (or branching out only to other blind pores).

In contrast to the marked anomalies noted above, the linear kinetic relations predicted by eq 8 and 9 were obeyed quite closely (N_2 data), as illustrated in Figure 6. Anomalous behavior was revealed in late-time sorption kinetics by a discrepancy in the experimental values of D_2 obtained from $Q^a(t)$ and $Q^d(t)$ (0.34×10^{-4} and 0.23×10^{-4} cm²/s, respectively) and the corresponding values of the intercept of the linear plot on the $Q(t)$ axis [-0.35 and -0.15 for $Q^a(t)$ and $Q^d(t)$, respectively, as against a normal value of -0.21]. In early-time permeation kinetics there was a discrepancy between D_3 (=0.39×10^{-4} cm²/s) and D_4 (=0.20×10^{-4} cm²/s). These values deviate significantly and in opposite senses from the "Fickian" value D_{expt} (=$0.30_2 \times 10^{-4}$ cm²/s). The same applies to the absorption and desorption values of D_2 quoted above and even to the intercepts of the corresponding late-time sorption plots. These findings are very interesting and suggestive, but
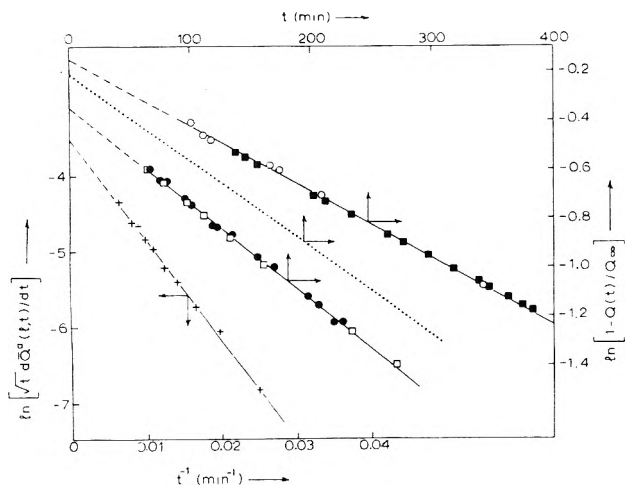
Figure 6. Typical late-time sorption and early-time permeation kinetics for N_2: $Q^a(l, t)$, +; $Q^a(t)$, ●; $Q^d(t)$, O; $Q^{a*}(t)$, ■; $Q^{d*}(t)$, □; "Fickian" sorption line corresponding to D_{expt}, ⋯.

further investigation is required before their significance can be assessed with confidence.

Correlation with the Macroscopic Structure of the Compact. Having confirmed that the observed "non-Fickian" anomaly is due to X dependent S and D, we now proceed to examine its nature in more detail. How time-lag analysis can be used for this purpose has already been shown.[4] We indicate here briefly how early-time sorption kinetics can be analyzed similarly, bearing in mind that D_{expt} and S_{expt} can now be considered identical with $\tilde{D}$ and $\tilde{S}$, respectively, of ref 6. Putting ($0 \leq \omega \leq 1$)

$$\omega = \int_0^X S(X)\, dX / \int_0^l S(X)\, dX = \int_0^X S(X)\, dX / l\tilde{S}$$

and $\tilde{C} = \tilde{S}a$, eq 1 yields

$$\frac{\partial \tilde{C}}{\partial t} = \frac{\partial}{\partial \omega}\left[\frac{\tilde{D}}{l^2}\left(\frac{DS^2}{\tilde{D}\tilde{S}^2}\right)\frac{\partial \tilde{C}}{\partial \omega}\right]$$

Furthermore,

$$Q^a(t) = \frac{1}{l}\int_0^l C(X, t)\, dX = \int_0^l \tilde{C}(X, t)\, d\omega$$

It follows that $DS^2/\tilde{D}\tilde{S}^2 = PS/\tilde{P}\tilde{S} = 1$ yields the "Fickian" line of Figure 5. For $PS/\tilde{P}\tilde{S} < 1$ (>1) at $\omega = 0$ (and hence $X = 0$) and increasing with ω (and hence with X), the $Q^a(t)$ curve should deviate negatively (positively) from the "Fickian" line and be concave (convex) upward initially.

A detailed examination has been reported[4] of the relation between the compaction process and the macroscopic nonhomogeneity of the resulting compact, expressed for simplicity in terms of variable porosity, $\epsilon(X)$, only. The present case would be rather more complicated, because the marked tendency of the graphite platelets to become oriented (mainly at right angles to the direction of compression)[15] and the resulting effect on D[16] is also likely to vary with X. Furthermore, in "multiply compacted" or "segmented" plugs like the present one, macroscopic nonhomogeneity may be expected both within a segment and from one segment to the next in a manner which is difficult to predict with certainty.[4] Nevertheless, L_E^a data for asymmetric segmented compacts (like the present one) were found to be consistent with a more or less monotonic intersegmental variation of S, D (ignoring the intrasegmental one).[4]

The present L_E^a data (which confirm and amplify earlier results[7]) follow the same pattern as the said data from one gas to another in the order of increasing adsorbability [cf.

Table II here with Table I column iii and Figures 3 and 4 of ref 6]. Furthermore, the algebraic sign of $\Delta L_E^a = \Delta L_h^a$ shown in Table II (following the interpretation of ref 6), as well as the shape of the $Q^a(t)$ curves shown in Figure 5 (following the interpretation given here), are consistent with a general tendency of $S^2 D$ in the plug to increase (decrease) from the side of the fixed (mobile) piston inward. In accordance with the interpretation of ref 4 for gases of modest adsorbability, this would, in turn, be consistent with a higher degree of compaction in the earlier segments. Table II shows that ΔL_E^a is much less dependent on the adsorbability of the gas than L_E^a. Whether this is attributable to the fact[17] that ΔL_h^a is considerably more dependent on intrasegmental nonhomogeneity than L_h^a is not known at present. It is hoped that further work now in progress will permit more detailed structural analysis.

Conclusion

The present study demonstrates the capability of the recently developed method of time-lag analysis[5,6] for precise identification of the nature of "non-Fickian" behavior of a relatively simple penetrant–membrane system. The method is of general applicability and systems with concentration dependent D and S can also be dealt with.[6,18] We have shown, further, that analysis of early-time sorption kinetics can provide very useful confirmatory and supplementary information. Interesting possibilities of obtaining information from late-time sorption and early-time permeation [$Q^a(l, t)$] kinetics have also been revealed, but their fuller exploitation must await development of adequate theoretical background.

Concerning the anomalous behavior of the diffusion system examined here, we find strong evidence for X dependence of S and D, but no positive evidence of time dependence. The possibility that an effect of the latter type may exist is not excluded by the analysis under certain specified conditions, but its magnitude cannot be substantial. Independent theoretical grounds for expecting little effect from blind pores, even when present in quantity (except in rather unusual circumstances), have been noted. It is also noteworthy that the particle orientation effects mentioned in the previous section should favor rather than hinder blind pore formation in our plug. Hence, there are, at present, strong arguments against the theory[1-3] which ascribes time-lag anomalies in segmented compacts to the effect of blind pores acting in a nearly macrohomogeneous medium.

References and Notes

(1) R. M. Barrer and T. Gabor, *Proc. R. Soc. London, Ser. A*, **251**, 353 (1959); **256**, 267 (1960).
(2) R. Ash, R. W. Baker, and R. M. Barrer, *Proc. R. Soc. London, Ser. A*, **304**, 407 (1969).
(3) R. Ash, R. M. Barrer, J. H. Clint, R. J. Dolphin, and C. L. Murray, *Phil. Trans.*, **275**, 255 (1973).
(4) J. H. Petropoulos and P. P. Roussis, *J. Chem. Phys.*, **48**, 4619 (1968).
(5) J. H. Petropoulos and P. P. Roussis, *J. Chem. Phys.*, **47**, 1491 (1967).
(6) J. H. Petropoulos and P. P. Roussis, *J. Chem. Phys.*, **47**, 1496 (1967).
(7) P. P. Roussis and J. H. Petropoulos, *J. Chem. Soc., Faraday Trans. 2*, **73**, 1025 (1977).
(8) P. P. Roussis and J. H. Petropoulos, *J. Chem. Soc., Faraday Trans. 2*, **72**, 737 (1976).
(9) J. Crank, "Mathematics of Diffusion", 2nd ed, Oxford University Press, London, 1975, Chapters 4 and 10.

(10) J. H. Petropoulos and P. P. Roussis, *J. Polym. Sci., Part C*, **No. 22**, 917 (1969).

(11) R. C. Goodknight and I. Fatt, *J. Phys. Chem.*, **65**, 1709 (1961).

(12) J. H. Petropoulos and P. P. Roussis in "Permeability of Plastic Films and Coatings to Gases, Vapors and Liquids", H. B. Hopfenberg, Ed., Plenum Press, New York, N.Y., 1974, p 219.

(13) F. A. Long and D. Richman, *J. Am. Chem. Soc.*, **82**, 513 (1960).

(14) R. C. Goodknight, W. A. Klikoff, Jr., and I. Fatt, *J. Phys. Chem.*, **64**, 1162 (1960).

(15) R. E. Nightingale in "Nuclear Graphite", R. E. Nightingale, Ed., Academic Press, New York, N.Y., 1962, p 106.

(16) R. M. Barrer and J. H. Petropoulos, *Surf. Sci.*, **3**, 126 (1965).

(17) J. H. Petropoulos and P. P. Roussis, *J. Chem. Phys.*, **51**, 1332 (1969).

(18) J. H. Petropoulos and P. P. Roussis, *J. Chem. Phys.*, **50**, 3951 (1969).

Isotopic Mass Effects in the Diffusion of Small Light Solutes in a Solvent of Larger and Heavier Molecules

K. R. Harris and R. Mills*

Research School of Physical Sciences, Australian National University, Canberra, A.C.T. 2600, Australia (Received April 4, 1977)

An experimental search has been made for isotopic mass effects in a system where small light molecules diffuse in a solvent of larger and heavier molecules. No effect was observed within the experimental precision of a few tenths of a percent. This result does not agree with the hard-sphere molecular dynamics study of Alder, Alley, and Dymond.

In a recent review on isotopic effects in diffusion Mills and Harris[2] have pointed out that the available experimental evidence shows, in general, that a change in the isotopic mass of diffusing tracer molecules or ions has no observable effect on their diffusion rate. There are however some exceptions to this rule. The work of Dunlop et al.[3] and Albright and Aoyagi,[4] for example, shows that, for trace amounts of benzene diffusing in a series of *n*-alkanes, there is a small isotopic effect which seems to increase as the solvent alkane becomes smaller and lighter. For the opposite case that of mass effects for small, light molecules diffusing in a solvent of large molecules there are presently no experimental results.

However, molecular dynamics machine calculations have been made which are relevant to the latter case. For instance Alder, Alley, and Dymond[1] reported data for hard sphere systems undergoing mutual diffusion where the size and mass of the solute and solvent could be independently varied and the motion of a single tracer particle followed. Their results showed appreciable mass effects which were attributed to the effect of correlated motions on the diffusion rate.

It seemed worthwhile therefore to undertake experimental studies to see if such mass effects are evident in the diffusion rate of isotopic solutes. In real systems undergoing diffusion, it is difficult to vary both the size and mass of tracer species independently. However, in this study we have used as tracers normal and deuterated benzene and cyclohexane thus effectively keeping the size and shape constant in each case but allowing the isotopic mass to be varied. The solvent chosen was octamethylcyclotetrasiloxane (OMCTS).

Experimental Section

The diaphragm-cell technique was used for the tracer diffusion measurements and has been fully described in the monograph by Mills and Woolf.[5] The two benzene and two cyclohexane species were tritiated by a technique[6] which ensured that there was only one tritium atom in each molecule. The molecular masses were therefore well specified. The starting materials for the tritiation were redistilled Analar benzene and cyclohexane. In the above

TABLE I: Tracer-Diffusion Coefficients for Benzene and Cyclohexane Diffusing in OMCTS at 25 °C

Mass no.	Mass ratio solute/solvent	Size ($\overline{V}^{1/3}$) ratio solute/solvent	$10^9 D_i$ m² s⁻¹	No. of runs
78 ⎫	1/3.8	1/1.52	1.085 ± 0.1%	2
80 ⎬ Bz	1/3.7	1/1.52	1.084 ± 0.1%	4
85 ⎭	1/3.5	1/1.52	1.087 ± 0.3%	4
86 ⎫ Cy	1/3.44	1/1.42	0.825	1
97 ⎭	1/3.05	1/1.42	0.823	1

technique[6] use of an organoaluminum dihalide catalyst ensures that tritiation is extremely rapid so that there are virtually no degradation products. As an additional check on the purity of our labeled compounds we measured the tracer diffusion of tritiated benzene in pure benzene, the result agreeing with literature values to within a few tenths of a percent. OMCTS was obtained from PCR Inc., Gainesville, Fla., and used without further purification.

Results and Discussion

The tracer diffusion coefficients of normal and deuterated benzene and cyclohexane diffusing in OMCTS are shown in Table I as a function of mass number. In the case of benzene the value given at mass number 78 is that of the limiting mutual diffusion coefficient for the system as reported by Marsh.[7] If benzene is component 1 and OMCTS component 2, then the limiting mutual coefficient $^1D_{12} = {}^1D_1$ as $C_1 \rightarrow 0$ where $^1D_1$ is the limiting tracer diffusion coefficient. The value of 1.085×10^{-9} m² s⁻¹ for $^1D_{12}$ reported by Marsh has recently been confirmed by Shankland and Dunlop.[8] There are no mutual diffusion data for the cyclohexane/OMCTS system.

As stated in the introductory paragraphs Alder, Alley, and Dymond[1] have reported data for hard sphere systems in the mass and size ratio ranges given in Table I. In addition Czworniak, Andersen, and Pecora[9] have used the data given by Alder et al. to formulate general expressions which can be used to calculate the effect of a change in the isotopic mass. Calculations from the former data would lead one to expect changes in the diffusion coefficient of 2–3% and the latter expressions of the order of

7%. It is not clear why the two estimates should differ but, in any case, no trend of this kind is evident in Table I where the precision is at least ±0.3%.

It can be concluded therefore that the mass dependence of the correlated particle motion which is evident in hard-sphere molecular dynamics calculations is not reproduced in the systems studied here.

References and Notes

(1) B. J. Alder, W. E. Alley, and J. H. Dymond, *J. Chem. Phys.*, **61**, 1415 (1974).

(2) R. Mills and K. R. Harris, *Chem. Soc. Rev.*, **5**, 215 (1976).
(3) S. J. Thornton and P. J. Dunlop, *J. Phys. Chem.*, **78**, 846 (1974); I. R. Shankland, P. J. Dunlop, and L. W. Barr, *Phys. Rev.*, **12**, 2249 (1975); I. R. Shankland, P. S. Arora, and P. J. Dunlop, *J. Phys. Chem.*, **81**, 1518 (1977).
(4) J. G. Albright and K. Aoyagi, *J. Chem. Phys.*, **64**, 81 (1976).
(5) R. Mills and L. A. Woolf, "The Diaphragm Cell", ANU Press, Canberra, 1968.
(6) M. A. Long, J. L. Garnett, and R. S. W. Vining, *J. Am. Chem. Soc.*, **94**, 8632 (1972).
(7) K. N. Marsh, *Trans. Faraday Soc.*, **64**, 894 (1968).
(8) I. R. Shankland and P. J. Dunlop, personal communication.
(9) K. J. Czworniak, H. C. Andersen, and R. Pecora, *Chem. Phys.*, **11**, 481 (1975).

Potential Dependence of the Electrochemical Transfer Coefficient. Reduction of Some Nitro Compounds in Aprotic Media

Jean-Michel Saveant* and Didier Tessier

Laboratoire d'Electrochimie de l'Université de Paris VII, 2 place Jussieu, 75221 Paris Cedex 05, France (Received June 1, 1977)

The electrochemical reduction rates of three aliphatic and aromatic nitro compounds, *tert*-nitrobutane, nitrodurene, and nitromesitylene, have been determined as a function of potential in acetonitrile and dimethylformamide. No significant interference of either reactant adsorption or associated chemical reactions was detected. The measurements were carried out using convolution potential sweep voltammetry with sweep rates up to more than 2000 V s^{-1}. A rather large potential range was available under these conditions for observing an eventual variation of the electrochemical transfer coefficient with potential. It was observed that the transfer coefficient does vary with potential for each compound in each solvent, clearly beyond experimental uncertainty. The magnitude of the variation increases with the standard rate constant, being of the same order of magnitude as predicted by the Marcus theory, whether or not the double layer effect is corrected for. An advantage of the chosen systems is indeed that the double layer effect is small since the reduction is monoelectronic and involves an uncharged reactant. This is an important reason why the present results suffer much less ambiguity than in previous attempts to detect a potential dependence of the transfer coefficient.

The modern theories of electron transfer at electrodes,[1-5] based on an harmonic approximation, predict a quadratic dependence of the activation free energy upon the electrode potential and therefore a linear dependence of the electrochemical transfer coefficient.

For the electrode reaction (A + 1e$^-$ ⇌ B) with no associated chemical reaction, the rate law can be expressed as

$$\frac{i}{FS} = k(E)\left[(C_A)_0 - (C_B)_0 \exp\frac{F}{RT}(E - E^\circ)\right]$$

where $(C_A)_0$ and $(C_B)_0$ are the concentrations of the reactants just outside the diffuse part of the double layer, E is the electrode potential, E° the standard potential, i the current, and S the electrode surface area. $k(E)$ is then given by

$$-\frac{RT}{F}\ln\frac{k(E)}{Z_{el}} = z\phi_r + \frac{\lambda}{4F} + \frac{E - E^\circ - \phi_r}{2} + \frac{F}{4\lambda}(E - E^\circ - \phi_r)^2 \quad (1)$$

(λ is the reorganization factor, ϕ_r the potential of the plane of the reaction site vs. solution, z the charge number of the reactant, Z_{el} the electrochemical collision factor.) There

are two ways for defining the transfer coefficient which lead, of course, finally to identical results:[6]

$$\alpha = 0.5 + \frac{F}{4\lambda}(E - E^\circ - \phi_r) \quad (2)$$

$$\bar{\alpha} = 0.5 + \frac{F}{2\lambda}(E - E^\circ - \phi_r) \quad (3)$$

with

$$2\alpha = \bar{\alpha} + 0.5 \quad (4)$$

Since $\bar{\alpha}_{ap} = -(RT/F)\,\partial\ln k(E)/\partial E$, $\bar{\alpha}$, and then α, can be derived from the slope of the $k(E) - E$ plot according to

$$\bar{\alpha} = \left[\bar{\alpha}_{ap} - z\frac{\partial\phi_r}{\partial E}\right]\Big/\left[1 - \frac{\partial\phi_r}{\partial E}\right] \quad (5)$$

During the last 10 years there have been several attempts to detect an experimental variation of α with potential and test the validity of eq 2.[8-15] The major difficulty in achieving this task arises from the uncertainties in the estimation of ϕ_r as a function of potential. The difficulty is twofold. On one hand, if ϕ_r varies with potential in a strongly nonlinear manner, the potential dependence of the apparent transfer coefficient, $\bar{\alpha}_{ap}$, will be to a large extent caused by a factor (eq 5) whose de-

Chart I

System	Cathodic scan									Anodic scan								
	A	B	C	D	E	F	G	H	I	J	K	L	M	N	O	P	Q	R
1	2166	724	216	72.2	23.6	6.60	2.40	0.75	0.15	2161	669	212	67.7	22.1	6.96	2.34	0.77	0.14
2	2194	707	228	66.1	22.6	6.55	2.42	0.65	0.25	2076	596	205	56.1	20.4	6.41	2.10	0.64	0.21
3	2322	651	221	69.4	23.5	6.96	2.31			2227	722	218	69.4					
4		659	238	65.1	23.6	6.56												
5	2165	750	218	71.3	22.9	6.95	2.39	0.70	0.24	2171	729	208	68.8	21.9	6.70	2.30		
6	2304	647	221	69.3	23.2	6.99	2.36											
7	2262	666	233	64.9	23.9													

termination is uncertain, obscuring thus the intrinsic potential dependence of α.

On the other hand a knowledge of ϕ_r is also required to extract the reorganization factor λ from the experimental data according to eq 1 in order to test the validity of eq 2. The more highly charged the reactant the more dramatic the ϕ_r effects and the ensuing uncertainties on α and λ determination.

As discussed in detail recently by Weaver and Anson,[8] most previous work suffers from such uncertainties being concerned with highly charged systems (Cr^{3+}|-Cr^{2+},[9,11] V^{3+}|V^{2+},[10] Fe^{3+}|Fe^{2+},[12,13] $Fe(CN)_6^{3-}$|$Fe(CN)_6^{4-}$,[12] Hg^{2+}|Hg^{14}) and potential regions where the $\partial\phi_r/\partial E$ factor might be significant. In the same paper, it is shown that in the case of a singly charged complex, $Cr(H_2O)_5-OSO_3^+$, α does not exhibit any detectable potential dependence when estimating ϕ_2 on the basis of the Gouy–Chapman–Stern (GCS) model of the double layer and of the assumption that the reaction site is located in the outer Helmoltz plane ($\phi_r = \phi_2$). The same conclusion seems to hold also for a dipositive and a tripositive ion in the same series.

In contrast with this behavior, we have recently reported[15] a definite potential dependence of α, clearly beyond the experimental uncertainty, in the reduction of *tert*-nitrobutane in acetonitrile (ACN) and dimethylformamide (DMF).

This variation of α with potential is of the same order of magnitude as predicted by eq 2 whether or not the Frumkin correction is carried out. An obvious advantage of such a neutral molecule/anion radical system is that the ϕ_r effects are small. The kinetic measurements were carried out using convolution potential sweep voltammetry,[16] for the cathodic scan only and for sweep rates ranging from 0.2 to 200 V s^{-1}.

Under these conditions the potential range in which the α variation was observed was 300–350 mV. One of the purposes of the present work was to extend this potential range to 700–950 mV for the same systems using the information contained in the reoxidation i–E curve and sweep rates up to 2300 V s^{-1} [17] in order to see if our preliminary observations are confirmed. We will also report results obtained with two other nitro compounds: nitrodurene and nitromesitylene in ACN and DMF which give rise to faster electron transfers and discuss the prediction that the α variation should then be larger (eq 2).

Experimental Section

The experiments were carried out at 22 °C in ACN and DMF containing 0.1 M tetrabutylammonium iodide on a mercury electrode. The origin and characteristics of the solvents and of *tert*-nitrobutane were the same as in ref 15. Nitrodurene and nitromesitylene were Fluka products purum grade and were used without further purification.

The cell, electrodes, instrumentation, and procedures for cyclic voltammetry, digitalization, convolution, and corrections (sphericity, ohmic drop, and double layer

charging) have been described in ref 17 and references therein. The reference electrode in ACN was an $Ag|AgClO_4$ 0.01 M couple in the same solvent which is 290-mV positive to aqueous SCE. In DMF the reference electrode was an $Ag|AgI$ electrode in DMF which is 420-mV negative to aqueous SCE.

Results

The potential-dependent rate, $k(E)$, was derived from current vs. potential (i–E) and convoluted current vs. potential (I–E) curves according to

$$-\log \frac{k(E)}{D_A^{1/2}} = \log \frac{I_1 - I\left[1 + \exp\frac{F}{RT}(E - E_{1/2})\right]}{i} \quad (6)$$

where D_A is the diffusion coefficient of the reactant, I_1 the limiting convoluted current, and $E_{1/2}$ the reversible half-wave potential.

The $E_{1/2}$ values were obtained from a combined analysis of the i–E and I–E curves as previously described.[15] Assuming the diffusion coefficients of A and B to be practically the same, the standard potentials, $E°$, where considered equal to the $E_{1/2}$'s.

The values of D_A, listed in Table I, were obtained from a previous study of the same nitro compounds in DMF.[18] For ACN these values were multiplied by the ratio of the viscosity coefficients of the two solvents, 2.3. The resulting log $k(E)$–E plots are given in Figures 1 and 2.

For faster and faster systems, i.e., when the charge transfer rate increases and/or the sweep rate v decreases, the numerator on the right-hand side of eq 6 decreases and tends toward zero (Nernst law).

The accuracy of $k(E)$ then decreases; any error in I, I_1, E, $E_{1/2}$ and i has a more and more pronounced influence on $k(E)$ determination. On the other hand, the errors of I, E, and i become important at very high sweep rates, more for the anodic scan than for the cathodic scan.[17] Also, an error in $E_{1/2}$ has a more dramatic effect on the anodic part than on the cathodic part of the log $k(E)$–E plot.

For these reasons, *tert*-nitrobutane in ACN and DMF and nitrodurene in ACN + 2% H_2O provide optimal conditions for obtaining good accuracy over a large range of sweep rates for both the anodic and cathodic scans. This results in a large potential domain available for the observation of the potential dependence of α. The situation is less favorable with the other systems as indicated on Figures 1 and 2 by the fact that less and less anodic curves can be used and that the sweep rate range decreases as the charge transfer rate increases.

In all cases the log $k(E)$–E plots appear as definitely bent toward the potential axis.

The apparent transfer coefficient $\bar{\alpha}_{ap}$ was then obtained by differentiation of the above plots. It is seen in Figures 3 and 4 that the variation of $\bar{\alpha}_{ap}$ with potential is roughly linear in each case. $\partial\alpha/\partial E$ was derived from these last plots as well as the error in its determination according to a least-squares procedure.
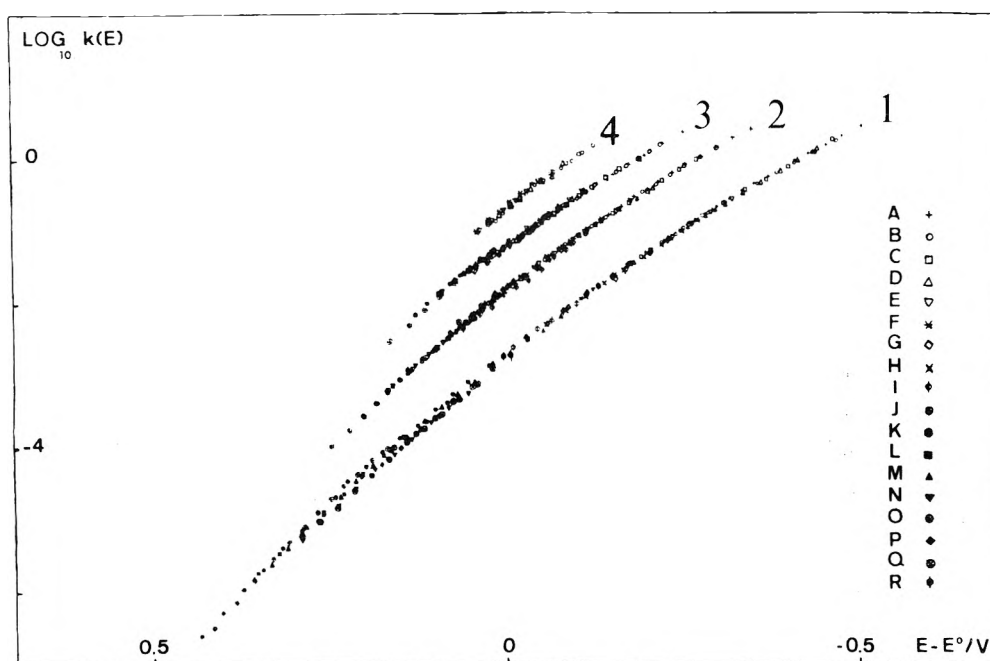
Figure 1. Potential dependent rate constant in ACN with 0.1 M Bu$_4$NI: (1) 3.0 mM *tert*-nitrobutane; (2) 2.0 mM nitrodurene; + 2% H$_2$O; (3) 2.1 mM nitrodurene; (4) 1.64 mM nitromesitylene. Sweep rates in V s^{-1}. See Chart I for definition of symbols.

To analyze these results, let us assume that the reaction site is located at or beyond the outer Helmoltz plane (OHP). Then $0 < |\phi_r| \le |\phi_2|$. On the other hand, ϕ_2 lies between zero and the value predicted by the GCS theory. It follows that ϕ_r also lies between zero and the potential at the OHP according to the GCS theory. For $\phi_r = 0$, the experimental values of $\partial\alpha/\partial E$, immediately deduced from $\partial\bar\alpha_{ap}/\partial E$, are those given in Table I, column 10. On the other hand, eq 1 can be rewritten, taking into account that in the present case $z = 0$, as

$$k(E) = k_{s,ap} \exp\left[-\frac{\alpha F}{RT}(E - E^\circ)\right] \qquad (7)$$

with

$$k_{s,ap} = k_S \exp\left[\frac{\alpha F}{RT}\phi_r\right] \qquad (8)$$

and

$$k_S = Z_{el} \exp(-\lambda/4RT) \qquad (9)$$

k_S, which is here equal to $k_{s,ap}$, was found satisfactorily constant over the log $k(E)-E$ plots. Its average values are given in Table I, column 7. Taking for the electrochemical collision frequency the values (Table I, column 5) derived from the kinetic theory of gases ($Z = (RT/2\pi M)^{1/2}$, where M is molar mass) the reorganization factor λ (Table I, column 8) can be derived from k_S according to eq 9.

Finally the potential dependence of α predicted by the Marcus theory (Table I, column 11) is derived from λ according to eq 2. The value of the transfer coefficient at $E = E^\circ + \phi_r(= E^\circ)$ is also given (column 9) for each system.

For $\phi_r = \phi_2(GCS)$, ϕ_2 was obtained from previous measurements of the double layer capacity of tetra-butylammonium solutions with a nonadsorbable anion (ClO$_4^-$) in ACN[19] and DMF.[18] The zero charge potential was determined by electrocapillary measurements and was found as -0.90 V in ACN and -0.10 V in DMF with the reference electrodes used here. The resulting ϕ_2-E plots are shown in Figures 5 and 6. It is seen that they are linear

over most of the useful potential range, being slightly bent in its positive extremity. When correcting the values of the apparent transfer coefficient according to eq 5, it was found that $\partial\bar\alpha/\partial E$ was very close to $\partial\bar\alpha_{ap}/\partial E$ and that the observed curvature of the log $k(E) - E$ plots cannot be ascribed as a consequence of the slight curvature of the ϕ_2-E plots. Indeed

$$\frac{\partial\bar\alpha}{\partial E} = 1 \bigg/ \left[\left[1 - \frac{\partial\phi_2}{\partial E}\right]\frac{\partial\bar\alpha_{ap}}{\partial E} + \bar\alpha_{ap}\left[(\partial^2\phi_2/\partial E^2)\bigg/\left(1 - \frac{\partial\phi_2}{\partial E}\right)^2\right]\right] \qquad (10)$$

which shows that the effect of ϕ_2 is to render $\partial\bar\alpha/\partial E$ a little larger than $\partial\bar\alpha_{ap}/\partial E$. The maximal value of $\partial^2\phi_2/\partial E^2$ is 0.05 V^{-1}. Thus, for e.g., $\partial\bar\alpha_{ap}/\partial E = 0.40$ V^{-1}, $\partial\bar\alpha/\partial E = 0.45$ V^{-1}.

The values of k_S, λ, and $\alpha(E = E^\circ + \phi_r)$ were calculated as in the preceding case, but taking now into account the values of ϕ_2 represented in Figures 5 and 6. The potential dependence of α as predicted by the Marcus theory is finally given in the last column of Table I.

Discussion

As noted before[15] in the case of *tert*-nitrobutane, the values of the uncorrected standard constant in DMF are somewhat smaller than those previously found by Peover and Powell.[18] This may result from a difference in the amount of residual water in the two series of experiments since water is very likely to preferentially solvate the anion radical.

In each solvent, the rate of electron transfer increases when passing from *tert*-nitrobutane to nitromesitylene, reflecting a decrease in the solvent reorganization energy. This is related to changes in the relative localization of the negative charge on the nitro group rather than to the size of the particle. The radius being estimated as inversely proportional to $Z_{el}^{2/3}$, the reorganization energy according to the Marcus theory would be proportional to $Z_{el}^{2/3}$. The ratio of the λ's of *tert*-nitrobutane and nitromesitylene would then be predicted as equal to 1.2 whereas it is actually 1.6 in ACN and 1.5 in DMF. Between nitrodurene and nitromesitylene the prediction is in the opposite di-
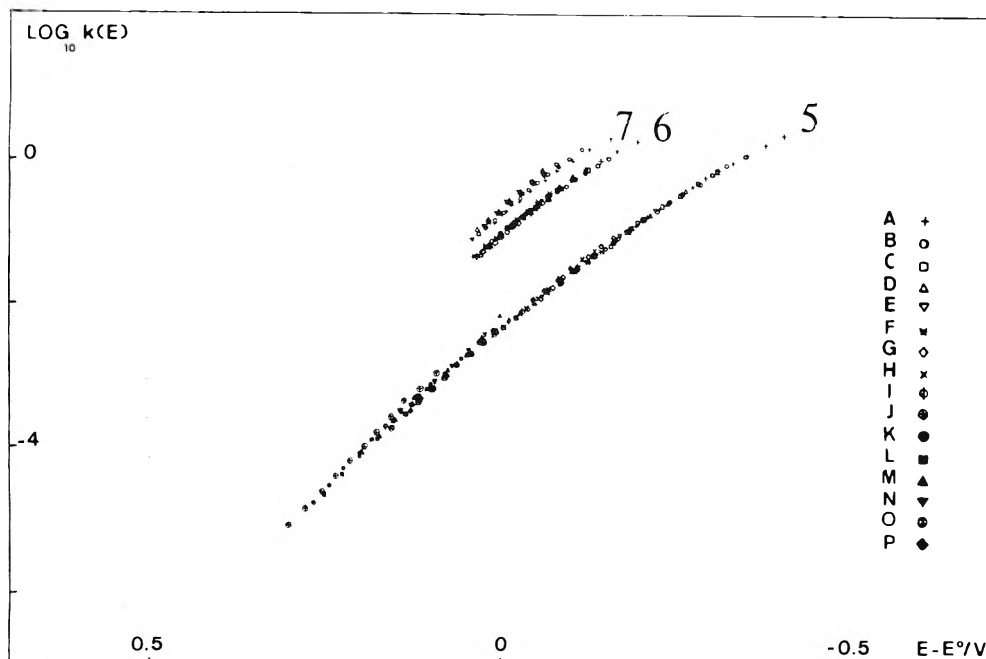
Figure 2. Potential dependent rate constant n DMF with 0.1 M Bu$_4$NI: (5) 2.5 mM *tert*-nitrobutane; (6) 2.3 mM nitrodurene; (7) 1.82 mM nitromesitylene. Sweep rates in V s^{-1}. See Chart I for definition of symbols.
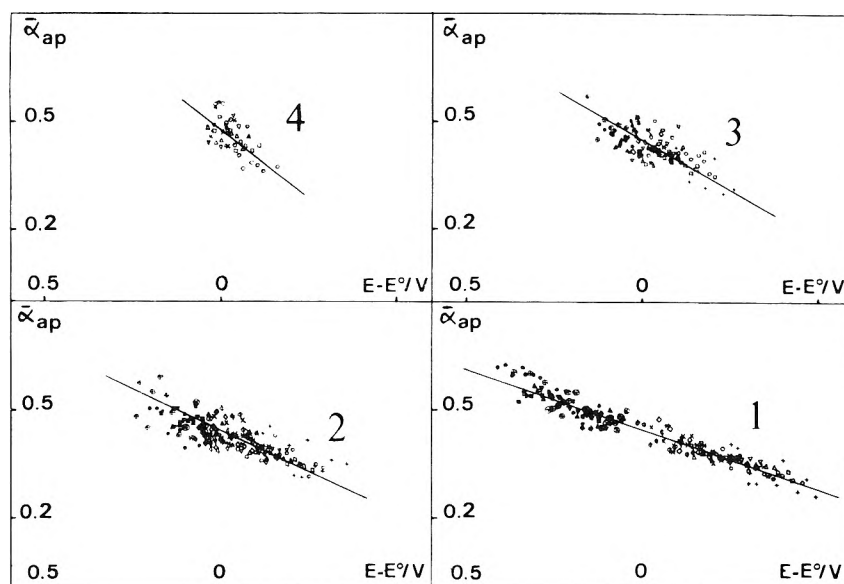
Figure 3. Variation of the apparent transfer coefficient with potential in ACN. Same symbols as in Figure 1.

rection as compared to what is actually observed. On the other hand, it is clear that localization of the charge on the nitro group is more pronounced in the case of the aliphatic compound, *tert*-nitrobutane, than for the two aromatic derivatives. Localization also increases from nitrodurene to nitromesitylene owing the larger electron-donating effect of four methyl groups instead of three.

For the same compound, the standard rate constant is smaller in ACN than in DMF. This reflects the larger solvating power of ACN as compared to DMF, or, more probably, the effect of specific solvation by residual water which is more active in solvating negatively charged particles in ACN than in DMF being less complexed by the first solvent than by the second in accordance with their relative basicities. Similar effects have been noted in the study of the disproportionation equilibrium of anion radicals.[20,21] As expected, this difference decreases when passing from *tert*-nitrobutane to nitromesitylene which corresponds to a decrease of the overall solvation energy. The preferential solvation by water is also clearly evi-

denced by the results obtained with purposely added water (nitrodurene in ACN with 2% water).

As regards the potential dependence of α the present results obtained with *tert*-nitrobutane confirm and reinforce the preceding observations[15] being concerned with a much more extended potential range. With nitrodurene and nitromesitylene the α variation is also clearly apparent although the observations were possible over a smaller potential range. Passing from one compound to the other or varying the nature and composition of the solvent, it is seen that the observed variation of α is of the same order of magnitude as predicted by the Marcus theory whether or not the double layer correction is carried out.

These observations contrast with those of Weaver and Anson[8] who found no significant potential dependence of α in the reduction of chromium(III) complexes in water. The nature and magnitude of the reorganization energy is however different in the two cases: with the nitro compounds in ACN or DMF it involves essentially solvent polarization around the nitro group[18] whereas with the
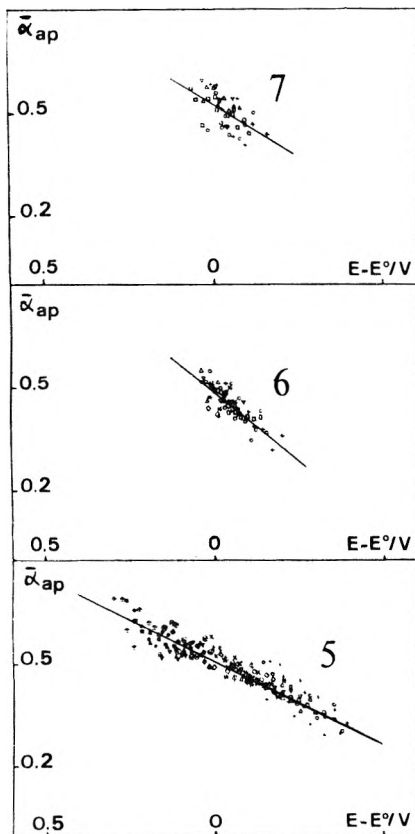
Figure 4. Variation of the apparent transfer coefficient with potential in DMF. Same symbols as in Figure 2.
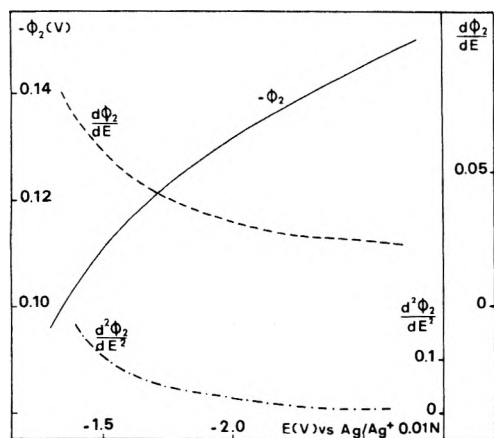
Figure 5. Potential difference between OHP and solution in ACN + 0.1 M Bu$_4$NI and its first and second derivatives.
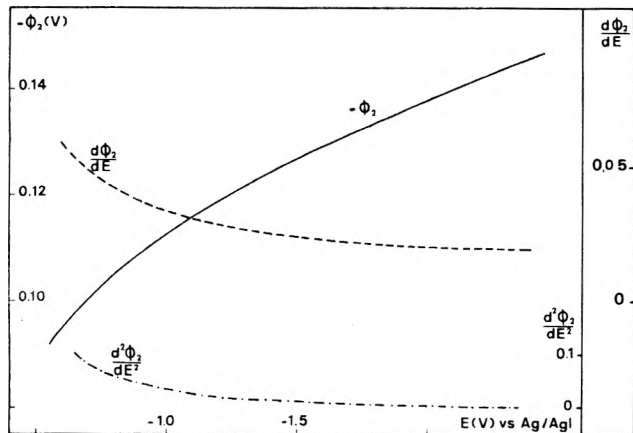
Figure 6. Potential difference between OHP and solution in DMF + 0.1 M Bu$_4$NI and its first and second derivatives.

TABLE I

Solvent	Reactant	$-E^o$, V	D_A, cm^{2}s^{-1}	Z_{el}, cm s^{-1}	$\partial\alpha/\partial E$, V^{-1}	$\phi_r = 0$ k_s, cm s^{-1}	λ/F, V	α ($E^o + \phi_r$)	$\partial\alpha/\partial E$, V^{-1} Expt	Pred (Marcus)	$\phi_r = \phi_2^a$ k_s, cm s^{-1}	λ/F, V	α ($E^o + \phi_r$)	$\partial\alpha/\partial E$, V^{-1} Expt	Pred (Marcus)
ACN	*tert*-Nitrobutane	1.998	3.0 × 10^{-5}	6200	0.33 (±0.01)	2.0 (±0.2) 10^{-3}	1.52 (±0.01)	0.44	0.165 (±0.006)	0.165 (±0.002)	1.9 (±0.2) 10^{-2}	1.29 (±0.01)	0.41	0.174 (±0.006)	0.194 (±0.002)
DMF	*tert*-Nitrobutane	1.277	1.3 × 10^{-5}	6200	0.48 (±0.03)	4.8 (±1.0) 10^{-3}	1.43 (±0.03)	0.51	0.240 (±0.015)	0.175 (±0.003)	5.0 (±1.1) 10^{-2}	1.19 (±0.03)	0.46	0.249 (±0.016)	0.210 (±0.004)
ACN + 2% H$_2$O	Nitrodurene	1.619	1.9 × 10^{-5}	4700	0.45 (±0.04)	1.6 (±0.1) 10^{-2}	1.28 (±0.01)	0.44	0.225 (±0.018)	0.195 (±0.002)	1.2 (±0.1) 10^{-1}	1.08 (±0.01)	0.40	0.245 (±0.020)	0.232 (±0.002)
ACN	Nitrodurene	1.714	1.9 × 10^{-5}	4700	0.55 (±0.06)	6.0 (±0.5) 10^{-2}	1.15 (±0.01)	0.45	0.275 (±0.031)	0.218 (±0.002)	4.7 (±0.4) 10^{-1}	0.94 (±0.01)	0.40	0.294 (±0.033)	0.267 (±0.003)
DMF	Nitrodurene	1.031	8.4 × 10^{-6}	4700	0.79 (±0.19)	9.3 (±0.6) 10^{-2}	1.10 (±0.01)	0.49	0.39 (±0.10)	0.227 (±0.002)	7.2 (±0.5) 10^{-1}	0.89 (±0.01)	0.41	0.41 (±0.1)	0.280 (±0.003)
ACN	Nitromesitylene	1.667	1.9 × 10^{-5}	4900	0.75 (±0.10)	2.0 (±0.1) 10^{-1}	1.03 (±0.01)	0.48	0.37 (±0.05)	0.243 (±0.001)	1.64 (±0.06)	0.81 (±0.01)	0.40	0.40 (±0.08)	0.307 (±0.002)
DMF	Nitromesitylene	1.003	8.4 × 10^{-6}	4900	0.60 (±0.32)	2.0 (±0.1) 10^{-1}	1.03 (±0.01)	0.52	0.30 (±0.16)	0.243 (±0.002)	1.84 (±0.08)	0.80 (±0.01)	0.47	0.31 (±0.17)	0.312 (±0.002)

[a] As in Figures 4 and 5.

chromium complexes the reorganization energy is markedly larger and involves a much more important contribution of the vibration factor.[22] It is thus conceivable that the harmonic approximation is less valid in the second case than in the first.

On the other hand, it is noted that the value of α at $E = E° + \phi_2$ is smaller than predicted by the Marcus theory (0.5), the difference being more important in ACN than in DMF. A possible explanation of this phenomenon is that the solvation mode is different in the starting molecule and in the anion radical especially as far as preferential solvation by water is concerned. It is indeed likely that the primary interaction between the anion radical and water is the formation of a 1–1 adduct which would be involved in a Born-type solvation rather than the anion radical itself. In the framework of an harmonic approximation the parabola representing the potential energy of the product as a function of the reaction coordinate would then be more closed up than that corresponding to the reactant due to a strong close distance interaction between the negative charge and the water molecule in the 1–1 adduct. This would result in a standard value of α (for $E = E° + \phi_2$) smaller than 0.5. The observation that this phenomenon is more pronounced in ACN than in DMF agrees well with water being more active for solvating the anions in the first solvent than in the second.

"Electrochimie Organique").

References and Notes

(1) R. A. Marcus, *J. Chem. Phys.*, **43**, 679 (1965).
(2) R. A. Marcus in "Dalhem Worksnop on the Nature of Seawater, Dalhem Konferenzen", E. D. Goldberg, Ed., Abakon Verlagsgesellschaft, West Berlin, 1975, pp 477–504.
(3) N. S. Hush, *J. Chem. Phys.*, **28**, 962 (1958).
(4) V. G. Levich in "Advances in Electrochemistry and Electrochemical Engineering", Vol. 4, P. Delahay and Tobias, Ed., Interscience, New York N.Y., 1966.
(5) R. R. Dogonadze in "Reactions of Molecules at Electrodes", N. S. Hush, Ed., Wiley-Interscience, London, 1971.
(6) The existence of two possible formal definitions of the transfer coefficient has been pointed out by Bonnaterre and Cauquis[7] and recently rediscussed by Weaver and Anson.[8]
(7) R. Bonnaterre and G. Cauquis, *J. Electroanal. Chem.*, **35**, 287 (1972).
(8) M. J. Weaver and F. C. Anson, *J. Phys. Chem.*, **80**, 1861 (1976).
(9) R. Parsons and E. Passeron, *J. Electroanal. Chem.*, **12**, 525 (1966).
(10) D. M. Mohilner, *J. Phys. Chem.*, **73**, 2652 (1969).
(11) F. C. Anson, N. Rathjen, and R. D. Frisbee, *J. Electrochem. Soc.*, **117**, 477 (1970).
(12) D. H. Angell and T. Dickinson, *J. Electroanal. Chem.*, **35**, 55 (1972).
(13) E. Momot and G. Bronoel, *C. R. Acad. Sci. Paris*, **278**, 319 (1974).
(14) P. Bindra, A. P. Brown, M. Fleischmann, and D. Pletcher, *J. Electroanal. Chem.*, **58**, 39 (1975).
(15) J. M. Saveant and D. Tessier, *J. Electroanal. Chem.*, **65**, 57 (1975).
(16) J. C. Imbeaux and J. M. Saveant, *J. Electroanal. Chem.*, **44**, 169 (1973).
(17) J. M. Saveant and D. Tessier, *J. Electroanal. Chem.*, **77**, 225 (1977).
(18) M. E. Peover and J. S. Powell, *J. Electroanal. Chem.*, **20**, 427 (1969).
(19) W. R. Fawcett and R. O. Loufty, *Can. J. Chem.*, **51**, 230 (1973).
(20) F. Ammar and J. M. Saveant, *J. Electroanal. Chem.*, **47**, 115 (1973).
(21) C. P. Andrieux and J. M. Saveant, *J. Electroanal. Chem.*, **57**, 27 (1974).
(22) J. N. Hale in "Reactions of Molecules at Electrodes", N. S. Hush, Ed., Wiley-Interscience, New York, N.Y., 1971, pp 246–247.

Mercury(II) Iodide in Terphenyls. Solubility and Vapor Pressure

Y. Marcus* and H. Barak

Department of Inorganic and Analytical Chemistry, The Hebrew University, Jerusalem, Israel (Received April 22, 1977)

The solubility of mercury(II) iodide in *m*-terphenyl and its vapor pressure in dilute solution in *p*-terphenyl were measured over a temperature range near its melting point. The results are compared with the expectation from solubility parameter theory, and it is concluded that the transfer of the mercury(II) iodide from the liquid to its solution in either of the terphenyls, either directly or via the vapor, is considerably more endothermic than predicted from that theory, indicating self-interactions of the solvent which are disrupted in these processes.

Introduction

In the course of an investigation into the nature of mercury(II) iodide species in molten alkali nitrates by its distribution between the salt melts and terphenyl solutions,[1,2] it became necessary to characterize the terphenyl phases further. Raman spectroscopic measurements[3] showed that only relatively weak interactions between the solute and solvent occur, and that solvates, if formed, do not have bonds with appreciably covalent character. The results do not preclude, however, interactions by dispersion (London) forces, and, indeed, a noticeable difference between the interactions of mercury(II) iodide with *m*-terphenyl on the one hand and with *p*-terphenyl on the other was observed. Distribution ratios of trace mercury(II) iodide between the former and various alkali nitrate melts were roughly one order of magnitude larger than those between the latter and these melts.[1] It is therefore the aim of the present study to provide thermodynamic information on two equilibrium properties of the solutions: the solubility and the vapor pressure of mercury(II) iodide

in these terphenyls. The temperature dependence of these quantities provides free-energy, enthalpy, and entropy data on the transfer of mercury(II) iodide from its liquid and gaseous states to the dissolved state, and thereby information on its interactions with the terphenyl solvent. This information is valuable also for characterizing terphenyl phases of known activity of mercury(II) iodide for defining its activity in alkali nitrate phases in equilibrium with them.[2]

The two terphenyls used for the present study were selected for the suitability of their liquid ranges for equilibration with molten alkali nitrates: 1,3-diphenylbenzene (*m*-terphenyl) has $T_m = 360$ K (87 °C) and $T_b = 636$ K (363 °C) for work especially with lithium nitrate containing melts, and 1,4-diphenylbenzene (*p*-terphenyl) has $T_m = 486$ K (213 °C) and $T_{subl} = 700$ K (427 °C) for work with potassium or cesium nitrate containing melts. Mercury(II) iodide has a liquid range, $T_m = 530$ K (257 °C) and $T_b = 627$ K (354 °C), compatible with those of the two terphenyls. The solubility of mercury(II) iodide in,
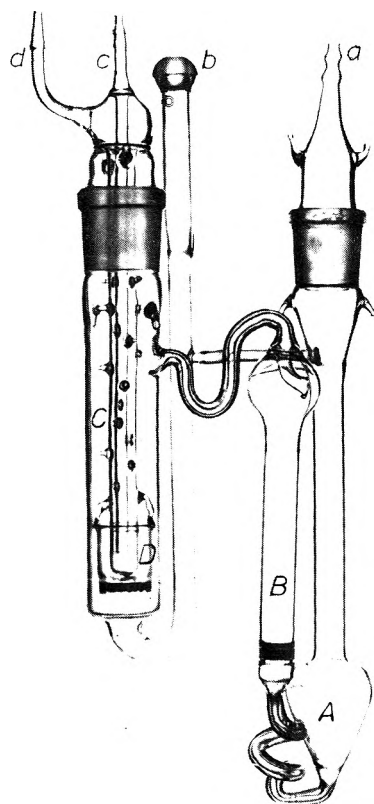
Figure 1. The vessel used for vapor pressure measurements (see text for the explanation of the letters).

Figure 2. The solubility (log s, mole fraction scale) of mercury(II) iodide in terphenyl as a function of the temperature T, K: rectangles, experimental data for m-terphenyl with probable error limits (the datum above the melting point signifies unlimited miscibility); circles, experimental data for p-terphenyl; continuous curve, log s^{id} (eq 5); dashed curve, log s^{id} + log s^{dsp} + log s^{sze} for m-terphenyl (from eq 5, 6, and 9).

and the interaction with, several aromatic hydrocarbons has been reported,[4] but only for room temperature, where the solubility is rather low, <0.01 m. The vapor pressure of pure liquid mercury(II) iodide is known,[5] but not that of its solutions, while the vapor pressure of the terphenyls is, again, known.[6]

Experimental Section

Materials. Reagent grade materials were used without further purification. These included mercury(II) iodide (Malincrodt, AR), m-terphenyl (Eastman Organic Chemicals, White Label), p-terphenyl (Fluka, scintillatron grade), and benzene (Frutarom, AR).

Solubility Measurements. Quantities of mercury(II) iodide and terphenyl were heated together in a tube with stirring, immersed in a constant temperature bath. Samples were removed from the terphenyl phase and weighed, and the terphenyl was dissolved in a known volume of benzene. The mercury(II) iodide was determined by weighing the residue and correcting for the small amount dissolving in the benzene.[4] Attainment of equilibrium was checked by sampling at different times at a given temperature, and on increasing and decreasing the temperature stepwise.

Vapor Pressure Measurements. A transpiration method was employed using the vessel shown in Figure 1. Known weights of terphenyl and of mercury(II) iodide were placed in compartment A. The portion A-B of the vessel was placed in the constant temperature bath, so that the material melted and reached thermal equilibrium. A small pressure of purified nitrogen was applied at a, pushing the melt to compartment B through the coarse sintered glass disk at its bottom, and then the nitrogen was allowed to bubble through the melt at a rate of 30-60 $cm^3 h^{-1}$. The gas carried with it the vapors, which condensed on the cold finger C (cooled by water entering at c and exiting at d). Any flakes of condensed material falling off were collected in basket D. The vessel was connected via exit b to a

second condenser. After passage of a certain volume of nitrogen gas, the liquid mixture was sampled and the condensate was collected in its entirety (nothing was found in the second condenser in series), dissolved in benzene and equilibrated with aqueous 1 M potassium iodide. The benzene phase was dried for the determination of the terphenyl by weight, while the aqueous phase was submitted to atomic absorption determination of the mercury

Results

Solubility in m-Terphenyl. Experiments above the melting point of mercury(II) iodide, at 543 K, showed the two liquids to be mutually miscible in all proportions, producing a dark orange homogeneous liquid. However, a series of experiments at temperatures below the melting point, at 484-525 K, showed limited solubility: solid yellow mercury(II) iodide was in equilibrium with an orange liquid, with results shown in Figure 2. The solubility increases with the temperature according to the expression

$$\log s = -0.379 \pm 0.015 -$$
$$(0.0163 \pm 0.006)(530 - T/K) \qquad (1)$$

where s is the solubility expressed in mole fractions and 530 K = T_m is the melting point of the mercury(II) iodide.

Solubility in p-Terphenyl. A few experiments were made to ascertain the solubility in p-terphenyl relative to that in m-terphenyl (Figure 2). Because of the short temperature range where mercury(II) iodide is solid and p-terphenyl is liquid, no extensive solubility curve was determined.

Vapor Pressure in p-Terphenyl. The range of concentrations employed was between 2 × 10^{-4} and 10^{-3} mole fractions, and the range of temperatures between 513 and 633 K, the latter being near the normal boiling point of mercury(II) iodide. The vapor was found to be enriched in mercury(II) iodide with respect to the liquid, from about
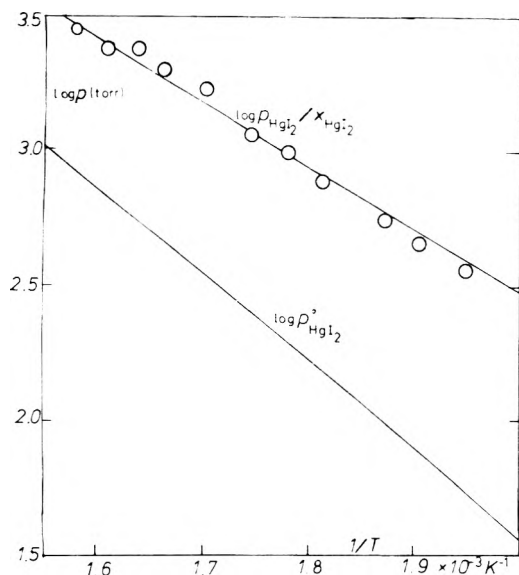
Figure 3. The vapor pressure of mercury(II) iodide p (in Torr) against the reciprocal of the absolute temperature, $1/T$, K^{-1}: circles, p_{HgI_2}/x_{HgI_2} data for solutions in p-terphenyl; upper curve, eq 3; lower curve, $p^{\circ}_{HgI_2}$ data for pure liquid mercury(II) iodide.[5]

19-fold at the lowest temperature to about 6-fold at the highest. The vapor pressure was calculated from the expression

$$p_{HgI_2} = x_{HgI_2}(l)p^{\circ}_{ptp}[1 - (n(l)/n(v)) \times$$
$$\ln (x_{HgI_2}(v)/x_{HgI_2}(l))] \qquad (2)$$

where p°_{ptp} is the vapor pressure of pure p-terphenyl,[6] and n is the total number of moles of the mixture in the liquid (l) and in the vapor (v) phases, the latter condensed from the transporting nitrogen on the cold finger. Since the solutions are dilute, $n(l)$ is not appreciably different from the initial amount of p-terphenyl in the system. The results are shown in Figure 3 as a plot of log $(p_{HgI_2}/x_{HgI_2}(l))$ against the reciprocal of the absolute temperature. In the temperature range of measurement a straight line is obtained

$$\log (p_{HgI_2}/x_{HgI_2}(l)) = (7.177 \pm 0.011) -$$
$$(2349 \pm 6)/T \qquad (3)$$

with p_{HgI_2} expressed in Torr (1 Torr = 133.32 N m^{-2}). It yields $\Delta H^v = 45.0$ kJ mol^{-1} for the enthalpy of vaporization of the mercury(II) iodide from its dilute solutions in p-terphenyl, and $\Delta S^v = 137.4$ J K^{-1} mol^{-1} for the entropy change. This vapor pressure corresponds to a positive deviation from Raoult's law (Figure 3).

Discussion

The solubility of mercury(II) iodide in m-terphenyl (mtp), log s, can be expressed as arising from the sum of several terms

$$\log s = \log s^{id} + \log s^{disp} - \log s^{size} + \log s^{inter} \qquad (4)$$

as follows.

(i) The ideal solubility contribution s^{id} arises from conversion of solid mercury(II) iodide to the liquid, which then mixes ideally with the terphenyl

$$\log s^{id} = [-\Delta h^F_{HgI_2}/(\ln 10)RT_m +$$
$$\Delta c_{p,HgI_2}/(\ln 10)R](T_m - T)/T -$$
$$(\Delta c_{p,HgI_2}/R) \log T_m/T \qquad (5)$$

where $\Delta h^F_{HgI_2} = 18.83$ kJ mol^{-1} is the molar heat of fusion[8] and $\Delta c_{p,HgI_2} = 20.08$ J K^{-1} mol^{-1} is the molar difference in

heat capacity[8] between solid and liquid mercury(II) iodide.

(ii) The contribution from dispersion forces is estimated from the solubility parameters

$$\log s^{disp} = -\phi_{mtp}{}^2 v_{HgI_2}(\delta_{mtp} - \delta_{HgI_2})^2/(\ln 10)RT \qquad (6)$$

where $\phi_{mtp} = (1 - s)/(1 - s(1 - r))$ is the volume fraction of m-terphenyl, $r = v_{HgI_2}/v_{mtp}$, v being the molar volume,[9,10] and $\delta = (\Delta u^v/v)^{1/2}$ is the solubility parameter. The molar energy of vaporization Δu^v is obtained from the vapor pressure expressions

$$\log p = A + B/T + C \log T \qquad (7)$$

$$\Delta u^v = -R(\ln 10)B + R(C - 1)T \qquad (8)$$

with $B = -4626$ K and $C = -5.53$ for mercury(II) iodide[5,8] and $B = -5202$ K and $C = -6.24$ for m-terphenyl.[6] In the range of measurement, 480–530 K, δ_{HgI_2} decreases from 27.23 to 26.24 J$^{1/2}$ cm$^{-3/2}$, and δ_{mtp} from 16.96 to 16.38 J$^{1/2}$ cm$^{-3/2}$, the latter values being considerably lower than that quoted[11] for 363 K, namely, 21.5 J$^{1/2}$ cm$^{-3/2}$, which is consistent with neither the vapor pressures,[6] nor the present solubility data.

(iii) The contribution from the discrepancy between the molecular sizes of the solute and the solvent is estimated from athermal solution theory as

$$\log s^{size} = -\log[1 - \phi_{mtp}(1 - r)] +$$
$$\phi_{mtp}(1 - r)/\ln 10 \qquad (9)$$

where all the terms have already been defined.

(iv) The remaining contribution arises from specific interactions, which have not yet been accounted for. These may include interactions between the π-electron systems of the terphenyl with the solute or changes in the self-interaction of solute or solvent molecules on mixing.

There is no way of calculating item (iv), log s^{inter}, directly from independent data, so it was obtained from eq 4 and the experimental solubility data (Figure 2), items (i), (ii), and (iii) being calculated from the independent data described, but with the experimentally obtained ϕ_{mtp}. The resulting quantity ranges from log $s^{inter} = -0.276$ at 480 K to +0.054 at 530 K, and can be expressed adequately by

$$\log s^{inter} = 3.640 - 1878/T \qquad (10)$$

from which the interaction enthalpy is found to be +36.0 kJ mol^{-1}, an endothermic quantity. This is interpreted as indicating that a self-interaction of either solvent or solute molecules must be overcome for dissolution to occur, which is not compensated sufficiently by an exothermic enthalpy of mutual interaction. Such a self-interaction of solvent molecules has been noted on comparing the entropy of vaporization at the normal boiling point with Trouton's constant, and has been ascribed to their π-electron systems.[6]

Since the molar volume and its temperature variation for p-terphenyl is quite similar to those quantities for m-terphenyl, item (iii) is not expected to differ, nor, of course, item (i) which is solvent independent. The difference in item (ii) is due to the somewhat larger δ_{ptp} compared to δ_{mtp} (arising from $B = -5622$ K and $C = -7.41$ in eq 7 and 8 for p-terphenyl[6]), leading to a somewhat more negative value of log s^{disp}. In the temperature range of measurement this difference amounts to 0.292 $\pm$ 0.002 units in log s^{disp}, being insensitive to the temperature, due to the compensating effect of the variation in $\phi_{(m \text{ or } p)tp}$. The few data available for log s in p-terphenyl are consistent with a solubility curve displaced 0.25 units downward, independently from the temperature (Figure 2). Hence log s^{inter} for solubility in p-terphenyl should have

the same slope with $1/T$ as eq 10 shows, leading to the same endothermic interaction enthalpy.

The p-terphenyl solutions of which the vapor pressures have been measured are much more dilute than the saturated solutions treated above. The calculation of the vapor pressure according to eq 2 depends on the assumption of the validity of Raoult's law and of Henry's law in these dilute solutions. The activity of mercury(II) iodide on the mole fraction scale is given by

$$a_{HgI_2} = x_{HgI_2} \exp(-42.70 + 5240/T + 5.53 \ln T) \quad (11)$$

on combining eq 3 with the corresponding equation for the pure liquid[5,8]

$$\log p^\circ_{HgI_2} = 25.73 - 4626/T - 5.53 \log T \quad (12)$$

The activity coefficient (Henry's law constant) $f_{HgI_2} = a_{HgI_2}/x_{HgI_2}$ varies from 7.56 to 3.49 in the temperature range of measurements, 513–633 K. The assumption of the validity of Henry's law is supported by the observation[1] that the distribution ratio of mercury(II) iodide between p-terphenyl and alkali nitrate melts is independent of its concentration in the range $5 \times 10^{-5} < x_{HgI_2} < 5 \times 10^{-3}$, within which the vapor pressure data were obtained. Distribution data normalized to a given concentration in the terphenyl are thus at a given activity of the solute (at a given temperature), or a given chemical potential, from which interactions in the nitrate melts may be deduced.[2]

These data can serve also to obtain the thermodynamic quantities of transfer from the liquid mercury(II) iodide via the vapor phase to the dilute solution. Equation 11 yields

$$\Delta g^{tr} = 43.6 - 0.355T + 0.0460T \ln T \text{ kJ mol}^{-1} \quad (13)$$

for the Gibbs free energy of transfer, and from $\Delta h^{tr} = -T^2[\partial(\Delta g^{tr}/T)/\partial(1/T)]_{P,x=0}$

$$\Delta h^{tr} = 43.6 - 0.0460T \text{ kJ mol}^{-1} \quad (14)$$

for the enthalpy change. This endothermic enthalpy must be invested in the isobaric and isothermal transfer of mercury(II) iodide from its liquid state to its (infinitely) dilute solution state in p-terphenyl. This is roughly one-half the amount of enthalpy that must be invested to transfer it from the (supercooled) liquid state to the saturated solution in p- or in m-terphenyl at a somewhat lower temperature (see above). The difference between

the two processes may be ascribed to the larger disruptive effect that the solute has in the second process, leading to higher concentrations, on the attractive interactions of the terphenyls[6] already referred to. Obviously, at these higher concentrations, Henry's law is no longer obeyed. The present data do not yield evidence of any mutual attractive interactions of the mercury(II) iodide solute and the terphenyl solvents. This is contrary to the implication in the room-temperature solubility study[4] in aromatic solvents such as benzene, toluene, p-xylene, and mesitylene, but is consistent with the conclusions from the Raman spectroscopic study.[3] Since the available data[12] rule out the self-interaction of the mercury(II) iodide, the interpretation in terms of the disruption of the self-interaction of the terphenyls[6] remains. This disruptive interaction seems to require the same enthalpy for the two terphenyls. An enthalpic contribution differing somewhat for the two terphenyls is the contribution to $\log s^{disp}$ arising from a small difference in δ_{mtp} and δ_{ptp}. This leads to about 0.3 of an order of magnitude ratio in the solubility, not sufficient to explain the order of magnitude difference in the distribution ratios, alluded to in the Introduction. Whether the remainder arises from an entropic contribution remains to be seen when the distribution energetics[1] can be compared.

References and Notes

(1) H. Barak, Ph.D. Thesis, The Hebrew University of Jerusalem, 1976; H. Barak and Y. Marcus, to be published.
(2) Y. Marcus in "Propriétés Thermodynamiques et Utilization des Millieux Ioniques Fondus", C.N.R.S., Marseille, 1974.
(3) H. Barak, A. Loewenschuss, and Y. Marcus, *Spectrosc. Lett.*, in press.
(4) I. Eliezer, *J. Chem. Phys.*, **42**, 3625 (1965).
(5) "Landoldt-Börnstein Tables", II2a 1960, p 50. See also ref 8.
(6) F. W. Reiter, H. Kind, and R. Nehren, *Ber. Bunsenges. Phys. Chem.*, **74**, 470 (1970); see also R. W. Burkhardt, USAEC Reports NAA-SR-Memo-2671 (1958) and NAA-SR-Memo-4493 (1959); F. C. Silvey, NAA-SR-Memo-4187 (1959); J. A. Ellard and W. H. Yanko, USAEC Report IDO-11008 (1961).
(7) J. H. Hildebrand, J. M. Prausnitz, and R. L. Scott, "Regular and Related Solutions", Van-Nostrand-Reinhold, New York, N.Y., 1970.
(8) I. Barin and O. Knacke, "Thermochemical Properties of Inorganic Substances", Springer, Berlin, 1973, p 349.
(9) G. J. Janz and J. D. E. McIntyre, *J. Electrochem. Soc.*, **109**, E42 (1962).
(10) J. Opdycke, J. P. Dawson, R. K. Clark, J. J. Ewing, and H. H. Schmidt, *J. Phys. Chem.*, **68**, 2385 (1964).
(11) R. K. Clark and H. H. Schmidt, *J. Phys. Chem.*, **69**, 3682 (1965).
(12) G. A. Jeffrey and M. Vlasse, *Inorg. Chem.*, **6**, 396 (1966); A. J. Melveger, R. K. Khanna, B. R. Guscott, and E. R. Lippincot, *ibid.*, **7**, 1630 (1967).

Fumarate and Maleate as Spin Traps for Acyl Radicals. Decarboxylation of the Adduct Radicals to Yield 1-Carboxy-3-oxyallyl Radical Dianions

S. Steenken* and M. Lyda

Institut für Strahlenchemie im Max-Planck-Institut für Kohlenforschung, Stiftstrasse 34-36, D-4330 Mülheim, West Germany (Received June 14, 1977)

Publication costs assisted by Institut für Strahlenchemie

Using in situ electron spin resonance it is shown that alkyl, α-hydroxyalkyl, α-carboxyalkyl, and acyl radicals, produced by photochemical α cleavage of oxo compounds RCOR' (R or R' = H, alkyl, α-hydroxyalkyl, α-carboxyalkyl, or carboxyl), react with fumarate and maleate by addition to the olefinic bond to yield the corresponding adduct radicals. With respect to radical scavenging ability, the fumarate dianion and the maleate monoanion are ~50 times more efficient than the maleate dianion. The acyl adducts $RCOCH(CO_2^-)\dot{C}HCO_2^-$ undergo a heterolytic decarboxylation reaction to yield 1-carboxy-3-oxyallyl radical dianions $RC(O^-)=CH\dot{C}HCO_2^-$ and CO_2. The activation energy for this process is ~9.5 kcal/mol if R = CH_3 or C_2H_5. The allyl radical dianions produced exist in two different conformations which originate from related preferred conformations of the allyl radical precursors $RCOCH(CO_2^-)\dot{C}HCO_2^-$.

Introduction

Acyl radicals $R\dot{C}O$, frequently encountered in photochemical reactions involving ketones and aldehydes, are difficult to detect by ESR spectroscopy since their spectra are generally characterized by rather broad lines.[1] The detection of acyl radicals may, however, be facilitated by trapping them with nitroso compounds to yield nitroxide radicals,[2] by addition to the aci anion of nitromethane,[3,4] or by decarboxylative substitution of α-oxocarboxylic acids to yield semidione radicals.[5,6] These scavenging reactions involve addition of $R\dot{C}O$ to N=O, C=N, and C=O double bonds, respectively. Acyl radicals are also able to add to C=C double bonds,[7] but little ESR information on the radicals thus formed is available. Since fumaric acid has been found to be an efficient scavenger for various types of radical,[8] it was decided to study whether fumaric acid is also capable of trapping acyl radicals. Of special interest in this reaction was the question whether the adduct radicals decarboxylate in a way analogous to that observed[5,6] in the reaction of $R\dot{C}O$ with α-oxocarboxylic acids.

Experimental Section

The in situ photolysis experiments were performed as described[9] using a Philips Sp 1000 super-high-pressure mercury arc lamp and quartz optics for focussing the light onto the ESR cell. The far-UV (<250 nm), visible, and IR components of the light were removed by a Schott UG 5 filter. Fumaric and maleic acid, obtained from Fluka, Basel, were "purissimum" quality. Acetaldehyde was Merck analytical grade. The ketones used ("purum" quality, Fluka) were fractionally distilled. Their purity, after distillation, was ≥98% (by GC). Glyoxylic acid, glycolaldehyde, glyceraldehyde, and 4-oxopent-2-enoic acid were of "purum" quality (Fluka) and used as received.

For CO_2 determinations, deoxygenated solutions in 1-cm optical cells were photolyzed at room temperature with UV light from a medium-pressure Hg lamp (Osram HPK). CO_2 was identified by gas chromatography using a 1-m column filled with charcoal at 60 °C and applying the method described by Weeke et al.[10] With this method CO_2 cannot be determined if N_2O is present.

The g factors and coupling constants were determined from simultaneous measurements of field and microwave frequency taking account of the difference in magnetic field between the ESR cell and NMR probe positions. The coupling constants and g factors are estimated to be accurate to 30 mG and 5×10^{-5}, respectively. Where necessary, corrections for second-order effects[11] were made.

Results and Discussion

1. *Radicals Formed by Reaction of Fumarate and Maleate with $CH_3\dot{C}O$ and Alkyl Radicals.* Photolysis of oxo compounds RCOR' in solvents of weak H-donor properties provides a convenient source of acyl radicals. If R' is characterized by a higher degree of α branching or α substitution than R, Norrish type I cleavage of electronically excited RCOR' results predominantly in $R\dot{C}O$ and $\dot{R}'$.[1,12,13] For example, if R = CH_3 and R' = C_2H_5, $CH_2CH(CH_3)_2$, $CH(CH_3)_2$, $C(CH_3)_3$, CH_2OH, $CH(CH_3)OH$, or $C(CH_3)_2OH$, α fragmentation leads to $CH_3\dot{C}O$, the ESR spectrum of which can be observed at <-70 °C, and to $\dot{R}'$.[1]

On photolysis at ~0 °C of 0.1-0.4 M aqueous solutions of the methyl alkyl ketones described, only $\dot{R}'$ radicals were observed. The fact that $CH_3\dot{C}O$ is not detected is probably due[1] to the broad lines of $CH_3\dot{C}O$ at 0 °C as compared to -70 °C. On adding fumarate to these solutions, the stationary concentration of $\dot{R}'$ decreases. If the pH of the solutions is in the range 7-10, lines due to other radicals become visible (Figure 1). The steady state concentration of these radicals increases with increasing [fumarate] up to a saturation level at ~20 mM fumarate while the amplitudes of the lines due to $\dot{R}'$ decrease correspondingly. The same effects are observed when fumarate is replaced by maleate. However, the concentration of maleate necessary to obtain the same reduction in the stationary concentration of $\dot{R}'$ or to observe the same steady state concentration of the newly formed radicals is larger by a factor of ~50 than in the case of fumarate. On photolysis of equimolar solutions of CH_3COR' in the presence of fumarate the concentration of all the radicals formed increases in the series R' = C_2H_5 ~ $CH_2CH(CH_3)_2$ < $CH(CH_3)_2$ ~ CH_2OH < $CH(CH_3)OH$ < $C(CH_3)_2OH$ ~ $C(CH_3)_3$, which parallels the tendency[1,12,13] of electronically excited CH_3COR' to undergo α fragmentation.

The spectra observed on reaction of fumarate or maleate with the species originating from decomposition of electronically excited CH_3COR' are assigned to (a) alkyl ad-
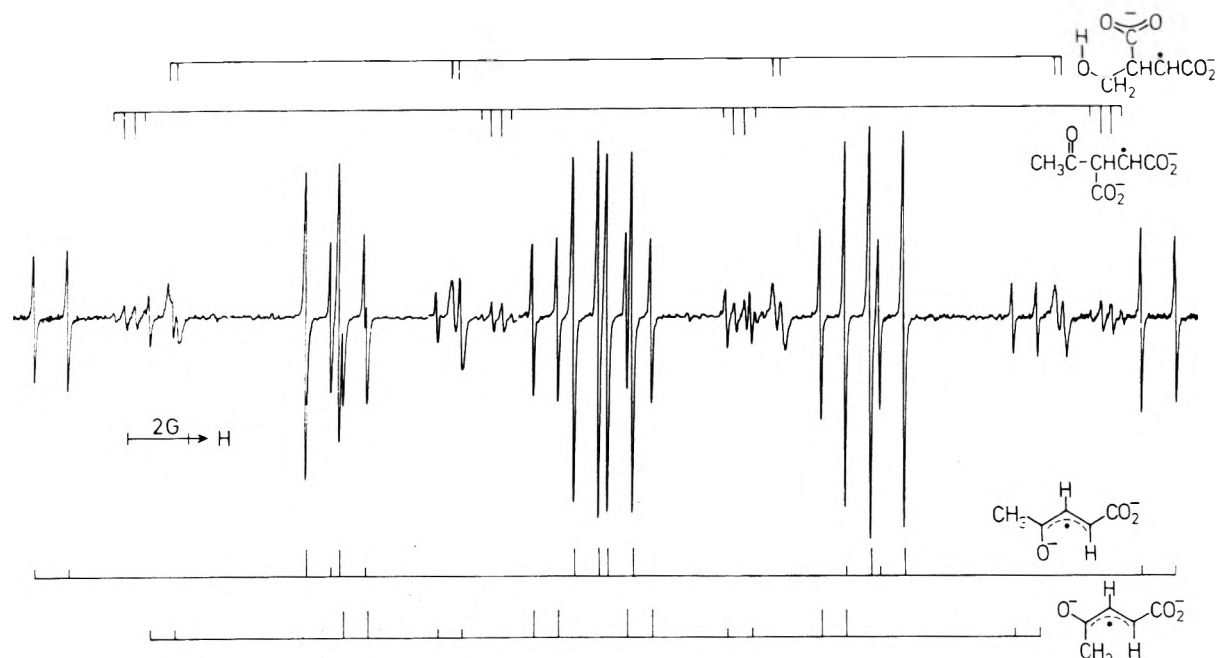
Figure 1. ESR spectra of radicals obtained on photolysis of 0.29 M hydroxyacetone in the presence of 21 mM fumarate at pH 10.5 and ~ 3 °C.

ducts $R'CH(CO_2^-)\dot{C}HCO_2^-$, (b) the acetyl adduct $CH_3COCH(CO_2^-)\dot{C}HCO_2^-$, and (c) $CH_3C(O^-)=CH\dot{C}HCO_2^-$, an allyl radical which is present in two isomeric forms (I and II). Isomer I is characterized by a larger stationary concentration ([I]/[II] = 2.4 at ~ 0 °C), larger coupling constants, and a lower g factor as compared to isomer II (Table I).

The alkyl adducts $R'CH(CO_2^-)\dot{C}HCO_2^-$ were identified by comparison of the coupling constants for C_α and C_β and the g factors with those[8] of identical or similar radicals and by additional couplings due to and characteristic of R' (Table II).

In order to confirm the assignment of the acetyl adduct, $CH_3\dot{C}O$ was produced by an alternative method. An aqueous solution containing 0.5 M acetaldehyde and 5 mM fumarate was irradiated using the in situ radiolysis[14] ESR method. In this system the OH radicals formed react with acetaldehyde to yield[15] acetyl radicals. Besides $CH_3COCH(CO_2^-)\dot{C}HCO_2^-$, the two isomers (I and II) of $CH_3C(O^-)=CH\dot{C}HCO_2^-$ were observed. The ratio [I]/[II] was the same as in the case of formation of I and II using photochemically produced acetyl radicals.[16] From a dependence on pH of the stationary concentrations of $CH_3COCH(CO_2^-)\dot{C}HCO_2^-$ and $R'CH(CO_2^-)\dot{C}HCO_2^-$ in the fumarate system, the pK_a values of these adduct radicals are estimated to be 5–6, in agreement with values reported[17,18] for similar radicals.

The allyl radical $CH_3C(O^-)=CH\dot{C}HCO_2^-$ was identified by producing it independently (using the in situ radiolysis ESR method) by reduction at pH >6 of 4-oxopent-2-enoic acid with the hydrated electron, $\dot{C}O_2^-$, or ketyl radical anions $R_1R_2\dot{C}O^-$ (R_1 and R_2 = H or CH_3, reaction 1). $\dot{C}O_2^-$

$$CH_3\overset{O}{\underset{\|}{C}}CH=CHCO_2^- + e_{aq}^- \; (\dot{C}O_2^-, \; \overset{R_1}{\underset{R_2}{\diagdown}}\dot{C}\text{-}O^-)$$

$$\rightarrow CH_3\overset{O^-}{\underset{|}{C}}CH=CHCO_2^- \longleftrightarrow CH_3\overset{O^-}{\underset{|}{C}}=CH\dot{C}HCO_2^- \; (- \; CO_2,$$
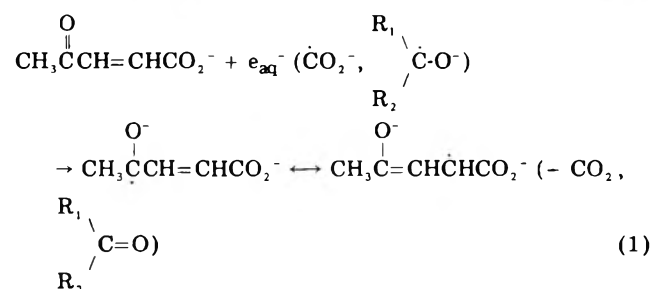
$$\overset{R_1}{\underset{R_2}{\diagdown}}C=O) \tag{1}$$

and $R_1R_2\dot{C}O^-$ were generated by H abstraction from formate and R_1R_2CHOH by OH radicals. For $CH_3C\text{-}(O^-)=CH\dot{C}HCO_2^-$ four isomeric forms (A–D, R = CH_3) are
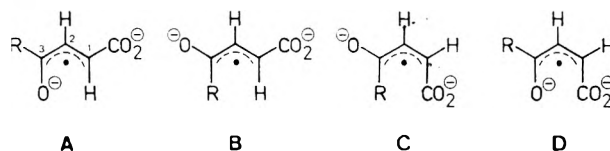
conceivable of which only two were observed. On the basis of their ESR parameters, these two isomers are identical with I and II.

Of the four conformers, D should be the least stable due to the close proximity of the negatively charged oxyl and carboxyl groups. In C the distance between the centers of charge is larger. However, as seen from molecular models, steric interaction between R and CO_2^- is considerable, except in the case where R = H. In B the distance between the centers of charge is maximal. Some steric interaction between R and C_1–H is, however, possible. Therefore, for voluminous R's conformer A is expected to be the most stable conformation. On the basis of these considerations it is suggested that the allyl type radicals formed on reduction of 4-oxopent-2-enoic acid or on reaction of $CH_3\dot{C}O$ with fumarate have the conformations A and B. Assignment of I to A is then possible on the basis of the experimental observation (Table I) that the ratio A/B of the stationary concentrations of the isomers increases from 1.4 to ≥8.8 in going from R = H to R = C_6H_5. Some support for this assignment may also be derived from a comparison of the coupling constants of the methyl group in I and II with those[19] in trans and cis-1-methallyl radicals. The methyl couplings in trans-1-methallyl, which corresponds to conformation A, are larger by a factor of 1.2 than those in cis-1-methallyl, which corresponds to B. In I and II the ratio of the methyl coupling constants is 1.4.

From the dependence on pH of the stationary concentration of $CH_3C(O^-)=CH\dot{C}HCO_2^-$, produced by reaction of e_{aq}^- with 4-oxopent-2-enoic acid, the pK_a value of the radical is estimated to be 6–7. The lifetime of the monoanion or neutral radical must be much shorter than

TABLE I: Coupling Constants (Gauss) and g Factors of 1-Carboxy-3-oxyallyl Radical Dianions in Aqueous Solution at 0-5 °C
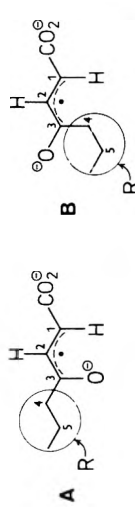
Oxo compound(s) photolyzed	Radical	R	Conformation	a_1	a_2	a_3	a_4	a_5	$[A]/[B]$ [b]	g	Notes
HCOX (X = CO$_2^-$, CH$_2$OH, CH(OH)CH$_2$OH)	XI	H	A	10.18	0.35	9.50				2.00366	
	XII	H	B	10.16	≤0.07	8.32			1.4	2.00388	
CH$_3$COX (X = C$_2$H$_5$, CH$_2$CH(CH$_3$)$_2$, CH(CH$_3$)$_2$, C(CH$_3$)$_3$, CH$_2$OH, CH(CH$_3$)OH, C(CH$_3$)$_2$OH)	I	CH$_3$	A	9.85	1.12		9.00(3)			2.00359	
CH$_3$CH$_2$COX (X = C$_2$H$_5$, CH(CH$_3$)$_2$)	II	CH$_3$CH$_2$	B	9.54	0.80		6.41(3)			2.00380	
	III	CH$_3$CH$_2$	A	9.88	1.17		6.61(2)	≤0.05	2.4	2.00356	
	IV	CH$_3$CH$_2$	B	9.53	0.83		4.22(2)	≤0.05	3.5	2.00378	
CH$_3$CH$_2$CH$_2$COCH$_2$CH$_2$CH$_3$	V	CH$_3$CH$_2$CH$_2$	A	9.76	1.18		6.16(2)	0.29(2)	≥4.5	2.00355	c, d
(CH$_3$)$_2$CHCOCH(CH$_3$)$_2$	VI	(CH$_3$)$_2$CH	A	9.77	1.25		3.78	0.14(6)	≥6.3	2.00355	e
HOCH$_2$COCH$_2$OH	VII	HOCH$_2$	A	10.13	0.50		8.37(2)	0.11	≥7.0	2.00350	f, g
$^-$O$_2$CCH$_2$COCH$_2$CO$_2^-$	VIII	$^-$O$_2$CCH$_2$	A	9.85	0.95		6.79(2)			2.00359	
$^-$O$_2$CCH$_2$COCH$_2$CO$_2^-$	IX	$^-$O$_2$CCH$_2$	B	9.42	0.60		3.97(2)		3.8	2.00382	
C$_6$H$_5$COX (X = H, CO$_2^-$)	X	C$_6$H$_5$	A	8.61	0.19		2.21 (para), 1.95(2) (ortho), 0.68(2) (meta)		≥8.8	2.00346	h

[a] The indices of the coupling constants a refer to the protons bonded to C$_1$-C$_5$ as indicated above. [b] This ratio decreases by ≤10% in going from 0 to 30 °C. [c] Solvent H$_2$O/tert-butyl alcohol 1.25:1, 15 °C. [d] a_6 ≤ 0.1 G. [e] Solvent H$_2$O/tert-butyl alcohol 2:1, 10 °C. [f] a_5 refers to OH. [g] At 20-30 °C further lines are observed which are possibly due to an isomer of type B. [h] Solvent H$_2$O/tert-butyl alcohol 5:1, 20 °C.

TABLE II: Coupling Constants (Gauss) and g Factors of α,β-Dicarboxyalkyl Radical Dianions in Aqueous Solution at 0-10 °C
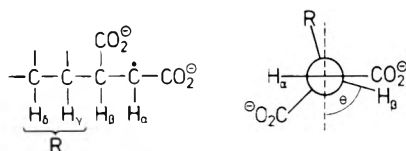
R	a_α	a_β	a_γ	a_δ	g	Notes
H	20.42	23.59(2)			2.00325	a
CH_3	20.18	10.16	0.73(3)		2.00325	b
CH_3CH_2	20.04	8.42	0.53, 0.25	0.24(3)	2.00326	
$CH_3CH_2CH_2$	20.02	8.10	0.62, $\leqslant$0.16	0.31(2)	2.00324	
$(CH_3)_2CH$	19.82	5.34	0.83	0.41(3), 0.20(3)	2.00328	c
$(CH_3)_3C$	19.72	5.36		0.34(9)	2.00331	
$HOCH_2$	20.22	9.51	0.25, 0.08		2.00327	b
$HOCH_2CH(OH)$	20.32	10.72	1.31	0.13(2)	2.00323	d
$CH_3CH(OH)$	20.49	7.14	$\leqslant$0.11	0.27(3)	2.00332	b
$(CH_3)_2COH$	19.97	5.88	Not resolved		2.00329	b, e
CO_2^-	20.16	8.35			2.00334	b
$^-O_2CCH_2$	20.23	10.27	0.49, $\leqslant$0.07		2.00327	
CH_3CO	20.39	12.18		0.34(3)	2.00326	
CH_3CH_2CO	20.42	11.74		0.58, 0.22	2.00325	

^{a} From ref 20. ^{b} Similar parameters are reported in ref 8. ^{c} At 30 °C the δ protons are equivalent (a_δ = 0.21 G(6), a_γ = 0.94 G). ^{d} See footnote 31. ^{e} 30 °C.
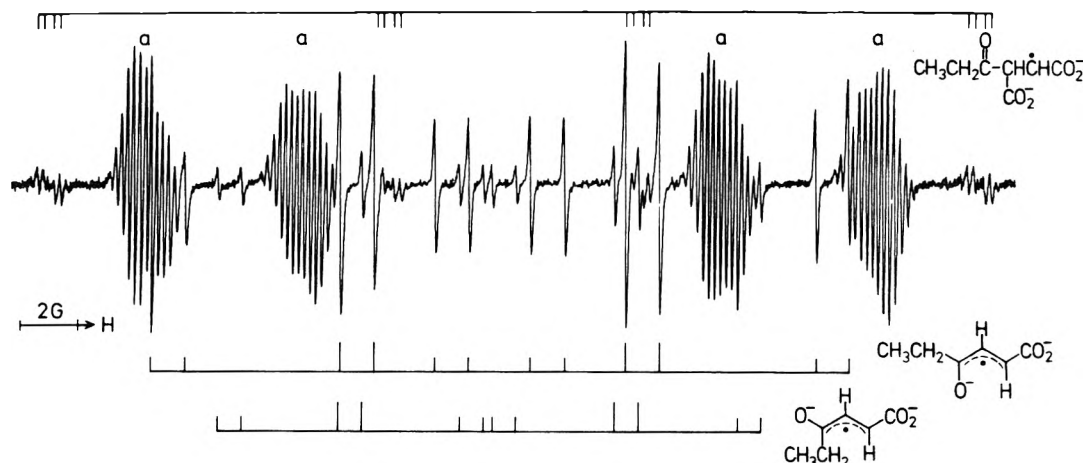
Figure 2. ESR spectra of radicals observed on photolysis of 0.13 M ethyl isopropyl ketone in the presence of 34 mM fumarate at pH 9.4 and ~3 °C. The letters "a" denote groups of lines due to $(CH_3)_2CHCH(CO_2^-)\dot{C}HCO_2^-$.

that of the dianion radical. This is concluded from the low signal-to-noise ratio of lines observed at pH $\leq$6.

2. *Radicals Formed by Reaction of Fumarate with Species Obtained from Photolysis of RCOR' (R, R' $\neq$ CH$_3$).* Reaction of 20-40 mM fumarate at pH 7-10 with $CH_3CH_2\dot{C}O$ and $CH_3\dot{C}H_2$ or $(CH_3)_2\dot{C}H$, produced[1] by photolysis of 0.2 M diethyl ketone or ethyl isopropyl ketone, respectively, yields the radicals $R'CH(CO_2^-)$-$\dot{C}HCO_2^-$ (R' = C_2H_5 or $(CH_3)_2CH$), CH_3CH_2COCH-$(CO_2^-)\dot{C}HCO_2^-$, and two isomers (III and IV) of a radical which is assigned the structure $CH_3CH_2C(O^-)$=$CH\dot{C}HCO_2^-$ (Figure 2). III and IV differ with respect to g factor, coupling constants, and relative stationary concentrations (Table I) in a way similar to that observed for I and II. [III]/[IV] = 3.5 as compared to 2.4 for [I]/[II]. On the basis of the ESR parameters and of their relative abundance, III and IV are assigned to conformations A and B, respectively ($R = C_2H_5$).

On reaction of 10-20 mM fumarate with $CH_3CH_2CH_2\dot{C}O$ and $CH_3CH_2\dot{C}H_2$, produced[1] by photolysis of 50 mM di-n-propyl ketone, the radical $CH_3CH_2CH_2CH(CO_2^-)\dot{C}HCO_2^-$ and only one isomer (V) of $CH_3CH_2CH_2C(O^-)$=$CH\dot{C}HCO_2^-$ were detected. The acyl adduct

$CH_3CH_2CH_2COCH(CO_2^-)\dot{C}HCO_2^-$ could not be positively identified. The ESR parameters of V (Table I) are similar to those observed for radicals I and III. A second isomer of $CH_3CH_2CH_2C(O^-)$=$CH\dot{C}HCO_2^-$ would have been detected if present with a signal-to-noise ratio of 2. Assuming equal line width and microwave saturation behavior for this isomer and V the ratio [V]/[second isomer] is determined to be $\geq$4.5. On the basis of a comparison of its coupling constants and g factor with those of I and III, conformation A (R = $CH_3CH_2CH_2$) is suggested for V.

On reaction of fumarate at pH 8-10 with $^-O_2CCH_2\dot{C}O$ and $\dot{C}H_2CO_2^-$, produced[9] by photolysis of 50 mM 1,3-dicarboxyacetone, two radicals were observed (Figure 3): the allyl radical $^-O_2CCH_2CH(O^-)$=$\dot{C}HCO_2^-$, of which two isomers (VIII and IX) were present, and the adduct of $\dot{C}H_2CO_2^-$ to fumarate, $^-O_2CCH_2CH(CO_2^-)\dot{C}HCO_2^-$. This radical has been prepared[20] by H abstraction from tricarballylic acid. In support of the addition mechanism of formation, the concentration of $^-O_2CCH_2CH(CO_2^-)\dot{C}HCO_2$ increases with increasing concentration of fumarate in the range 2-40 mM while that of $\dot{C}H_2CO_2^-$ decreases correspondingly. The radical was also prepared by photolysis of 0.1 M H_2O_2 in the presence of 1 M acetate and 10 mM
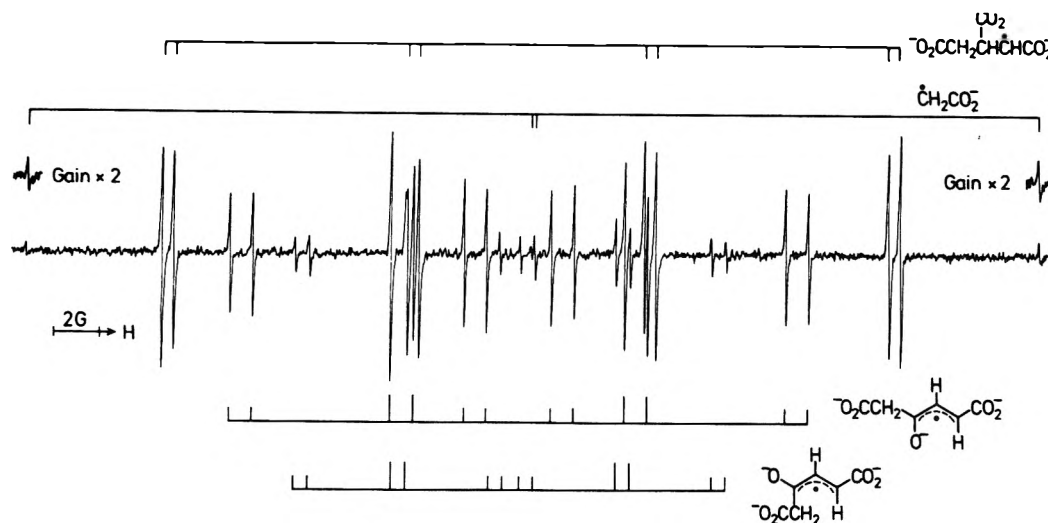
Figure 3. ESR spectra of radicals produced by photolysis of 50 mM acetone-1,3-dicarboxylate in the presence of 32 mM fumarate at pH 10.4 and 20 °C.
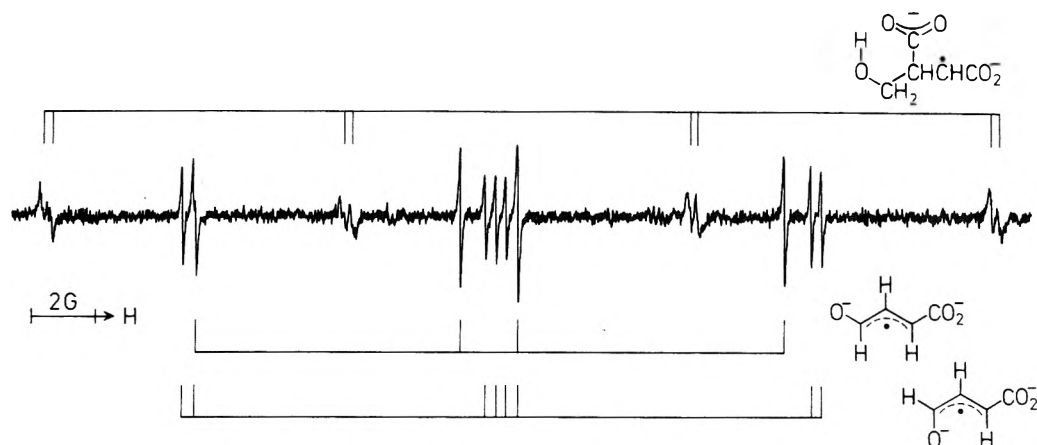
Figure 4. ESR spectra of radicals obtained on photolysis of 0.17 M glycolaldehyde in the presence of 22 mM fumarate at pH 9.7 and ~3 °C.

fumarate. In this system ~50% of the photolytically produced OH radicals react with acetate to yield $\dot{C}H_2CO_2^-$ which then adds to fumarate.

The formyl radical $H\dot{C}O$, used to produce XI and XII, the two observed isomers of $HC(O^-)=CH\dot{C}HCO_2^-$, was generated from three different compounds: by acetone sensitized α cleavage[5,6] of glyoxylate $HCOCO_2^-$ and by α fragmentation of electronically excited glycolaldehyde[21] or glyceraldehyde. In all cases the occurrence of α cleavage follows also from the presence of the adduct radicals $HC(CO_2^-)_2\dot{C}HCO_2^-$, $HOCH_2CH(CO_2^-)\dot{C}HCO_2^-$, and $HOCH_2CH(OH)CH(CO_2^-)\dot{C}HCO_2^-$, respectively (Table II and Figure 4). Pivaldehyde, which is an efficient source of $H\dot{C}O$ when photoexcited in nonaqueous media,[1,22] cannot successfully be used in aqueous solution at pH >7 since it apparently undergoes a Cannizzaro reaction.

The assignment of the coupling constants measured for XI and XII (Table I) to the individual protons of XI and XII is based on a comparison with coupling constants determined for the corresponding conformers of $DC-(O^-)=CD\dot{C}HCO_2^-$ and $HC(O^-)=CD\dot{C}HCO_2^-$, obtained[23] by aldol condensation of glyoxylate with deuterated acetaldehyde followed by water elimination and one-electron reduction. Comparison of the coupling constants of $HC(O^-)=CH\dot{C}HCO_2^-$ with those[24] of $HC(O^-)=CH\dot{C}H_2$ indicates that replacement of H by CO_2^- leads to an overall reduction of the unpaired spin density in the allylic system. This is suggested to be due to the contribution of mesomeric structures such as $HC(O^-)=CHCH=CO_2^-\cdot$ to the delocalization of the unpaired spin.

TABLE III: Yield of CO_2 (Arbitrary Units) Obtained on Photolysis[a] of 0.4 M CH_3COR in the Presence of 5 mM Fumaric or Maleic Acid at pH 4

	Yield of CO_2		
R	Fumaric acid	Maleic acid	Notes
CH_3	c	c	
C_2H_5	51	46	
$(CH_3)_2CH$	96	105	
$(CH_3)_3C$	87	100	b

[a] Under the conditions employed the yield of CO_2 was linearly dependent on UV dose. [b] Solvent H_2O/*tert*-butyl alcohol 1:1. [c] Not measureable.

3. *Studies on the Mechanism of Formation of Allyl Radicals.* On photolysis of aqueous solutions of the oxo compounds described in the presence of fumaric or maleic acid carbon dioxide is formed as a reaction product. The yield of CO_2 is independent of pH between pH 2 and 10. From Table III it is evident that the yields of CO_2, obtained by photolysis of CH_3COR in the presence of fumaric or maleic acid, show the same dependence on R as the steady state concentrations of the radicals I and II (see section 1) and that the yields reflect the tendency[1] of electronically excited CH_3COR to undergo α cleavage.

In order to clarify whether the CO_2 produced is due to reaction with $CH_3\dot{C}O$ or with $\dot{R}$, a 0.5 M aqueous solution of CH_3CHO, containing 5 mM fumaric acid and saturated with He, was ^{60}Co γ irradiated at pH 4. Under these conditions the OH radicals produced by the γ radiation

$(G(\text{OH}) = 2.8)$ react quantitatively with CH_3CHO to yield[15] $CH_3\dot{C}O$. If the H atoms generated by the radiation react with CH_3CHO also by abstraction of the aldehydic H, $G(CH_3\dot{C}O)$ and, since $CH_3\dot{C}O$ is scavenged by fumarate, $G(CH_3COCH(CO_2^-)\dot{C}HCO_2^-)$ are calculated to be 3.2. $G(CO_2)$ was found to be 3.3. In a second experiment CH_3CHO was replaced by CH_3OH. In this case $\dot{C}H_2OH$, produced with $G \geq 2.5$, reacts with fumarate to give a hydroxyalkyl adduct (see section 1 and ref 8). $G(CO_2)$ was found to be <0.1. In order to test whether alkyl adducts give rise to CO_2, the radical $CH_3CH(CO_2^-)\dot{C}HCO_2^-$ was produced by H abstraction from methylsuccinic acid using OH radicals produced by γ radiolysis of a He saturated solution. In this system $G(CH_3CH(CO_2^-)\dot{C}HCO_2^-) \approx 1.8$.[25] At pH 4 $G(CO_2)$ was found to be only 0.1. It is therefore concluded that the CO_2 formed on photolysis of CH_3COR in the presence of fumarate or maleate originates from reaction of $CH_3\dot{C}O$. The involvement of acyl radicals in the production of CO_2 follows also from the effect of fumarate on the yield of CO from photolysis of di-hydroxyacetone. On photoexcitation this compound undergoes α cleavage to yield $HO\dot{C}H_2$ and $HOCH_2\dot{C}O$ followed by decarbonylation of $HOCH_2\dot{C}O$.[9] Addition of fumarate to an aqueous solution of dihydroxyacetone results in a decrease in the photochemical yield of CO and in the production of CO_2.

The trapping of $HOCH_2\dot{C}O$ by fumarate is supported by the results of ESR experiments. When fumarate is added to a 0.2 M aqueous solution of dihydroxyacetone at ~ 0 °C, the amplitudes of the lines due to $HOCH_2\dot{C}O$ ($a = 1.90$ G(2), $g = 2.00074$) decrease and new lines, assigned to $HOCH_2C(O^-)=CH\dot{C}HCO_2^-$ (VII), are detected. An analogous observation is made with respect to the benzoyl radical which, like $HOCH_2\dot{C}O$, is exceptional among the acyl radicals in that it may be observed[26] by ESR at ~ 0 °C. Addition of fumarate at pH ~ 10 to a 0.1 M solution of benzaldehyde under photolysis results in the disappearance of $C_6H_5\dot{C}O$ and in the production of $C_6H_5C(O^-)=CH\dot{C}HCO_2^-$ (X).

The experimental results may thus be rationalized in terms of the reaction

$$
\text{R\dot{C}O} + \begin{array}{c} ^-O_2C \\ \diagdown \\ / \\ H \end{array} C=C \begin{array}{c} H \\ \diagup \\ \diagdown \\ CO_2^- \end{array} \xrightarrow{A} \begin{array}{c} O\ CO_2^- \\ \| \ | \\ RC\text{-}CH\dot{C}HCO_2^- \end{array}
$$

$$
\xrightarrow{B} \begin{array}{c} O^- \\ | \\ RC=CH\dot{C}HCO_2^- \end{array} + CO_2 \qquad (2)
$$
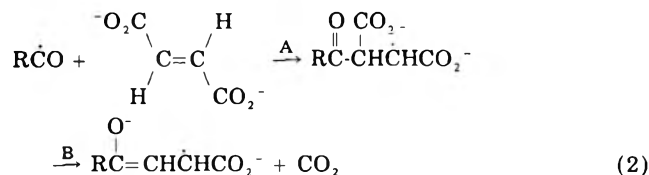
For $R = CH_3$ and C_2H_5 the acyl adducts, formed in step A, were observed by ESR (Table II). From measurements at pH 8–10 and ~ 0 °C of the dependence on [fumarate] of $[CH_3COCH(CO_2^-)\dot{C}HCO_2^-]$ and $[HOCH_2CH(CO_2^-)\dot{C}HCO_2^-]$, produced on photolysis of hydroxyacetone in the presence of fumarate, the rate constant for addition of $CH_3\dot{C}O$ to the fumarate dianion is determined to be a factor of ~ 1.5 larger than that for addition of $HO\dot{C}H_2$, which has been estimated[8] to be $\sim 10^7$ M^{-1} s^{-1}. From similar measurements at ~ 0 °C, using maleate instead of fumarate, it is concluded that the rate constants for addition to the maleate dianion of $CH_3\dot{C}O$, $C_2H_5\dot{C}O$ and the alkyl and α-hydroxyalkyl radicals generated (see section 1) are ~ 50 times lower than those for addition to fumarate dianion. A qualitatively similar observation has been made by Neta[8] with respect to alkyl and α-hydroxyalkyl radicals.

At pH 8–10, the ratio of the steady state concentrations of $CH_3C(O^-)=CH\dot{C}HCO_2^-$ in the fumarate and maleate systems, respectively, decreases with increasing temperature. This ratio is proportional to $k(CH_3\dot{C}O + \text{fumarate})/k(CH_3\dot{C}O + \text{maleate})$. From the temperature de-

pendence of this ratio and using a procedure as described by Hamilton and Fischer,[27] the difference in the activation energies for addition of $CH_3\dot{C}O$ to the dianions of fumarate and maleate, respectively, is calculated to be 2.3 ± 0.2 kcal/mol.

The monoanion of maleic acid seems to react with acyl, alkyl, and α-hydroxyalkyl radicals faster than the dianion. This is concluded from the observation that the steady state concentrations of the adduct radicals increase by a factor ≥ 20 on decreasing the pH from, e.g., 10, to ~ 6.5. Since at this pH the adduct radicals are still almost fully ionized[28] and their lifetimes therefore unchanged as compared to pH 10, the increase in stationary concentration must be due to an increase in production rate which is suggested to result from the presence at pH ~ 6.5 of maleate monoanions (pK_2(maleic acid) = 6.1). Protonation of the carboxylate group probably leads to a decrease in electron density at the olefinic bond. The enhanced reaction rate of acyl, alkyl, and α-hydroxyalkyl radicals with maleate monoanion may therefore be interpreted as reflecting the nucleophilic character[7b] of these radicals. This conclusion is in agreement with the fact that the radicals described, which react with fumarate, do not observably react with hydroxyfumarate[6] or dihydroxyfumarate,[29] in which the electron density at the C=C double bond is increased by the OH group(s).

From the experimental observation that the yield of CO_2 on production of $CH_3\dot{C}O$ in the presence of fumaric acid is independent of pH in the pH region 2–10 it is concluded that un- or monodissociated fumaric acid ($pK_1 = 3.0$, $pK_2 = 4.4$) reacts in the same manner as the dianion, i.e., by eq 2. The fact that adduct radicals cannot be observed by ESR below pH ~ 5 is attributed to their much shorter lifetimes[18] when present in their monoanion or neutral forms.

On increasing the temperature of solutions under photolysis containing CH_3COR and fumarate or maleate from 0 to 30 °C, the concentration of $CH_3COCH(CO_2^-)$-$\dot{C}HCO_2^-$ decreases and that of $CH_3C(O^-)=CH\dot{C}HCO_2^-$ increases. A plot[27] of the logarithm of the ratio $[CH_3C(O^-)=CH\dot{C}HCO_2^-]/[CH_3COCH(CO_2^-)\dot{C}HCO_2^-]$ vs. $[K]^{-1}$ yielded a straight line. From its slope the activation energy for decarboxylation from the acetyl adduct to yield the allyl radical (step 2B) is calculated to be 9.5 ± 0.5 kcal/mol, taking 4.4 kcal/mol for the activation energy for diffusion of water.[30] Using the same procedure, the activation energy for decarboxylation of $CH_3CH_2COCH(CO_2^-)\dot{C}HCO_2^-$ to yield $CH_3CH_2C(O^-)=CH\dot{C}HCO_2^-$ is determined to be 9.7 ± 0.5 kcal/mol.

4. *Structure and ESR Parameters of the Adduct Radicals* $RCH(CO_2^-)\dot{C}HCO_2^-$. In Table II are summarized the g factors and coupling constants for the adduct radicals in aqueous solution at ~ 0 °C. With one exception,[31] the ESR parameters are in excellent agreement with data previously reported[8] for a number of the radicals. It is obvious that a_α is practically independent of the nature of R which demonstrates that substitution at the β position is without influence on the density of the unpaired spin at C_α. The changes of a_β on changing R must therefore result from conformational alterations induced by R. For the case of R = H the two β protons are equivalent ($a_\beta = 23.59$ G).[20] The equivalence results from free rotation about C_α–C_β as can be shown by calculating a_β on the basis of increments[32] for the carboxyl groups at C_α and C_β.[33]

a_β decreases systematically with increasing size of R which indicates that rotation about C_α–C_β becomes increasingly hindered,[34] as noted previously.[8] On the basis of the experimental a_β values the preferred conformation

of the adduct radicals is as symbolized by structure 1 (R
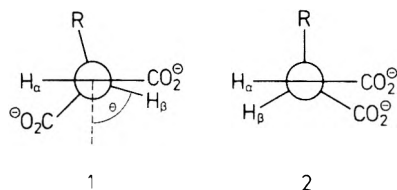
= acyl, alkyl, or α-hydroxyalkyl). Using the relation $\cos^2\theta = a_\beta(\text{obsd})/(2 \times 23.59)$, the θ values were calculated. Except for R = H, $\theta = (65 \pm 5)°$ for all the radicals listed in Table II. In all cases where R is larger than CH_3 rotation about C_β–C_γ is additionally restricted as can be seen from the magnetic nonequivalence of chemically equivalent protons at C_γ (Table II).

With respect to H_α and H_β, conformation 1 is characterized by a *transoid* configuration. If decarboxylation occurs from this conformation (R = acyl), the allyl radical conformers A and B result which are also trans with respect to H–C_1 and H–C_2, which correspond to H_α and H_β. In order for the acyl adducts to give rise to the allyl conformers C and D the acyl adducts would have to assume conformation 2, which is highly unfavorable due to steric hindrance and electrostatic repulsion between the ionized carboxyl groups.

The methylene protons at C_δ in the radical $CH_3CH_2COCH(CO_2^-)\dot{C}HCO_2^-$ are magnetically nonequivalent (Figure 2 and Table II). This indicates that rotation about C_γ–C_δ is restricted. By analogy with those alkyl adducts where R is more voluminous than CH_3 it may be assumed that rotation about C_β–C_γ is also hindered. If this is the case there are two subgroups for conformation 1, i.e., 1.1 and 1.2. Conformers 1.1 and 1.2 result in the
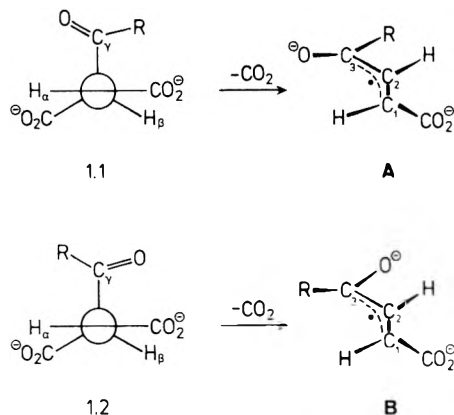
allyl radical conformers A and B, respectively. The increase with increasing size of R in the ratio [A]/[B] (Table I) is attributed to preference for conformation 1.1 as compared to conformation 1.2, in which, according to molecular models, considerable steric interaction between R and the CO_2^- group at C_β is possible if R is larger than CH_3.

Conclusion

It has been shown that acyl radicals react with fumarate and maleate by addition to yield α,β-dicarboxyalkyl radical dianions which undergo a heterolytic decarboxylation

reaction to yield 1-carboxy-3-oxyallyl radical dianions and CO_2. Maleate and, especially, fumarate may thus be used as sensitive probes for the detection of acyl radicals, which are extremely difficult to observe directly by ESR due to the broad lines of their ESR spectra at ambient temperatures. Identification of the acyl radicals is possible since the coupling constants of the protons at C_4 and C_5 of the allyl radical (the former protons at C_β and C_γ of the acyl radical) are generally larger than the line width of the allyl radicals. Furthermore, in systems containing fumarate or maleate, the production of CO_2 seems to be a specific indicator for acyl radicals. Measurement of CO_2 in such systems may thus provide a method for quantitative determination of the yields of acyl radicals produced in photo or radiation chemical reactions.

References and Notes

(1) H. Paul and H. Fischer, *Helv. Chim. Acta*, **56**, 1575 (1973).
(2) M. J. Perkins and B. P. Roberts, *J. Chem. Soc., Perkin Trans. 2*, 297 (1974).
(3) H. Zeldes and R. Livingston, *J. Am. Chem. Soc.*, **90**, 4540 (1968).
(4) B. C. Gilbert, J. P. Larkin, and R. O. C. Norman, *J. Chem. Soc., Perkin Trans. 2*, 1272 (1972).
(5) S. Steenken and D. Schulte-Frohlinde, *Angew. Chem.*, **87**, 250 (1975); S. Steenken, E. D. Sprague, and D. Schulte-Frohlinde, *Photochem. Photobiol.*, **22**, 19 (1975).
(6) S. Steenken, *Photochem. Photobiol.*, **22**, 157 (1975).
(7) For a review see (a) C. Walling, "Free Radicals in Solution", Wiley, New York, N.Y., 1957, p 273, and (b) F. Minisci, *Top. Current Chem.*, **62**, 1 (1976).
(8) P. Neta, *J. Phys. Chem.*, **75**, 2570 (1971).
(9) S. Steenken, W. Jaenicke-Zauner, and D. Schulte-Frohlinde, *Photochem. Photobiol.*, **21**, 21 (1975).
(10) F. Weeke, E. Bastian, and G. Schomburg, *Chromatographia*, **7**, 163 (1974).
(11) R. W. Fessenden, *J. Chem. Phys.*, **37**, 747 (1962).
(12) J. G. Calvert and J. N. Pitts, "Photochemistry", Wiley, New York, N.Y., 1966.
(13) B. Blank, A. Henne, and H. Fischer, *Helv. Chim. Acta*, **57**, 920 (1974).
(14) K. Eiben and R. W. Fessenden, *J. Phys. Chem.*, **75**, 1186 (1971).
(15) H. Schultze and D. Schulte-Frohlinde, *Z. Naturforsch. B*, **29**, 91 (1974).
(16) The radical $CH_3CH(OH)CH(CO_2^-)\dot{C}HCO_2^-$ was also observed. This species is formed by reaction of e_{aq}^- with acetaldehyde followed by protonation and addition to fumarate (see ref 8).
(17) H. Fischer, K.-H. Hellwege, and M. Lehnig, *Ber. Bunsenges. Phys. Chem.*, **72**, 1166 (1968).
(18) M. Simic, P. Neta, and E. Hayon, *J. Phys. Chem.*, **73**, 4214 (1969).
(19) J. K. Kochi and P. J. Krusic, *Chem. Soc., Spec. Publ.*, **No. 24**, 154 (1970).
(20) G. P. Laroff and R. W. Fessenden, *J. Chem. Phys.*, **55**, 5000 (1971).
(21) K.-G. Seifert and J. Bargon, *Angew. Chem.*, **85**, 768 (1973).
(22) H. Paul, *Chem. Phys. Lett.*, **32**, 472 (1975).
(23) S. Steenken, to be submitted for publication.
(24) M. Simic, P. Neta, and E. Hayon, *J. Phys. Chem.*, **77**, 2662 (1973).
(25) As determined by ESR measurements on the sites of H abstraction by OH from methylsuccinate at pH 7.
(26) S. Adam, H. Güsten, S. Steenken, and D. Schulte-Frohlinde, *Justus Liebigs Ann. Chem.*, 1831 (1974).
(27) E. J. Hamilton and H. Fischer, *Helv. Chim. Acta*, **56**, 795 (1973).
(28) As concluded from corresponding measurements using fumarate instead of maleate and as judged from pK_a values of similar radicals reported in ref 17 and 18.
(29) A similar observation is reported in ref 8.
(30) From an Arrhenius plot of fluidity data obtained from Landolt-Börnstein, Vol. a, "Transport Phenomena I", Berlin, 1969, p 581.
(31) It is suggested that the radical described in ref 8 is the formylmethyl adduct $HC(O)CH_2CH(CO_2^-)\dot{C}HCO_2^-$, formed by base-catalyzed elimination of OH^- from $HOCH_2\dot{C}HOH$ (K. M. Bansal, M. Grätzel, A. Henglein, and E. Janata, *J. Phys. Chem.*, **77**, 16 (1973)) followed by addition of $\dot{C}H_2CHO$ to fumarate.
(32) H. Fischer, *Z. Naturforsch. A*, **20**, 428 (1965).
(33) Relevant ESR data were taken from W. C. Vasudeva, *J. Chem. Soc., Perkin Trans. 2*, 697 (1975).
(34) In support of restricted rotation about C_α–C_β, $CH_3\dot{C}(CO_2^-)CH_2CO_2^-$, a radical closely related to those discussed, shows an alternating line width effect involving methylene protons.

Electrical Conductivity of Cadmium Oxide

Jae Shi Choi, **Young Hwan Kang, and Keu Hong Kim**

Department of Chemistry, Yonsei University, Seoul, Korea *(Received May 19, 1976; Revised Manuscript Received August 31, 1977)*

The electrical conductivity of n-type polycrystalline CdO has been measured from 25 to 650 °C under oxygen pressures, P_{O_2}, of 10^{-5} to 10^2 mmHg. Plots of log σ vs. T at constant oxygen pressure are found to be linear, and the conductivity dependence of oxygen pressure at the above temperature range is closely approximated by $\sigma \propto P_{O_2}^{-1/6}$. The conductivities of specimens pretreated in Cd vapor at different temperatures are higher than those of the specimens before treatment. This shows that the concentration of conduction electrons is associated with an excess of Cd or a deficiency of oxygen. It was also found that, for a given oxygen pressure, the slope of log σ vs. T is positive up to about 400 °C, then becoming negative for further increase in temperature. This is explained by the increasing number of free electrons and by the effect of the scattering mechanism on the electrons which are presumed to originate from the nonstoichiometric excess of Cd atoms in interstitial positions or from the oxygen vacancy donors.

Introduction

It is well known that cadmium oxide is a n-type semiconductor with semimetallic conductivity due to the fact that it has an excess of cadmium atoms in it. The physical properties of cadmium oxide along with its defect structure have been extensively investigated. Several papers have been published on compressed tablets[1,2] and sputtered films[3-5] of the oxide.

Nevertheless, there is no agreement on whether the principal defects are cadmium interstitials or oxygen vacancies. For example, Cimino[1] and Faivre[6] have investigated the defect structure of CdO by measuring the lattice parameter and concluded that Cd interstitials are the important defects. Koffyberg[7] also concluded that the principal defects in nonstoichiometric CdO are cadmium interstitials. Haul,[8] however, found through lattice diffusion studies that the predominating defects are oxygen vacancies and showed that the proportion of vacancies can be estimated, giving a value of 4.4×10^{-4} for pure CdO at 790 °C and 0.16 atm of O_2. Lakshmanan[4] also found from the optical and electrical properties of CdO films that the principal defects are oxygen vacancies.

The purpose of the present investigation is to determine the principal defects in CdO and to explain the electrical conduction mechanism of the oxide by measuring its electrical conductivity under various conditions.

Experimental Section

Specpure cadmium rod 1.0 cm in diameter supplied by the Johnson-Mathey Co. was used in the preparation of CdO. The rod was cut into sheet, etched in dilute nitric acid, washed with distilled water, and then kept in a vacuum desiccator. Oxidation was carried out in air at 300 °C for 640 h or more in a platinum crucible with quenching in air. The prepared sample was pulverized in an agate mortar. After drying at 200 °C for several hours, it was compressed into pellets under a pressure at 600 kg/cm² under vacuum. A sample from the complete oxidation of the cadmium sheet was identified as CdO by x-ray (Cu Kα) diffraction. The prepared samples were ground with no. 1/10 emery paper and then the pellets were cut into rectangular form with dimensions of 0.2 cm × 0.5 cm × 0.9 cm. Each sample was etched in 20% $(NH_4)_2S_2O_8$ and dilute nitric acid and washed with distilled water, dried, and then annealed in air at 900 °C. After annealing, each was quenched rapidly to room temperature.

TABLE I: Impurities in CdO Prepared from the Cadmium Metal Detected by Spectroscopic Analysis

Element	Impurities, ppm	Element	Impurities, ppm
Al	5	Cu	<1
Ca	4	Mg	<1
Si	1	Na	<1
Cr	<1	Fe	<1

The impurities detected by emission spectroscopy are shown in Table I. The sample was chocolate brown and had a density of 7.0 g/cm³.

The samples (hereafter called CdO-II, -III, -IV) for probing the true defects of cadmium oxide were prepared from the oxide (CdO-I) in the following manner: they were obtained by heating the CdO-I with cadmium metal in a Pyrex container under 10^{-5} mmHg at 577, 627, and 677 °C, respectively, for 20 h in an electric furnace, and quenched in air. After polishing with an abrasive paper, the CdO samples were etched in dilute nitric acid and 20% $(NH_4)_2S_2O_8$, and dried at 100 °C.

The main details of the furnace assembly, the conductivity measurement circuitry, and a four-probe contact model have been reported on in a previous paper.[9] The quartz sample container in the electric furnace was connected with a high vacuum system through a glass joint. Conductivity was measured by Valdes' method.[10] When all the distances between adjacent probes are equal ($S_1 = S_2 = S_3 = S$), and the ratio of the value of the leading edge to the first probe is greater than 2, conductivity can be calculated as follows

$$\sigma = \frac{1}{2\pi S} \frac{I}{V}$$

Here σ is the conductivity (ohm^{-1} cm^{-1}), I is the current through the sample, and V is the floating potential across the inner probes. The temperature was measured by a pyrometer connected to a thermocouple placed in the electric furnace where the sample and thermocouple were fastened in the sample container. For the potential difference (V) and current (I) measurements, a Leeds and Northrup Type K-4 potentiometer was connected to the inner probes and a Keithley Instruments 610 B electrometer connected to the outer probes. The current through the sample ranged from 4.0×10^{-3} to 9.5×10^{-2} A, and the potential between 4.4×10^{-6} and 8.5×10^{-4} V.
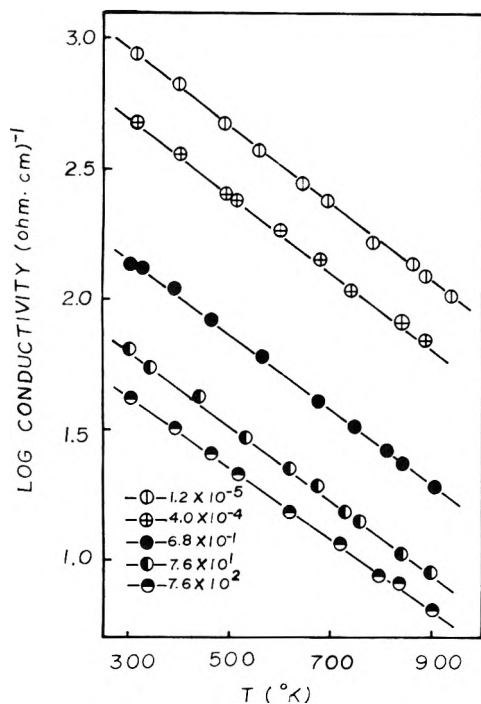
Figure 1. log conductivity vs. T for CdO under various oxygen pressures (mmHg).
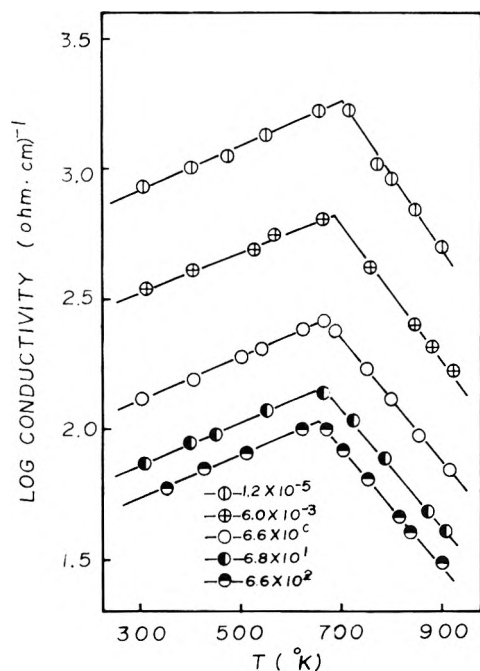
Figure 2. log conductivity vs. T for CdO pretreated with Cd at 900 K under various oxygen pressures (mmHg).

When measuring electric conductivity, the oxygen pressure required was established using pure oxygen obtained from the Matheson gas products or a mixture of 0.001% oxygen in nitrogen from the Matheson Co.

Results

The purpose of the present investigation was to determine conductivity dependence on temperature and oxygen pressure, and the type of structural defect in CdO. Measurements of conductivity were made on samples of CdO-I and CdO-III at different oxygen pressures in the region of 10^{-5} to 10^2 mmHg at various temperatures.

The conductivity measurements were reproducible and no time effects were observed in the samples in the range
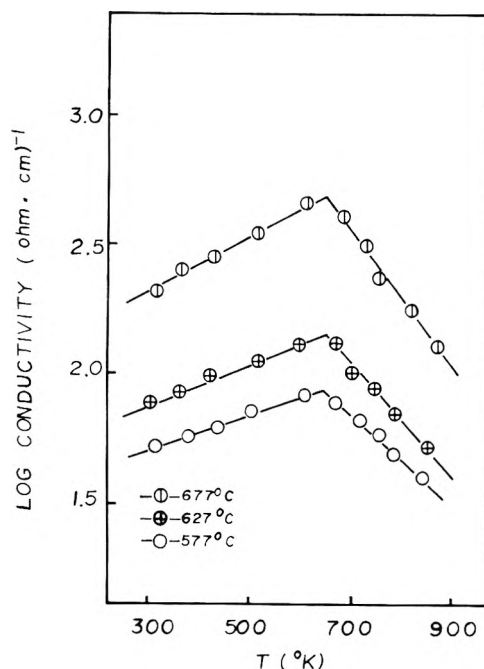
Figure 3. log conductivity vs. T for CdO pretreated with Cd at various temperatures under 6.8×10^1 mmHg.

TABLE II: $-1/n$ Values Obtained from the Equation $\log \sigma = -1/n \log P_{O_2} +$ Constant for CdO at Various Temperatures

Temp, °C	$-1/n$ values	Temp, °C	$-1/n$ values
100	$-1/5.9$	400	$-1/6.2$
200	$-1/6.0$	500	$-1/6.1$
300	$-1/6.0$	600	$-1/6.3$

of 25–650 °C where the electrical properties have been analyzed.

log σ values of CdO-I and CdO-III were plotted as a function of the absolute temperature at given oxygen pressures, as shown in Figures 1–3 which also show the temperature dependence of electric conductivity. The small decrease of conductivity with rise in temperature in CdO-I is typical of the behavior of a degenerate semiconductor. This result agrees with past reports but forms a contrast to conductivity data presented by Helwig,[3] Hogarth,[11] and Jarzebski.[12] Judging from the above data, specimen CdO-I is a n-type semiconductor. In the case of specimen CdO-III, however, the conductivity increases linearly with rise in temperature up to about 400 °C and then decreases linearly for temperatures ranging from about 400 to 650 °C; the two specimens have practically the same temperature dependence above 400 °C. The conductivity is higher than for CdO-I, and from Figure 3 it may be concluded that the conductivity varied with the cadmium vapor pressure as determined by the treatment temperature.

The influence of oxygen pressure has been studied in the range from 10^{-5} to 10^2 mmHg at given temperatures. The results are illustrated in Figures 4 and 5 which show that the conductivity at constant temperature is proportional to the concentration of free electrons. Thus, the expression for the conductivity dependence on oxygen pressure can be written as

$$\log \sigma = (-)1/n \log P_{O_2} + \text{constant}$$

The values of $(-)1/n$ are shown in Tables II and III.

Discussion

In calculating σ, there are some differences between metals and semiconductors. In metals, since the electron
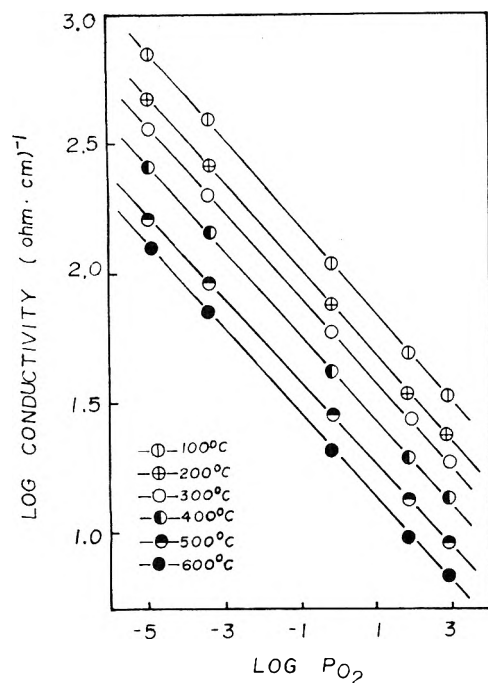
Figure 4. log conductivity vs. log P_{O_2} for CdO at various temperatures.

Figure 5. log conductivity vs. log P_{O_2} for CdO pretreated with Cd at 900 K.

TABLE III: $-1/n$ Values Obtained from the Equation $\log \sigma = -1/n \log P_{O_2}$ + Constant for CdO Pretreated with Cd at 900 K at Various Temperatures

Temp, °C	$-1/n$ values	Temp, °C	$-1/n$ values
100	$-1/6.3$	400	$-1/6.2$
200	$-1/6.2$	500	$-1/6.0$
300	$-1/6.1$	600	$-1/6.1$

concentration is constant, the parameter controlling the variation of σ is the relaxation time τ. In semiconductors, the concentration, n, is by far the most important parameter. We have

$$\sigma = (n_e e \mu_e) + (n_h e \mu_h) = |e|(n_e \mu_e + n_h \mu_h)$$

electrons	holes
in	in
conduction	valence
band	band

When we consider the mobility in intrinsic semiconductors, however, we expect the relaxation time to be limited by the same process that is operative in the case of metals: lattice scattering. Thus, the conductivity is in inverse proportion to temperature.[13]

The electrical properties of CdO are strongly dependent upon the mode of preparation. The conductivity, for example, may be either degenerate or nondegenerate depending arbitrarily on the degree of sintering, the temperature of measurement, subsequent heat treatment, etc.[14] For the degenerate type one may assume that the resistance increases with rise in temperature; in the nondegenerate type the resistance decreases with rise in temperature. Our samples are considered fully degenerate materials.

The conditions for degeneracy require a high impurity concentration and many defects. This is the case for highly doped semiconductors and metals.[15] Under the usual preparation conditions the cadmium oxide is of the oxygen deficient type. According to Koffyberg,[7] it also appears that the donors are doubly ionized over the entire temperature range, i.e., low ionization energy. Thus it may be supposed that cadmium oxide and metal are similar in

their electric properties. The difference arises as follows: in metals the activated electrons are those at the top of the Fermi surface; they have large K values or small wavelengths, and very large velocities $(V \approx V_F)$. In semiconductors the conducting electrons (or holes) are near the band edges, so as $K \to 0$, λ is large, and velocities are very low.[13] From this viewpoint the fully degenerate CdO comes under the classification as a semimetal which has low carrier concentration. As is evident from Figure 1, the conductivity decreases with increasing temperature, with the reduction of mobility due to lattice scattering.

Considering the effect of oxygen pressure on conductivity, there are two possible mechanisms based on the formation of two different defects, i.e., oxygen vacancy and Cd interstitial.

(a) *Oxygen Vacancies (CdO-I).* A transport mechanism[8] involving vacancies in the anion sublattice is proposed; oxygen vacancies (V_o) are formed together with electrons by the following disorder reaction:

$$O_o = V_o^{\cdot\cdot} + 2e' + {}^1/_2 O_2(g) \tag{1}$$
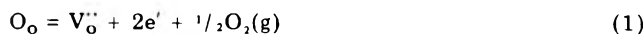
If the electrons can be associated with Cd_{Cd} ions on lattice sites, thus leading to the formation of donor terms, the following equilibrium has to be considered in this respect:

$$3Cd_{Cd} + 2O_o = 2V_o^{\cdot\cdot} + Cd''_{Cd} + 2Cd'_{Cd} + O_2(g) \tag{2}$$
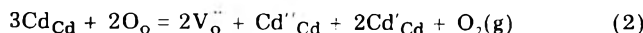
Application of the law of mass action would result

$$[V_o^{\cdot\cdot}] \propto P_{O_2}^{-3/16}$$

If it is taken into account that in eq 1 and 2 the following concentrations are the same in view of stoichiometric respect

$$2[V_o^{\cdot\cdot}] = [e'] \quad \text{and} \quad [V_o^{\cdot\cdot}] = [Cd'_{Cd}] = 2[Cd''_{Cd}]$$

substitution of these relations into the above equation gives

$$[e'] \propto P_{O_2}^{-3/16} \quad \text{or} \quad \sigma \propto [e'] \propto P_{O_2}^{-3/16} \tag{3}$$

This electrical conductivity dependence on the oxygen pressure is not consistent with the experimental value of

−1/6. This disagreement indicates that disorder in CdO cannot be represented by the above equilibria, Haul's results[8] not withstanding.

If disorder in CdO can be represented by equilibrium 1 alone, the electrical conductivity dependence on oxygen pressure can be obtained with the neutrality condition 2 $[V_o''] = [e']$ in eq 1:

$$[e'] \propto P_{O_2}^{-1/6} \quad \text{or} \quad \sigma \propto [e'] \propto P_{O_2}^{-1/6} \tag{4}$$

This predicted value of −1/6 is in good agreement with experimental dependence on oxygen pressure; disorder in CdO can be represented by eq 1.

(b) *Cadmium Interstitials (CdO-I)*. Formation of ionized cation interstitials can be represented as follows:

$$Cd_i^x = Cd_i^{\cdot} + e' \tag{5}$$

Physically, this corresponds to transferring a neutral cadmium atom from the vapor phase to an interstitial position. According to Koffyberg,[16] the interstitial cadmium ion would be completely ionized. There would be a second ionization step

$$Cd_i^{\cdot} = Cd_i^{\cdot\cdot} + e' \tag{6}$$

A combination of eq 5 and 6 results in

$$Cd_i^x = Cd_i^{\cdot\cdot} + 2e' \tag{7}$$

In the case where a doubly ionized Cd interstitial exists in CdO, the equilibrium can be written by

$$Cd_{Cd} + O_o = Cd_i^{\cdot\cdot} + 2e' + {}^1/_2O_2(g) \tag{8}$$
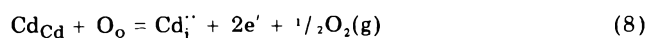
With the neutrality condition $2[Cd_i^{\cdot\cdot}] = [e']$, the oxygen pressure dependence on electrical conductivity can be obtained

$$[e'] \propto P_{O_2}^{-1/6} \quad \text{or} \quad \sigma \propto [e'] \propto P_{O_2}^{-1/6} \tag{9}$$

This predicted value of −1/6 is in good agreement with experimental dependence on oxygen pressure; in the case where a Cd interstitial exists in Cd-excess CdO, the disorder reaction can be represented by equilibrium 8.

Further evidence concerning the nature of the defect structure and conduction mechanism comes from consideration of the temperature and oxygen pressure dependences of electrical conductivity for CdO-II. These data are shown in Figures 2 and 5. The temperature dependence changes to yield maxima at about 400 °C in the log σ vs. T curve as illustrated in Figure 2. Such behavior is not similar to the results obtained for CdO-I and has not been reported in any other papers. The data in Figure 2 may be interpreted as follows: (1) below about 400 °C the newly diffused cadmium provides additional electrons which may predominate in the conduction mechanism, the concentration of conduction electrons increasing with increasing temperature and therefore so also does the conductivity; (2) above about 400 °C other mechanisms such as lattice scattering play a role in limiting the mobility.

The plots of conductivity for both CdO-I and CdO-III indicate that the slopes are the same in the region of 400–650 °C. Thus, we can say that oxidation of the diffused cadmium has occurred at about 400 °C. This result agrees well with the Vieltange report[17] that oxidation of cadmium in air is negligible up to 400 °C. As the departure from stoichiometry increases, the conductivity increases greatly. This assumption presupposes a close relationship between excess cadmium and electrical conductivity.

The results on the observed oxygen pressure dependence are summarized in Table II. According to the discussion above, the excess cadmium formed through the diffusion process can be accommodated in one of two ways.

(c) *Interstitial Cadmium (CdO-II)*.

$$Cd(g) = Cd_i^{\cdot\cdot} + 2e' \tag{10}$$

When the additional cadmium is found to be situated at interstitial positions, since the diffused cadmium is also doubly charged and so able to contribute electrons to the conduction band, the conductivity should be expressed by the relation

$$\sigma \propto P_{O_2}^{-1/6} \tag{11}$$

(d) *Oxygen Vacancies (CdO-II)*.

$$Cd(g) + O_o = V_o^{\cdot\cdot} + Cd_{Cd} + 2e' + {}^1/_2O_2(g) \tag{12}$$
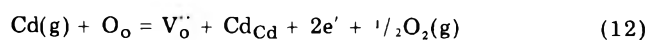
In the case where the diffused cadmium exists in the lattice site, the concentration of the electrons and doubly charged oxygen vacancies are related by eq 12. Thus, the concentration of electrons will also be a function of the ambient oxygen pressure. The electron concentration will increase with increasing cadmium vapor and oxygen pressure dependence on electrical conductivity may also be written as eq 4 according to disorder reaction 1.

The observed oxygen pressure dependence of −1/6 suggests that from the electrical conductivity measurement alone it appears impossible to distinguish between cadmium interstitial or oxygen vacancy being a predominant defect in Cd-excess CdO. The present results, therefore, imply that for CdO-I type the disorder reactions can be represented by equilibria 1 and 8, and for CdO-II type by equilibria 10 and 12.

References and Notes

(1) A. Cimino and M. Marezio, *J. Phys. Chem. Solids*, **17**, 57 (1960).
(2) R. W. Wright, *Proc. Phys. Soc., London, Sect. A*, **64**, 350 (1951).
(3) G. Helwig, *Z. Phys.*, **132**, 621 (1952).
(4) T. K. Lakshmanan, *J. Electrochem. Soc.*, **110**, 548 (1963).
(5) M. Volkmann, *Z. Angew. Phys.*, **25**, 171 (1968).
(6) R. Faivre, *Ann. Chim.*, **19**, 11 (1944).
(7) F. P. Koffyberg, *Solid State Commun.*, **9**, 2187 (1971).
(8) R. Haul and D. Just, *J. Appl. Phys.*, **33**, 487 (1962).
(9) J. S. Choi, H. Y. Lee, and K. H. Kim, *J. Phys. Chem.*, **77**, 2430 (1973).
(10) L. B. Valdes, *Proc. IRE*, **42**, 420 (1954).
(11) C. A. Hogarth, *Proc. Phys. Soc., London, Sect. B*, **64**, 691 (1951).
(12) Z. M. Jarzebski, *Bull. Acad. Pol. Sci., Ser. Sci. Chim.*, **17** (4), 221 (1969).
(13) R. A. Levy, "Principles of Solid State Physics", Academic Press, New York, N.Y., 1970, pp 381–388.
(14) E. F. Lamb and F. C. Tompkins, *Trans. Faraday Soc.*, **58**, 1424 (1962).
(15) M. M. Cohen, "Introduction to the Quantum Theory of Semiconductors", Gordon and Breach Science Publishers, New York, N.Y., 1972, pp 207–211.
(16) F. P. Koffyberg, *Can. J. Phys.*, **49**, 435 (1971).
(17) M. Vieltange, *J. Therm. Anal.*, **3**(3), 265 (1971).

Isomer Numbers of Nonrigid Molecules. The Cyclohexane Case

Jack E. Leonard

Department of Chemistry, Texas A & M University, College Station, Texas 77843 (Received May 2, 1977)

An extended Polya theorem method for computing the isomer number for any number of achiral ligands on an achiral nonrigid skeleton is discussed using cyclohexane as an example. It is shown that the primary advantage of the method is its relation to the chemist's notion of the structure's motions, removing the need for a nonrigid model system and also alleviating the possibility of error in selecting such a system on the basis of group isomorphism alone. With this extension of the Polya theorem, the number of diamutamers (isomers obtained by rearranging ligands on a skeleton) of any achiral skeleton can be computed, and the number of enantiomeric isomers distinguished without the need for inspection of physical models.

In a recent article my collaborators and I showed that the notion of point groups could be extended to include the rotations, inversions, ringflips, and fluxional motions of nonrigid molecules.[1] Furthermore, by combining this with the very powerful pattern counting method of Polya,[2] it is possible to count by group theoretical methods the number of isomers possible for such nonrigid molecules. Thus, our extension renders it possible to count by the well-established Polya theorem method[3] the number of possible isomers of an achiral skeleton substituted with any number of different achiral ligands. Furthermore, by employing the appropriate decomposition of the group (such as the removal of all rotation-reflection operators), it is possible to draw significant conclusions regarding the symmetries of the possible isomers.[4]

We illustrated these points by considering a problem of long standing in organic chemistry: counting the number of isomers of a substituted cyclohexane skeleton (Figure 1a). This problem was shown very early[1] to be reducible to the equivalent problem of counting the possible isomers of a planar projection cyclohexane (Haworth projection, Figure 1b). The Polya method for rigid molecules yields the wrong cyclohexane isomer number when applied to chair form cyclohexane (which has D_{3d} symmetry), but the correct answers for the D_{6h} Haworth skeleton. Yet the theoretical justifications for selecting the Haworth projection have been rather muddled in the literature (see ref 2-5 in ref 1). In our paper we showed that combining the point group operation R_6 (a ring flip from one chair form to another, followed by a 60° rotation to bring the final state in to alignment with the initial one; see Figure 2) with the D_{3d} symmetry of the rigid skeleton leads to a Polya cycle index which is identical with that derived from the point group D_{6h} operating on the same 12 substituent positions of the Haworth cyclohexane skeleton ($Z(D_{6h}; 12)$). Having obtained this result it is possible, from either cycle index, to calculate the number of cyclohexane isomers expected with any number of substituents. In passing it was mentioned that the permutation groups for the two groups $D_{3d}R_6$ and D_{6h} operating on appropriately labeled chair form and planar projection cyclohexane, respectively, were in fact identical.

In a response published in this Journal,[5] Flurry showed that using the established group theoretical method of the semidirect product it is much easier to show that the symmetry group of the ring flipping cyclohexane (either boat or chair) is isomorphic to D_{6h} and, further, that the method is simpler than the Polya cycle index. Indeed, it must be a simpler proof of isomorphism since, as we

TABLE I: Cycle Indices for Calculating Cyclohexane Isomer Numbers

Chairform Cyclohexane (Rigid D_{3d} Symmetry)

$$Z(D_3; 12) = \frac{1}{6}[f_1^{12} + 2f_3^4 + 4f_2^6]$$

$$Z(D_{3d}; 12) = \frac{1}{12}[f_1^{12} + 2f_3^4 + 4f_2^6 + 2f_6^2 + 3f_1^4 f_2^4]$$

Planar-Projection (Haworth) Cyclohexane = Chairform Cyclohexane (Nonrigid $D_{3d}R_6$ Symmetry)

$$Z(D_6; 12) = \frac{1}{12}[f_1^{12} + 2f_3^4 + 7f_2^6 + 2f_6^2]$$

$$Z(D_{6h}; 12) = \frac{1}{24}[f_1^{12} + 4f_3^4 + 12f_2^6 + 4f_6^2 + 3f_1^4 f_2^4]$$

All Planar Cyclohexane

$$Z(D_6; 12) = \frac{1}{12}[f_1^{12} + 2f_3^4 + 7f_2^6 + 2f_6^2]$$

$$Z(D_{6h}; 24) = \frac{1}{24}[2f_1^{12} + 4f_3^4 + 14f_2^6 + 4f_6^2] =$$

$$\frac{1}{12}[f_1^{12} + 2f_3^4 + 7f_2^6 + 2f_6^2]$$

pointed out, the Polya cycle index cannot be used to prove isomorphism: the same cycle index may be derivable from very different point sets. *If* the point sets have a similar decomposition *and* if the generating symmetry groups are identical, *then* the cycle indexes are the same; the converse does not hold.

However while misconstruing a minor point in our paper, Flurry then proceeds to obscure the major point: our method of nonrigid point groups allows a correct count of the isomers of any achiral skeleton containing any number of achiral substituents. If one were to accept his criterion of isomorphism as sufficient, then it would have to be admitted that the all planar structure (Figure 1c) provides an equally acceptable basis for counting isomers.[6] However, it can be seen immediately that no enantiomers are possible by substituting this skeleton with achiral ligands, since *all* isomers have a σ_h mirror plane. Unlike the isomorphism criterion, the Polya cycle index clearly indicates the isomer number equivalence of the nonrigid chairform cyclohexane and the rigid Haworth structure *and* the nonequivalence of either of these to the all planar cyclohexane structure (Table I). Notice that the cycle index for the rotations only group ($Z(D_6; 12)$) is the same
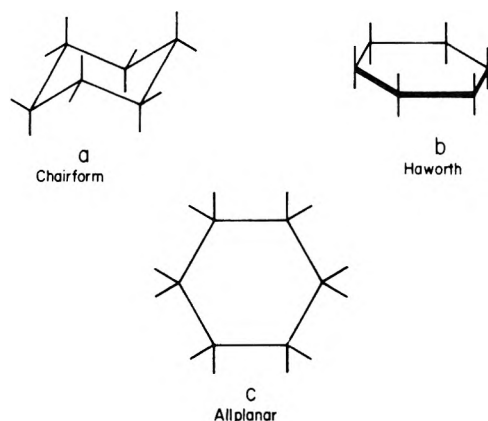
Figure 1. Representations of cyclohexane.
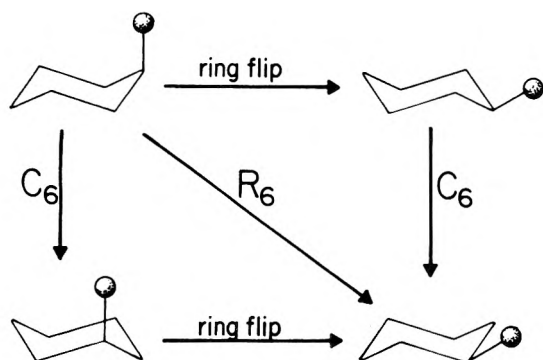
Figure 2. The ring-flip-rotation operator, R_6.

as the rotation-reflection cycle index ($Z(D_{6h}; 12)$) for the all planar structure. As we pointed out this identity means that all *diamutamers* (that is, structures obtained by permuting a fixed set of ligands on a given skeleton) are achiral, since the introduction of the nonphysical rotation-reflection operators does not reduce the number of isomers which are not interconvertible by the rotation operators alone. On the other hand, the cycle indices for the rotation group only and for the full group are not identical for the chair form and Haworth cyclohexanes, confirming that enantiomeric diamutamers (such as *trans*-1,2-dibromocyclohexane) are possible in this system.

By selecting the model of a ring flipping cyclohexane molecule for the purposes of isomer counting, we obtained as a side result the observation that the Haworth rigid structure would have to work as well, since it generates the same cycle index. On the other hand, by focusing on isomorphism Flurry has opened the door to an obviously flawed skeleton for isomer counting.

The final test of a self-consistent theoretical approach is its usefulness in actual application. From this standpoint both group isomorphism and Polya theorem calculations have been very useful and important within their own domains. The usefulness of Polya theorem isomer counts is not significantly enhanced by showing that it can be applied to a nonrigid cyclohexane because a rigid model for the system has long been available. However, the same method can be applied to many other systems such as ethane, propane, ferrocene, and dibenzenechromium for which no nonrigid isomer counting model exists.[7] Since there is no previous example of the actual use of these nonrigid point groups in the literature, an appendix illustrating their use in the cyclohexane case is included.

This method's utility is not limited solely to providing the isomer number, since it can also be used to provide symmetry information not easily obtained without physical models. Indeed, this extension of the rigid point groups now provides a means of computing the isomer number
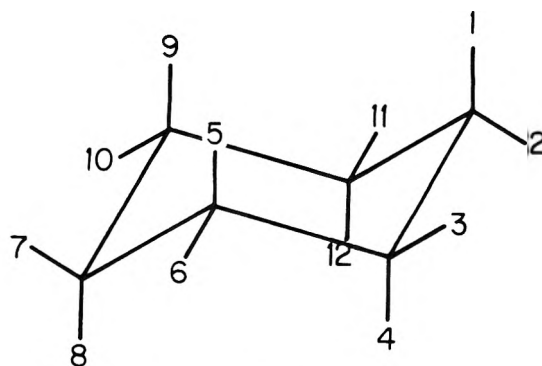
Figure 3. Numbering system for cyclohexane.

TABLE II: Isomer Numbers for the Cyclohexane Skeleton (Represented by C_6) Substituted with up to Four Achiral Ligands[a]

Formula	Diamutamers	Diastereomers	Enantiomeric pairs	Achiral isomers
C_6A_{12}	1	1	0	1
$C_6A_{11}B$	1	1	0	1
$C_6A_{10}B_2$	8	7	1	6
$C_6A_{10}BD$	11	7	4	3
$C_6A_9B_3$	19	12	7	5
$C_6A_9B_2D$	55	31	24	7
C_6A_9BDE	110	58	52	6
$C_6A_8B_4$	50	32	18	14
$C_6A_8B_3D$	165	89	76	13
$C_6A_8B_2D_2$	265	147	118	29
$C_6A_8B_2DE$	495	255	240	15
$C_6A_7B_5$	66	38	28	10
$C_6A_7B_4D$	330	174	156	18
$C_6A_7B_3D_2$	660	344	316	28
$C_6A_7B_3DE$	1320	672	648	24
$C_6A_7B_2D_2E$	1980	1008	972	36
$C_6A_6B_6$	90	55	35	20
$C_6A_6B_5D$	462	243	219	24
$C_6A_6B_4D_2$	1190	626	564	62
$C_6A_6B_4DE$	2310	1170	1140	30
$C_6A_6B_3D_3$	1542	793	749	44
$C_6A_6B_3D_2E$	4620	2336	2284	52
$C_6A_6B_2D_2E_2$	7000	3558	3442	116
$C_6A_5B_5D_2$	1386	702	684	18
$C_6A_5B_5DE$	2772	1404	1368	36
$C_6A_5B_4D_3$	2310	1173	1137	36
$C_6A_5B_4D_2E$	6930	3492	3438	54
$C_6A_5B_3D_3E$	9240	4656	4584	72
$C_6A_5B_3D_2E_2$	13860	6984	6875	108
$C_6A_4B_4D_4$	2940	1491	1449	42
$C_6A_4B_4D_3E$	11550	5814	5735	78
$C_6A_4B_4D_2E_2$	17430	8784	8646	138
$C_6A_4B_3D_3E_2$	23100	11616	11484	132
$C_6A_3B_3D_3E_3$	30804	15474	15330	144

[a] See text for meaning of terms.

for any substitution of an achiral skeleton with achiral ligands.

Appendix

Calculation of Isomer Numbers for Nonrigid Molecules Using Extended Point Groups and Polya's Method. An Illustrative Example. Step 1. Generating the Nonrigid Point Groups: $D_{3d}R_6$. Chair form cyclohexane has D_{3d}

symmetry. The new operation introduced to reflect the nonrigidity of this system, R_6, has the following self-multiplication:

$$R_6, R_6^2 \ (=C_3), R_6^3, R_6^4 \ (=C_3^2), R_6^5, R_6^6 \ (=E)$$

Thus, multiplication of the group D_{3d} by the R_6 operator yields the group $D_{3d}R_6$ with the operations: E, $2R_6^2$, $2C_3$, R_6^3, $3R_6 \cdot C_2$, i, $2i \cdot R_6$, $2S_6$, $i \cdot R_6^3$, $3\sigma_v \cdot R_6$

Step 2. The Cycle Index. Polya's pattern counting method depends on developing a polynomial to represent the allowed permutations of ligands on the skeleton. Since the point group shows all allowed permutations on the skeleton, we can conveniently use it to generate this "cycle index". The operator C_3 operating on the numbered cyclohexane in Figure 3 can be represented by the following permutation:

$$C_3 = (1\ 5\ 9)(2\ 6\ 10)(3\ 7\ 11)(4\ 8\ 12)$$

where (1 5 9) is read "position 1 is permuted to position 5 which is permuted to position 9 which is permuted to position 1". Since this cycle of the permutation permutes 3 elements, it is an f_3 cycle. Since four f_3 cycles are required to permute all twelve elements, this entire permutation can be represented as f_3^4. For a second example, the operation σ_v corresponds to the permutation

$$(1)(2)(3\ 11)(4\ 12)(5\ 9)(6\ 10)(7)(8) = f_1^4 f_2^4$$

Notice that $(1 \times 4) + (2 \times 4) = 12 =$ number of points permuted. For the full rotation-reflection group, then, the cycle index (normalized by dividing by the number of operations) is

$$Z(D_3R_6;\ 12\ \text{points}) = {}^1\!/_{12}[f_1^{12} + 2f_3^4 + 7f_2^6 + 2f_8^2]$$

Notice that if we only employ the *rotation* operations (including R_6) the cycle index is

$$Z(D_{3d}R_6;\ 12) = {}^1\!/_{24}[f_1^{12} + 4f_3^4 + 12f_2^6 + 4f_6^2 + 3f_1^4 f_2^4]$$

Step 3. Generation of the Characteristic Polynomial. If we wish to find out how many isomers there are of the form, say, $D_6A_4B_4D_2E_2$ (where A, B, D, and E represent achiral ligands), we need to substitute $(a^n + b^n + d^n + e^n$

$= \sum x_i^n)$ for each f_n in the cycle index:

$$Z(D_3R_6;\ 12) = {}^1\!/_{12}[(\Sigma x_i)^{12} + 7(\Sigma x_i^2)^6 + 2(\Sigma x_i^3)^4 + 2(\Sigma x_i^6)^2]$$

Step 4. Calculation of the Isomer Numbers. The total number of $C_6A_4B_4D_2E_2$ isomers is the coefficient of the term $a^4b^4d^2e^2$ in the expansion of the rotations-only cycle index, $Z(D_3R_6;\ 12)$. The isomer number is shown under the heading Diamutamers in Table II. By allowing for the nonphysical symmetry operations of the rotation-reflection group (using $Z(D_{3d}R_6;\ 12)$) we can reduce the isomer number to only the diastereomers. By further manipulations, then, we can determine the number of enantiomeric pairs $(Z(D_3R_6;\ 12) - Z(D_{3d};\ 12))$ and the number of achiral isomers (diastereomers–enantiomeric pairs). Incidentally, the table does not show it, but for a cyclohexane skeleton substituted with 12 different achiral ligands there are a total of 39 916 800 diamutamers, all of which are chiral, so that there are 19 958 400 enantiomeric pairs. The most complex substitution of the cyclohexane skeleton which still has achiral isomers is $C_6A_2B_2D_2E_2FGHI$. This substitution produces a total of 2 494 800 diamutamers of which 144 are achiral.

Using other nonphysical permutation operators it is possible to count positional isomers separately[4b] and probably other significant classes of molecules. We are currently attempting to computerize these calculations.

References and Notes

(1) J. E. Leonard, G. S. Hammond, and H. E. Simmons, *J. Am. Chem. Soc.*, **97**, 5052 (1975).

(2) (a) G. Polya, *C.R. Hebd. Seances Acad. Sci.*, **201**, 1167 (1935); (b) G. Polya, *Helv. Chim. Acta*, **19**, 22 (1936); (c) G. Polya, *Z. Kristallogr., Kristallgeom., Kristallphys., Kristallchem.*, **93**, 415 (1936); (d) G. Polya, *Acta Math.*, **68**, 145 (1937).

(3) B. A. Kennedy, D. A. McQuarrie, and C. H. Brubaker, Jr., *Inorg. Chem.*, **3**, 265 (1964); J. Sala-Pala and J. E. Guerchais, *C.R. Hebd. Seances Acad. Sci., Ser. C*, **268**, 2192 (1969); A. J. Menez, J. Sala-Pala, and J. E. Guerchais, *Bull. Soc. Chim. Fr.*, 46 (1970).

(4) (a) T. Hill, *J. Phys. Chem.*, **11**, 294 (1943); (b) W. J. Taylor, *ibid.*, **11**, 532 (1943).

(5) R. L. Flurry, Jr., *J. Phys. Chem.*, **80**, 77 (1976).

(6) I am indebted to Dr. D. Tavernier, Rijksuniversiteit-Gent, Belgium, for having brought this representation to my attention.

(7) J. E. Leonard, Thesis, California Institute of Technology (1971); *Diss. Abstr.*, **32B**, 5659 (1972). An earlier study on isomerism of ferrocenes (K. Schlögl, *Top. Stereochem.*, **1**, 39 (1967)) has the isomer numbers for the following formulas in error: XA7B2D and XA7BDE, where X is the ferrocene skeleton.

The American Chemical Society is pleased to offer two valuable services designed to help you escape drowning in a sea of publications. . . .

The **ACS Single Article Announcement.** A service available to both ACS members and nonmembers, the *ACS Single Article Announcement* is a semimonthly current awareness service based on 18 ACS journals. The announcement consists of the tables of contents from the latest issues of these journals. Single copies of articles (as tearsheets) may be ordered for a small charge.

The **ACS Customized Article Service.** Available to ACS members *only*. You may subscribe to this semimonthly service, featuring a comprehensive selection of articles from all ACS journals except *Chemical & Engineering News* and *Chemistry*. You'll receive the complete articles (on microfiche) and not just a list of references. Along with these,

you'll receive monthly hard copies of *Environmental Science & Technology*, or the *Journal of Medicinal Chemistry*, or *Biochemistry*, depending upon your choice of subject area. In addition, we'll send you the semimonthly *ACS Single Article Announcement*. Incidentally, if you have already entered your subscription to the journal included with your choice of subject area, just deduct the amount of the subscription (half the amount for a half-year subscription) from the price of the service.

Should either service not meet your expectations, we'll send you a refund for the unmailed portion of your subscription.

If you would like additional information or a sample of either service, please write to Dr. Lorrin R. Garson, Room 601, American Chemical Society, 1155 Sixteenth Street, N.W., Washington, D.C., 20036, USA.